Preliminary Design of a Small Hydrogen Peroxide Cooled Thrust Chamber for Additive Manufacturing

Fabio Kerstens

Master Thesis
Faculty of Aerospace Engineering
Department of Space Engineering

TU Delft

Preliminary Design of a Small Hydrogen Peroxide Cooled Thrust Chamber for Additive Manufacturing

by

Fabio Kerstens

In partial fulfillment of the requirements for the degree of

Master of Science in **Aerospace Engineering**

at Delft University of Technology,

to be defended publicly on Wednesday May 26, 2021 at 9:00 AM.

Student number:	4435796	
Supervisor:	Dr. A. Cervone	
Thesis committee:	Dr. J. Guo	TU Delft
	Dr. A. Cervone	TU Delft
	Ir. R. Noomen	TU Delft
	V. R. Huijsman MSc.	Dawn Aerospace

TU Delft

Preface

In front of you lies my thesis “Preliminary Design of a Small Hydrogen Peroxide Cooled Thrust Chamber for Additive Manufacturing”, written as a part of the Delft University of Technology course AE5810 “Thesis Space” to obtain the title of Master of Science. The study was performed at the startup space company, Dawn Aerospace, located in Delft (the Netherlands) and Christchurch (New Zealand) as a part of a “Future Launcher Preparatory Project” contract issued by the European Space Agency.

Over the full project duration, the world was facing a major crisis, in the form of the Covid-19 pandemic. Although I initially expected that this would not impact the project at all, reality turned out to be different. The last year, I spent most of my time in a small room, whilst living under the strict lockdown and isolation requirements set by the government. Not being able to physically meet up with friends, family, fellow students, or go to events in my free time, made my world extremely small and greatly impacted my overall happiness. At these times, you start realizing how much you value the simple things in life, such as having a nice chat with a fellow student at a coffee machine.

In those dark times, I cannot stress enough how valuable the advice and guidance of TU Delft supervisor Dr. Angelo Cervone has been. Although we have not been able to meet up in person during this project, the regular online update meetings and discussions proved of great value for this work.

I also want to thank Ralph Huijsman, the supervisor within Dawn Aerospace. Ralph helped me a lot from the Christchurch office in terms of the preparation of experiments and his advice during our weekly meetings. From Dawn Aerospace, I also want to acknowledge Peter van den Berg, Jeroen Wink, Felix Lindemann, Kapeel Samarawickrama, and Andreas Fischer for the fruitful discussions we had. Related or unrelated to the topic of this thesis. From NASA Marshal Space Flight Center, I want to acknowledge Paul Gradl, who repeatedly shared his industry experience in the field of additive manufacturing of liquid rocket engines. The positive collaboration with Paul Gradl, as well as Dr. Angelo Cervone, has resulted in a recently published article in the Acta Astronautica journal. Many thanks also go out to my former English teacher, Ad Stofmeel, who helped me with the final grammar and spell-check of this report.

Last but not least, I want to thank my friends and family. In particular, I want to mention my mother and brother, who always tried to bring out the best in me. Although the last few years have been quite turbulent, I could not have wished for better support. I would like to dedicate this research to my father, who has always been a true mentor for me and is now guarding me from heaven: I hope this work makes you proud.

Fabio Kerstens
Roosendaal, April 2021

Summary

Dawn Aerospace is a startup company that is developing a commercial launch vehicle solution for small spacecraft in the form of a reusable (sub)orbital spaceplane. This vehicle, designated Mk-II, is a rocket-powered supersonic plane that can take off and land at regular commercial airports. The vehicle is powered by a small bipropellant thruster which consumes the storable propellants 90% hydrogen peroxide and kerosene. To avoid the wall from melting, the thrust chamber is regeneratively cooled with hydrogen peroxide. The current thrust chamber follows a traditional bimetallic design which comprises a copper alloy liner that is placed in a high-strength closeout structure. A fundamental challenge of the design lies in the known catalytic behavior of copper alloys with hydrogen peroxide. Therefore, a proprietary coating must be applied on the cooling channels, to avoid direct contact between the copper alloy and hydrogen peroxide.

The current bimetallic Mk-II thrust chamber design is labor-intensive to fabricate and features a high part-count. For a second iteration of the thruster, Dawn Aerospace wants to investigate the use of an integral structure, fabricated with novel additive manufacturing (AM) techniques. To develop this AM thrust chamber, Dawn Aerospace has received a 385 k€ contract from the European Space Agency, as a part of the Future Launcher Preparatory Programme. In this work, a preliminary design study is provided for the AM thrust chamber. The proposed design is compared to the current, bimetallic, thrust chamber to estimate the impact on propulsive performance, dry mass, and pressure budget. The metal alloy that is considered for the AM thrust chamber is Inconel 718, which is selected for its (demonstrated) chemical compatibility with highly concentrated hydrogen peroxide.

For the preliminary design of the AM Mk-II thruster, a hybrid 1-D/2-D thrust chamber analysis software is developed. The software can be used to estimate the heat transfer in thrust chambers that rely on regenerative cooling, film cooling, or a combination of both. Boundary conditions for the hot gas and coolant are implemented using semi-empirical 1-D correlation. The temperature distribution in the chamber wall is numerically resolved using the finite element method on a planar (2-D) mesh. Validation of the model is achieved based on hydrogen peroxide film cooling experiments that are described in the literature, as well as hot-fire tests of the regeneratively cooled Mk-II thruster.

Based on the developed model, a number of simulations are executed. All designs are operated at a propellant mixture ratio of 8, a total mass flow rate of 1.125 kg/s, and use hydrogen peroxide for regenerative cooling and/or film cooling. The first simulation is based on a regeneratively cooled bimetallic reference thruster, comprised of NARloy-Z/Inconel 718. This thruster has operating conditions that are comparable to the Mk-II engine but should not be interpreted as the actual design used by Dawn Aerospace. Simulations show that the maximum chamber pressure for this design is 5 MPa, which is primarily constrained by burnout heat transfer constraints that are imposed by the hydrogen peroxide coolant. For the AM Inconel 718 design, a chamber pressure of 2 MPa is achievable, when relying solely on regenerative cooling. This pressure is primarily constrained by the maximum service temperature of the thrust chamber. For this design, a chamber pressure of 5 MPa is in range, when a hydrogen peroxide film coolant is injected near the wall of the thrust chamber. The film flow rate required in this design is 10% of the total mass flow rate.

A comparison of the film-cooled AM chamber to the bimetallic reference design shows a decrease in the vacuum specific impulse of 2.3%. From a mission-wide perspective, the design change corresponds to a change in the available Δv (delta-v) from 3.46 km/s to 3.38 km/s. The AM chamber without film cooling performs slightly worse and has a total available Δv of 3.28 km/s. When only considering the thruster performance, it is not beneficial to replace the bimetallic design with an AM design. The primary strength of the AM solution is that only one part is used for the thrust chamber. As a result, the total number of sealing interfaces can be reduced by more than 50%. Moreover, the proprietary coating that is required on the cooling channels can be mitigated, which has a positive impact on the manufacturing cost, as well as inspection time between hot-fire tests.

Contents

1 Introduction **1**
- 1.1 Additive Manufacturing of Thrust Chambers . . . 3
- 1.2 Hydrogen Peroxide in Rocketry Applications . . . 5
- 1.3 Mk-II Engine Development at Dawn Aerospace . . . 6
- 1.4 ESA Future Launcher Preparatory Programme . . . 7
- 1.5 Research Objective and Questions . . . 9
- 1.6 Thesis Structure . . . 10

2 Numerical Model **11**
- 2.1 Fluid Properties . . . 13
- 2.2 Thrust Chamber Sizing and Computational Domain . . . 18
- 2.3 Hot Gas Heat Transfer . . . 24
- 2.4 Regenerative Cooling . . . 27
- 2.5 Film Cooling . . . 35
- 2.6 Numerical Solution in the Solid Domain . . . 40
- 2.7 Chapter Summary . . . 45

3 Model Verification **46**
- 3.1 Grid Convergence Study . . . 46
- 3.2 Hot Gas Heat Transfer . . . 49
- 3.3 Wall Temperatures . . . 50
- 3.4 Mechanical Domain . . . 52
- 3.5 Chapter Summary . . . 55

4 Experimental Validation **56**
- 4.1 Rough Channel Heat Transfer Experiments in the Literature . . . 56
- 4.2 Film Cooling Experiments in the Literature . . . 60
- 4.3 Regenerative Cooling Experiments of the Mk-II Thruster . . . 68
- 4.4 Inconel 718 Immersion Screening Test . . . 79
- 4.5 Chapter Summary . . . 84

5 Model Results and Discussion **85**
- 5.1 Design Study Guidelines . . . 85
- 5.2 Bimetallic Reference Thrust Chamber . . . 90
- 5.3 Integral Additive Manufactured Inconel 718 Thrust Chamber . . . 92
- 5.4 Comparison of Design Options . . . 100
- 5.5 Discussion . . . 105

6 Conclusions and Recommendations **108**

Bibliography **110**

A Preliminary Test Plan ESA FLPP Project **116**

B Specifications of the Verification Engine **118**

C Additional User Information for TDCAS **119**

D Publication Acta Astronautica **123**

List of Figures

1.1 Schematic representation of regenerative cooling and a combination of regenerative and film cooling in the application of a bipropellant thruster propelled by hydrogen peroxide and kerosene. . . . 2
1.2 Manufacturing techniques used for the production of the Vulcain thrust chamber of Ariane 5 vehicle. . . . 3
1.3 State-of-the-art integral additively manufactured thrust chambers in the industry propelled by liquid oxygen and kerosene. . . . 4
1.4 Overview of the engine development for the Mk-II spaceplane. . . . 7
1.5 Overview of work packages of the ESA FLPP project. . . . 8

2.1 High level program architecture of TDCAS. . . . 12
2.2 Evolution of Mach number, specific heat ratio, and gas pressure in the verification engine. 13
2.3 Dynamic viscosity of 90% hydrogen peroxide. . . . 15
2.4 Liquid-vapor equilibrium of 90% hydrogen peroxide and water. . . . 17
2.5 Enthalpy change of vaporization for anhydrous hydrogen peroxide and water. . . . 18
2.6 Cartesian and cylindrical coordinate system and placement with respect to the thrust chamber. . . . 19
2.7 Ideal characteristic velocity of hydrogen peroxide-kerosene mixtures compared to frequently used storable and hydrocarbon propellant combinations. . . . 20
2.8 Structured quadrilateral planar mesh that is automatically generated by TDCAS. . . . 22
2.9 Thrust chamber resembled by planar mesh elements with uniform (coarse) spacing Δz. 22
2.10 Vacuum and sea level specific impulse as a function of the exit pressure. . . . 23
2.11 Schematic representation of thermal boundary layer in a rocket engine. . . . 25
2.12 Schematic representation showing the impact of build angle on surface roughness, compared to rectangular additively manufactured Inconel 718 test articles. . . . 29
2.13 Correlation between surface roughness, build angle, and hydraulic diameter in AM Inconel 718 cooling channels. . . . 30
2.14 Experimental data for heat transfer similarity function in Equation 2.38, as a function of the roughness Reynolds number. . . . 31
2.15 Schematic representation of axial boundary layer development at the entrance of the cooling channel. . . . 32
2.16 Derived wall temperatures for heat transfer experiments with 98% hydrogen peroxide in AISI 304, AISI 347, and Inconel 718 tubes . . . 33
2.17 Experimental burnout heat flux data for 90% and 98% hydrogen peroxide in Inconel 718 tubes. . . . 34
2.18 Experimental and simulation data for a small MMH film-cooled thruster, which clearly shows the transition from liquid to gaseous film cooling. . . . 35
2.19 Liquid film effectiveness as a function of the film Reynolds number. . . . 36
2.20 Relation between gaseous film effectiveness and entrainment flow ratio. . . . 39
2.21 Schematic overview of the architecture of the finite element solution algorithm in TDCAS. 42
2.22 Schematic overview of computational domain and boundary conditions. . . . 43

3.1 Impact of refinement depth parameter on generated planar mesh. . . . 46
3.2 Axial spacing convergence study for coolant temperature. . . . 47
3.3 Axial spacing convergence study for coolant pressure. . . . 47
3.4 Thermal domain mesh refinement study for node A, with refinement depth based on Figure 3.1. . . . 48
3.5 Mechanical domain mesh refinement study for nodes A-H, with refinement depth based on Figure 3.1. . . . 48

3.6 Comparison of hot gas convective heat transfer coefficient and adiabatic wall temperature predicted by TDCAS and RPA under a uniform wall temperature of 900 K. 49
3.7 Comparison of predicted wall temperatures by TDCAS and RPA for a constant wall thermal conductivity with 1-D and 2-D thermal solution. 50
3.8 Comparison of wall temperature at the nozzle throat, predicted using TDCAS and Ansys 2020 R2. 51
3.9 Unit hoop stress test in TDCAS with pressure vessel geometry. 53
3.10 Comparison of nodal displacement at the nozzle throat, predicted using TDCAS and Ansys 2020 R2. 53
3.11 Invalid equivalent stress at the throat plane and arbitrary stress-strain diagram of a ductile metal. 54

4.1 Schematic representation of test setup and typical additively manufactured test article used in the heat transfer studies of Stimpson et al. and Wildgoose et al. 57
4.2 Error in prediction of AM channel Nusselt number for different roughness models as a function of the Reynolds number and friction factor augmentation. 59
4.3 Hot-fire test of hydrogen peroxide film-cooled research thruster of Heo et al. 60
4.4 Wall temperature measurements in the film-cooled thruster of Heo 62
4.5 Comparison of film cooling measurements with simulation Heo and TDCAS for test HEO-F1. 63
4.6 Comparison of film cooling measurements with simulation Heo and TDCAS for test HEO-F2. 64
4.7 Schematic representation of liquid film distribution over perimeter of wall. 65
4.8 Comparison of film cooling measurements with simulation Heo and TDCAS for test HEO-F3. 66
4.9 Static test bench of Dawn Aerospace with instrumented thrust chamber assembly. . . . 68
4.10 High-level pressure-fed and pump-fed feed system architecture of the Mk-II engine that are used in thesis validation experiments in future ESA FLPP experiments. 69
4.11 Normalized experimental data for Mk-II engine test 31. 70
4.12 Hot-fire test of the Mk-II thruster at the test facility in New Zealand. 71
4.13 Integrated coolant heat load, chamber pressure, and mixture ratio for Mk-II bipropellant engine tests. 72
4.14 Theoretical and experimental characteristic velocity efficiency of the Mk-II thruster. . . . 73
4.15 Measured pressure drop in coolant passages during water flow tests of the Mk-II, compared to simulations. 74
4.16 Carbon layer thermal resistance in hydrocarbon thrusters operated with film cooling, compared to the carbon atom fraction in the combustion gas of 88% hydrogen peroxide and kerosene at a mixture ratio of 4, 6 and 6. 76
4.17 Correlation between energy balance and hot gas heat flux to coolant velocity ratio in heat transfer experiments with 98% hydrogen peroxide in Inconel 718 and AISI 347 tubes. . 78
4.18 Typical AM Inconel 718 test article which is used in the immersion screening tests. . . . 79
4.19 Laboratory setup used for immersion screening tests. 80
4.20 Immersion screening test of AM Inconel 718 in concentrated hydrogen peroxide at ambient temperature and pressure, showing significant bubble formation at the surface of the unpassivated specimen. 81
4.21 Immersion screening test with AM Inconel 718 at 343 K, showing boiling-like phenomena. 82
4.22 Microscope image of a passivated test article before and after immersion in hydrogen peroxide at ambient conditions and at 343 K. 83

5.1 Predicted sea level and vacuum specific impulse at different chamber pressures with operating boundaries at a fixed nozzle exit pressure and specific impulse quality factor. 88
5.2 Predicted sea level and vacuum thrust at different chamber pressures with operating boundaries at a fixed nozzle exit pressure, thrust coefficient quality factor and mass flow rate. 88
5.3 Predicted adiabatic flame temperature for the combustion of 90% hydrogen peroxide and kerosene, with nominal and off-design operating points. 90

5.4 Parameter study showing the maximum gas side wall temperature and heat transfer limits for a bimetallic NARloy-Z/Inconel 718 thrust chamber as a function of chamber pressure, wall thickness, and channel count, at a constant cooling channel size of 0.8×0.8 mm. 91
5.5 Cooling channel geometry and coolant temperature and pressure for the bimetallic NARloy-Z/Inconel 718 thrust chamber design, at a chamber pressure of 5 MPa and mixture ratio of 8. 91
5.6 Gas side wall temperatures and hot gas heat flux for the bimetallic NARloy-Z/Inconel 718 thrust chamber design, at a chamber pressure of 5 MPa and mixture ratio of 8. . . . 92
5.7 Parameter study showing the maximum wall temperature and heat transfer limits for a regeneratively cooled AM Inconel 718 chamber, at constant cooling channel size of 0.8×0.8 mm and wall thickness of 0.5 mm. 93
5.8 Cooling channel geometry and coolant temperature and pressure for an AM Inconel 718 thrust chamber, at a chamber pressure of 2 MPa and mixture ratio of 8. 94
5.9 Gas side wall temperatures and hot gas heat flux for an AM Inconel 718 thrust chamber, at a chamber pressure of 2 MPa and mixture ratio of 8. 94
5.10 Impact of rib width and channel count on temperature distribution at the throat of the AM Inconel 718 thrust chamber with a chamber pressure of 2 MPa. 95
5.11 Parameter study showing the maximum wall temperature and heat transfer limits for a regeneratively and film-cooled AM Inconel 718 chamber, with a constant chamber pressure of 5 MPa, wall thickness of 0.5 mm, and a cooling channel size of 0.8×0.8 mm. 95
5.12 Cooling channel geometry and coolant temperature and pressure for an AM Inconel 718 thrust chamber at a chamber pressure of 5 MPa, mixture ratio of 8 and film cooling fraction of 0.10. 96
5.13 Gas-side wall temperature and heat flux profile for an AM Inconel 718 thrust chamber at a chamber pressure of 5 MPa, mixture ratio of 8 and film cooling fraction of 0.10. 96
5.14 Impact of surface roughness and coolant convection model on the pressure drop and maximum wall temperature in the AM thrust chamber. 97
5.15 Impact of surface roughness and coolant convection model on the pressure drop and maximum wall temperature in the bimetallic reference thrust chamber. 98
5.16 Reference (adiabatic) wall temperature and maximum gas-side wall temperature for different values of the liquid film effectiveness and reference entrainment factor. 98
5.17 Parameter study showing the impact of film cooling on the specific impulse for the AM thrust chamber. 99
5.18 Left: thrust chamber design of Jones, with removable liner, nozzle insert and (not shown) cylindrical structural closeout. Right: Mk-II thrust prior to hot-fire test. 100
5.19 Available Δv and allowable propellant mass for the proposed engine designs. 103
5.20 High-level production steps of the bimetallic and AM thrust chamber. 104

A.1 Schematic overview of different phases of the Mk-II FLPP development program. 116

B.1 Cooling channel and wall geometry of the verification engine described in Table B.1. . . 118

C.1 Structured mesh with nodal numbering. 122

List of Tables

1.1 Comparison of the combustion of hydrogen peroxide and kerosene to other common hydrocarbon and storable rocket propellant combinations. All data is evaluated at an expansion ratio of 16 and a chamber pressure of 4 MPa. 5
1.2 Comparison of cost involved for additive manufacturing of different metal alloys. 6
1.3 Top-level functional and performance requirements of the Mk-II thruster. 8

2.1 Thermal conductivity of 98.2% hydrogen peroxide and water up to the critical temperature. 16
2.2 Roughness measurements in additively manufactured Inconel 718 channels under different build angles. 29

3.1 Comparison of nodal temperatures predicted by TDCAS and Ansys. 52
3.2 Comparison of nodal displacements in the x- and y-direction predicted by TDCAS and Ansys 54

4.1 Comparison of experimental heat transfer studies in additively manufactured cooling channels with proposed Nusselt correlations. 58
4.2 Engine design parameters of hydrogen peroxide film-cooled thrusters. 61
4.3 Overview of test conditions of 90% hydrogen peroxide film-cooled thrusters of Kwak and Heo. 61
4.4 Comparison of predicted characteristic velocity to measurements in hydrogen peroxide film-cooled thrusters. 67
4.5 Overview of recent Mk-II engine bipropellant tests conducted with 88% hydrogen peroxide and kerosene. 70
4.6 Comparison of the experimental coolant integrated heat load to predictions TDCAS. . . 75
4.7 Calculated ratio of hot gas heat flux to coolant bulk velocity in Mk-II engine test cooled with 88% hydrogen peroxide. 78
4.8 Results of the immersion screening tests at ambient temperature for 7 days. 82
4.9 Results of the immersion screening tests at 343 K for 7 hours. 83

5.1 Estimated pressure budget for the proposed engine designs. All pressures are in MPa. 101
5.2 Comparison of the bimetallic reference design to the proposed additive manufactured integral designs. 102
5.3 Requirement compliance matrix (by design) for the proposed Inconel 718 additively manufactured chamber design. 105

B.1 Design parameters of the thrust chamber which is used for verification of TDCAS. . . . 118

List of Symbols and Abbreviations

Acronyms

AM	Additive Manufacturing
CEA	Chemical Equilibrium with Applications
CT	Computed Tomography
DED	Directed Energy Deposition
ESA	European Space Agency
FLPP	Future Launchers Preparatory Programme
NASA	National Aeronautics and Space Administration
NIST	National Institute of Standards and Technology
MMH	Monomethylhydrazine
PBF	Powder Bed Fusion
RMS	Root Mean Square
RPA	Rocket Propulsion Analysis
RP-1	Rocket Propellant 1
TDCAS	Two Dimensional Combustor Analysis Software
TRL	Technology Readiness Level
UDMH	Unsymmetrical dimethylhydrazine

Roman Symbols

A	Area	m^2
c^*	Characteristic velocity	m/s
c_F	Thrust coefficient	–
c_d	Discharge coefficient	–
c_p	Specific heat capacity	J/(kg K)
c_w	Cooling channel width	m
c_r	Cooling channel height	m
$\mathbf{C}$	Constitutive tensor	Pa
D	Diameter	m
E	Modulus of elasticity	Pa
e^*	Roughness Reynolds number	–
f	Darcy-Weisbach friction factor	–
f_v	Vapor fraction	–
F	Thrust force / view factor	N / –
$\mathbf{f}$	Body force vector	N
g_0	Gravitational acceleration at sea level	m/s^2
g	Heat transfer similarity function	–
H	Specific enthalpy	J/kg
I_{sp}	Specific impulse	s
k_s	Equivalent sand grain roughness	m
L^*	Characteristic length	m
l_w	Cooling channel land/rib width	m
$\dot{m}$	Mass flow rate	kg/s
M_W	Molecular weight	kg/mol
M	Mach number	–
MR	Mixture ratio	–
$\mathbf{n}$	Unit normal vector	–
N	Number of cooling channels	–
Nu	Nusselt number	–

p	Pressure	Pa
Pr	Prandtl number	–
q	Heat flux (scalar)	$\mathrm{W/m^2}$
Q	Heat transfer rate	W
r	Radius	m
R	Universal gas constant	$\mathrm{J/(mol\,K)}$
R^*	Radius of curvature	m
R_f	Recovery factor	–
Re	Reynolds number	–
T	Temperature	K
t_{cl}	Closeout thickness	m
t_w	Gas-side wall thickness	m
$\mathbf{u}$	Displacement vector	m
V	Volume	$\mathrm{m^3}$
v	Velocity	m/s
z	Axial position, m	

Greek Symbols

α	Heat transfer coefficient	$\mathrm{W/(m^2\,K)}$
β	Coefficient of linear thermal expansion	1/K
γ	Specific heat ratio	–
$\boldsymbol{\varepsilon}$	Strain vector	–
ϵ	Emissivity	–
η	Efficiency / effectiveness	–
λ	Thermal conductivity	$\mathrm{W/(m\,K)}$
μ	Dynamic viscosity	$\mathrm{kg/(m\,s)}$
ν	Poisson ratio	–
ρ	Density	$\mathrm{kg/m^3}$
$\boldsymbol{\sigma}$	Cauchy stress vector	Pa
χ	Decomposition rate constant	$\mathrm{s^{-1}}$
ψ_L	Reference entrainment factor	–
ψ_M	Local entrainment factor	–
ω	Film cooling fraction	–

Subscripts

a	Ambient
am	Arithmetic mean film properties
aw	Adiabatic wall
c	Combustion chamber
cf,g	Gaseous film coolant
cf,l	Liquid film coolant
co	Regenerative coolant
crit	Evaluated at the critical point
e	Nozzle exit
el	Elastic
fu	Fuel
g	Core combustion flow
h	Hydraulic
o	Stagnation / total
ox	Oxidizer
ref	Reference conditions
t	Nozzle throat
th	Thermal
w	Chamber wall

1 Introduction

The global demand for launch services for small satellites is growing rapidly. Forecasts of Euroconsult predict that between 2018 and 2027 over 7000 spacecraft will be launched [1]. For the launcher industry, they project a revenue of 15.7 billion US$, which is almost six times higher than the 2.7 billion US$ turnover between 2008 and 2017. The promising market opportunities that present themselves for putting small satellites into orbit attract many aerospace start-up companies that are developing new launch vehicles. Previous market studies include at least 25 companies that are developing small launch vehicles in the United States [2]. On a global scale, this list is much larger and the exact length is hard to quantify.

One of the companies that is developing a launch service solution is Dawn Aerospace, located in the Netherlands and New Zealand. Most launch vehicles that are currently on the market are launched vertically and discard rocket stages once they run out of propellants. The vehicle concept of Dawn Aerospace is vastly different and based around a reusable orbital spaceplane which is propelled by a 100 kN class liquid rocket engine. This vehicle, designated Mk-III, is designed to take off and land horizontally from commercial airports. This way, the already existing global aviation infrastructure can be used, rather than relying on an expensive spaceport for each mission. At most commercial airports, dedicated facilities for transferring cryogenic rocket propellants, such as liquid oxygen or liquid hydrogen, are nonexistent. The propellant combination that is used in the Mk-II vehicle comprises a 90% hydrogen peroxide solution and aviation kerosene. Kerosene fueling facilities are readily available at almost all airports, whereas hydrogen peroxide can easily be transported and stored due to its non-cryogenic nature (per 49 CFR 173.243 transport regulations [3]).

For in-flight validation of important design features of the Mk-III spaceplane and thruster, Dawn Aerospace has developed the Mk-II. This 280 kg vehicle is significantly smaller than the 18,000 kg Mk-III and capable of sub-orbital flight to altitudes exceeding 100 km. The Mk-II spaceplane can also carry payloads up to 4 kg for research in a microgravity environment. The reusable Mk-II is propelled by a 2.5 kN class liquid rocket engine which also consumes 90% hydrogen peroxide and kerosene. Once injected into the combustion chamber the hydrogen peroxide and kerosene react to form a hot gas mixture, primarily consisting of carbon dioxide and water. The chemical reaction releases large amounts of energy, which heats the hot gas to a temperature exceeding 2700 K. This temperature is far above the melting temperature of most metal alloys.

To avoid melting of the chamber wall, cooling of the thrust chamber is required. Previous research of the author [4] has revealed that passive cooling techniques, which include radiation cooling, ablative cooling, thermal barrier coatings, or operation of the chamber as a heat sink are unsuitable for steady-state operation of the Mk-II thruster. These cooling techniques simply fail to remove sufficient heat from the structure or introduce an unacceptable increase in the subsystem dry mass. Besides, thermal barrier coatings are known for cracking and spalling after repeated thermal cycling of the thrust chamber [5]. This makes this design option less suitable for the Mk-II thruster, which has to survive over 100 thermal cycles without major refurbishments.

Active cooling techniques on the other hand, which include regenerative cooling and film/transpiration cooling, are proven to be effective in launch vehicle applications for keeping the chamber wall at acceptable temperatures [6]. In regenerative cooling, shown schematically in Figure 1.1 on the left, a (cold) fluid flows through cooling passages located in/around the chamber wall. This fluid absorbs some of the heat released and cools the wall. In regeneratively cooled thrust chambers, thin walls of high thermal conductivity, such as copper, are often preferred, which best leverage the cooling capabilities of the coolant and minimize thermal strains in the structure [7]. In these structures, the coolant and hot gas are physically separated by the chamber wall. On the contrary, in film cooled engines, the coolant is injected near the wall inside the trust chamber. This concept is shown in Figure 1.1 on the right in combination with regenerative cooling. The film coolant acts as an isolating barrier between the hot gas and wall and greatly reduces the heat load to the structure [8]. Film cooling can be very effective in thrust chamber designs where the wall is constructed from a low thermal conductivity material, such as Inconel or steel. This investigation is limited to regenerative and film cooling. Transpiration cooling, which relies on tiny pores in the chamber wall for coolant injection, is not considered in this work because of the complexity of fabrication[1] and inspection [9].

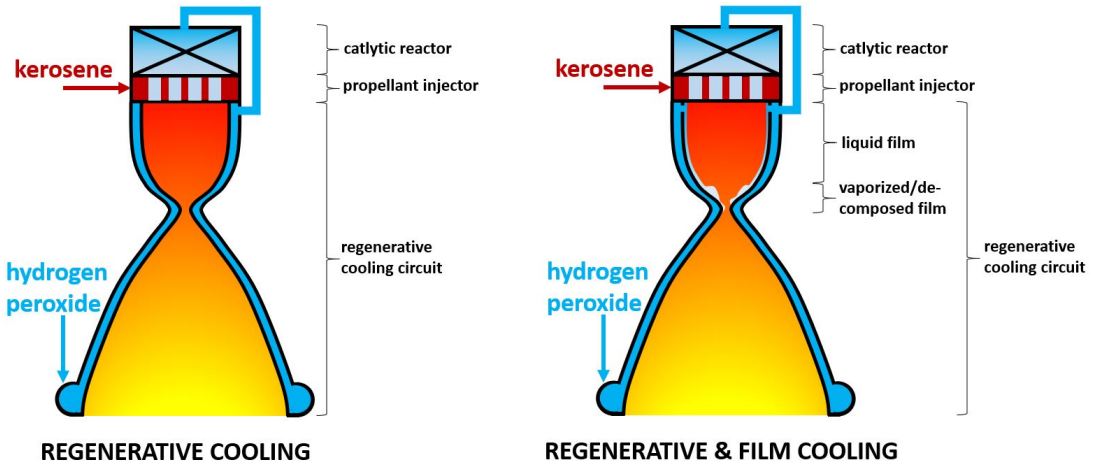

Figure 1.1: Schematic representation of regenerative cooling (left) and a combination of regenerative and film cooling (right) in the application of a bipropellant thruster propelled by hydrogen peroxide and kerosene.

Historically, many manufacturing techniques have been used to create regenerative cooled liquid rocket engines, including forging, forming, casting, machining, electroplating, and brazing [10]. A relevant example of this is the European Vulcain engine, which is used in the Ariane 5 launch vehicle. Several important production steps of this engine are depicted in Figure 1.2. First, the net shape of the thrust chamber liner is realized, by machining a raw copper alloy bar. Hereafter, the cooling channels are carved in the liner and the structural closeout is deposited, for example through electroplating. The closeout structure is typically realized from a high-strength metal, such as Inconel or steel, thereby creating a bimetallic structure. Lastly, flanges, coolant manifolds, thrust vectoring brackets, etc. are attached to the thrust chamber. It is worth mentioning that the current iteration of the Mk-II thruster also relies on a bimetallic design with a copper alloy liner. The fabrication process of the Mk-II thrust chamber is similar to Figure 1.2. Nevertheless, noticeable differences exist in the production of the closeout structure and interfaces near the nozzle throat, which are explained in section 1.3.

Many of the production steps shown in Figure 1.2 involve manual labor, which can greatly increase the overall fabrication cost of the thruster. Not noted in this figure are the rigorous inspections and tests that occur in-between different production steps or transportation of parts to/from different subcontractors, which can both be relevant cost components. What is more, in this “traditional” production process, a lot of waste material is created. An example of this is shown in Figure 1.2-1, where a copper alloy bar stock is machined down on both the inside and outside according to the profile of the chamber. The volume of the final part that is obtained represents only a small percentage of the initial volume of

[1] This may especially be true for additively manufactured chambers realized with the powder bed fusion process. The small pores in the chamber wall could get clogged with excess powder, thereby blocking the pore. This is a problem that is often seen in additively manufactured thrust chambers and explained in more detail in section 1.1.

the bar stock. These traditional manufacturing processes have considerable flight heritage and lend themselves excellently for the economy of scale [4]. Nevertheless, for most rocket engines, the economy of scale does not apply, making these fabrication methods costly from a monetary and schedule perspective. This is especially true when the thruster is designed to be reusable.

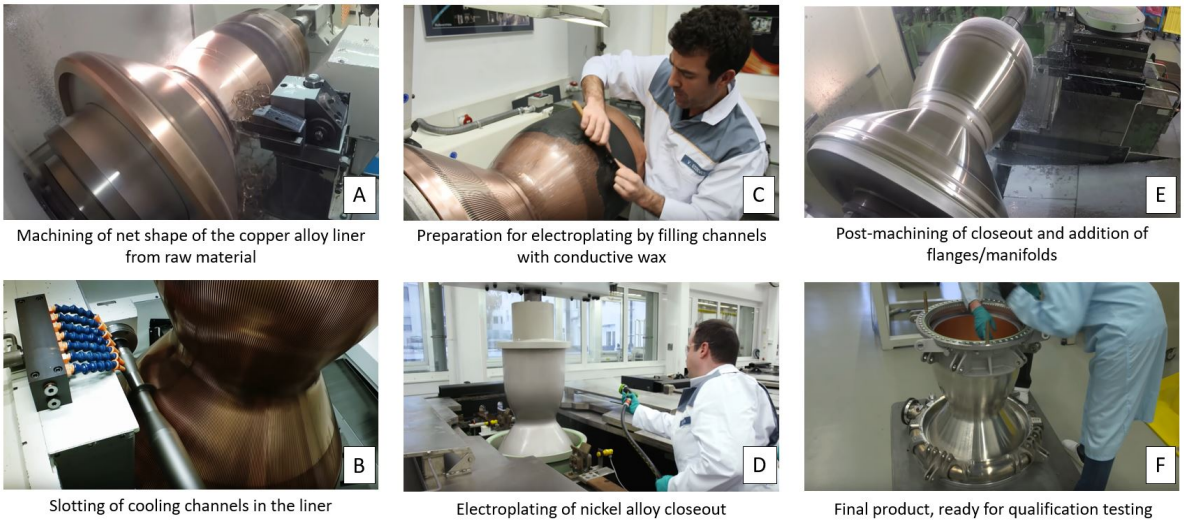

Figure 1.2: Manufacturing techniques used for the production of the Vulcain thrust chamber of Ariane 5 vehicle. Images are taken from the documentary “Mit Vollgas ins All - Die Erfolgsgeschichte der Ariane 5” produced by “Welt Nachrichten” in 2019.

1.1. Additive Manufacturing of Thrust Chambers

Nowadays, many aerospace companies, including Launcher, Orbex, Relativity Space, Rocket Lab USA, Aerojet Rocketdyne, Avio, and Virgin Orbit consider additive manufacturing for the fabrication of thrust chambers [4, 11]. Additive manufacturing (AM), also often referred to as *3-D printing*, is a production technique where 3-D shapes, generated on a computer, are realized by joining raw materials together. This usually follows a layer-by-layer approach, where the 3-D shape is discretized in several 2-D blueprints. The machine fuses the material together at the designated locations, and hereafter continues to the next layer. This process continues until the net shape of the part is realized. Once the part is finished, it is removed from the build plate and can be post-processed. This novel production technique lends itself excellently for mass optimization, part-count reduction, and realizing complexly shaped parts [12]. Furthermore, on small batch sizes, AM parts often outperform traditionally manufactured parts in terms of cost and production time [13].

The application of AM to liquid rocket engines is still an active area of research [10, 11]. Most publications in the open literature are based on thrusters that are regeneratively cooled with kerosene [14, 15], liquid hydrogen [16], or liquid methane [17]. Yet, little to no studies consider AM applied to small hydrogen peroxide cooled thrusters. Unlike hydrogen, methane, and kerosene, hydrogen peroxide is a monopropellant that can exothermically decompose in oxygen and steam. This makes the design of cooling systems much more intricate, as explained in more detail in section 1.2. As part of the Future Launchers Preparatory Programme (FLPP) of the European Space Agency (ESA), Dawn Aerospace has received a contract to develop a second iteration of the Mk-II thruster as an integral AM structure. The integral structure implies that both the closeout and thrust chamber liner are realized from one single metal alloy. Examples from the industry are shown in Figure 1.3, for an integral superalloy design and integral copper alloy design. Thrust chambers A and C in this illustration are designed to serve as the main propulsion system of an orbital class launch vehicle. All thrusters shown in Figure 1.3 rely on the combustion of liquid oxygen and kerosene.

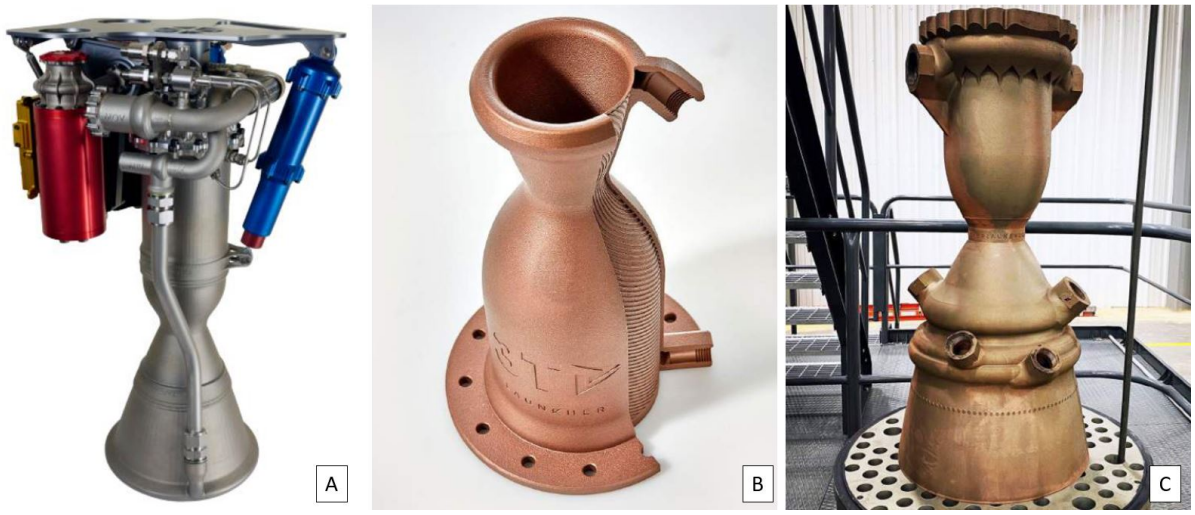

Figure 1.3: State-of-the-art integral additively manufactured thrust chambers in the industry propelled by liquid oxygen and kerosene. A) Rutherford engine of Rocket Lab. B) Subscale E-1 engine of Launcher Inc. C) Full scale E-2 engine of Launcher Inc. (reprinted from refs. [18, 19]).

The AM production process that is considered for the ESA FLPP project is laser powder bed fusion (L-PBF). In L-PBF machines, a build plate is covered with a thin layer of metal powder in an inert environment. A laser (heat source) is used to selectively melt the powder together to realize a net shape. Once one layer is completed, the build plate is lowered, recoated with powder, and once again selectively melted together. The unmelted powder provides limited support for overhang structures and has to be removed when the build is finished. The powder removal in thrust chambers can be very challenging, especially in the narrow cooling passages where it can easily get trapped [20]. The aerospace startup company Launcher Inc has also shared via their public channels that three cooling channels of their 98 kN AM thruster (shown in Figure 1.3-C) ruptured as a consequence of powder blockage during a hot-fire test on October 2020 at NASA Stennis Space Center.

Potential powder consolidation in the cooling channels is just one of the new challenges that are introduced by AM of thrust chambers. As a consequence of the layer-by-layer manufacturing method, AM parts are typically characterized by anisotropic material properties and high residual stresses post-built [21]. Therefore, additional heat treatments are often introduced to achieve the desired microstructure. Besides, AM parts typically have some degree of porosity [12]. In the thin-walled regenerative cooling structure, these pores could result in some of the coolant fluid leaking into the chamber, as demonstrated in ref. [22]. Accordingly, hot isostatic pressing is often used post-built, which aids in the densification of the part [11]. Another major challenge of AM thrust chambers is the high surface roughness that is achieved. This is already clearly visible when comparing Figure 1.2-A to Figure 1.3-B. The increase in surface roughness results in a much higher pressure drop over the cooling passages, which could greatly challenge upstream turbomachinery requirements. What is more, it is well-known that heat transfer in hydraulically rough channels is vastly different to hydraulically smooth channels [23–25]. Lastly, the poor surface quality in AM cooling channels could challenge the chemical compatibility with the coolant, especially when reactive fluids like hydrogen peroxide are used [26].

It is worth noting that, besides L-PBF, several other AM techniques exist, such as directed energy deposition or cold spraying. These techniques are summarized in a recent publication of the author [11], which is co-authored by thesis supervisor Dr. Angelo Cervone, and Paul Gradl from NASA Marshall Space Flight Center. An abstract of this paper, which has recently been published in Acta Astronautica, is reprinted in Appendix D. The reader is encouraged to study this paper for a more in-depth explanation of AM applied to liquid rocket engines. In the present investigation, these different techniques are not discussed in more detail since these are not taken into consideration for the ESA FLPP project.

1.2. Hydrogen Peroxide in Rocketry Applications

As mentioned before, a unique feature that distinguishes the Mk-II from several other hydrocarbon liquid rocket engines that are currently used in the industry is the fact that it uses 90% hydrogen peroxide as an oxidizer. Compared to other common propellant combinations, the specific impulse performance of systems operating with hydrogen peroxide (H_2O_2) and kerosene (RP-1) is relatively low, as shown in Table 1.1. Nevertheless, because of the high density of hydrogen peroxide, the density specific impulse exceeds that of cryogenic alternatives, which facilitates the use of small storage tanks on-board the spaceplane. Moreover, hydrogen peroxide and kerosene are both storable at ambient conditions, which cannot be said for liquid oxygen (LO_2) and liquid methane (LCH_4). Additionally, hydrogen peroxide provides a green alternative for commonly used propellant combinations of nitrogen tetroxide (N_2O_4) with unsymmetrical dimethylhydrazine (UDMH), monomethylhydrazine (MMH), or anhydrous hydrazine (N_2H_4), which are all highly toxic and carcinogenic.

Table 1.1: Comparison of the combustion of hydrogen peroxide and kerosene to other common hydrocarbon and storable rocket propellant combinations. All data is evaluated at an expansion ratio of 16 and a chamber pressure of 4 MPa.

Propellants	90% H_2O_2 RP-1	98% H_2O_2 RP-1	N_2O_4 UDMH	LO_2 RP-1	LO_2 LCH_4
Density fuel, kg/m3	820	820	793	820	422.8
Density oxidizer, kg/m3	1388	1437	1440	1141	1141
Mixture ratio(1)	7.9	6.5	2.5	2.6	3.2
Specific impulse, sec(2)	279.9	289.3	301.3	313.5	324.2
Density specific impulse, kg s/L	360.3	377.6	352.4	322.5	262.8
Cryogenic propellants	None	None	None	LO_2	Both
Toxic propellants	None	None	Both	None	None

(1) Mixture ratio for optimum specific impulse, at given pressure and expansion ratio.

(2) Specific impulse at optimum expansion, assuming shifting equilibrium flow conditions.

The use of hydrogen peroxide as a regenerative coolant in rocketry applications introduces several major design challenges. First off, the fluid is thermodynamically unstable by nature and decomposes into oxygen and steam over time [27]. This decomposition reaction follows the chemical reaction presented in Equation 1.1.

$$H_2O_2 \rightarrow H_2O + 0.5O_2 \tag{1.1}$$

The reaction is highly exothermic and is accompanied by an enthalpy change of $-2884\,\mathrm{kJ/kg}$ when liquid water and gaseous oxygen are formed from liquid hydrogen peroxide [26]. Mind the negative sign for the enthalpy change, which implies that energy is released. Excessive decomposition of the oxidizer in the cooling passages could result in a thermal runaway [27]. Hence, it is of paramount importance to keep the reaction rate under control. The rate at which hydrogen peroxide decomposes is primarily driven by temperature. Several other factors are known for impacting the decomposition rate, which includes the surface-to-volume ratio of the channel, the surface treatment, the surface passivation, the hydrogen peroxide concentration, and the presence of stabilizers in the propellant [28]. Concerning surface treatment, Kuntz et al. [26] describe that: “the surface finish should be as smooth as possible” in hydrogen peroxide applications. In AM thrust chambers, the surface finish is generally poor whereas the surface-to-volume ratio is high[2]. Moreover, the fluid is operated at high temperatures ($>373\,\mathrm{K}$) inside the cooling passages, which increases the rate at which decomposition occurs. At these elevated temperatures, the vapors of hydrogen peroxide can be ignitable, which may trigger a deflagration or detonation [27].

Another fundamental design challenge lies in the poor chemical compatibility of many metal alloys with hydrogen peroxide. On one hand, the corrosive nature of hydrogen peroxide could facilitate bronzing, corrosion, or even dissolving of the metal alloy that is in contact with the fluid. On the other hand, the

[2]For reference, a cooling channel of size 1×1 mm has a surface to volume ratio of 4 cm^{-1}, which is much higher than typical values (0.4-2.4 cm^{-1}) reported by Ventura [29] for hydrogen peroxide storage vessels.

metal alloy may act as a catalyst or could heavily promote the decomposition reaction. Much of the modern-day knowledge about hydrogen peroxide material compatibility dates back to research of the FMC Industrial Chemicals Group in the 1960s [30]. In this work, several metals, ceramics, polymers, coatings, and lubricants are submerged in concentrated hydrogen peroxide. FMC provides an extensive list of metal alloys that show good chemical compatibility with hydrogen peroxide, which includes wrought or 1000-series aluminum, tantalum, and zirconium. Several 300-series and precipitation hardened stainless steel alloys are mentioned for moderate chemical compatibility when passivated before contact with hydrogen peroxide[3]. Poor chemical compatibility is reported for most other (transitional) metals, which include copper, titanium, nickel, and cobalt [30]. Schumb et al. [32] particularly mention avoiding copper-containing alloys, as these can act as a catalyst in the decomposition reaction.

In the same time period, Kuntz et al. [26] conducted short-duration compatibility experiments with concentrated hydrogen peroxide at temperatures up to 405 K, to assess the usability of this propellant for regenerative cooling. They include passivated Inconel 718, Hastelloy C, Hastelloy X, and stainless steel alloys 304, 316, and 347. They observe that all materials, except Hastelloy X, show a good short-duration (1 hour) compatibility with only light signs of bronzing on the Inconel 718, Hastelloy C, and 347 steel test articles. It is worth noting that all these experiments are based on mirror-polished test articles, that have a surface finish superior to AM test articles. Experience with AM alloys could not be found in the open literature.

In this thesis, an integral thrust chamber realized from AM Inconel 718 will be investigated. This selection follows from a trade-off and feasibility study described in the preceding literature study [4] and the positive experience of Kuntz et al. at high temperatures. Other promising solutions based on the expected chemical compatibility are tantalum and aluminum alloys. Yet, the commercial availability of these materials for AM is much lower than Inconel 718. Additionally, sales quotes received from several commercial partners revealed that Inconel 718 provides a very economical choice, as shown in Table 1.2. It is important to note that all costs that are presented in this table are based on simple rectangular test articles. Prices may differ for the production of a full thrust chamber.

Table 1.2: Comparison of cost involved for additive manufacturing of different metal alloys.

Base	Alloy	Density, g/cm^3	Price, €/g	Quotes received
Tantalum	Tantalum	16.69	25.5	1
Copper	CuCr1Zr	8.90	8.3-33.1	3
Copper	CuNi2SiCr	8.84	8.3-28.3	2
Nickel	Inconel 625	8.44	9.0-26.4	2
Nickel	Inconel 718	8.22	1.9-26.9	4
Nickel	Hastelloy X	8.22	9.1-27.0	2
Cobalt	Co-28Cr-6Mo	8.47	29.5	1
Aluminum	Scalmalloy	2.67	24.4	1

1.3. Mk-II Engine Development at Dawn Aerospace

Dawn Aerospace has already conducted several hot-fire tests with the current iteration of the Mk-II thruster. This thruster is regeneratively cooled with hydrogen peroxide and relies on a copper alloy liner that is placed in a cylindrical closeout structure (see also Figure 1.4-A and Figure 1.4-B). As discussed in section 1.2, copper alloys are generally considered incompatible with concentrated hydrogen peroxide. Therefore, Dawn Aerospace has developed a proprietary coating, which is electroplated on the surface of the cooling channels. This way, the copper alloy is physically separated from the hydrogen peroxide. The empty volume between the liner and cylindrical closeout in the convergent-divergent part of the nozzle is filled with an aluminum nozzle insert, as depicted in Figure 1.4-A. Sealing between the liner, nozzle insert, and closeout is achieved with o-rings. The concept of a nozzle insert is very similar to the heritage Gamma engines that were used in the Black Knight launch vehicle [33].

[3] During passivation, the metals are treated to create a protective film on the surface, which reduces the chemical reactivity [31].

The Mk-II engine is designed to operate in a pump-fed, closed cycle. After passing through the regenerative cooling channels, the hydrogen peroxide is injected into a catalytic reactor, which decomposes the liquid in gaseous oxygen and steam. The reaction products that leave the reactor have a temperature of approximately 1019 K and are injected into the combustion chamber. Here, the hot oxygen-rich gas mixes and reacts with the atomized kerosene. Since the decomposition temperature is far above the auto-ignition temperature of kerosene, no separate igniter is required. This greatly simplifies the start-up procedures.

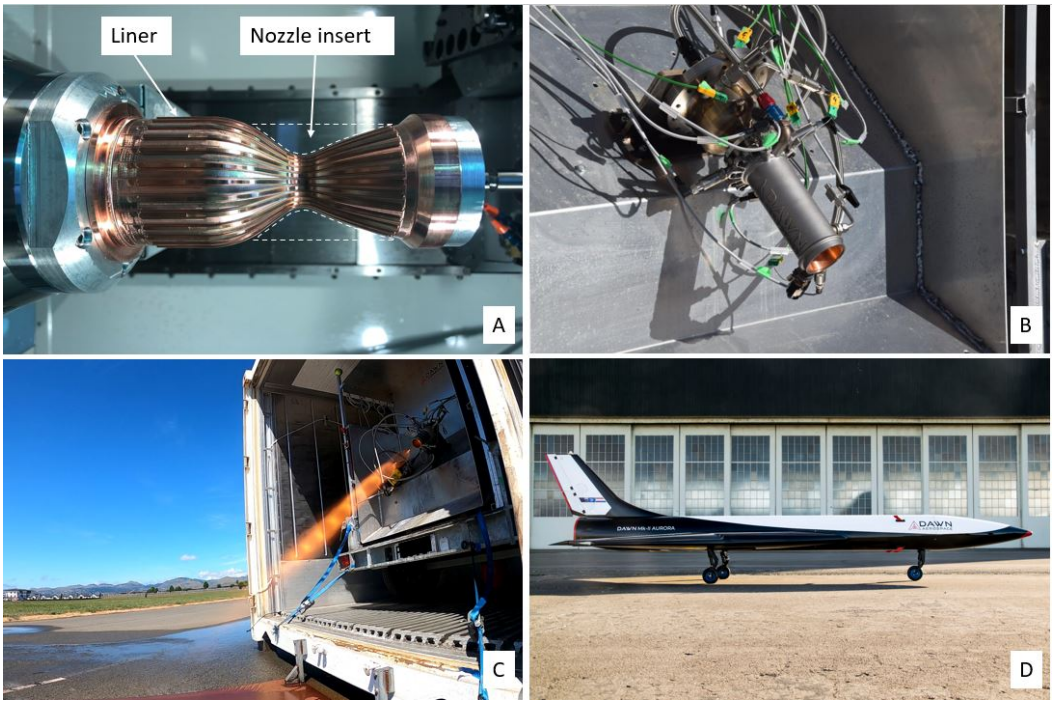

Figure 1.4: Overview of the engine development for the Mk-II spaceplane. A) Machined copper alloy thrust chamber liner. B) Liner integrated in structural closeout, placed on the test bench. C). Hot-fire test of the regeneratively cooled Mk-II thruster with hydrogen peroxide and kerosene. D) Mk-II spaceplane in which the thruster is integrated.

The current design iteration of the Mk-II engine with copper alloy liner has successfully been hot-fired with >20 starts, as depicted in Figure 1.4-C. This bimetallic engine will be used during the maiden flight of the Mk-II vehicle (Figure 1.4-D). Although the current iteration of the Mk-II thruster works, the production process is labor-intensive and requires skilled machine operators. Furthermore, the proprietary plating which is used on the copper alloy liner is known for flaking off after repeated thermal cycling of the engine (similar to a thermal barrier coating). Therefore, the engine requires a rigorous inspection after each test and potentially re-plating. Furthermore, for simplicity of fabrication, the current chamber design uses a cylindrical closeout structure with a two-piece nozzle insert. As a result, the total assembly has a high part-count with many sealing interfaces. Closing off all leakage paths between the liner, closeout, and nozzle insert has proven to be a great challenge, especially when the liner thermally expands as a consequence of the high temperature. These deficiencies of the design could potentially be resolved when the production process is shifted to additive manufacturing.

1.4. ESA Future Launcher Preparatory Programme

The relevance of this work is stressed by a recent contract that Dawn Aerospace received from ESA. This FLPP contract (ESA-STS-FLP-SoW-2020-0003) has a value of 385 k€ and aims to further develop launch vehicle technology in Europe. The work to be performed for this particular contract is shown in Figure 1.5. Task 1 and 2 of this contract were largely discussed in the literature study conducted before this thesis [4] and follow-up publication in Acta Astronautica [11]. This thesis is mainly focused on the work that is required for tasks 3-6. It should be mentioned that several other full-time employees of Dawn Aerospace work on the ESA FLPP project and that the preliminary design studies performed in this thesis only cover a small part of a much larger work package.

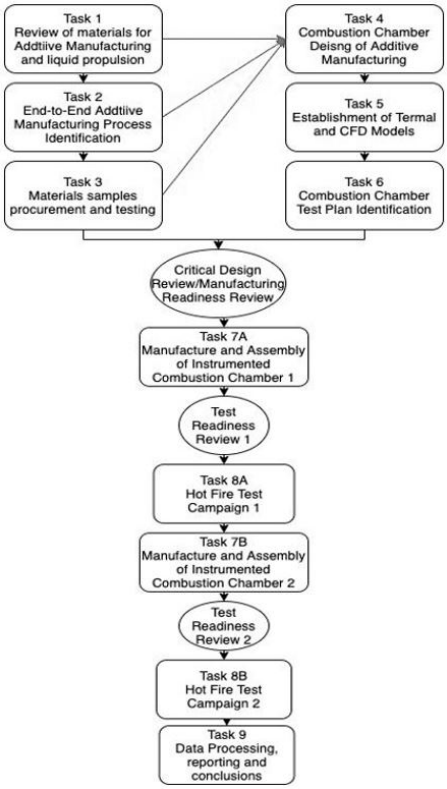

Figure 1.5: Overview of work packages of the ESA FLPP project (reprinted from ESA-STS-FLP-SoW-2020-0003).

The schedule of the FLPP project is tight, with a planned finish date in December 2021. At the end of this project, two AM thrust chambers have to be designed, manufactured, and tested. This tight schedule is taken into consideration in trade-offs performed in this thesis, favoring design concepts with a high technology readiness level (TRL) over concepts with a relatively low TRL ($\leq$6). There are several requirements for the AM Mk-II engine that are set based on mutual agreement of ESA specialists and the Dawn Aerospace management. These are listed in Table 1.3 and can be seen as top-level requirements for this thesis.

Table 1.3: Top-level functional and performance requirements of the Mk-II thruster.

Identifier	Description
REQ-001	The engine shall produce a thrust of at least 2300 N at sea level.
REQ-002	The engine shall produce a thrust of at least 2700 N in vacuum.
REQ-003	The engine shall have a specific impulse greater than 236.5 s at sea level.
REQ-004	The engine shall have a specific impulse greater than 273.6 s in vacuum.
REQ-005	The engine shall operate using stabilized 90% high test peroxide as oxidizer.
REQ-006	The engine shall operate using kerosene as fuel.
REQ-007	The engine shall operate at a chamber pressure between 40 and 120 bar.
REQ-008	The engine shall have a dry mass of no more than 12 kg.
REQ-009	The engine shall survive a continuous operation of no more than 300 s.
REQ-010	The engine shall survive 10 restarts with an accumulated burn time of no more than 1500 s, without replacement of consumables.
REQ-011	The engine shall survive 100 restarts with an accumulated burn time of no more than 25000 s, without major overhaul.

1.5. Research Objective and Questions

The objective of this research is to compare the use of an integral additive manufactured combustion chamber to a bimetallic chamber realized with traditional manufacturing techniques. This is achieved by developing a model to predict steady-state thermal loading in the wall and proposing a preliminary design solution based on customer requirements. In the developed model, both the thermal and mechanical loads will be investigated. In this research, the "customer" is seen as ESA, that imposes requirements that are listed in Table 1.3. Moreover, the "integral additive manufactured combustion chamber" refers to the AM Inconel 718 chamber, whereas the "bimetallic chamber" refers to the current design of the Mk-II thruster. Based on the research objective, the following primary research question is proposed:

Is it advantageous to realize the thrust chamber of a small, hydrogen peroxide cooled, rocket engine as an integral additively manufactured structure, instead of a bimetallic structure created with traditional manufacturing methods?

Especially the term "hydrogen peroxide cooled" is of paramount importance in this research question since it greatly reduces the available design space (based on chemical compatibility). To answer the primary research question, the following sub-questions are introduced:

1. What is the short duration compatibility of the AM alloy with 90% hydrogen peroxide?
2. Is it required to passivate the AM alloy before exposure to 90% hydrogen peroxide?
3. What is the (hydraulic) surface roughness of the AM alloy?
4. How can the steady-state thermal-mechanical loading of the thrust chamber wall be simulated?
   (a) Which semi-empirical model is suitable to predict the gas-side heat transfer?
   (b) Which semi-empirical model is suitable to predict the coolant side heat transfer?
   (c) Can a linear elastic structural model be used to predict the stress in the wall introduced by the combined thermal and hydraulic loads?
5. What is an adequate cooling configuration for an integral AM thrust chamber that meets customer requirements?
   (a) Which parameters constrain the feasible operating space of the thruster?
   (b) Can film cooling extend the operating regime of the proposed design?
6. How does the proposed AM thrust chamber design compare to the current bimetallic thrust chamber used in the Mk-II spaceplane?
   (a) Which interfaces can be removed in the proposed AM design?
   (b) How does the dry mass of the proposed AM design differ from the current design of the Mk-II thruster?
   (c) How does the coolant pressure drop of the proposed AM design differ from the current design of the Mk-II thruster?

Since Dawn Aerospace is a commercial company that operates in a highly competitive environment, data concerning thruster design or test results cannot be shared in the public domain. To answer research question 6, a hypothetical "bimetallic reference" engine is proposed in this thesis. This reference engine has a size and performance comparable to the real Mk-II engine but only exists on paper. For validation of the developed model, experimental data of the real Mk-II engine is used and presented in a normalized format.

1.6. Thesis Structure

As mentioned in section 1.4, this thesis closely follows the statement of work of the ESA FLPP project presented in Figure 1.5. First, in chapter 2, the developed numerical model is discussed. This overlaps well with task 5 of the ESA FLPP project. The software verification steps that are performed are touched on in chapter 3. Experimental validation of the developed model is presented in chapter 4. Since hot-fire tests of the AM thruster for the FLPP project are planned for fall/winter 2021, no hot-fire test data of this engine design can be included without introducing an unacceptable delay in the thesis schedule. Data that is available and used for validation comprises hot-fire tests of the regeneratively cooled bimetallic Mk-II thruster, hot-fire tests of hydrogen peroxide film-cooled thrusters developed by the Korea Advanced Institute of Technology, and air flow experiments in AM cooling channels. Furthermore, chapter 4 describes the results of immersion screening tests that were conducted during this thesis. These experiments are used to validate the chemical compatibility of AM Inconel 718 with 90% hydrogen peroxide. This data could not be found in the open literature and overlaps with task 3 of the ESA FLPP project.

Based on the validated numerical model, chapter 5 proposes a preliminary design for the AM Mk-II thruster, which overlaps with task 4 of the ESA FLPP project. This chapter also contains a requirement compliance matrix and answers the sub-questions that were listed in the previous section. The conclusion and recommendations of this research can be found in chapter 6.

In Appendix A, a conceptual test plan that can be used during the ESA FLPP experiments is proposed. This test plan can be linked to task 6 in Figure 1.5. This is followed in Appendix B by a description of the engine design that is used during software verification activities. Appendix C provides additional information about the developed simulation tool and the required user inputs. Lastly, the abstract submitted to and accepted by Acta Astronautica is reprinted in Appendix D.

2

Numerical Model

The preliminary design of a regeneratively cooled liquid rocket engine poses a multidisciplinary problem. On one hand, the designer must have a detailed understanding of the thermal loading of the wall and heat transfer to the coolant fluid. This services as a first measure to assess potential overheating of either the wall or coolant fluid. On the other hand, the designer must know how mechanical stresses evolve in the wall, to verify the structural integrity of the design. A detailed understanding of stress and strain in the wall is also required for predicting the useful life of the thrust chamber [34]. This is especially relevant when considering chamber designs with well-defined requirements for reusability, such as the Mk-II thruster for the ESA FLPP project (REQ-009 to REQ-011 in Table 1.3).

Historically, 1-D, 2-D, and 3-D models have been used for predicting heat transfer and stress in the chamber wall [35–38]. 1-D modeling techniques are powerful in terms of computational cost, but provide limited to no knowledge about the temperature distribution inside the wall. This can be problematic when studying materials with low thermal conductivity, like AM Inconel 718. On the other hand, 2-D planar models provide a detailed overview of the temperature field in the chamber wall and reveal potential thermal gradients in both the circumferential and radial direction. The outputs of a 2-D conduction model can directly be used in a plane strain structural model, as demonstrated in ref. [39]. Lastly, 3-D models *can* provide the most accurate prediction of the temperature field in the wall, since circumferential, radial, and axial conduction are considered. Yet, these methods are also associated with the highest computational cost, making them less favorable for the preliminary design.

In the present work, a hybrid 1-D/2-D model is proposed to study the evolution of temperature and stress in the chamber wall. Conduction and mechanical deformation are both resolved in 2-D based on the finite element method. For the boundary conditions - the hot gas flow and coolant flow - models with 1-D property evolution in the stream-wise direction are used. The full program, designated the Two Dimensional Combustor Analysis Code (TDCAS), is developed in Matlab using an object-oriented programming approach.

The structure of this chapter follows the program architecture, which is depicted in Figure 2.1. The primary inputs in TDCAS include property databases for the hot gas, coolant, and wall (blue boxes), as well as a set of user-defined operating conditions (yellow box). The properties of the wall material that is studied in this thesis, Inconel 718, are obtained from ref. [40]. On the other hand, fluid models that have been used to predict properties of the hot gas mixture and hydrogen peroxide coolant are discussed in section 2.1. The core of TDCAS, indicated with white boxes in Figure 2.1, contains a set of functions that are used to resolve the numerical domain and define its boundary conditions. First off, the general techniques used for sizing the thrust chamber are explained in section 2.2. This section is followed by an explanation of the boundary conditions that are introduced for the convective and radiative heat transfer from the hot gas (section 2.3). Section 2.4 follows with a brief explanation of the boundary conditions on the (regenerative) coolant side. This is followed by an explanation of the implemented film cooling model in section 2.5. Lastly, section 2.6 briefly mentions how the boundary conditions are used to obtain the 2-D numerical solutions in the thrust chamber wall.

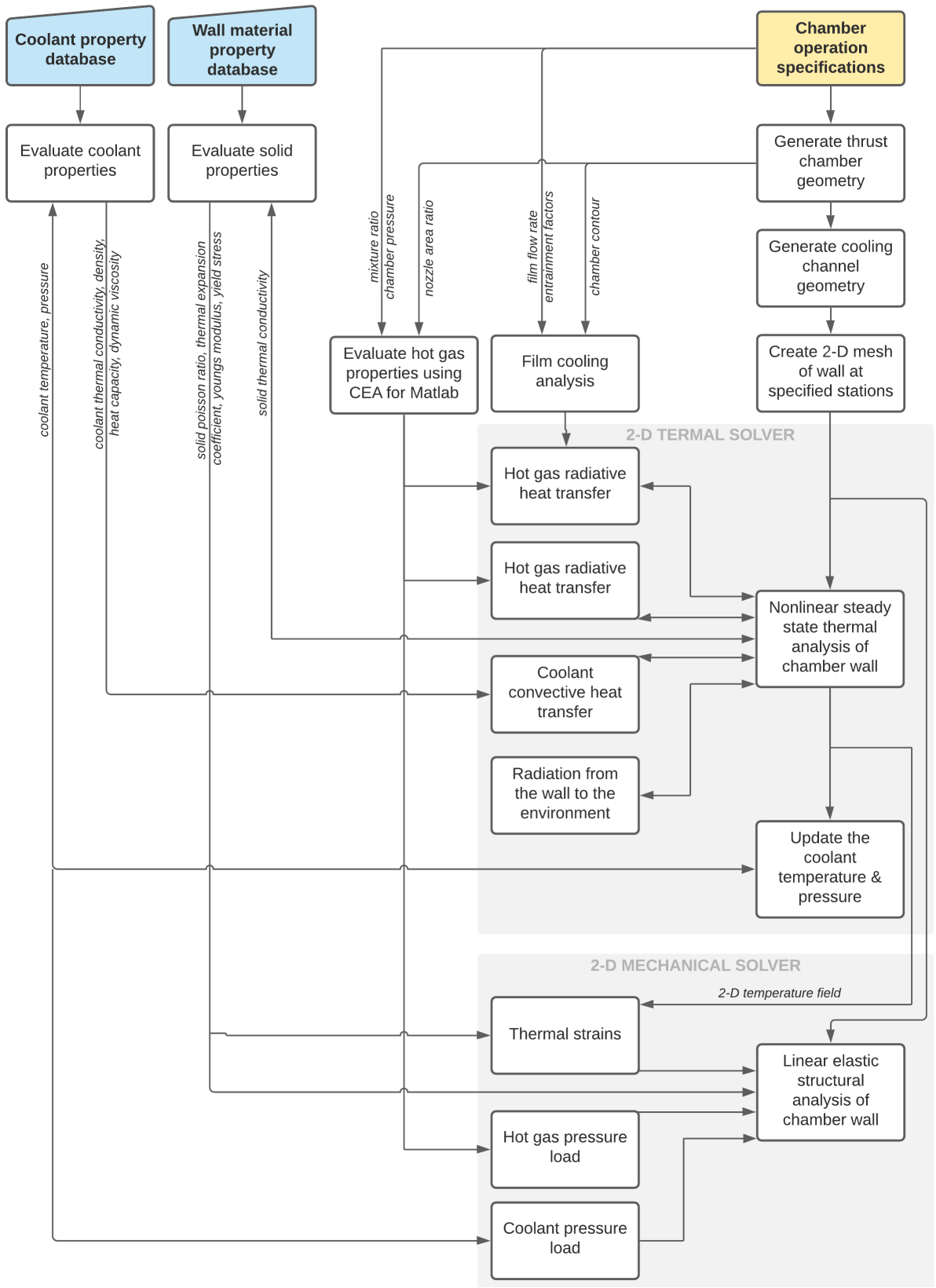

Figure 2.1: High level program architecture of TDCAS.

2.1. Fluid Properties

To model the heat transfer in the combustion chamber, data concerning the thermophysical fluid properties is required. In the application of a regeneratively cooled thruster, two fluid domains are distinguished: the hot combustion gases and the film/regenerative coolant flow. First, subsection 2.1.1 details on the fluid properties of the hot combustion gas. Hereafter, relevant fluid property models for the hydrogen peroxide coolant are discussed in subsection 2.1.2.

2.1.1. Combustion Gas

In the combustion chamber, the fuel and oxidizer react to form a hot gas mixture. For the combustion of 90% hydrogen peroxide and kerosene, this hot gas mixture has a temperature of roughly 2700 K. The hot gas flow travels downstream where it enters the convergent-divergent nozzle. At the inlet of the nozzle, the flow is typically subsonic, which means that the velocity does not exceed the local speed of sound [7]. Downstream of the nozzle throat, which is the most narrow section in the nozzle, the flow is supersonic. This implies that the flow velocity exceeds the local speed of sound, which is indicated by a Mach number higher than 1 in Figure 2.2. As a result of the acceleration and expansion of the gas in the nozzle temperature and pressure decrease. Therefore, one can expect the local gas properties in the nozzle to deviate from the stagnation gas properties in the combustion chamber. The magnitude of different gas properties, including density, heat capacity, specific heat ratio, viscosity, and thermal conductivity in the nozzle are predicted using the Chemical Equilibrium with Applications (CEA) tool [41]. CEA, developed by the National Aeronautics and Space Administration (NASA), is a validated open-source software that predicts gas properties for a 1-D flow in a rocket nozzle. The software can be used online in a web browser, or offline in a Matlab interface using a copy that can be obtained from the NASA software repository (reference number MFS-33320-1). In the present work, this offline copy with Matlab interface is used.

The main inputs that are required to run an analysis in CEA, are the chamber pressure, mixture ratio, and propellant combination. Additionally, the user must specify the nozzle *contraction ratio* and *expansion ratio*. The contraction ratio relates the cross-section area of the combustion chamber to the area of the nozzle throat. The expansion ratio, on the other hand, represents the ratio between the nozzle exit area and throat area. Outputs of the CEA analysis include the gas pressure, temperature, density, average molecular weight, Mach number, specific heat at constant pressure, specific heat ratio, thermal conductivity, dynamic viscosity, and mole fractions of the species in the gas. CEA also outputs ideal performance parameters of a rocket engine, such as characteristic velocity, thrust coefficient, and specific impulse. More on these performance parameters will be explained in subsection 2.2.4.

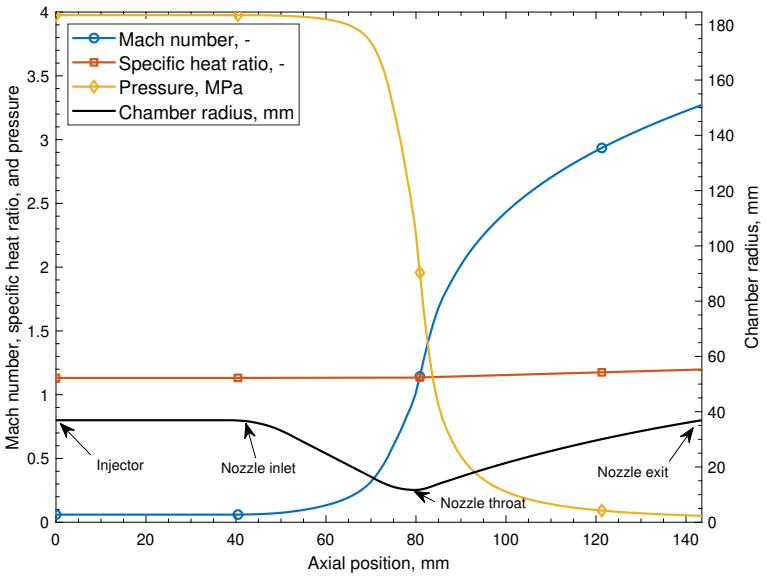

Figure 2.2: Evolution of Mach number, specific heat ratio, and gas pressure in the verification engine.

In TDCAS, the hot gas properties are obtained at the injector plane, the nozzle inlet, the nozzle throat, and the nozzle exit. In-between these four stations, the temperature, pressure, and density of the gas are obtained from the well-known isentropic flow relations, which are presented in Equations 2.1-2.3 [42].

$$\frac{T_o}{T} = 1 + \frac{\gamma - 1}{2} M^2 \tag{2.1}$$

$$\frac{p_o}{p} = \left(1 + \frac{\gamma - 1}{2} M^2\right)^{\frac{\gamma}{\gamma - 1}} \tag{2.2}$$

$$\frac{\rho_o}{\rho} = \left(1 + \frac{\gamma - 1}{2} M^2\right)^{\frac{1}{\gamma - 1}} \tag{2.3}$$

In these expressions, T denotes the temperature, p the pressure, ρ the density, M the local Mach number, and γ the specific heat ratio of the gas. Parameters with subscript “o” represent stagnation properties, which are obtained from CEA. The local Mach number which is used in the isentropic flow relations is obtained from the Mach-area relation, noted in Equation 2.4 [42].

$$\frac{A}{A_t} = \frac{1}{M} \left(\frac{2 + (\gamma - 1) M^2}{\gamma + 1}\right)^{\frac{\gamma + 1}{2(\gamma - 1)}} \tag{2.4}$$

Since the local area ratio (A/A_t) is known from the geometry of the thrust chamber, the Mach number can be obtained using an iterative calculation. The specific heat ratio which is used in Equations 2.2-2.4 is obtained from CEA as a function of the gas temperature. Figure 2.2 shows that axial variations in the specific heat ratio are present, albeit very small. This illustration also shows the evolution of the gas pressure and Mach number in the combustion chamber and nozzle. The engine geometry and operating conditions are described in Appendix B.

In this work, most gas properties, including those in Figure 2.2, are based on *shifting equilibrium* flow. This implies that the chemical equilibrium of the combustion reaction shifts when the gas expands in the nozzle. As a result, the gas composition changes in the axial direction. An exception to this is the Bartz correlation which is introduced in subsection 2.3.1. For this correlation, *frozen flow* transport properties are assumed [43]. When the gas flow is said to be frozen, the chemical composition is invariant in the axial direction. Despite the constant gas composition, transport properties still vary in the axial direction as a function of the gas temperature.

2.1.2. Hydrogen Peroxide Coolant

The coolant that is used in the Mk-II thruster is 90% hydrogen peroxide. This implies the solution contains 90% hydrogen peroxide and 10% water by weight. For regenerative cooling simulations in TDCAS, the primary properties of interest are density, heat capacity, viscosity, and thermal conductivity. Additional fluid properties that are of interest for the film cooling analysis are the saturation temperature and enthalpy change of vaporization. Before opening the discussion, it is important to note that available data for hydrogen peroxide is very limited, compared to common cryogenic rocket propellants like liquid hydrogen, liquid methane, or liquid oxygen. This is a major research gap that is also mentioned for other storable propellants, such as hydrazine [44]. The best data set that could be extracted from the open literature is presented in this section. This data set primarily consists of experimental measurements at low temperatures and extrapolated data for higher temperatures.

Density

The density of 90% hydrogen peroxide is obtained from the work of Kuntz et al. [26], who provide a summary of experimental density measurements between 273-466 K described in the literature. The data points are corrected for the decomposition of the hydrogen peroxide at higher temperatures. These measurements, which are not repeated here, are correlated using the linear approximation shown in

Equation 2.5. In this expression, and all others mentioned in this section, temperature (T) is inserted in Kelvin and density (ρ) is obtained in kg/m^3. The linear density approximation is correlated with a relative standard error of 0.51%.

$$\rho = 1709 - 1.08T \tag{2.5}$$

Heat Capacity

The heat capacity (c_p) of 90% hydrogen peroxide is described in the work of Ahlert and Younts [45] and based on experiments with fluid temperatures up to 464 K. They linearly correlate the data using Equation 2.6, which is reported to have an accuracy better than 2%. In this correlation, the heat capacity is obtained in J/(kg K).

$$c_p = 2510 + 0.883T \tag{2.6}$$

Dynamic Viscosity

For the dynamic viscosity (μ) of 90% hydrogen peroxide, the data documented by Kuntz et al. [26] is used. This data set summarizes experimental measurements in the literature at temperatures ≤323 K as well as extrapolated data of Rocketdyne up to 436 K. This particular data set is depicted in Figure 2.3 with the circular markers. In the present work, an exponential curve is fitted through this data set, which extrapolates the viscosity to even higher temperatures. This trend line follows Equation 2.7 and outputs the dynamic viscosity in centipoise as a function of the temperature in Kelvin. The function is fitted with a relative standard error of 2.25%.

$$\mu = 6.54 \cdot 10^{-2} \exp\left(\frac{494.95}{T - 125.77}\right) \tag{2.7}$$

One may observe from Figure 2.3 that Equation 2.7 agrees well with measurements and extrapolated data provided by Kuntz et al. In practice, the hydrogen peroxide regenerative coolant is not operated above 408 K, which lies well within the data set of Kuntz et al.

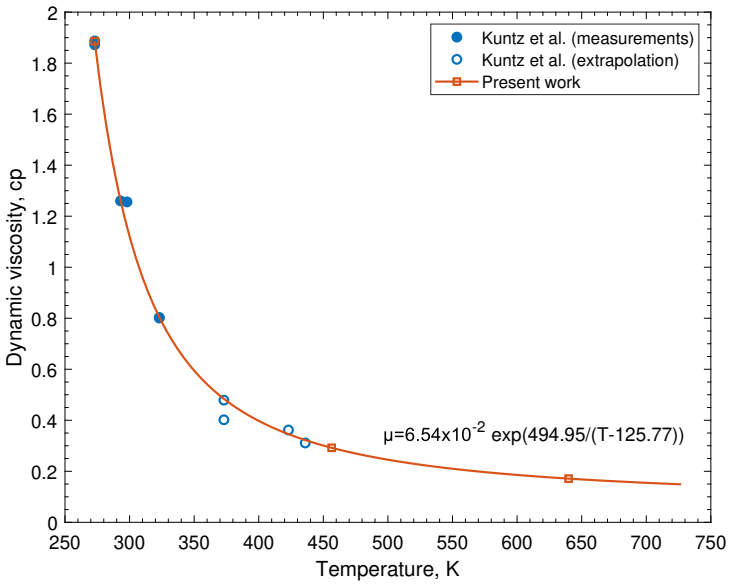

Figure 2.3: Dynamic viscosity of 90% hydrogen peroxide (data from ref. [26]).

Thermal Conductivity

The last transport property that is required to describe the hydrogen peroxide heat transfer characteristics is the thermal conductivity (λ). Kuntz et al. [26] present experimental data for 98.2% hydrogen peroxide at 273 K and 298 K and 50% hydrogen peroxide at 298 K. Measurements for 90% hydrogen peroxide could not be found in the open literature, although it is expected that these values are similar to 98.2% hydrogen peroxide. Provided the absence of measurements at higher temperatures, Kuntz et al. estimate the thermal conductivity of 98.2% hydrogen peroxide up to the critical temperature, as listed in Table 2.1. For this prediction, they use the thermal conductivity of water, which is well described in the literature[1]. In their model, they divide the temperature and conductivity of water by corresponding values at the critical point, thereby obtaining T/T_{crit} and λ/λ_{crit}. These parameters are also known as the *reduced fluid properties*. Since hydrogen peroxide is a water-like fluid, they assume that the reduced property curves of water also hold for hydrogen peroxide. Based on the reduced property curve of water and measured thermal conductivity at 273 K and 298 K, they estimate the critical thermal conductivity of 98.2% hydrogen peroxide. Combined with the known critical temperature of 98.2% hydrogen peroxide, the temperature-dependent thermal conductivity is found, as shown in Table 2.1.

It is worth noting that a similar technique for estimating the thermal conductivity of 98.2% hydrogen peroxide is mentioned by Constantine and Cain [28]. Values published in this piece of literature agree well with the method of Kuntz et al. at temperatures below 300 K but diverge at higher temperatures. Nevertheless, differences between the two simulations are small. For instance, at a temperature of 400 K, the data of Constantine and Cain shows a thermal conductivity which is 12% lower than the model of Kuntz et al. In this investigation, the extrapolation approach described in the previous paragraph was repeated, which showed an overall better match with the model of Kuntz et al. Therefore, this data set is used throughout the remainder of this work.

Table 2.1: Thermal conductivity of 98.2% hydrogen peroxide and water up to the critical temperature (hydrogen peroxide data from ref. [26] and NIST).

T, K	$\lambda_{H_2O_2}$, mW/(m K)	λ_{H_2O}, mW/(m K)	T, K	$\lambda_{H_2O_2}$, mW/(m K)	λ_{H_2O}, mW/(m K)
273(1)	555.6	561.0	478	733.8	660.9
278	559.0	568.6	500	726.9	644.8
298(1)	586.7	607.2	544	699.2	594.5
322	630.0	642.4	566	678.4	559.8
345	664.6	663.9	589	654.2	519.1
366	694.0	676.6	611	624.8	474.7
389	714.8	682.6	633	591.9	425.7
411	728.6	683.5	655	552.1	—
433	737.3	680.0	678	510.6	—
455	739.0	672.5	727	249.2	—

Saturation Temperature

The liquid-vapor equilibrium for 90% hydrogen peroxide is obtained from the work of Constantine and Cain [28] and shown in Figure 2.4. Constantine and Cain document the saturation pressure based on experimental findings of Scatchard et al. [46] up to 363 K and extrapolate this data to the critical temperature. The corresponding curve is based on the assumption that the hydrogen peroxide solution is homogeneous and that a single boiling point exists. For reference, the liquid-vapor equilibrium of pure water is also shown, with data obtained from the open-source databases of NIST. The region below the saturation curves represents the liquid phase of the fluid, whereas the region above the saturation curve corresponds to the gaseous phase. The upper end of the liquid-vapor equilibrium curve is bounded by the critical point, which is estimated at a pressure of 24.5 MPa and temperature of 718 K for 90% hydrogen peroxide [27]. At temperatures and pressures which exceed critical conditions, the fluid is said to be *supercritical*. Based on the current design of the Mk-II thruster, it is reasonable to assume that neither the hydrogen peroxide film coolant nor regenerative coolant is operated in the supercritical phase.

[1] For example in the open online databases of the National Institute of Standards and Technology (NIST).

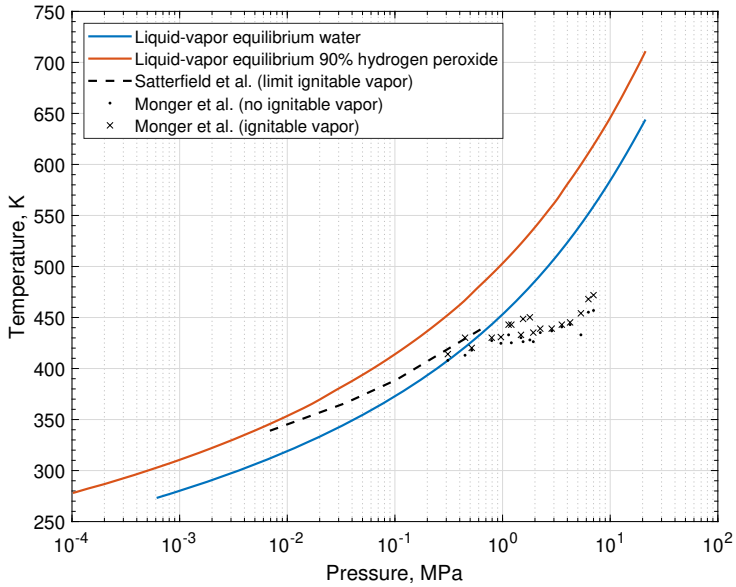

Figure 2.4: Liquid-vapor equilibrium of 90% hydrogen peroxide and water (data from refs. [28, 47, 48] and NIST).

Several pieces of literature [47, 48] also describe an “explosive vapor range” close to the boiling point, which marks a range in which the hydrogen peroxide vapor is ignitable. It is stressed that hydrogen peroxide is not explosive (for instance, like gun powder), but it *can* rapidly decompose at elevated temperature. Davis et al. [27] note that in the explosive range, the presence of an ignition source can trigger a self-accelerating decomposition reaction of the vapor which may result in deflagration or detonation.

The limit temperature at which an ignitable vapor composition is achieved is experimentally determined by Satterfield et al. [48] at pressures between 6.9 and 690 kPa and shown with the dashed line in Figure 2.4. This pressure range is extended up to 7 MPa in the work of Monger et al. for 90% hydrogen peroxide. Results of their experimental work are also shown in Figure 2.4, with crosses indicating measurements where vapor ignition was achieved. These results show a fair agreement with the work of Satterfield et al.

Interestingly, both data sets are located below the liquid-vapor saturation curve of 90% hydrogen peroxide. Therefore, it is expected that decomposition occurs upon vaporization of the hydrogen peroxide, provided that an ignition source is present. A similar observation is posed by Cai et al. [49], who mention a fast, self-sustaining decomposition of hydrogen peroxide upon boiling. According to Corpening et al. [50], this “fast” decomposition of 90% hydrogen peroxide vapor is characterized by a concentration half-life of approximately 1 ms. The heat that is released in the decomposition reaction further accelerates the vaporization rate, a concept that will be explained in more detail in section 2.5. It is expected that the ignitable vapor limit is only associated with vapor phase decomposition and not with liquid phase decomposition. Experiments at high temperatures are required to validate this hypothesis.

Enthalpy Change of Vaporization

The last fluid parameter required in TDCAS is the enthalpy change, or heat, of vaporization ($\Delta_v H$). This parameter represents the amount of energy that must be added to the fluid to achieve a liquid-gas phase change. The required heat to vaporize a substance reduces with increasing temperature and is zero at the critical point. Kuntz et al. [26] provide an overview of the calculated heat of vaporization of anhydrous hydrogen peroxide at temperatures between 273 K and 423 K. This data originates from a publication of Becco and is shown in Figure 2.5 on the right with square markers. Foley and Giguère [51] report a heat of vaporization of 1549.8$\pm$0.8 kJ/kg at 273 K, which agrees well with the data set of Kuntz et al. A correlation that relates the heat of vaporization of anhydrous hydrogen peroxide to the temperature is mentioned in the work of Heo [52] and Kang [53] and shown in Equation 2.8.

$$\Delta_v H_{H_2O_2} = 0.021066T^2 - 25.817T + 18412 \tag{2.8}$$

Notice that the heat of vaporization in this expression is obtained in cal/(g mol), as a function of the temperature in °C. No validity range is provided for this expression. Equation 2.8 is also plotted in Figure 2.5 as a function of the reduced temperature. One can immediately see this expression correlates poorly with data of Kuntz et al. What is more, the slope is unclear and tends to flatten near the critical point. A further investigation in the literature revealed that Equation 2.8 is also mentioned by Schumb et al. [54], who also highlight an overpredictive trend compared to experimental measurements. Schumb et al. state that the equation is best used at temperatures moderately above 298 K (reduced temperature of 0.41) which could explain the unclear trend near the critical point.

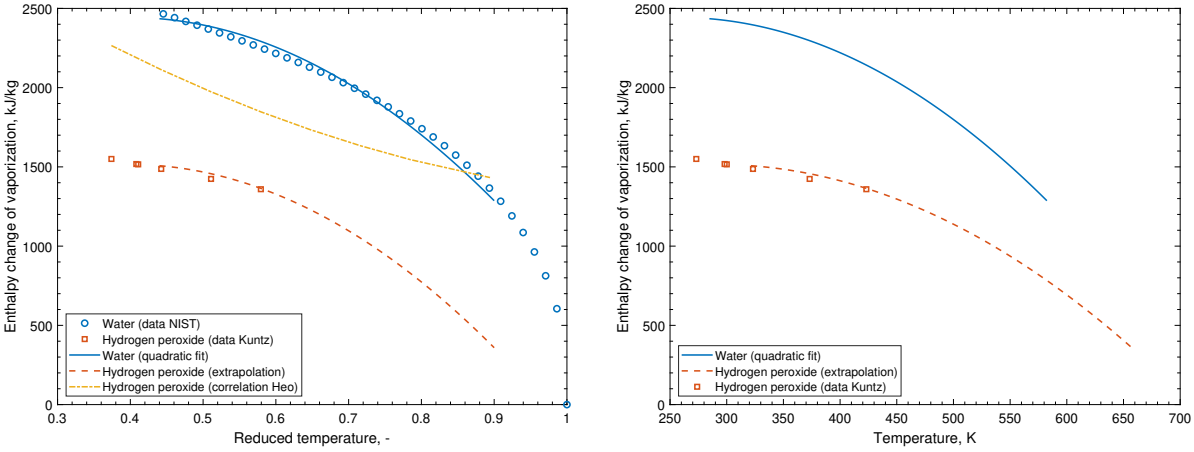

Figure 2.5: Enthalpy change of vaporization for anhydrous hydrogen peroxide and water (data from refs. [26, 55] and NIST).

In the present investigation, the enthalpy change of vaporization for hydrogen peroxide is estimated based on reference data for water and the data points of Kuntz et al. The reference data for water, illustrated with the circular markers in Figure 2.5, is obtained from the database of NIST. A quadratic trend line is fitted through the data points for water in the reduced temperature interval 0.44 to 0.9. To estimate the enthalpy change of vaporization for hydrogen peroxide, this curve is translated to match the data set of Kuntz et al. Hereafter, the reduced temperatures are multiplied with the critical temperature of anhydrous hydrogen peroxide (assumed to be 730 K, [27]), to obtain the curve shown in Figure 2.5 right. This estimated curve follows Equation 2.9,

$$\Delta_v H_{H_2O_2} = -0.0086T^2 + 4.99T + 790.19 \tag{2.9}$$

where the heat of vaporization is obtained in kJ/kg and temperature inserted in Kelvin. The estimated curve agrees well with data presented by Kuntz et al. and approaches zero with increasing temperature. The temperature range for which this curve is estimated is 321-657 K. For the preliminary design considered in this report, the estimated enthalpy change of vaporization noted in Equation 2.9 is used.

2.2. Thrust Chamber Sizing and Computational Domain

In TDCAS, the geometry of the thrust chamber and integrated cooling channels are automatically calculated. This section provides a brief overview of the most important calculations involved in this process; for a detailed description of all required user inputs, the reader is referred to Appendix C. The reference frames that are used for sizing the thruster and in the numerical model are briefly discussed in subsection 2.2.1. Hereafter, subsection 2.2.2 describes how the thrust chamber contour is generated. This is followed by a description of the structured mesh of the chamber wall, which is used in all 2-D finite element analyses (subsection 2.2.3). Lastly, subsection 2.2.4 touches on the performance estimation models that are implemented in TDCAS.

2.2.1. Reference Frames

In TDCAS, both the cylindrical and Cartesian coordinate systems are used, as illustrated in Figure 2.6. The cylindrical reference frame (r,θ,z) is used for describing the cooling channel and engine geometries. The origin of the reference frame is placed at the injector plane, with the r direction pointing towards to fuel inlet port of the injector (not shown in Figure 2.6). Also shown in the picture are the nozzle inlet plane, nozzle throat plane, and nozzle exit plane, which are frequently mentioned in the discussion in this report.

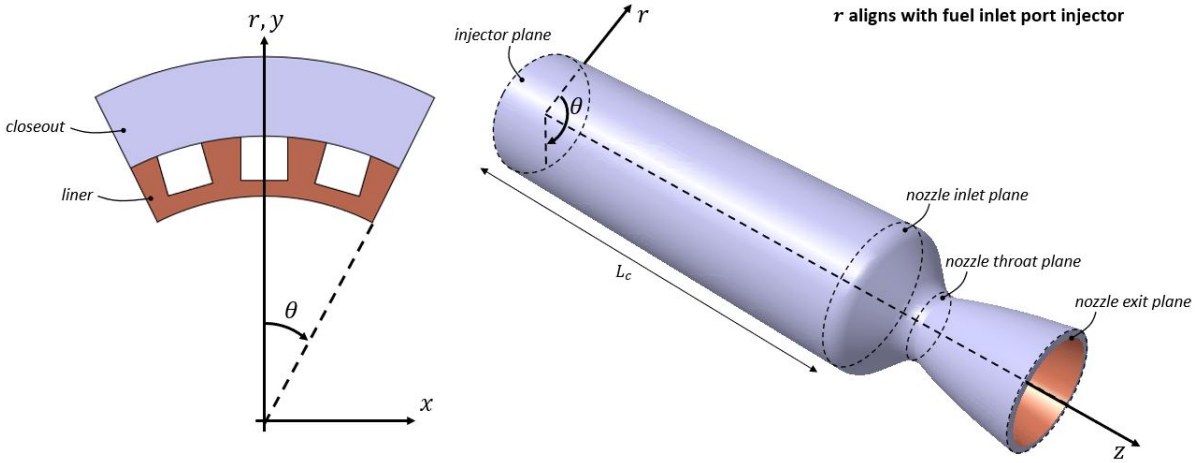

Figure 2.6: Cartesian and cylindrical coordinate system and placement with respect to the thrust chamber.

The 2-D Cartesian coordinate system (x,y) is used for all planar finite element computations of the wall. The origin of this axis system is located at the centerline of the thrust chamber, which aligns with the z-axis of both the cylindrical coordinate system and Cartesian coordinate system.

2.2.2. Thrust Chamber Contour

Based on the propellant mixture ratio, chamber pressure, and propellant combination that the user enters in TDCAS, the cross section area of the nozzle throat (A_t) is calculated, using Equation 2.10. Since the chamber has a circular geometry, the geometrical throat radius (r_t) can directly be derived from the throat area.

$$A_t = \frac{(c^*)_{eff} \cdot \dot{m}}{p_o} \tag{2.10}$$

In Equation 2.10, $(c^*)_{eff}$ represents the effective characteristic velocity, $\dot{m}$ the total mass flow rate in the chamber, and p_o the nozzle stagnation pressure. The characteristic velocity is uniquely defined for a given gas composition and could be seen as a measure for combustion performance. The characteristic velocity can be obtained from Equations 2.11 and 2.12 [7].

$$(c^*)_{eff} = \eta_c \cdot c^* \tag{2.11}$$

$$c^* = \sqrt{\frac{R \cdot T_o}{M_W \cdot \gamma \left(\frac{\gamma+1}{2}\right)^{\frac{1+\gamma}{1-\gamma}}}} \tag{2.12}$$

One may notice that Equation 2.12 follows directly from ideal rocket theory. In the above-mentioned expressions, η_c denotes the characteristic velocity quality factor, R the universal gas constant, T_o the nozzle stagnation temperature, M_W the molar mass of the hot gas, and γ the specific heat ratio of the gas. The latter three properties are all obtained from CEA. From Equation 2.12, one can conclude that a

light gas mixture (low M_W) or high combustion temperature facilitates a high characteristic velocity. The molar mass depends on the gas composition, which is directly related to the propellants that are used (kerosene and hydrogen peroxide in the Mk-II), as well as the temperature. The stagnation temperature is related to the energy that is released by the chemical reaction in the combustion chamber, which can also be related to the propellant combination and mixture ratio. When the combustion process is ideal, which implies no losses in the energy release, T_o is also often referred to as the *adiabatic flame temperature*. An example of the ideal characteristic velocity of common hydrocarbon and storable propellant combinations considered in the introduction of this report is shown in Figure 2.7. Curves in this plot are obtained from an analysis in CEA, assuming shifting equilibrium flow conditions and a unity characteristic velocity quality factor.

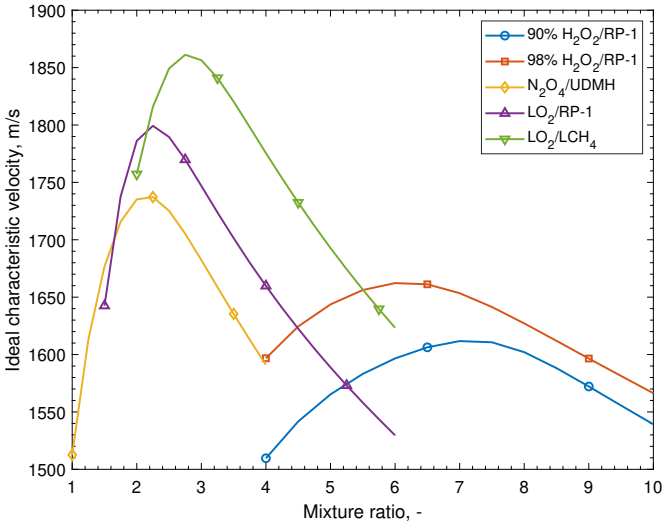

Figure 2.7: Ideal characteristic velocity of hydrogen peroxide-kerosene mixtures compared to frequently used storable and hydrocarbon propellant combinations. All data is based on a chamber pressure of 4 MPa and shifting equilibrium flow conditions.

In reality, the combustion reaction is almost always associated with finite losses. In this investigation, these losses are captured in the introduced quality factor. The characteristic velocity quality factor is mainly driven by losses in the injection, atomization, and mixing of the propellants [56]. This results in an incomplete energy release. For a well-designed thruster, Huzel and Huang [7] report that η_c is typically between 87% and 103%[2]. Sutton [57] on the other hand reports a typical value for η_c >95%. The exact value taken for the characteristic velocity efficiency follows from experiments in the Mk-II thruster, which are described in subsection 4.3.2.

After defining the throat area, TDCAS determines the cross-section area at the exit plane of the nozzle (A_e), based on Equation 2.13 [7]. This expression relates the earlier introduced chamber pressure and specific heat ratio, as well as the static pressure gas at the nozzle exit plane (p_e), to the nozzle area ratio. The latter term is also often referred to as the *expansion ratio* of the nozzle. In TDCAS, the nozzle exit pressure is a user input.

$$\frac{A_e}{A_t} = \frac{\left(\frac{2}{\gamma+1}\right)^{\frac{1}{\gamma-1}} \left(\frac{p_o}{p_e}\right)^{\frac{1}{\gamma}}}{\sqrt{\frac{\gamma+1}{\gamma-1}\left(1-\left(\frac{p_e}{p_o}\right)^{\frac{\gamma-1}{\gamma}}\right)}} \tag{2.13}$$

[2]The exact reason for the efficiency greater than 100% is not given in the original piece of literature, but it is expected that this is caused by the definition of the ideal characteristic velocity (Equation 2.12). The molar mass, specific heat ratio, and flame temperature that are used in this expression are subjected to several simplifying assumptions in CEA. Furthermore, the analysis settings may impact the solution. For instance, when combusting 90% hydrogen peroxide and kerosene at a chamber pressure of 4 MPa and mixture ratio of 8, a shifting equilibrium flow analysis provides an ideal characteristic velocity of 1602 m/s, whereas a frozen flow analysis provides a characteristic velocity of 1579.2 m/s.

Based on the geometry of the nozzle at the throat and exit plane, the contour of the nozzle can be calculated. In TDCAS a parabolic nozzle contour is used. Sizing parameters of this parabolic curve are obtained from the work of Rao [58], who studied nozzle contours that optimize the thrust output. The length of the nozzle, defined as the distance between the throat plane and exit plane, is set to 80% of a conical nozzle with 15° half angle. This provides a good balance between divergence losses and dry mass [57].

The geometry of the thrust chamber upstream of the throat, i.e. the cylindrical/barrel chamber section and nozzle convergent section, is obtained from the empirical characteristic length (L^*). One may envision the characteristic length as a parameter that determines how long propellants remain in the combustion chamber. If the characteristic length is too short, propellants may not come to complete combustion, resulting in a reduction in the characteristic velocity. On the other hand, a large characteristic length increases the chamber mass and results in more heat being transferred to the coolant. The volume of the combustion chamber (V_c) can be obtained as a function of the characteristic length and throat area, as shown in Equations 2.14 and 2.15 [7].

$$V_c = L^* \cdot A_t = \frac{L^* \cdot c^* \cdot \dot{m}}{p_o} \tag{2.14}$$

$$V_c = \pi r_c^2 L_c + V_{con} \tag{2.15}$$

In these expressions, r_c denotes the chamber radius, L_c the length of chamber barrel (see also Figure 2.6), and V_{con} the volume of the cone-shape convergent section of the nozzle. The optimal characteristic length for a thrust chamber depends on many parameters, including the propellant combination, injector configuration, and chamber geometry. For 90% hydrogen peroxide and kerosene, a wide range of values for characteristic length is reported in the open literature. Cong et al. [59] achieve good results at a characteristic length of 0.8 m. The injector configuration that is used is not mentioned in the publication. Jo et al. [60] use an axial (showerhead) injector and find no obvious improvements when the characteristic length exceeds 1.07 m. A slightly higher value of 1.34 m is used by Heo [52], who also uses an axial injector. Axial injectors are simple in design, but provide relatively poor atomization and mixing performance compared to more advanced designs, such as a coaxial swirl injector or self-impinging doublet/triplet injector [7]. For the proposed AM Mk-II thruster, a characteristic length of 0.6 m is used. This follows from positive test experience at Dawn Aerospace with the current propellant injector design.

2.2.3. Mesh Generation

The mesh that is used in TDCAS consists of a 2-D (cross-section) representation of a channel-cooled thrust chamber. This geometry is described by an inner wall with thickness t_w, a channel with width c_w and height c_r, and closeout with thickness t_w. Other parameters that are required to define the geometry are the number of cooling channels N and internal chamber radius r, as depicted in Figure 2.8. Instead of modeling the full cross-section of the thrust chamber, TDCAS makes smart use of the symmetry planes in the structure. Therefore, only half a cooling channel is numerically resolved, with symmetry boundary conditions on the edges (as illustrated in Figure 2.8). This modeling concept is similar to that of ref. [39] and greatly reduces the computational cost. In TDCAS, the cooling channel geometry is inserted at discrete user-specified locations. In-between these locations, the geometry is obtained through linear interpolation.

The cooling channel definition (N, c_w, c_r, t_w, and t_{cl}) that is inserted by the user is converted to a structured, quadrilateral mesh with piece-wise linear elements. The mesh is automatically generated by TDCAS and can be refined with a user-defined refinement factor. This factor scales the maximum number of nodes that TDCAS is allowed to use for the mesh. By default, a mesh refinement factor of 1 is used in TDCAS.

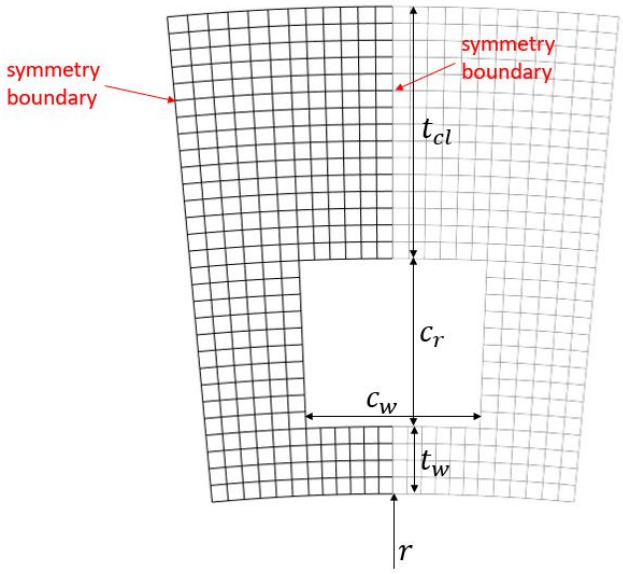

Figure 2.8: Structured quadrilateral planar mesh that is automatically generated by TDCAS.

The second parameter that controls the total number of nodes and elements, is the axial mesh spacing (Δz). This parameter is also user-defined, and controls the distance of each planar mesh, as depicted in Figure 2.9. By default, a 2 mm axial spacing is used in TDCAS, which provides a good balance between accuracy and computational cost. A more in-depth explanation of the mesh refinement factor and axial spacing is provided during the mesh refinement study, which can be found in section 3.1.

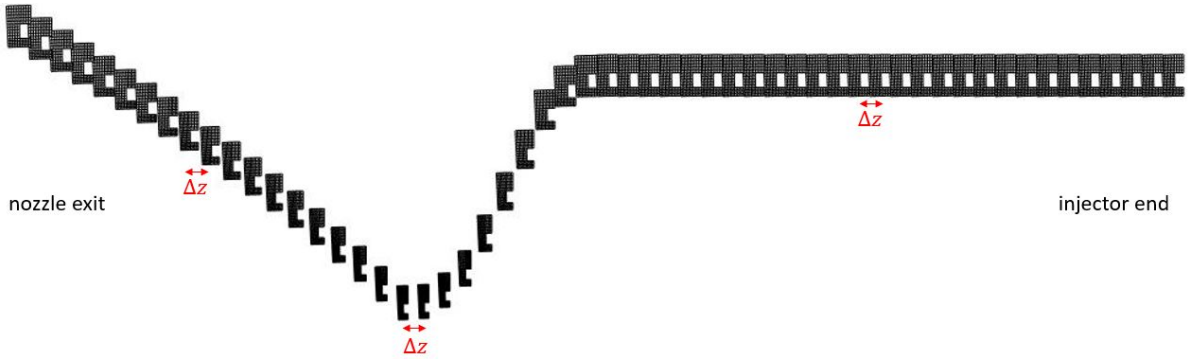

Figure 2.9: Thrust chamber resembled by planar mesh elements with uniform (coarse) spacing Δz.

2.2.4. Performance Estimation

To verify compliance with customer requirements REQ-001 to REQ-004 in a later part in this report, a performance estimation module is implemented in TDCAS. The overall thruster performance is measured in specific impulse (I_{sp}), as shown in Equation 2.16. The specific impulse is measured in seconds and a function of the characteristic velocity (c^*), thrust coefficient (c_F), and gravitational acceleration at sea level (g_0).

$$I_{sp} = \frac{(c_F)_{eff} \cdot (c^*)_{eff}}{g_0} \tag{2.16}$$

The effective thrust coefficient which is introduced in this expression can be seen as a measure for the ability of the nozzle to generate thrust. The thrust coefficient follows from Equations 2.17 and 2.18 and is a function of a quality factor (η_F), the thrust force (F), the chamber pressure (p_o), and the nozzle throat area (A_t).

$$(c_F)_{eff} = \eta_F \cdot c_F \tag{2.17}$$

$$c_F = \frac{F}{p_o \cdot A_t} \tag{2.18}$$

When applying ideal rocket theory, the thrust coefficient may also be written as a function of the gas specific heat ratio (γ), the chamber pressure (p_o), the nozzle exit pressure (p_e), the local atmospheric pressure (p_a), and the nozzle expansion ratio (A_e/A_t), as shown in Equation 2.19 [7].

$$c_F = \sqrt{\frac{2\gamma^2}{\gamma-1}\left(\frac{2}{\gamma+1}\right)^{\frac{\gamma+1}{\gamma-1}}\left(1-\left(\frac{p_e}{p_o}\right)^{\frac{\gamma-1}{\gamma}}\right)} + \frac{A_e}{A_t}\left(\frac{p_e - p_a}{p_o}\right) \tag{2.19}$$

The (ideal) thrust coefficient is mainly dependent on the flow and expansion in the nozzle and to a lesser extend on the combustion process. The first term in Equation 2.19 is also known as the thrust coefficient for *optimal expansion*. A condition for optimal flow expansion is achieved when the pressure at the nozzle exit is equal to the local atmospheric pressure. When the nozzle exit pressure exceeds the local atmospheric pressure, the flow is said to be *under-expanded*. On the other hand, an exit pressure much lower than the atmospheric pressure results in an *over-expanded* flow.

From Equation 2.19, one may conclude that a high nozzle pressure ratio (p_o/p_e) is beneficial for achieving a high thrust coefficient. Furthermore since the thrust coefficient, and thus specific impulse, changes with atmospheric pressure, there exists an altitude at which the expansion is optimal[3]. The altitude of optimal expansion follows from the defined nozzle exit pressure, which is typically based on optimization of the ascent profile of the vehicle. A nozzle exit pressure of 1 atm results in optimal expansion at sea level but may introduce major performance losses due to over-expansion of the flow at higher altitudes/in vacuum. This is clearly visible in Figure 2.10 on the left. On the other hand, when the nozzle exit pressure is too low, severe over-expansion with potential flow separation may occur at sea level [61]. In the absence of a detailed ascent trajectory simulation, it is assumed that the spaceplane spends 1/3 of its flight in the lower atmosphere (near sea level) and 2/3 of its flight in the upper atmosphere (near vacuum). Based on this assumption, the weighted specific impulse is calculated, as shown in Figure 2.10 on the right. In this investigation, the nozzle exit pressure is set to 65 kPa, which provides a good balance between sea level and vacuum performance whilst avoiding flow separation. It is recommended to revisit this value when detailed ascent trajectory simulations are available.

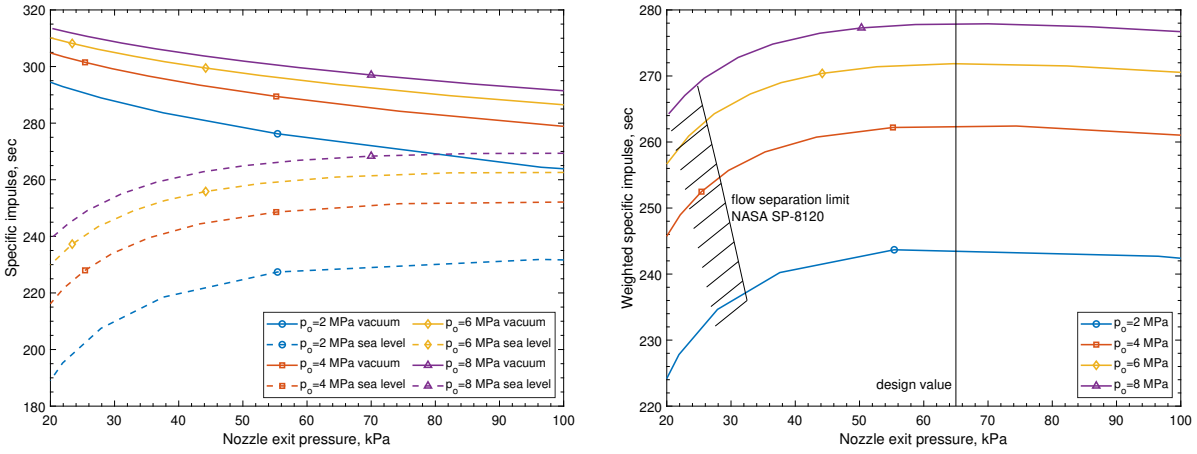

Figure 2.10: Vacuum and sea level specific impulse as a function of the exit pressure. All data is based on the combustion of 90% hydrogen peroxide and kerosene, at a mixture ratio of 8, assuming shifting equilibrium flow conditions. Weighted specific impulse is the sum of 1/3 the sea level specific impulse and 2/3 the vacuum specific impulse.

[3]Provided that the nozzle has a fixed geometry. For altitude-adaptive nozzles, such as an aerospike, this is not a concern.

Similar to the characteristic velocity, a quality factor is introduced to correct for non-ideal performance. This quality factor is experimentally obtained from the thrust coefficient, as a function of the measured thrust, chamber pressure, and known throat area. In the absence of experimental data for a particular thruster design, designers may rely on typical values that are provided in the literature. For a well-designed thruster, Huzel and Huang [7] report that η_F is typically between 92% and 100%. On the other hand, Sutton [57] documents a typical value for η_F >90%.

So far, the discussion assumes no presence of a film coolant in the combustion chamber. Several experimental studies [52, 62, 63] have demonstrated that it is very reasonable to expect a moderate to high performance reduction when a film coolant is used. This mainly translates itself into a loss in characteristic velocity. To estimate these losses, a model introduced by Berman and Andrysiak [64] is used, which is shown in Equation 2.20. This model assumes that the combustion chamber can be divided into two distinct zones that operate at a different mixture ratio: a hot core flow and a cold film coolant flow near the chamber wall.

$$c^* = \omega c^*_{cf} + (1-\omega)\eta_c c^*_g \tag{2.20}$$

In Equation 2.20, ω denotes the film cooling fraction, which represents the ratio between the film coolant mass flow rate and total mass flow rate. Subscript “cf” denotes the film coolant properties, whereas subscript “g” denotes the core stream properties. One must pay special attention that the total mass flow rate includes contributions from the oxidizer and fuel in the core flow, as well as the film coolant. The characteristic velocity of the core stream (c^*_g) is evaluated at the core mixture ratio (MR_g), which follows from Equations 2.21 and 2.22.

$$MR_g = \frac{(\dot{m}_{ox})_g}{\dot{m}_{fu}} = MR - \omega(MR+1) \tag{2.21}$$

$$MR = \frac{\dot{m}_{ox}}{\dot{m}_{fu}} = \frac{(\dot{m}_{ox})_g + \dot{m}_{cf}}{\dot{m}_{fu}} \tag{2.22}$$

The validity of these expressions extends to the use of the oxidizer as a film coolant; a different result is obtained when the film coolant comprises the fuel. The total mixture ratio (MR) is a function of the oxidizer mass flow rate ($\dot{m}_{ox}$), the fuel mass flow rate ($\dot{m}_{fu}$) and the film flow rate ($\dot{m}_{cf}$). Without the presence of a film coolant, the film cooling fraction is zero and the core mixture ratio is equal to the total mixture ratio. Under the presence of a film coolant, the core mixture ratio decreases. This has a direct impact on the characteristic velocity, as can be seen in Figure 2.7.

The last parameter that is required for solving Equation 2.20 is the characteristic velocity of the film layer. Similar to the core flow, this parameter is a function of the local mixture ratio, which depends on the mixing of the core flow with the film layer. In the present investigation, it is assumed that the (hydrogen peroxide) film coolant does not react with the core stream, but does fully decompose in oxygen and steam. As a result, the characteristic velocity of the film is taken as 935 m/s, which follows from CEA for the decomposition reaction of 90% hydrogen peroxide. Since mixing with the core stream is neglected, this likely presents a conservative estimate for the performance. The validity of this simplifying assumption is investigated in subsection 4.2.3.

2.3. Hot Gas Heat Transfer

At the center of the thrust chamber, the core stream moves at a high velocity and has a high temperature. At the (stationary) wall of the chamber, the gas velocity is zero and the gas temperature is equal to the temperature of the wall (T_w). These large gradients introduce a thin velocity and temperature boundary layer, which is schematically shown in Figure 2.11. The exact temperature profile in the boundary layer is governed by conduction heat transfer and frictional dissipation [42]. Because a temperature gradient exists in the fast-moving boundary layer, a heat flow will be present. This heat flow, also known as convection, is directed from the hot gas to the (colder) wall and is one of the driving thermal loads in the thrust chamber. The convective heat transfer models that are used in TDCAS are discussed in subsection 2.3.1.

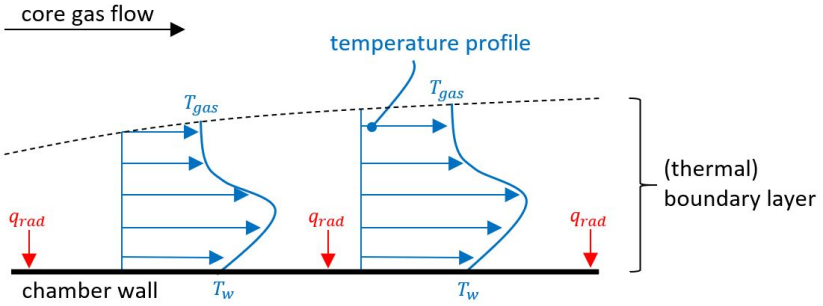

Figure 2.11: Schematic representation of thermal boundary layer in a rocket engine.

Besides convection, the hot gas also emits heat in the form of thermal radiation (q_{rad}). Although the radiative heat transfer in thrust chambers is typically an order of magnitude smaller than convective heat transfer [57], it is still included in this report in subsection 2.3.2 for completeness.

Before entering the discussion, three dimensionless constants are introduced: The Nusselt number, the Reynolds number, and the Prandtl number. The Nusselt number, shown in Equation 2.23, is a function of the earlier introduced heat transfer coefficient (α), thermal conductivity (λ), and hydraulic diameter (D_h). This constant relates the convective heat transfer to the conductive heat transfer.

$$Nu = \frac{\alpha \cdot D_h}{\lambda} \tag{2.23}$$

The hydraulic diameter equals four times the flow area, divided by the perimeter of the conduit. The Reynolds number, presented in Equation 2.24, relates the inertial forces in the fluid to the viscous forces. This parameter is a function of the bulk flow velocity (v), fluid density (ρ), hydraulic diameter (D_h), and dynamic viscosity (μ).

$$Re = \frac{\rho \cdot v \cdot D_h}{\mu} \tag{2.24}$$

The Prandtl number, shown in Equation 2.25, relates the frictional dissipation to the thermal diffusivity. This parameter is a function of the thermal conductivity (λ), heat capacity (c_p), and dynamic viscosity (μ), which are uniquely defined for a fluid at a given temperature and pressure.

$$Pr = \frac{c_p \cdot \mu}{\lambda} \tag{2.25}$$

Equations 2.23 to 2.25 are not only relevant for the hot gas heat transfer, but also for the regenerative cooling and film cooling models introduced later in this report.

2.3.1. Convection

In its most general one-dimensional form, the heat that is transferred through convection can be calculated using Equation 2.26, which is also known as Newton's law of heating and cooling.

$$Q = \alpha \cdot A \cdot (T_{ref} - T_w) \tag{2.26}$$

In Equation 2.26, α denotes the heat transfer coefficient, A the area over which heat is being transferred, T_{ref} the reference temperature of the hot gas, and T_w the wall temperature. The reference temperature is taken as the adiabatic wall temperature, which represents the temperature that the chamber wall would obtain when it is fully isolated. The adiabatic wall temperature is defined in Equation 2.27 [65],

$$T_{aw} = T + R_f \left(T_o \cdot \eta_c^2 - T\right) \tag{2.27}$$

where T represents the static gas temperature, T_o the stagnation gas temperature, R_f the recovery factor, and η_c the characteristic velocity efficiency. The static and stagnation gas temperature follow from CEA and the isentropic flow relations, which were introduced earlier in this report. For first-order estimations, Huzel and Huang [7] note that this recovery factor may be estimated as $Pr^{0.5}$ for laminar boundary layers, or $Pr^{0.33}$ for turbulent boundary layers. In this investigation, it is assumed that the flow in the nozzle is turbulent. For the combustion of hydrogen peroxide and kerosene, the Prandtl number of the gas is generally less than one. As a result, the turbulent recovery factor is also less than one.

In the present work, two empirical models are considered for predicting the heat transfer coefficient that is used in Equation 2.26. The first model, proposed by Bartz [66], is shown in Equation 2.28 and is derived for gas flow in rocket nozzles. This correlation is derived from fully developed flow through straight pipes and corrected to obtain a good agreement with experimental heat transfer data in a subscale rocket nozzle.

$$\alpha_g = \left[\frac{0.026}{D_t^{0.2}}\left(\frac{\mu^{0.2}c_p}{Pr^{0.6}}\right)_0\left(\frac{p_0}{c^*}\right)^{0.8}\left(\frac{D_t}{R_t^*}\right)^{0.1}\right]\left(\frac{A_t}{A}\right)^{0.9} s \tag{2.28}$$

$$s = \left(\frac{1}{2}\frac{T_w}{T_o}\left(1+\frac{\gamma-1}{2}M^2\right)+\frac{1}{2}\right)^{-0.68}\left(1+\frac{\gamma-1}{2}M^2\right)^{-0.12} \tag{2.29}$$

Newly introduced parameters in Equations 2.28 and 2.29 are the nozzle throat diameter (D_t), the dynamic viscosity (μ), the specific heat at constant pressure (c_p), and the throat radius of curvature (R_t^*). All transport properties in the Bartz equation (μ, c_p, Pr) are evaluated at stagnation conditions based on a frozen chemical composition of the boundary layer. Bartz introduces an empirical scaling constant of 0.026 by forcing agreement of Equation 2.28 with measurements at the nozzle throat. However, it should be mentioned that this value depends strongly on the boundary layer in the combustion chamber and can therefore vary between different engines [43].

The second correlation that is considered in this study originates from the work of Cinjarew and Dobrovolsky [67] and is presented in Equation 2.30. This expression is considered based on the positive experience described by Kirchberger [65], who studied heat transfer in small hydrocarbon rocket engines with a size comparable to the Mk-II thruster.

$$\alpha_g = \frac{0.01975\dot{m}^{0.82}}{D^{1.82}}\left(\lambda^{0.18}c_p^{0.82}\right)_{am}\left(\frac{T_{aw}}{T_w}\right)^{0.35} \tag{2.30}$$

Newly introduced parameters in this expression are the local chamber diameter (D) and the hot gas thermal conductivity (λ). In the original 1955 publication, Cinjarew and Dobrovolsky describe that the boundary layer transport properties are evaluated at the wall temperature. However, a more recent investigation of Kirchberger et al. [68] in small hydrocarbon rocket engines has demonstrated that more realistic results are obtained when the transport properties are evaluated at the film temperature. The film temperature, designated with subscript “am”, is taken as the arithmetic mean between the gas and wall temperature. This approach is adopted in the present work. The gas properties at this arithmetic mean temperature are obtained from CEA by solving a chemical equilibrium problem with assigned pressure and temperature.

2.3.2. Radiation

Besides convective heat transfer from the hot gas, energy may also be transferred through radiation. The magnitude of the radiative heat transfer primarily depends on the composition and temperature of the gas. Coats [56] describes that the major emitting molecules in the hot combustion gas are water, carbon dioxide, and carbon monoxide. Contrary, symmetrical molecules such as hydrogen and oxygen are noted to have no relevant emission bands in rocket applications [69]. Under the assumption that both the hot gas and chamber wall act as a *grey medium*[4], the net radiative heat flux may be written as shown in Equation 2.31 [65].

[4] This implies that the emissivity and absorbtivity are independent of the wavelength at which radiative energy exchange occurs.

$$q_{rad} = 5.67 \cdot 10^{-8} \left(\frac{T_g^4 - T_w^4}{\frac{1}{\epsilon_g} + \frac{1}{\epsilon_w} - 1} \right) \tag{2.31}$$

In this expression, T_g and T_w denote the temperature of the gas and wall respectively, whereas ϵ_g and ϵ_w represent the corresponding emissivities. The value placed in front of the term in brackets is also known as the Stefan-Boltzmann constant. A fundamental challenge of Equation 2.31 is that the exact values for the emissivities are not trivial to determine. The emissivity of the chamber wall may vary as a function of temperature or when carbon is deposited on the wall[5]. On the other hand, the emissivity of the gas is dependent on the species that are present in the gas and the corresponding radiation spectrum.

Instead of Equation 2.31, one can also rely on numerical estimations for the radiative heat transfer, by solving the integro-differential radiative transfer equation [4]. This approach requires detailed knowledge about the multidimensional radiation intensity and physical properties of the gas [70], which is also not trivial to obtain. Furthermore, solving the radiative transfer equation can be computationally expensive.

In the present work, an empirical approach is taken to get a first-order estimation of the hot gas radiative heat transfer. Kirchberger et al. [68] mention two empirical correlations to predict the radiative heat flux (in W/m^2) in small hydrocarbon rocket engines. These are noted separately for water and carbon dioxide in Equations 2.32 and 2.33.

$$q_{H_2O} = 5.74 \left(\frac{p_{H_2O} \cdot r_c}{10^5} \right)^{0.3} \left(\frac{T_g}{100} \right)^{3.5} \tag{2.32}$$

$$q_{CO_2} = 4 \left(\frac{p_{CO_2} \cdot r_c}{10^5} \right)^{0.3} \left(\frac{T_g}{100} \right)^{3.5} \tag{2.33}$$

In the above-mentioned expressions, r_c denotes the chamber radius in meters, T_g the gas temperature in Kelvin, and p the partial pressures of water and carbon dioxide in Pascal. The partial pressure of the gas species is obtained from the product of the chamber pressure and the mole fraction of the corresponding species. Kirchberger et al. have validated Equations 2.32 and 2.33 against radiation experiments at pressures between 0.1 and 6 MPa and temperatures between 1000 K and 2516 K. It is worth mentioning that the chamber pressure of the current iteration of the Mk-II thruster lies within the prescribed pressure range. Moreover, the adiabatic flame temperature of the combustion of 90% hydrogen peroxide and kerosene (~2700 K resp.) is very close to the experimental temperature limit of Kirchberger et al. Both expressions are implemented in TDCAS and can be included in or excluded from the 2-D heat transfer analysis with a simple boolean user input.

2.4. Regenerative Cooling

This section describes the setup of the 1-D regenerative cooling model. First, subsection 2.4.1 explains the empirical Nusselt correlations that are considered for predicting the coolant heat transfer in rough conduits. Second, in subsection 2.4.2, the impact of channel curvature and flow development on the coolant heat transfer is discussed. This is followed in subsection 2.4.3 by a description of the coolant temperature rise and pressure drop models that are implemented in TDCAS. Lastly, the hydrogen peroxide operating limits are briefly discussed in subsection 2.4.4.

2.4.1. Convection

In TDCAS, the convective heat transfer on the coolant side of the wall is modeled with empirical Nusselt correlations that are obtained from the literature. Traditionally, most Nusselt correlations have been derived experimentally based on flow in hydraulically smooth, straight channels. It is well-known that surfaces with a high roughness promote turbulence in the flow, which can have a large impact on the

[5]Carbon deposition on the chamber wall is very common in kerosene-propelled thrusters.

heat transfer [23]. Compared to machined surfaces, as-built AM parts feature a considerably higher surface roughness. To put these two production processes into perspective, Cook [6] mentions a typical surface finish for milled copper alloy channels of 20 µin RMS (≈0.46 µm Ra), whereas Stimpson et al. [25] measure a surface roughness in the range 9.6-13.8 µm Ra in AM cooling passages. What is more, flow tests of Stimpson et al. reveal that the Nusselt number in AM channels can be more than three times higher compared to smooth channels. This stresses the importance of capturing roughness effects in heat transfer modeling. TDCAS includes two methods to calculate the convective heat transfer of the hydrogen peroxide coolant: a smooth channel Nusselt correlation with roughness correction factor and an expression that is specifically developed for heat transfer in rough conduits.

Smooth Channel Correlation with Correction Factor
In this modeling approach, the well-known Dittus-Boelter correlation, shown in Equation 2.34, is used for predicting the convective heat transfer of the coolant. Experiments with hydrogen peroxide in smooth channels have demonstrated that this expression yields a conservative estimate of the heat transfer [28, 71].

$$Nu_0 = 0.023 Re^{0.8} Pr^{0.4} \tag{2.34}$$

In the Dittus-Boelter equation, the Reynolds number (Re) and Prandtl number (Pr) are evaluated based on the bulk fluid temperature. The expression is valid for Prandtl numbers between 0.7 and 160, Reynolds numbers greater than 1×10^4, and a channel length-to-diameter ratio greater than 10 [23]. The latter constraint originates from the fact that the flow is not yet fully developed close to the inlet of the channel, which increases heat transfer.

To capture increased heat transfer due to channel roughness, a correction factor is applied to Equation 2.34. An expression that is frequently used in rocket engine heat transfer analyses is presented in Equation 2.35 [36, 72, 73].

$$\frac{Nu}{Nu_0} = \frac{1 + 1.5 Pr^{-1/6} Re^{-1/8} (Pr - 1)}{1 + 1.5 Pr^{-1/6} Re^{-1/8} \left(Pr \frac{f}{f_0} - 1 \right)} \frac{f}{f_0} \tag{2.35}$$

Equation 2.35 relates the heat transfer correction factor (Nu/Nu_0) to the bulk flow Reynolds number, the Prandtl number, and the rough conduit friction factor (f). The parameter f_0 also represents a friction factor, but for smooth channels (i.e. no surface roughness). Equation 2.35 is a modified form of a comparable correlation originally proposed by Nunner [74]. Therefore, this expression is designated as the “modified Nunner” correlation in this work.

A different technique to correct for the surface roughness effects is proposed by Norris, as documented in ref. [25]. This corrective term is given in Equation 2.36 and relates the Nusselt number augmentation to the friction factor augmentation and bulk flow Prandtl number.

$$\frac{Nu}{Nu_0} = \left(\frac{f}{f_0} \right)^{0.68 Pr^{0.215}} \tag{2.36}$$

Norris finds that the heat transfer no longer increases for f/f_0 greater than four. The friction factor which is used in Equations 2.35 and 2.36 can be obtained from the implicit Colebrook-White correlation, which is presented in Equation 2.37 [75].

$$\frac{1}{\sqrt{f}} = -2 \log_{10} \left(\frac{k_s}{3.7 D_h} + \frac{2.51}{Re \sqrt{f}} \right) \tag{2.37}$$

In Equation 2.37, k_s/D_h denotes the relative surface roughness, which is a function of the hydraulic diameter (D_h) and the equivalent sand grain roughness (k_s). The latter value is typically obtained from hydraulic characterization tests with a fluid that has well-described thermophysical properties,

such as water or air. For the bimetallic Mk-II thrust chamber, the equivalent sand grain roughness is experimentally determined in subsection 4.3.3. For the investigated AM Inconel chamber, roughness figures reported in the work of Stimpson et al. [25] and Wildgoose et al. [76] are used. Both Stimpson et al. and Wildgoose et al. use the same test setup and measure the actual hydraulic diameter of straight cooling channels using CT scans. Roughness measurements are provided for the arithmetic mean roughness height (Ra) and the equivalent sand grain height k_s. A selection of their data that is relevant to this study is included in Table 2.2.

Table 2.2: Roughness measurements in additively manufactured Inconel 718 channels under different build angles (data from refs. [25, 76]).

Angle, deg	D_h design, µm	D_h actual, µm	Ra, µm	k_s, µm	Ra/D_h	k_s/D_h	Shape
45	610	664	13	120	0.020	0.180	Rectangular
45	631	632	11	114	0.017	0.180	Rectangular
45	750	725	11	139	0.015	0.192	Circular
45	834	920	14	212	0.015	0.230	Rectangular
45	1000	988	16	128	0.016	0.129	Circular
45	1250	1230	16	135	0.013	0.110	Circular
45	1261	1275	11	102	0.009	0.080	Rectangular
60	750	775	9	109	0.011	0.141	Circular
60	1000	1031	10	97	0.010	0.094	Circular
60	1250	1310	11	98	0.008	0.074	Circular
90	750	808	9	115	0.011	0.142	Circular
90	1000	1055	9	78	0.009	0.074	Circular
90	1250	1327	12	133	0.009	0.100	Circular
Average k_s 45°: 136±36 µm				Average k_s 90°: 109±28 µm			
Average k_s 60°: 101±7 µm							

The first column in Table 2.2 shows the angle of the channels with respect to the build plate of the AM machine. This angle is defined in Figure 2.12. As a consequence of the layer-by-layer fabrication technique, one would expect to see an increase in surface roughness with build angles that deviate from 90°. The measurements clearly show a decrease in surface roughness between a build angle of 45° versus 60° and 90°, which is in line with expectations. Nevertheless, this reducing surface roughness trend is not observed between measurements at 60° and 90°. Furthermore, at a given build angle, moderate to large deviations exist in the relative surface roughness. These deviations are also present in the arithmetic mean roughness height. One may also observe that the equivalent sand grain roughness (measured in hydraulic characterization tests) is approximately a factor ten higher than the arithmetic mean roughness height (derived from CT scans). The reader must be aware that these roughness values are, by definition, not identical.

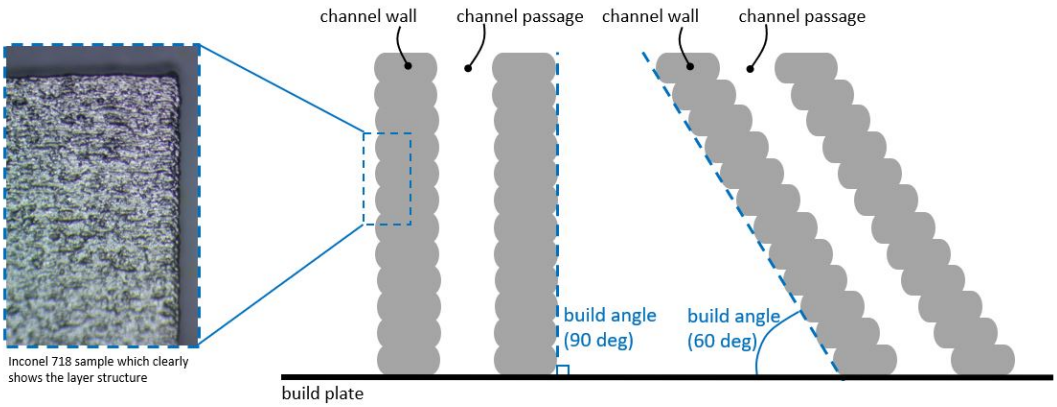

Figure 2.12: Schematic representation showing the impact of build angle on surface roughness, compared to rectangular additively manufactured Inconel 718 test articles.

In the cooling channels of an AM thrust chamber, the build angle changes with axial position. For example, one can expect a 90° build angle in the cylindrical section of the chamber and a build angle not equal to 90° in the convergent and divergent section of the nozzle. Consequently, it is expected that the hydraulic roughness of the cooling passages varies in the axial direction. In this investigation, a potential correlation between surface roughness, hydraulic diameter, and build angle is further investigated. This is done based on a plane fitting procedure with the reference data listed in Table 2.2. Both a linear and quadratic plane fit did not provide a good agreement with the test data. A spline interpolation, illustrated in Figure 2.13, reveals that there is no clear correlation between hydraulic diameter, build angle, and surface roughness. The actual roughness that is achieved in AM cooling channels is probably dependent on several other AM process parameters, such as the layer height, laser power, laser scan speed, metal alloy, and particle size distribution of the powder. Additionally, it is expected that the geometry of the part impacts the achieved surface roughness (for instance, straight channels versus a thrust chamber contour). More experiments are required to validate the predictability of the surface roughness in AM channels. In the absence of these measurements, it is decided to adopt a constant value for the equivalent sand grain roughness, based on the average value in Table 2.2. This value equals 121 µm.

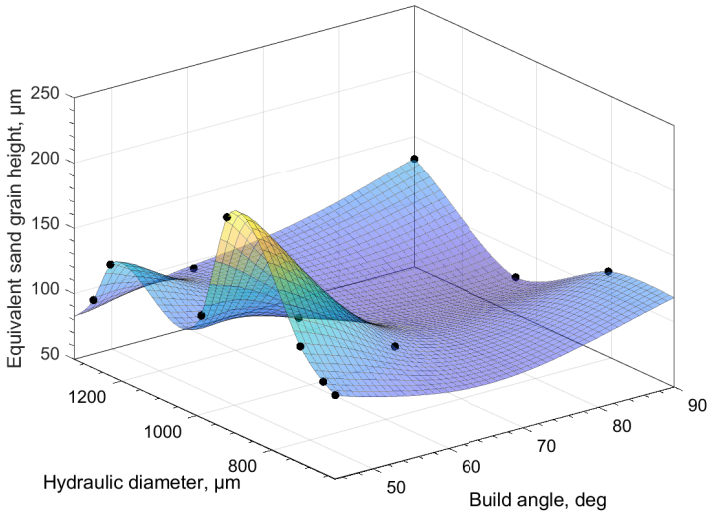

Figure 2.13: Correlation between surface roughness, build angle, and hydraulic diameter in AM Inconel 718 cooling channels.

Rough Channel Correlation

The second approach to model heat transfer in cooling channels with a rough surface is based on the work of Dipprey and Sabersky [24], who studied heat transfer of water in rough conduits with a relative surface roughness (k_s/D_h) between 0.0024 and 0.049. They present a semi-empirical correlation shown in Equation 2.38, which is derived for Prandtl numbers between 1.20 and 5.94.

$$Nu = \frac{\frac{f}{8} \cdot Re \cdot Pr}{1 + \sqrt{\frac{f}{8}}(g - A)} \tag{2.38}$$

Similar to Equation 2.35, the Reynolds number and Prandtl number are obtained at the coolant bulk temperature. The friction similarity function (A) is obtained as a function of the relative roughness and the friction factor, as shown in Equation 2.39.

$$A = \sqrt{\frac{8}{f}} + 2.5 \ln\left(\frac{2k_s}{D_h}\right) + 3.75 \tag{2.39}$$

The heat transfer similarity function (g) may be obtained from Figure 2.14. In this plot, the horizontal axis resembles the roughness Reynolds number (e^*), which follows from Equation 2.40. Dipprey and Sabersky describe roughness Reynolds numbers below 3 as hydraulically smooth, whereas a value above 70 is treated as fully rough. For a fully rough channel, the friction similarity function is constant and equal to 8.48.

$$e^* = \sqrt{\frac{f}{8}} \frac{k_s}{D_h} Re \tag{2.40}$$

Besides the application to water flow, the work of Dipprey and Sabersky is frequently used for liquid hydrogen cooling applications [34]. Although the operating conditions (Pr, Re) of 90% hydrogen peroxide in the Mk-II thruster lie within the validity range of Equation 2.38, no experiences with this correlation and 90% hydrogen peroxide could be found in the literature. The validity of this correlation in the application of the Mk-II is further investigated in subsection 4.3.3.

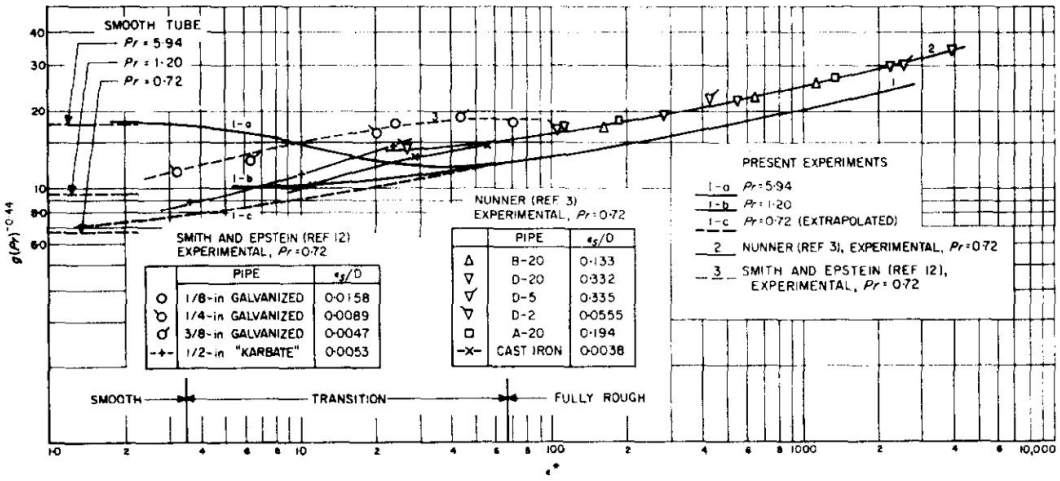

Figure 2.14: Experimental data for heat transfer similarity function in Equation 2.38, as a function of the roughness Reynolds number (reprinted from ref. [24]).

2.4.2. Impact of Channel Curvature and Flow Development

The coolant heat transfer and friction factor correlations discussed so far consider that the flow passes through a straight duct. Yet, due to the geometry of the thrust chamber, several bends are present in the cooling channel. When the coolant passes through a concave curved passage near the nozzle throat, for example, centrifugal forces push the fluid particles towards the inner chamber wall. On the other hand, for a convex bend, fluid particles are forced away from the inner wall. This phenomenon introduces vortices in the channels, which may locally increase or decrease the heat transfer. An empirical correction factor to account for this flow phenomena is provided in ref. [72] and shown in Equation 2.41.

$$\frac{Nu}{Nu_0} = \left(Re \left(\frac{D_h}{2R^*} \right)^2 \right)^{\pm 0.05} \tag{2.41}$$

In Equation 2.41, R^* denotes the radius of curvature of the bend. For a concave bend, the power term equals +0.05, whereas a convex bend is modeled using a -0.05 power term. The Nusselt number correction is only applied to the nozzle throat curvature, based on recommendations of Denies [36]. For all other locations, Nu/Nu_0 is unity. A fundamental shortcoming of Equation 2.41 is that it does not consider that the vortices develop and dissipate over a finite distance. Instead, a discrete corrective term is introduced for the bend at the nozzle throat. This limitation of the present approach may be mitigated when the coolant flow is numerically resolved.

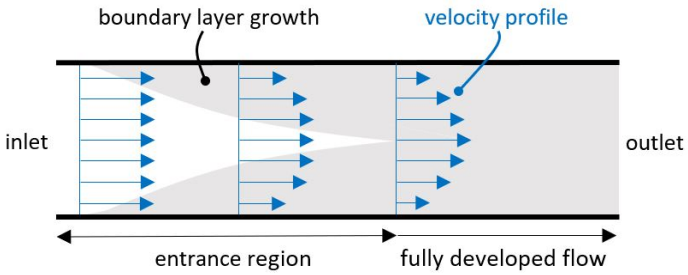

Figure 2.15: Schematic representation of axial boundary layer development at the entrance of the cooling channel.

A second corrective term is used to account for the fact that coolant flow near the channel entrance is not fully developed. In the entrance region, the velocity profile changes in the axial direction, and the boundary layer develops. This concept is schematically shown in Figure 2.15. The flow is said to be fully developed once the velocity profile does no longer differs with axial position [23]. Within the entrance region, the coolant heat transfer is much higher. This effect is captured in the correlation of Boelter, which is mentioned for regenerative cooling applications in ref. [72].

$$\frac{Nu}{Nu_0} = 2.88\left(\frac{D_h}{z}\right)^{0.325} \tag{2.42}$$

In Equation 2.42, z indicates the distance from the entrance of the cooling channel and D_h the hydraulic diameter of the conduit. It is noted that correlation is only valid when $Nu/Nu_0 \geq 1$ and $z/D_h > 5$.

2.4.3. Pressure Drop and Temperature Rise

The coolant heat transfer coefficient, as well as the hot gas heat transfer coefficient and radiative heat flux, serve as the primary boundary conditions to acquire the steady-state thermal solution in the thrust chamber wall. Once the solution is obtained at a given station along the chamber axis, the coolant temperature rise and pressure drop are calculated. The temperature rise of the coolant is obtained from Equation 2.43,

$$\Delta T_{co} = \frac{Q}{(\dot{m} \cdot c_p)_{co}} \tag{2.43}$$

where c_p denotes the heat capacity of the hydrogen peroxide, $\dot{m}$ the mass flow rate, and Q the total heat transferred to the coolant at the current station. The latter parameter is obtained by integrating the heat flux at the boundary of the cooling channel.

The pressure drop of the coolant is predicted based on the work of Naraghi & Foulon [77], who provide a pressure drop model which includes frictional losses and flow expansion losses[6]. For frictional losses, the well-known Darcy-Weisbach equation is used, which is shown in Equation 2.44.

$$\Delta p_{friction} = \left(\frac{f \cdot \rho_{co} \cdot v_{co}^2}{2D_h}\right)\Delta z \tag{2.44}$$

In this expression, the friction factor (f) may be obtained from Equation 2.37. It is worth mentioning that the flow velocity (v_{co}) and hydraulic diameter (D_h) can be controlled by the designer by carefully selecting the number of cooling channels and channel dimensions. The axial spacing (Δz) follows from the simulation set-up, whereas the fluid density (ρ_{co}) is obtained from the hydrogen peroxide fluid models that were introduced earlier in this report. For the pressure drop related to expansion or contraction of the passages, Naraghi and Foulon provide an empirical expression which is a function of the hydraulic

[6] In reality, one could introduce several other sources for pressure losses. Examples include losses due to flow acceleration, bends near the throat, and in the inlet/outlet manifolds. For modeling the pressure drop *in regenerative cooling channels*, these loss components are often neglected in the literature [72, 77–79].

diameter, the fluid density, and the flow velocity squared. This term is added to Equation 2.44. Simulations in TDCAS with the verification engine (Appendix B) reveal that the maximum pressure loss per unit length due to area change is almost a factor six smaller than losses introduced by friction.

2.4.4. Coolant Operation Limits

The total heat that can be transferred to the hydrogen peroxide coolant is bounded by the maximum service temperature of the fluid, as well as the ultimate, or burnout, heat flux. For cooling applications, Constantine and Cain [28] recommend a maximum service temperature of 394 K, with a hard limit at 408 K. More recent experimental studies of Bernier [80] reveal an “explosive phenomena” that is triggered by the rapid decomposition of the hydrogen peroxide when the fluid or wall temperature is approximately 423 K. The study is based on 98% hydrogen peroxide in AISI 304 microchannels at pressures in the range 3.7-21.4 MPa and flow rates in the range 230-680 mg/s. Interestingly, Bernier finds that the temperature limit of 423 K is independent of the coolant mass flow rate or pressure.

The temperature limit of both studies is reasonably close to the temperature at which the hydrogen peroxide vapor is ignitable, which was discussed in Figure 2.4. This could explain the rapid decomposition events that are observed by Bernier. In the present work, the upper limit of Constantine and Cain is used for the preliminary design of the thruster.

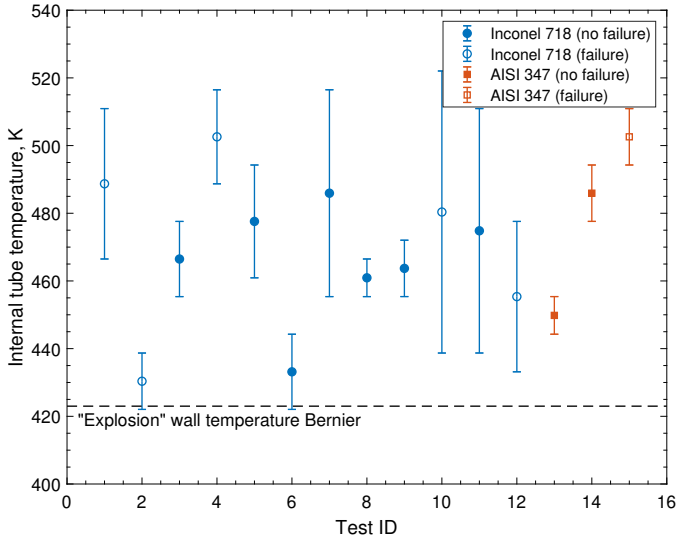

Figure 2.16: Derived wall temperatures for heat transfer experiments with 98% hydrogen peroxide in AISI 304, AISI 347, and Inconel 718 tubes (data from refs. [71, 80]).

Although the maximum service temperature of the hydrogen peroxide is constrained to 408 K, the chamber wall *can* reach higher temperatures. This is illustrated in Figure 2.16, which summarizes heat transfer experiments of Rousar & Van Huff [71] with 98% hydrogen peroxide in electrically heated Inconel 718 and 347 tubes. These experiments are conducted at fluid pressures in the range 5.7-32.4 MPa, flow velocities in the range 7.6-61 m/s, bulk fluid temperatures up to 375 K, and heat fluxes up to 78.4 MW/m^2. Notice that the upper value of the pressure range exceeds the critical pressure of hydrogen peroxide. One can observe from Figure 2.16 that all tests where a failure of the wall occurred are characterized by a temperature that exceeds the limit which Bernier established based on microchannel experiments. Moreover, Rousar & Van Huff also cite Devine et al. [81], who mention wall temperatures that exceed the local saturation temperature of 98% hydrogen peroxide upon failure of the tube. These observations are in good agreement with simulations of the bimetallic Mk-II thruster, which repeatedly reveal coolant-side wall temperatures close to the hydrogen peroxide saturation temperature. No thermal failure of the wall has occurred in corresponding hot-fire tests. It must be mentioned that none of the aforementioned studies *measure* the internal tube or channel wall temperature. Instead, this temperature is obtained by solving an inverse radial conduction problem or from steady-state heat transfer simulations.

When the wall temperature exceeds the fluid saturation temperature, small bubbles will form at the wall, caused by local boiling of the fluid [23]. This phenomenon, also known as *nucleate boiling*, greatly augments the heat transfer. The nucleate boiling heat transfer regime is bounded by the burnout heat flux (q_{ult}), after which the boundary layer transitions to an unstable gas film. The gas film greatly deteriorates the coolant heat transfer. Consequently, the wall temperature rapidly increases, which typically results in a thermal - or burnout - failure of the tube.

Interestingly, Rousar & Van Huff observe burnout failures of the tubes at wall temperatures much lower than the saturation temperature of 98% hydrogen peroxide. Furthermore, they do not observe a steep increase in the heat transfer at elevated temperatures in tests that are conducted below the critical pressure (steep increases in heat transfer are usually an indication of nucleate boiling). This suggests that there is no nucleate boiling phenomenon ongoing in hydrogen peroxide cooling channels when approaching burnout conditions. Instead, the burnout failures may originate from a deterioration of the heat transfer, caused by the exothermic decomposition of the hydrogen peroxide.

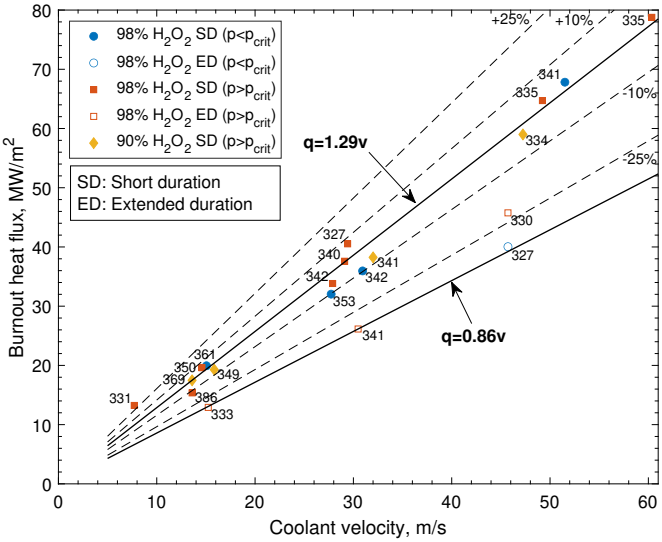

Figure 2.17: Experimental burnout heat flux data for 90% and 98% hydrogen peroxide in Inconel 718 tubes. Labels next to markers indicate the maximum bulk fluid temperature in Kelvin (measurements from ref. [71]).

To establish operating limits for regeneratively cooled thrust chambers that utilize hydrogen peroxide as coolant, Rousar & Van Huff correlate the burnout heat flux to the coolant velocity, as illustrated in Figure 2.17. The burnout heat flux represents the heat load that is introduced by the electrical heater upon failure of the tube. One may recall from Newton's law of cooling (Equation 2.26) that the maximum heat flux is directly related to the maximum coolant-side wall temperature. For this temperature, no clear failure trend could be observed in Figure 2.16. Based on the heat transfer experiments in Inconel 718 tubes, Rousar & Van Huff find that the impact of the pressure on the burnout characteristics is very small. They conclude that the burnout heat flux is primarily driven by the flow velocity of the hydrogen peroxide. For short duration (seconds) tests, they find that the correlation,

$$q_{max} = 1.29 v_{co} \tag{2.45}$$

fits all data with an error of $\pm 25\%$. Notice that the heat flux in Equation 2.45 is given in $\mathrm{MW/m^2}$ as a function of the flow velocity inserted in $\mathrm{m/s}$. Rousar & Van Huff also perform extended duration tests with 98% hydrogen peroxide. These tests are terminated after 5-10 minutes, or upon failure of the tube. Surprisingly, they find that a burnout failure occurs at a lower heat load. For these experiments, Equation 2.46 seems a more appropriate and conservative estimate.

$$q_{max} = 0.86 v_{co} \tag{2.46}$$

It is worth mentioning that the linear relation between coolant flow rate - which is proportional to the flow velocity - and burnout heat flux is also observed in the microchannel research of Bernier. For the preliminary design of the AM thrust chamber, Equation 2.46 is taken, which corresponds to a maximum heat-flux-to-velocity ratio of 0.86 MPa[7].

Provided the absence of more test data or described experiences in the open literature, it is recommended to perform more experimental research in the field of thermally stressed hydrogen peroxide. Preferably in cooling channels that have a high surface roughness. Heated hydrogen peroxide flow in rough channels is not studied in the considered pieces of literature and could further improve our understanding of the operating limits of the fluid.

2.5. Film Cooling

Although regenerative cooling is often an effective method to maintain the chamber wall at acceptable temperatures, additional internal cooling may be required to further reduce the wall temperature. This is especially relevant when thrust chamber materials with low thermal conductivity are used, as these structures are typically characterized by large thermal gradients in the wall. The film coolant essentially creates a physical fluid barrier between the hot gas and the wall, thereby reducing the heat that is transferred to the structure.

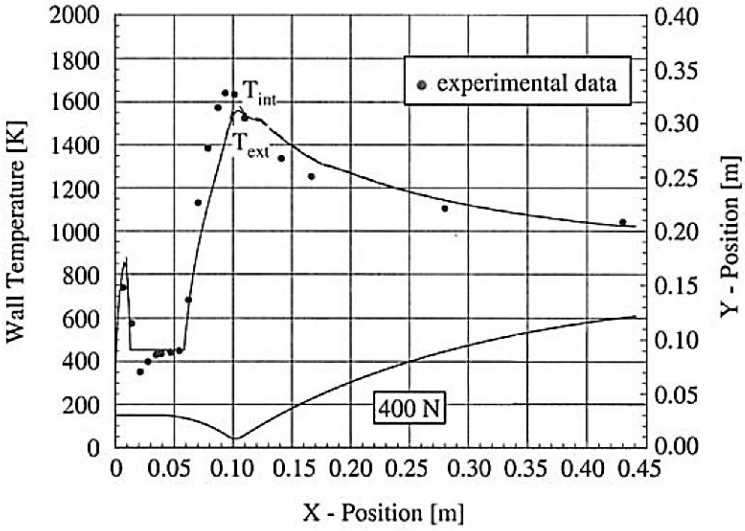

Figure 2.18: Experimental and simulation data for a small MMH film-cooled thruster, which clearly shows the transition from liquid to gaseous film cooling (reprinted from ref. [44]).

The fundamental challenge of any liquid film cooling analysis involves the calculation of the *dry-out* point. The dry-out point is the axial position in the thrust chamber where the majority of the liquid film has vaporized. Downstream of the dry-out point, the film temperature rapidly rises. As a result, the cooling effectiveness reduces and the wall temperature increases. This principle is illustrated in Figure 2.18, which shows a numerical simulation and measurements in an MMH film-cooled thruster. In this particular example, the dry-out point is located at an x-position of 6 cm.

In an “ideal” film-cooled engine, the film layer does not mix with the core flow and remains attached to the chamber wall. Under these assumptions, the liquid film dry-out point can easily be found using analytical heating and vaporization calculations. In reality, the assessment of the dry-out point is much more complex and the real cooling potential is much lower than the theoretical [82]. As a consequence of the liquid-gas interaction, capillary waves may develop on the surface of the film, which decreases the stability of the film layer [7]. Furthermore, several studies [52, 83] have described that the film effectiveness is greatly reduced when a monopropellant, such as hydrogen peroxide or hydrazine, is used as film coolant.

[7]The unit MPa follow directly from Equation 2.45: $(MW/m^2)/(m/s) = 1 \times 10^6\ (W\,s)/m^3 = 1 \times 10^6\ (kg)/(s^2\,m) = MN/m^2$.

Modeling these non-ideal flow phenomena is complicated. This requires a detailed simulation of the liquid-gas interaction of the film and core stream, as well as potential chemical reactions that occur in the vicinity of the film layer due to decomposition and/or turbulent mixing. A model of this kind would likely involve a study on its own and is considered beyond the scope of this work. A different technique that is often adopted in film cooling analyses is the use of semi-empirical correlations [8, 84, 85]. This approach is taken in the present investigation.

2.5.1. Liquid Film

The liquid phase film cooling model is based on research of Stechman et al. [82] which has been developed for small (4.4-4400 N thrust level) bipropellant thrusters. They provide a compelling validation case where the model is compared to experimental work in a thruster operating with the N_2O_4/MMH propellant combination. The model of Stechman et al. uses a 1-D energy balance to calculate the length of the liquid film (L), as shown in Equation 2.47. The use of semi-empirical 1-D models for liquid film cooling is also demonstrated in research of several other scholars [35, 83, 84, 86].

$$L = \eta_{cf,l}\left(\frac{\dot{m}_{cf}}{P}\right)\left(\frac{c_p(T_{cf,sat} - T_{cf,i}) + \Delta_v H_{cf}}{\alpha_g(T_{aw} - T_{cf,sat})}\right) \tag{2.47}$$

Newly introduced parameters in this expression are the peripheral flow rate ($\dot{m}_{cf}/P$) and the liquid film effectiveness ($\eta_{cf,l}$). The temperatures used in this expression are the film saturation temperature ($T_{cf,sat}$), the film injection temperature ($T_{cf,i}$), and the adiabatic wall temperature (T_{aw}). The liquid film effectiveness accounts for non-ideal film cooling effects, such as core flow entrainment and film instabilities. Stechman et al. provide this empirical constant as a function of the film coolant Reynolds number[8], as depicted in Figure 2.19. It is worth mentioning that a similar empirical curve is reported in ref. [83].

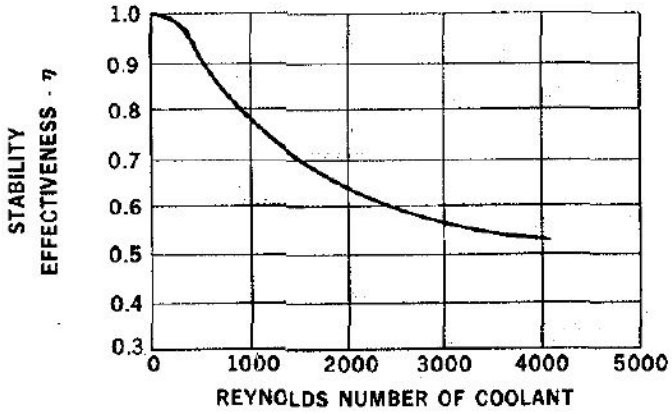

Figure 2.19: Liquid film effectiveness as a function of the film Reynolds number (reprinted from ref. [82]).

For convective heat transfer, a modified version of the correlation of Bartz is used, which accounts for large variations of transport properties in the boundary layer. This modified equation, shown in Equation 2.48, evaluates the transport properties at the mean film temperature (T_{am}), which is taken at the arithmetic mean of the gas temperature and wall temperature. Furthermore, the adiabatic wall enthalpy (H_{aw}) and wall enthalpy (H_w) are introduced in the expression. These are the specific enthalpies of the hot gas, evaluated at the adiabatic/inner wall temperature.

$$\alpha_g = \frac{0.026}{D_t^{0.2}}\left(\frac{\mu^{0.2}}{Pr^{0.6}}\right)_{am}\left(\frac{p_0}{c^*}\right)^{0.8}\left(\frac{A_t}{A}\right)^{0.9}\left(\frac{H_{aw} - H_w}{T_{aw} - T_w}\right)s \tag{2.48}$$

$$s = \frac{T^{0.8}}{T_o^{0.12} \cdot T_{am}^{0.6}} \tag{2.49}$$

[8] The film Reynolds number is defined as $Re = \dot{m}_{cf}/(D_c \pi \mu_{cf,l})$.

Stechman et al. also assume that there is heat transfer between the liquid film and thrust chamber wall. They derive Equation 2.50, which is based on a modified Reynolds analogy, combined with an expression for turbulent liquid flow over flat plates. A detailed derivation of Equation 2.50 is provided in the original piece of literature and not repeated here.

$$\alpha_{cf,l} = 0.0288 \frac{c_{p_{cf,l}}}{Pr_{cf,l}^{0.67} \mu_{cf,l}^{0.2} z^{0.2}} \left(\frac{\eta_{cf,l} \dot{m}_{cf} v_g \alpha_g Pr_g^{0.67} \rho_{cf,l}}{\pi r c_{p_g}} \right)^{0.4} \tag{2.50}$$

Parameters with subscript “cf,l” are evaluated at the liquid film temperature, whereas subscript “g” implies properties which are evaluated at the local core gas temperature. The reference temperature that is used for the convective heat transfer calculations from the film to the wall is set to the average film temperature (between injection and boiling), based on recommendations of Stechman et al.

It is worth mentioning that several researchers [55, 85, 87] have noted an accelerated vaporization rate in film cooling applications with liquids that can exothermically decompose, such as hydrogen peroxide or hydrazine. It is believed that this is caused by the formation of a thin monopropellant (and bipropellant) flame layer which surrounds the vaporizing liquid film droplets [88]. This phenomenon is also described by Davis et al. [27], who state that vaporizing hydrogen peroxide droplets “will undergo a self-sustaining thermal decomposition process manifested as a hot, nearly invisible vapor decomposition front close to the surface of the liquid”. It is reasonable to assume that the vaporized hydrogen peroxide decomposes rapidly, since the saturation temperature of hydrogen peroxide is generally much higher than the temperature at which the vapor is ignitable. This is clearly visible in Figure 2.4, which was introduced earlier in this report. From this illustration, one may also expect the water content in the hydrogen peroxide *solution* to boil just before the hydrogen peroxide content starts boiling. Experimental research of Won et al. [89] reveals that this difference in boiling point can result in micro-explosions in 90% hydrogen peroxide droplets, which they link to the accumulation of superheated water inside the droplets. These micro-explosions could accelerate the break-up of the liquid film droplets, thereby further reducing the film cooling potential. As mentioned in subsection 2.1.2, differences in boiling point are neglected in the present work, based on the fast rate at which vaporization is expected to occur. This simplifying assumption is also accepted by other scholars [50].

2.5.2. Gaseous Film

Downstream of the liquid dry-out point, the film composition consists of vaporized and decomposed hydrogen peroxide, as well as gas from the core stream that entrains in the film layer. In the present work, the gaseous film cooling model described in NASA space vehicle design criteria SP-8124 is used for modeling the gaseous film cooling regime [8]. This model is selected because it includes terms that capture the exothermic decomposition of the film coolant. What is more, several scholars [65, 90] have described positive experiences of this model in the application of small hydrocarbon thrusters with a size comparable to the Mk-II engine.

The theoretical basis of the NASA SP-8124 model is based on a two-stream mixing model, comprised of a core flow (subscript “g”) and gaseous film flow (subscript “cf,g”). The film effectiveness ($\eta_{cf,g}$) is taken as the mass fraction of the film coolant in the mixing layer at any location downstream of the vaporization point, divided by the mass fraction of the film in the mixing layer at the injection point. Mathematically, this implies Equation 2.51, where c_w denotes the composition of the gas in the mixing layer [91]. Note that the injection point of the gaseous film is defined as the liquid dry-out point, since the film is injected in the liquid state.

$$c_w = (\eta_{cf,g}) c_{cf} + (1 - \eta_{cf,g}) c_g \tag{2.51}$$

Naturally, the gaseous film cooling effectiveness decreases downstream of the injection point as a consequence of core flow entrainment. As a result, the composition of the mixing layer near the wall approaches the composition of the core flow (c_g) when $\eta_{cf,g}$ approaches zero. It is relevant to mention that the parameter c_{cf} is evaluated *at* the dry-out point and therefore represents a constant. Equation 2.51 may also be written as a function of the enthalpies of the core stream and gaseous film coolant evaluated at the adiabatic wall conditions, as demonstrated in Equation 2.52.

$$H_{aw} = (\eta_{cf,g})H_{cf,aw} + (1 - \eta_{cf,g})H_{e,aw} \tag{2.52}$$

The adiabatic wall enthalpy can also be written as shown in Equation 2.53. This expression captures the enthalpy evolution in the mixing layer and viscous sub-layer close to the wall due to high-speed effects. A detailed derivation is provided in ref. [91] and not repeated here.

$$H_{aw} = H_{o,g} - \eta_{cf,g}(H_{o,g} - H_{o,cf}) - (1 - Pr_w^{1/3})(H_{o,g} - H_g) \tag{2.53}$$

One may notice that the term $Pr^{1/3}$ follows directly from the turbulent recovery factor, which was introduced in subsection 2.3.1. Next, Equation 2.52 is substituted in Equation 2.53 and enthalpies are replaced by heat capacities and temperatures, as demonstrated in Equation 2.54.

$$\begin{aligned}\left[\eta_{cf,g}c_{p,cfg}T_{aw} - \eta_{cf,g}c_{p,cfg}T_{cfg} + \eta H_{cf,l}\right] + (1 - \eta_{cf,g})c_{p,g}T_{aw} = \\ c_{p,g}T_{o,g} - \eta_{cf,g}(c_{p,g}T_{o,g} - H_{o,cf}) - (1 - Pr_w^{1/3})(H_{o,g} - H_g)\end{aligned} \tag{2.54}$$

The term indicated in square brackets yields the total enthalpy of the film coolant at the adiabatic wall temperature. This represents the sum of the sensible enthalpy of the gaseous film and the enthalpy of the gas film at the vaporization point ($H_{o,cf}$). The latter parameter is taken as the sensible enthalpy of the liquid film plus the enthalpy change of vaporization. Rewriting Equation 2.54 to solve for T_{aw} and reordering several terms results in Equation 2.55, which is similar to the equation reported in NASA SP-8124. This final form is implemented in TDCAS.

$$T_{aw} = T_{o,g} - \frac{\eta_{cf,g}c_{p,cfg}(T_{o,g} - T_{cf,g}) + (1 - Pr_w^{1/3})(H_{o,g} - H_g)}{\eta_{cf,g}c_{p,cfg} + (1 - \eta_{cf,g})c_{p,g}} \tag{2.55}$$

The enthalpies, heat capacity, and total temperature of the core flow in Equation 2.55 follow directly from CEA. The Prandtl number of the flow is evaluated based on the mixture ratio near the wall. For the temperature and heat capacity of the gaseous film coolant at the injection location, the decomposition model described in NASA SP-8124 is used, which is detailed in the next paragraph.

Film Decomposition

Downstream of the dry-out point, the composition of the gaseous film layer consists of both vaporized and decomposed hydrogen peroxide. The decomposition model in NASA SP-8124 is based on the assumption that the film consists of only vaporized species at the dry-out point and of decomposed species (oxygen and steam) far downstream the dry-out point. The temperature and heat capacity of the gaseous film are given by Equation 2.56 and Equation 2.57,

$$T_{cf,g} = f_v T_{H_2O_2} + (1 - f_v)T_{H_2O,O2} \tag{2.56}$$

$$c_{p,cfg} = f_v(c_p)_{H_2O_2} + (1 - f_v)(c_p)_{H_2O,O2} \tag{2.57}$$

where f_v denotes the fraction of the gaseous film coolant that is in the vaporized state and consequently $(1 - f_v)$ the fraction of the film coolant in the decomposed state. The subscript "H_2O_2" denotes the vaporized hydrogen peroxide state, whereas "H_2O, O_2" denotes the decomposed state. The temperature of the vaporized hydrogen peroxide is set to the liquid saturation temperature, whereas the heat capacity of gaseous hydrogen peroxide is taken from the work of Giguère and Liu [92]. For the decomposed state, a temperature of 1019 K is used, which corresponds to the adiabatic decomposition temperature of 90% hydrogen peroxide. The heat capacity for the decomposed products is based on a homogeneous mixture of oxygen and steam, with properties taken from the databases of NIST.

The fraction of the gas in the vaporized state that is used in Equations 2.56 and 2.57 is given in Equation 2.58 as a function of distance downstream of the dry-out point (z), the core flow velocity (v_g) and the decomposition rate constant (χ) [8]

$$f_v = \exp\left(-\chi \int_L^z \frac{dz}{v_g}\right) \tag{2.58}$$

One may observe that the integral term in this expression represents the core transit time, which is monotonically increasing. As a result, the vapor fraction reduces (exponentially). The decomposition rate constant is based on experimental measurements of the wall temperature and should not be confused with the decomposition rate obtained from an Arrhenius-type correlation.

Core Stream Entrainment

The last undefined parameter in Equation 2.55 is the gaseous film effectiveness ($\eta_{cf,g}$). In the NASA SP-8124 model, this parameter represents a constant that is given as a function of the entrainment flow ratio, as illustrated in Figure 2.20.

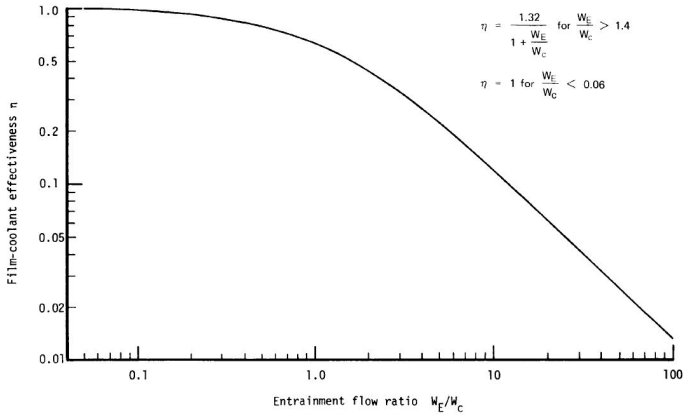

Figure 2.20: Relation between gaseous film effectiveness and entrainment flow ratio (reprinted from ref. [8]).

From this plot, one can observe that the film cooling effectiveness rapidly decreases when more of the core stream gets entrained and mixes with the gaseous film. The entrainment flow ratio follows from the empirical correlation presented in Equations 2.59, where $\dot{m}_E/\dot{m}_{cf}$ is identical to W_E/W_c in Figure 2.20 [8].

$$\frac{\dot{m}_E}{\dot{m}_{cf}} = \frac{\dot{m} - \dot{m}_{cf}}{\dot{m}_{cf}} \left[2\psi_L \frac{\bar{z}}{r_i} \sqrt{1 - \frac{(\dot{m}_E)_L}{\dot{m} - \dot{m}_{cf}}} - \left(\psi_L \frac{\bar{z}}{r_i}\right)^2 \right] + \frac{(\dot{m}_E)_L}{\dot{m}_{cf}} \tag{2.59}$$

In this expression, the r_i denotes the radius of the chamber at the vaporization point, $\dot{m}$ the total mass flow rate in the chamber, $\dot{m}_{cf}$ the film flow rate, ψ_L the reference entrainment fraction, and $\bar{z}$ the effective contour distance, given in Equation 2.60.

$$\bar{z} = \int_L^z \frac{r_i}{r} \frac{(\rho_g v_g)_{2D}}{(\rho_g v_g)_{1D}} \psi_M dz \tag{2.60}$$

The effective contour distance corrects for flow acceleration and turning in the nozzle and is a function of the core mass flux at the vaporization point $(\rho_g v_g)_{1D}$, the local core mass flux $(\rho_g v_g)_{2D}$, the chamber radius (r), and the local entertainment factor ψ_M. The last undefined parameter in Equation 2.59 is $(\dot{m}_E)_L/\dot{m}_{cf}$, which corrects for core stream entrainment upstream of the dry-out point. More details on this empirical term are provided in refs. [8, 93].

This concludes the NASA SP-8124 film cooling model. To resolve the adiabatic wall temperature, only two empirical user-inputs are required, which are:

- **The decomposition rate constant** (χ). Film cooling experiments with MMH mentioned in NASA SP-8124 reveal that a decomposition rate constant of approximately 3000 s^{-1} is suitable for this propellant. Since no data concerning the decomposition rate constant of hydrogen peroxide could be found, the value for MMH is taken as a starting point for the preliminary design.
- **The core stream entrainment factor** (ψ). This parameter is given as the product of the reference entertainment factor (ψ_L) and local entertainment factor (ψ_M). NASA SP-8124 provides a typical value for the reference entertainment factor of 0.025 to 0.06 when the local entrainment factor is unity. In the present work, the average of this range is taken as a starting point, which corresponds to a reference entrainment factor of 0.0425 and a local entrainment factor of 1.

2.6. Numerical Solution in the Solid Domain

In TDCAS, a numerical solver is integrated that resolves the 2-D temperature field and 2-D displacement field in the wall. The thermal solver outputs both the temperature and heat flux at any element inside the wall. This is helpful information during the preliminary design of a liquid rocket engine when a maximum service temperature is used as design criteria. Besides, information on the temperature distribution inside the wall is valuable when comparing experimental thermocouple readouts during a hot-fire test with simulations. This effective measurement-validation is demonstrated in the work of Fröhlich et al. [94] in the application of the European Vulcain engine for the Ariane 5 launch vehicle.

Although several scholars [36, 86] have used the approach of a maximum service temperature for the preliminary design of liquid rocket engines, it is also possible to limit the design load based on the stress in the wall. This can be achieved by a numerical simulation of the thrust chamber, where the nodal displacement, element strain, and element stress are resolved. In TDCAS, the numerical solution of these parameters is obtained in 2-D based on the plane strain assumption. This implies that the out-of-plane strain is zero, which corresponds to the axial direction of the thrust chamber. On the other hand, the stress in the out-of-plane direction is not zero by definition, as this unknown is numerically resolved. The 2-D plane strain representation in the application of thrust chambers is used by several other researchers [38, 39] and provides adequate results whilst being computationally much less expensive than a 3-D problem setup.

Many of the thrust chamber structural analysis studies in the literature [39, 95] are based around large cryogenic propulsion systems, such as the Vulcain engine or the Space Shuttle Main Engine. For simulation of these systems, elastoplastic structural analyses are commonly used, which numerically solve for both the elastic, plastic, and thermal strains. The operating point of these propulsion systems is vastly different from the expected operating conditions of the Mk-II thruster. For example, the Space Shuttle Main Engine operates at a chamber pressure 22.6 MPa and adiabatic wall temperature of 3600 K [95], whereas the Mk-II has a typical chamber pressure ∼4-6 MPa and an adiabatic wall temperature of 2750 K. Furthermore, the temperature of the hydrogen coolant used in the Space Shuttle Main Engine is substantially lower than the hydrogen peroxide used in the Mk-II. As a result of this large difference in load point, it is hypothesized that the chamber wall of the Mk-II could potentially be operated in the linear elastic regime, rather than in the combined elastic and plastic regime. Since only limited experience concerning linear elastic simulations in the application of a thrust chamber could be found in the literature [96], it was decided to further investigate this type of analysis in this report.

The finite element method implemented in TDCAS is based on a structured quadrilateral mesh (see also subsection 2.2.3) with piece-wise linear basis, or interpolation, functions. A high-level architecture of the implemented numerical solver is presented in Figure 2.21, which shows all major inputs and boundary conditions. Flowchart cells on the left side of this image indicate the 2-D conduction solver, which is explained in more detail in subsection 2.6.1. The right side of this image indicates the linear elastic solver, which is briefly explained in subsection 2.6.2. In this thesis, the finite element solver is self-written in Matlab, based on the following arguments:

- **Fit for purpose**. The developed code is specifically designed to simulate the thrust chamber of liquid rocket engines. The fact that sizing of the chamber and mesh generation are automatically performed in the same software allows for rapid iteration through different designs.
- **Cost**. An off-the-shelve numerical software package, like Ansys, can only be used for commercial applications after purchasing an expensive product license. Although the academic version of Ansys is freely available for non-commercial applications, it has several major limitations, such as the maximum number of nodes/elements that can be used in the mesh. Although open-source alternatives exist to Ansys, these are not (frequently) used by Dawn Aerospace. As a result, the use of these alternatives is less interesting.
- **Learning experience**. Before starting this thesis, the author had only limited practical experience in the field of numerical simulations. Therefore, one of the personal learning goals of this thesis was to get more familiar with numerical simulations related to heat transfer and structural deformation. Writing, debugging, and verifying a custom finite element code in Matlab provided a major learning experience that met the personal goals set for this project.

The exact implementation of the finite element method in TDCAS is based on the excellent description which is provided in the books of Bathe [97] and Zienkiewicz [98]. For convenience, this section only touches on the fundamental governing equations and boundary conditions, rather than providing a detailed derivation of all matrix equations. For this derivation or a more elaborate explanation of the finite element method for heat conduction and linear elasticity problems, the reader is referred to the work of Bathe or Zienkiewicz.

2.6.1. Governing Equations Heat Conduction

In the wall of the thrust chamber, heat is transferred by means of conduction. The conduction is modeled using the 2-D steady-state heat equation, which is presented in Equation 2.61 [23],

$$-\lambda_w \nabla^2 T = g(x,y) \tag{2.61}$$

Equation 2.61 is a partial differential equation, where T represents the temperature at a given node in the mesh, λ_w the thermal conductivity of the wall, and $g(x,y)$ a term that captures the potential presence of a heat source. The thermal conductivity is temperature-dependent and assumed to be identical in both the x- and y-direction. The particular value taken for this parameter follows directly from the material properties, which are provided in refs. [40, 99].

Boundary Conditions

The computational domain (Ω), together with boundary conditions (Γ), is illustrated in Figure 2.22. In the 2-D thermal simulation, the two symmetry planes of the computational domain (Γ_1 and Γ_2) are modeled as adiabatic, which introduces the boundary conditions noted in Equations 2.62 and 2.63,

$$\left.\frac{\partial T}{\partial n}\right|_{\Gamma_1} = 0 \tag{2.62}$$

$$\left.\frac{\partial T}{\partial n}\right|_{\Gamma_2} = 0 \tag{2.63}$$

where n represents the vector normal to the boundary. The adiabatic boundary conditions imply that the heat flux across to boundary is zero. The convection boundary conditions are added on the interface of the coolant and hot gas, noted by Γ_4 and Γ_5 in Figure 2.22. These boundary conditions are modeled using Equations 2.64 and 2.65.

$$\lambda_w \left.\frac{\partial T}{\partial n}\right|_{\Gamma_4} = \alpha_g (T_{aw} - T) \tag{2.64}$$

$$\lambda_w \frac{\partial T}{\partial n}\bigg|_{\Gamma_5} = \alpha_c (T_{co} - T) \tag{2.65}$$

The parameters that are used for the hot gas heat transfer coefficient (α_g) and adiabatic wall temperature follow directly from the earlier discussed Bartz equation or Cinjarew equation (subsection 2.3.1) and the film cooling analysis (section 2.5). On the other hand, the heat transfer coefficient for the coolant (α_c) follows from the modified Nunner, Norris or Dipprey-Sabersky correlation, as discussed in subsection 2.4.1. The coolant bulk temperature (T_{co}) that is used in the boundary is dependent on the heat transfer at the downstream computational stations, as demonstrated in Equation 2.43.

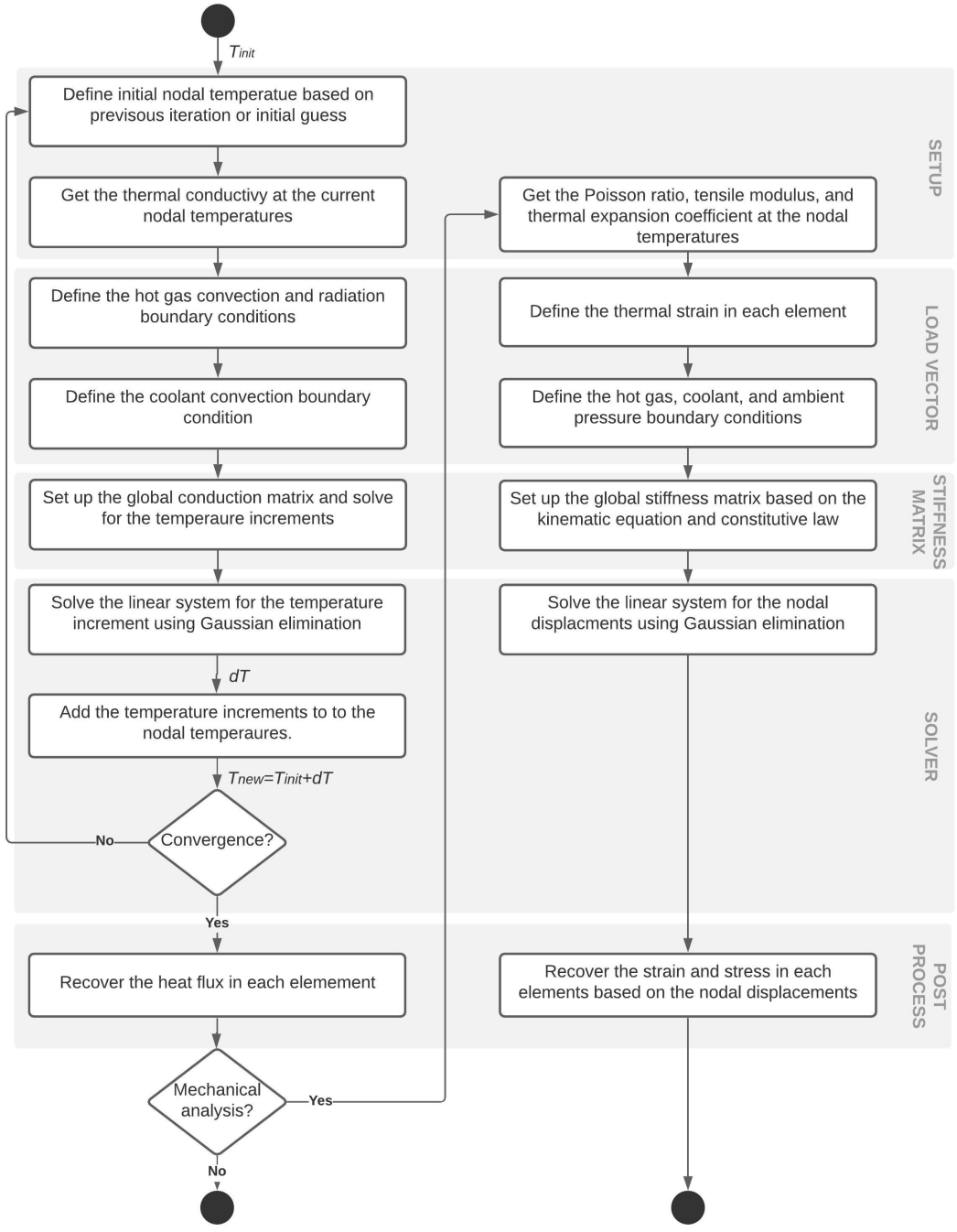

Figure 2.21: Schematic overview of the architecture of the finite element solution algorithm in TDCAS.

Lastly, a boundary condition for the hot gas radiative heat transfer is implemented using Equation 2.66,

$$\lambda_w \frac{\partial T}{\partial n}\bigg|_{\Gamma_4} = q_{rad} \tag{2.66}$$

where q_{rad} denotes the radiative heat flux. The radiative heat flux is obtained from the semi-empirical correlations of Kirchgberger et al. that were mentioned in subsection 2.3.2. These expressions are solely a function of the hot gas temperature, pressure, and chamber radius. This means that q_{rad} is a constant for a given thruster operating point and chamber geometry. For completeness, a radiative heat transfer coupling from the (external) wall to the environment is also included, which is implemented using Equation 2.67 [97]

$$\lambda_w \frac{\partial T}{\partial n}\bigg|_{\Gamma_3} = \underbrace{\left[5.67 \cdot 10^{-8} \cdot F \cdot \epsilon \left(T_a^2 + T^2\right)\left(T_a + T\right)\right]}_{\alpha_{rad}} \left(T_a - T\right) \tag{2.67}$$

The radiation heat transfer to the environment is a function of the view factor (F), the wall emissivity (ϵ), and the ambient temperature (T_a). The term between square brackets is often referred to as the radiative heat transfer coefficient α_{rad}. Although this coupling is not necessarily relevant for the regeneratively cooled thruster wall, it does extend the capabilities of TDCAS to also resolve the thermal field of radiation-cooled thrust chambers or nozzle extensions in the future. Moreover, this type of boundary condition could also be used for the hot gas radiation, provided that a good estimate of the gas emissivity is available. For this application, the ambient temperature is replaced by the temperature of the hot gas stream.

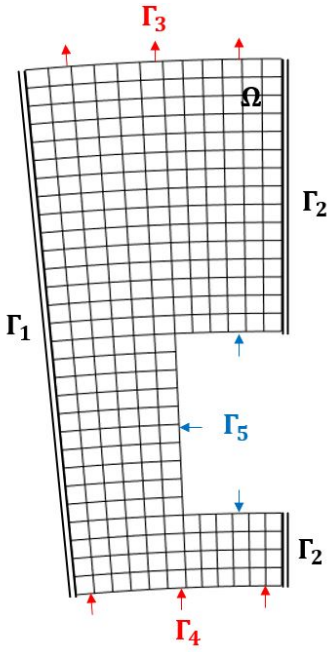

Figure 2.22: Schematic overview of computational domain and boundary conditions.

When heat transfer coefficients and the thermal conductivity of the wall are independent of the wall temperature, and radiation energy exchange to the environment is neglected, the system described in Equations 2.61-2.67 is linear and can be solved using basic matrix operations. Yet, in the application of a thrust chamber, the hot gas heat transfer coefficient *is* a function of the wall temperature, which makes the boundary condition nonlinear. In TDCAS, these nonlinearities are resolved using an iterative Newton-Rhapson solution algorithm. The algorithm requires an initial guess for the nodal temperatures and resolves the nodal temperature increment (see also Figure 2.21). This increment is added to the initial guess until convergence is achieved. Convergence is defined based on Equation 2.68,

$$\frac{||dT||}{||T||} \leq 1 \cdot 10^{-6} \tag{2.68}$$

where $||dT||$ denotes the norm of the nodal temperature increments and $||T||$ the norm of the nodal temperatures. To avoid infinite loops in the solver, the maximum number of iterations is limited to 100. In practice, convergence is typically achieved in 10-20 iterations.

2.6.2. Governing Equation Mechanical Deformation

In the linear elastic simulation, the partial differential equation presented in Equation 2.69 is numerically solved [97]. In this expression $\boldsymbol{\sigma}$ represents the Cauchy stress tensor and $\mathbf{f}$ the body force vector.

$$\boldsymbol{\nabla} \cdot \boldsymbol{\sigma} + \mathbf{f} = \mathbf{0} \tag{2.69}$$

In the linear elasticity regime, the stress is directly related to the elastic strain ($\boldsymbol{\varepsilon}_{el}$) component, following the constitutive equation (Equation 2.70). The constitutive tensor ($\mathbf{C}$) is a 3×3 matrix that follows directly from Hooke's law. The tensor is a function of the tensile modulus (E) and the Poisson ratio (ν), which are uniquely defined for a given material as a function of the temperature. As a result, the simulation of the linear elastic mechanical domain requires nodal temperatures as input. These are obtained from the steady-state thermal simulation.

$$\boldsymbol{\sigma} = \mathbf{C} \cdot \boldsymbol{\varepsilon}_{el} \tag{2.70}$$

$$\mathbf{C} = \frac{E}{(1+\nu)(1-2\nu)} \begin{bmatrix} 1-\nu & \nu & 0 \\ \nu & 1-\nu & 0 \\ 0 & 0 & 1-2\nu \end{bmatrix} \tag{2.71}$$

Note that Equation 2.71 is only valid for 2-D plane strain simulations. The definition of the constitutive tensor is different for 2-D plane stress, 2-D axisymmetric, or 3-D simulations. The last equation required to fully resolve the mechanical domain is the kinematic equation, which relates the nodal displacements to the strain in the wall. This is given by Equation 2.72,

$$\boldsymbol{\varepsilon} = \begin{bmatrix} \frac{\partial u}{\partial x} \\ \frac{\partial v}{\partial y} \\ \frac{\partial u}{\partial y} + \frac{\partial v}{\partial x} \end{bmatrix} = \begin{bmatrix} \frac{\partial}{\partial x} & 0 \\ 0 & \frac{\partial}{\partial y} \\ \frac{\partial}{\partial y} & \frac{\partial}{\partial x} \end{bmatrix} \begin{bmatrix} u \\ v \end{bmatrix} \tag{2.72}$$

where u and v denote the nodal displacements in the x- and y-direction respectively. Equation 2.72 represents the total strain in the wall, which is composed of an elastic ($\boldsymbol{\varepsilon}^{el}$) and thermal ($\boldsymbol{\varepsilon}^{th}$) strain contribution, as shown in Equation 2.73.

$$\boldsymbol{\varepsilon} = \boldsymbol{\varepsilon}_{el} + \boldsymbol{\varepsilon}_{th} \tag{2.73}$$

The thermal strain, shown in Equation 2.74, follows directly from the solution of the 2-D thermal domain. This strain component is given as a function of the coefficient of thermal expansion (β), the wall temperature in the elements (T), and the zero-strain reference temperature (T_{ref}).

$$\boldsymbol{\varepsilon}^{th} = \beta(T - T_{ref}) \begin{bmatrix} 1 & 1 & 0 \end{bmatrix}^T \tag{2.74}$$

One must bear in mind that the thermal strain is a hydrostatic strain component. This implies that it only adds to the strain components in the x- and y- direction, whereas the contribution to the shear component (xy-direction) is zero.

Boundary Conditions
In the mechanical domain, the symmetry boundaries Γ_1 and Γ_2 in Figure 2.22 represent a “roller” constraint, which is implemented using Equations 2.75 and 2.76. Physically, this constraint implies that the structure is free to deform in the direction tangent to the boundary. In the direction normal to the boundary, no deformation is permitted.

$$\mathbf{u} \cdot \mathbf{n}\Big|_{\Gamma_1} = 0 \tag{2.75}$$

$$\mathbf{u} \cdot \mathbf{n}\Big|_{\Gamma_2} = 0 \tag{2.76}$$

The primary load that is acting on boundaries Γ_3, Γ_4, and Γ_5 is the pressure, which is implemented using Equations 2.77-2.79 [39].

$$\mathbf{n} \cdot \boldsymbol{\sigma} \cdot \mathbf{n}\Big|_{\Gamma_3} = p_a \tag{2.77}$$

$$\mathbf{n} \cdot \boldsymbol{\sigma} \cdot \mathbf{n}\Big|_{\Gamma_4} = p_g \tag{2.78}$$

$$\mathbf{n} \cdot \boldsymbol{\sigma} \cdot \mathbf{n}\Big|_{\Gamma_3} = p_{co} \tag{2.79}$$

In these expressions, p_a denotes the ambient pressure, p_{co} the coolant pressure and p_g the local chamber pressure.

2.7. Chapter Summary

In this chapter, the fundamental assumptions and modeling approach of the Two Dimensional Combustor Analysis Software (TDCAS) were discussed. This tool was developed for the preliminary sizing of a small additively manufactured thruster, propelled by 90% hydrogen peroxide and kerosene. This chapter provides a detailed description of the fluid properties of 90% hydrogen peroxide (section 2.1), as well as the fundamental steps taken for sizing of the thrust chamber (section 2.2). The core of TDCAS consists of a solution algorithm that predicts the steady-state temperature and mechanical stress in the wall. This algorithm is based on the finite element method to resolve a 2-D nonlinear conduction problem and linear elasticity problem (section 2.6).

In the current release of the program, the boundary conditions for the hot gas convection are resolved using correlations posed by Bartz and Cinjarew, whereas radiation is modeled using a semi-empirical correlation of Kirchgberger et al. (section 2.3). The boundary conditions for coolant convection are based on the modified Nunner, Norris, or Dipprey-Sabersky equation, which are developed for fluid flow in rough conduits (section 2.4). The steady-state temperature solution can be obtained with or without the presence of a film coolant. For film cooling, the liquid model of Stechman et al. is used, in combination with the gaseous model of NASA SP-8124 (section 2.5).

3

Model Verification

To gain confidence in the correct implementation of the 2-D models explained in the previous chapter, several software verification steps are carried out. First, a grid convergence study is performed, which is detailed in section 3.1. Hereafter, sections 3.2 and 3.3 compare the results of the thermal solver in TDCAS to validated commercial software packages. Verification steps for the mechanical solver are detailed in section 3.4. Unless described otherwise, all verification activities performed in this section involve an arbitrary Inconel 718 verification engine design, which is described in Appendix B.

3.1. Grid Convergence Study

In subsection 2.2.3, it was discussed how TDCAS automatically creates a structured 2-D mesh. It was noted that the refinement of the mesh can be controlled by the refinement depth parameter and the axial spacing of the computational stations. For a properly set up numerical simulation, the obtained result shall become independent of the computational domain. In other words, further refinements of the mesh do not result in an appreciable change in the acquired solution.

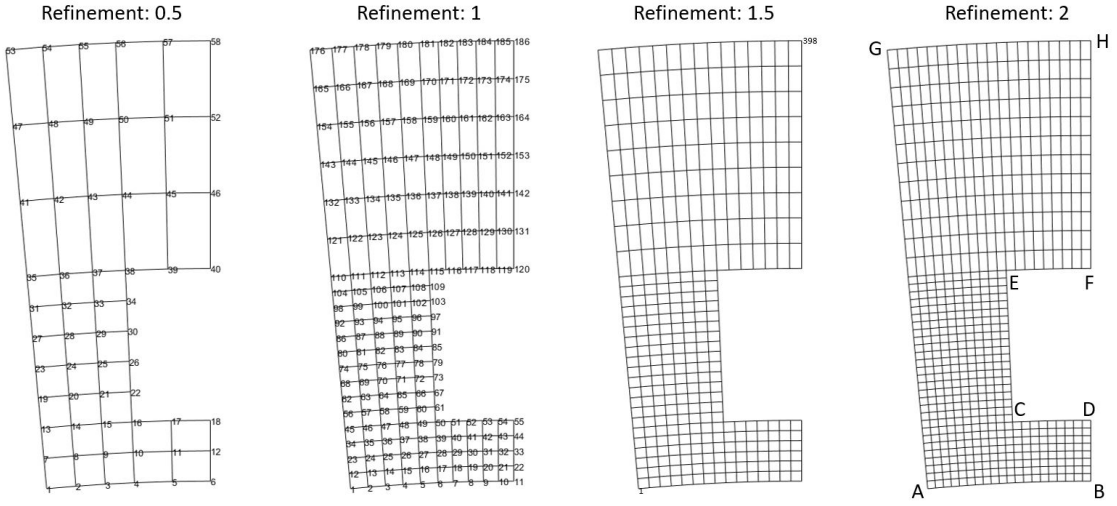

Figure 3.1: Impact of refinement depth parameter on generated planar mesh (evaluated for verification engine at nozzle throat).

First, variations in axial spacing are studied, based on the default mesh with refinement depth 1 (Figure 3.1). Since heat conduction and strain in the axial direction of the thrust chamber are neglected, the axial spacing does not directly impact the obtained solution. Yet, the axial spacing does impact the evolution of the coolant temperature and pressure, which act as boundary conditions in both the thermal and mechanical solver. Therefore, both axial spacing and mesh refinement are studied separately.

For the axial refinement, a spacing of 6 mm, 4 mm, 2 mm, 1 mm, and 0.1 mm are studied, as shown in Figure 3.2. The plot clearly shows that the impact of axial spacing on the resolved coolant temperature is very small. As it is difficult to verify convergence base on the normalized temperature, relative percentage differences with respect to the finest spacing (0.1 mm) are considered in Figure 3.2 right. The relative differences clearly show a decreasing offset with decreasing axial spacing, with the maximum difference less than 0.5% for the 6 mm axial spacing setup.

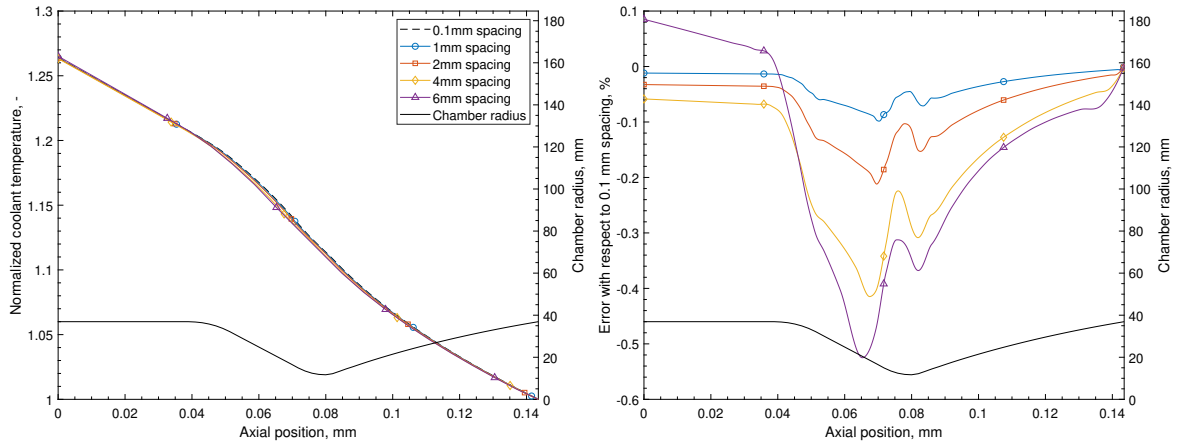

Figure 3.2: Axial spacing convergence study for coolant temperature.

Using an identical approach, the coolant bulk pressure convergence can be studied, as depicted in Figure 3.3. Similar to the coolant temperature, the largest error is observed around the nozzle throat where the flow velocity, and thus also the pressure drop, are highest. Additionally, the plot clearly shows a decreasing error when the axial spacing is reduced. Based on the grid convergence study, an axial spacing of 2 mm is selected, which provides a good balance between accuracy (<0.5% error w.r.t. most refined spacing) and computational cost.

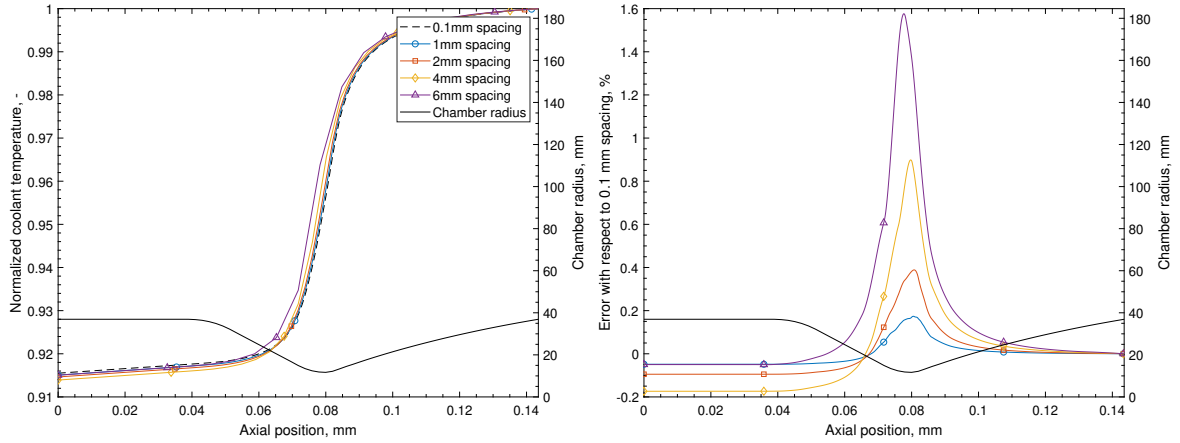

Figure 3.3: Axial spacing convergence study for coolant pressure.

Second, variations in refinement of the planar mesh are considered, using a refinement depth of 0.5, 1, 1.5 and 2, as illustrated in Figure 3.1. The default mesh (refinement 1) counts 150 elements and 186 nodes, whereas the most refined mesh consists of 690 nodes. When studying the convergence of the temperature on the mesh, it is not practical to compare solutions at every single node. Instead, the resolved temperature is only compared below the rib (node A in Figure 3.1), which marks the location where the temperature is expected to be highest. Results at this node - for the four refinement depths and axial spacing of 2 mm - are presented in Figure 3.4. For ease of visualization, all temperatures are normalized with respect to the maximum temperature observed in the most refined mesh. Data presented in this figure highlights negligible changes in the predicted temperature when the refinement depth is greater than 1. Therefore, this refinement depth is adopted for all future calculations.

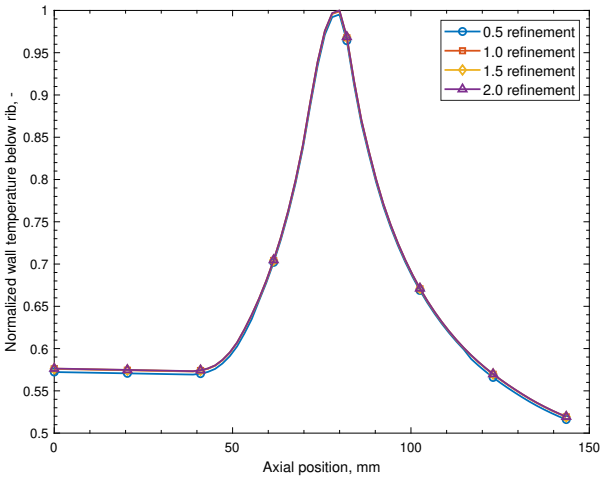

Figure 3.4: Thermal domain mesh refinement study for node A, with refinement depth based on Figure 3.1.

The last grid convergence study considered covers the mechanical domain. In this verification activity, the mesh of the verification engine design is refined and the equivalent stress at distinct nodes is studied. These nodes correspond to the eight labeled corner nodes, A-H, in Figure 3.1 on the right. The grid convergence study is carried out at the throat plane, with boundary condition implemented as described in subsection 2.6.2.

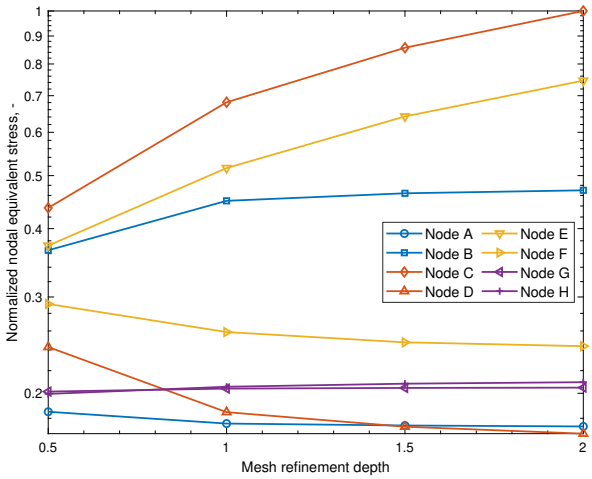

Figure 3.5: Mechanical domain mesh refinement study for nodes A-H, with refinement depth based on Figure 3.1.

The results obtained during this convergence study are visualized in Figure 3.5 for different mesh refinement depths. The plot clearly shows a convergence of the equivalent stress at nodes A, B, D, F, G, and H for refinement depths greater than 1. At nodes, C and E, no state of convergence was achieved. In the mesh, these two nodes correspond to the 90° corners of the cooling channel. Physically, these corners will result in a concentration of stress. Numerically, these sharp corners introduce a singularity in the solution algorithm, where stresses approach infinity upon further refinement of the mesh [98]. Therefore, the fact that the equivalent stress at nodes C and E does not converge is reasonable, provided the aforementioned arguments. It is noted that in reality, stress values will not take an infinite magnitude; this is purely a consequence of the numerical operations taken. The singularities in the solution could be avoided by mitigating sharp corners in the mesh, for example by including edge fillets or chamfers. This is not included in the current version of TDCAS but would be a relevant addition for future work on the developed software.

3.2. Hot Gas Heat Transfer

Although the grid convergence study verifies that the obtained numerical solution becomes independent of the grid spacing, it does not tell anything about the correctness of the implemented thermal and mechanical boundary conditions. To verify that these are implemented correctly, intermediate and final results of TDCAS are compared against results obtained from the software package Rocket Propulsion Analysis (RPA)[1]. RPA is a validated commercial software package which is developed for the preliminary design of rocket engines [35]. Like CEA, RPA can predict the 1-D combustion gas properties and performance parameters. However, unlike CEA, RPA can also perform a 1-D steady-state thermal analysis of a regeneratively cooled thrust chamber. This makes the software more versatile for preliminary design purposes.

First, the correct implementation of the hot gas convection correlations is verified, by comparing results of TDCAS to outputs of RPA. In RPA, the gas-side convective heat transfer is obtained from the correlation of Bartz (Equation 2.28). To isolate the hot gas convection from conduction in the wall and coolant convection, a constant wall temperature of 900 K is assumed. Results of this comparison are presented in Figure 3.6 for the convective heat transfer coefficient and adiabatic wall temperature. This image reveals an excellent agreement between the modeling of the Bartz equation in TDCAS and RPA. The modified Bartz equation, proposed in the film cooling model of Stechman et al., agrees well with the standard Bartz equation despite showing small deviations downstream of the nozzle throat. The correlation of Cinjarew on the other hand predicts a significantly lower heat transfer coefficient. Dependent upon the axial position in the nozzle, the predicted heat transfer coefficient is 22-35% less than the value that is obtained from the Bartz equation. It must be noted that this plot does not tell anything about the validity of any of the proposed convection models in the context of the Mk-II thruster. However, one *can* verify that the Bartz equation is correctly implemented in TDCAS, when considering RPA as reference. What is more, the much lower convective heat transfer that is predicted with the Cinjarew equation - compared to the Bartz equation - is also reported by Werling et al. [100]. Although this does not fully conclude on the correct implementation of the Cinjarew model, it does demonstrate that this lower trend is also observed by other scholars.

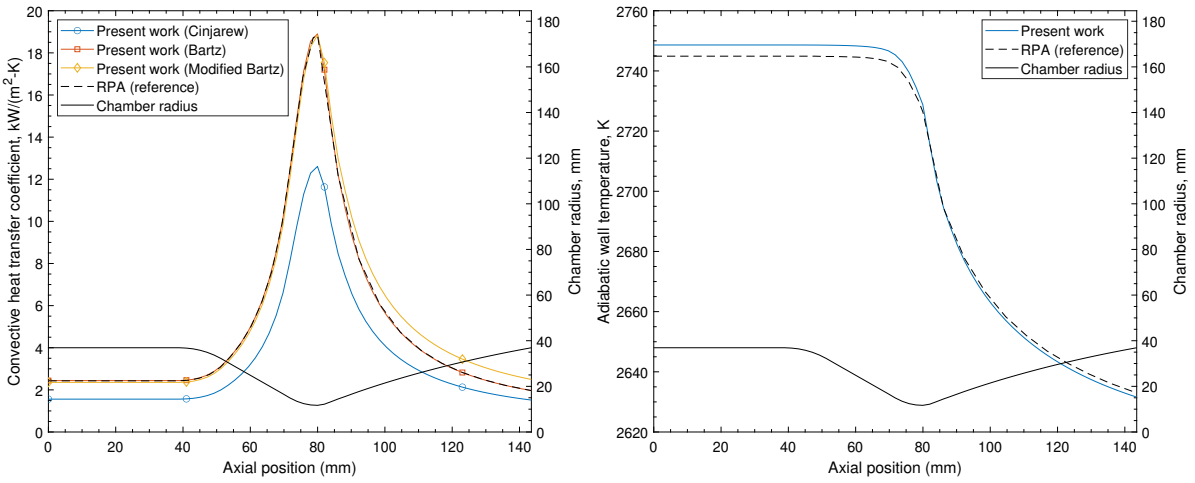

Figure 3.6: Comparison of hot gas convective heat transfer coefficient and adiabatic wall temperature predicted by TDCAS and RPA under a uniform wall temperature of 900 K.

The adiabatic wall temperature predicted by TDCAS and RPA, depicted in Figure 3.6, shows a good agreement. There exist some minor differences far upstream and downstream of the throat. Yet, these differences are only 4 K at the injector plane and 1 K at the nozzle exit plane, which is negligibly small compared to the magnitude of the adiabatic wall temperature (>2600 K). The difference in adiabatic wall temperature can be traced to the fact that RPA uses a slightly different gas composition than CEA. From this comparison, one can verify that the adiabatic wall temperature is correctly calculated in TDCAS, when considering RPA as reference.

[1]More info about this software can be found on the website of the developer: `https://www.rocket-propulsion.com`.

3.3. Wall Temperatures

In the previous section, the correct implementation of the hot gas heat transfer was verified by comparing the results of TDCAS to RPA. In this section, this verification is extended by also comparing predicted wall temperatures between the two computational tools. Before opening the discussion, it is important to mention that the user cannot modify the heat transfer correlations for the coolant in RPA. For any coolant that is not kerosene, methane, or hydrogen, RPA assumes the standard Dittus-Boelter correlation for convective heat transfer[2]. Hence, no corrections are applied for either curvature, roughness, or flow development. Although this is a problem that may challenge the *validity* of the solution in RPA, the results of RPA can still be used to *verify* that the solution algorithm in TDCAS is correctly implemented, provided that the same heat transfer correlation is used (Dittus-Boelter, without corrections). Besides, RPA also assumes a constant thermal conductivity in the wall, rather than a temperature-dependent value which is used in TDCAS. Lastly, RPA estimates 2-D heat transfer effects through the ribs using a correction factor based on classical fin theory, which is described in Equation 3.1 [23].

$$\frac{(\alpha_c)_{fin}}{\alpha_c} = \left(\frac{c_w}{c_w + l_w}\right) + \eta_{fin}\left(\frac{2c_r}{c_w + l_w}\right) \qquad \eta_{fin} = \frac{\tanh\left(\sqrt{\frac{2\alpha_c l_w}{\lambda_w}}\frac{c_r}{l_w}\right)}{\sqrt{\frac{2\alpha_c l_w}{\lambda_w}}\frac{c_r}{l_w}} \tag{3.1}$$

In this expression, α_c denotes the coolant heat transfer coefficient, c_w the channel width, c_r the channel height, l_w the land (rib) width, η_{fin} the fin efficiency factor, and λ_w the thermal conductivity of the chamber wall. The net heat flux through the wall follow from the 1-D energy balance noted in Equation 3.2,

$$q = \underbrace{\alpha_g(T_{aw} - T_{wg})}_{convection} = \underbrace{\frac{\lambda_w}{t_w}(T_{wg} - T_{wc})}_{conduction} = \underbrace{(\alpha_c)_{fin}(T_{wc} - T_{co})}_{convection} \tag{3.2}$$

where T_{aw} denotes the adiabatic wall temperature, T_{wg} the gas-side wall temperature, T_{wc} the coolant-side wall temperature, T_{co} the bulk temperature of the coolant, and t_w the thickness of the wall separating the coolant from the hot gas. This expression is also implemented in TDCAS. This way, the user can select to perform either a 2-D thermal analysis or a 1-D thermal analysis of the thrust chamber wall. To verify the correctness of implementation of the iterative thermal solver in TDCAS, we first compare results for a constant wall thermal conductivity and Dittus-Boelter heat transfer correlation (without roughness corrections).

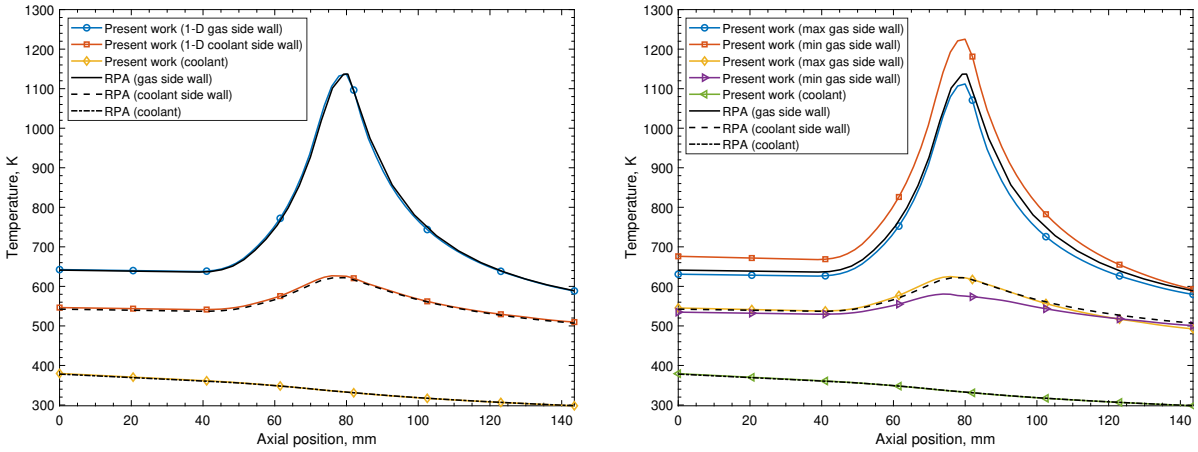

Figure 3.7: Comparison of predicted wall temperatures by TDCAS and RPA for a constant wall thermal conductivity with 1-D (left) and 2-D (right) thermal solution.

[2]For reference, RPA uses the Nusselt correlation $Nu = 0.021Re_{co}^{0.8}Pr_{co}^{0.4}(0.64 + 0.36T_{co}/T_w)$ for kerosene, $Nu = 0.0185Re_{co}^{0.8}Pr_{co}^{0.4}(T_{co}/T_w)^{0.1}$ for liquid methane, and $Nu = 0.033Re_{co}^{0.8}Pr_{co}^{0.4}(T_{co}/T_w)^{0.57}$ for liquid hydrogen [35].

Results based on 1-D and 2-D heat transfer in the wall are depicted in Figure 3.7. When the wall is resolved in 1-D, the results agree excellently with RPA. This is expected, since the simulation set-up is identical. This provides confidence in the correct implementation of the 1-D thermal solver in TDCAS. More interesting are results for the 2-D thermal field, presented in Figure 3.7 on the right. Since the 2-D solver considers conduction in both the radial and circumferential direction, and the wall is non-symmetric due to the presence of ribs, we expect to see thermal gradients in both directions. This expectation is confirmed by simulations, which reveal a maximum temperature difference of 113 K at the nozzle throat. The maximum wall temperature occurs below the rib, whereas the minimum temperature is obtained below the channel.

The simulated wall temperatures based on a 1-D analysis in RPA are in fair agreement with the wall temperatures predicted by the 2-D analysis in TDCAS, yet fail to predict the increase in temperature below the rib. Comparable observations are also documented by Sung and Anderson [101] in the application of copper alloy thrust chambers. They document a maximum wall temperature difference of 50 K between a 1-D and 2-D code, concerning a predicted 2-D wall temperature of 545 K. For low conductivity chambers, like Inconel, thermal gradients are generally much larger, as demonstrated in Figure 3.7. Since thermal strains that develop in the wall are proportional to the temperature, this can result in a reasonable increase in strain in the wall. For the reference engine studied in Figure 3.7, the corresponding thermal strain is underpredicted by 7% when a 1-D simulation is used.

Interestingly, the bulk coolant temperature rise appears to be very insensitive to the use of a 1-D or 2-D conduction solver. A similar observation is made by Denies [36], who compared a 1-D analysis to a 3-D heat transfer simulation, in which the coolant flow is also numerically resolved. In these simulations, the predicted coolant temperature also showed to be very insensitive to the use of a multidimensional heat transfer analysis code. Yet, the predicted wall temperature was found to be much lower when using a 1-D code, compared to a multidimensional conduction model.

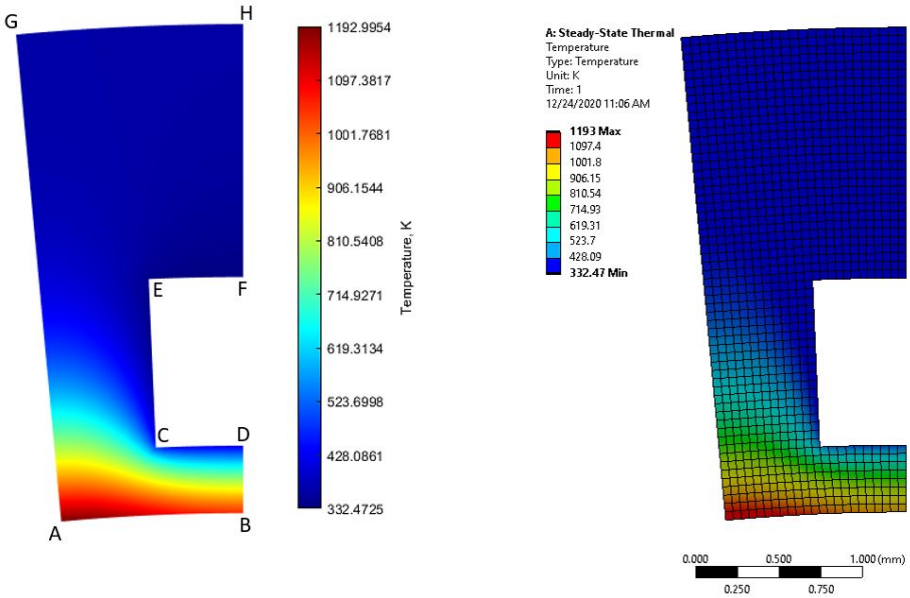

Figure 3.8: Comparison of wall temperature at the nozzle throat, predicted using TDCAS (left) and Ansys 2020 R2 (right).

The comparison of TDCAS to RPA is suitable to observe that the general order of magnitude of values is correct. Furthermore, it is known from section 3.1 that the numerical solution converges when the mesh is refined. Additionally, from section 3.2, one can learn that the hot gas heat transfer correlations are correctly implemented. As a last step of verification, the 2-D results of TDCAS are compared to a steady-state thermal simulation in Ansys 2020 R2. Ansys is an off-the-shelve numerical software package that can be used to study a large variety of physical problems, including heat transfer, fluid dynamics, and structural mechanics. In Ansys, the heat transfer problem is solved at the nozzle throat plane of the verification engine design. The automatic mesh generator of Ansys is used to create a coarse and fine mesh, depicted in Figure 3.8 right. The coarse mesh is set up with a minimum element

size of 0.1 mm, corresponding to 313 elements in the computational domain. The fine mesh is set up with a minimum element size of 0.05 mm, resulting in 1194 elements. Nusselt numbers for the hot gas and coolant heat transfer are obtained from the correlation of Bartz and the modified Nunner expression discussed earlier in this report.

A graphical comparison of the temperature field predicted by TDCAS and Ansys is presented in Figure 3.8. One may observe that the minimum and maximum temperatures that are predicted by the two solvers are in excellent agreement. Moreover, a qualitative assessment shows a good agreement of the temperature field. Eight nodes, labeled A-H in Figure 3.8 left, are defined at which the temperature is probed. The results for both TDCAS and Ansys are listed in Table 3.1.

Table 3.1: Comparison of nodal temperatures (in Kelvin) predicted by TDCAS and Ansys.

Node	TDCAS-C(1)	Ansys-C	Difference	TDCAS-F(2)	Ansys-F	Difference
A	1191.6	1191.7	0.01%	1193.0	1193.0	0.00%
B	1051.4	1051.1	0.03%	1052.0	1051.9	0.01%
C	488.1	486.1	0.42%	491.5	490.9	0.11%
D	418.8	418.8	0.01%	419.1	419.1	0.00%
E	340.5	340.5	0.01%	340.9	341.0	0.01%
F	332.4	332.4	0.00%	332.5	332.5	0.00%
G	363.1	363.1	0.02%	363.7	363.8	0.01%
H	359.2	359.2	0.02%	359.7	359.8	0.01%

(1) Coarse mesh, 313 elements.

(2) Fine mesh, 1194 elements.

From Table 3.1, one can conclude that the temperature at the reference nodes agrees excellently between TDCAS and Ansys, with an absolute error less than 0.42% for the coarse mesh and less than 0.11% for the fine mesh. Moreover, the difference between the two codes decreases when both meshes are refined. The small differences that remain present between TDCAS and Ansys are expected to be caused by round-off errors or discretization errors.

3.4. Mechanical Domain

The first verification step that is used for the mechanical solver involves a heavily simplified geometry. The geometry selected for this application is a thrust chamber with no cooling channels, for which both the stress and temperature can be obtained analytically. The planar wall studied in these unit tests has a radius of 8.03 mm, wall thickness of 1 mm, and is exposed to an internal pressure of 1 MPa. The reference material used in the unit tests is Inconel 718, with material properties as specified in ref. [40]. When uncoupled from the thermal domain, the wall acts as a standard pressure vessel, in which the hoop stress can be obtained from thin-walled theory, described in Equation 3.3.

$$\sigma = \frac{p \cdot r}{t} \tag{3.3}$$

In Equation 3.3, p is the internal pressure (1 MPa), r the radius (8.03 mm), and t the wall thickness (1 mm). From Equation 3.3, the hoop stress in the planar cylinder section equals 8.03 MPa. The same setup is loaded in TDCAS, with corresponding results (for a section of the wall) presented in Figure 3.9. From these results, one can observe that the numerical solution is in excellent agreement with the analytical solution. At the centerline of the cylinder, the numerical estimate equals 8.1 MPa, which is a difference of less than 0.9% from the analytical estimate. This difference decreased upon refinement of the mesh.

The second geometry considered for verification is the planar thrust chamber wall of the verification engine design. This geometry is considerably more complex than the standard pressure vessel geometry considered in Figure 3.9 and lacks a proper analytical solution. Therefore, results for nodal displacement are compared to Ansys, to get an indication of the correctness of implementation. The procedure adopted is very similar to the numerical comparison of the thermal domain, discussed earlier in section 3.3.

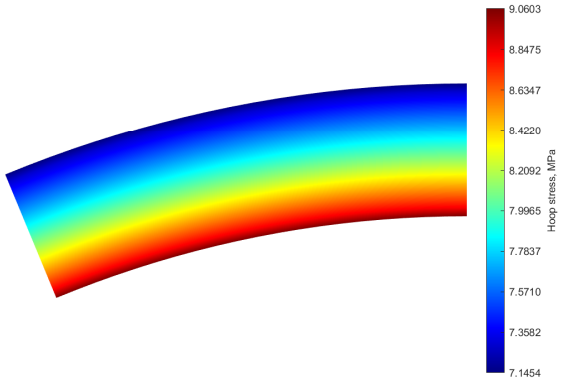

Figure 3.9: Unit hoop stress test in TDCAS with pressure vessel geometry.

Both simulations are set up with a hot gas pressure of 2.28 MPa acting on boundary A-B in Figure 3.10 and a coolant pressure of 6.93 MPa, acting on boundaries C-D, C-E, and E-F. To independently verify the mechanical domain from the thermal domain, thermal strains are not included in this comparative analysis. The results for the total deformation of the wall under the aforementioned load case are depicted in Figure 3.10. From this figure, one can distinguish a good agreement between deformation results predicted by TDCAS and Ansys.

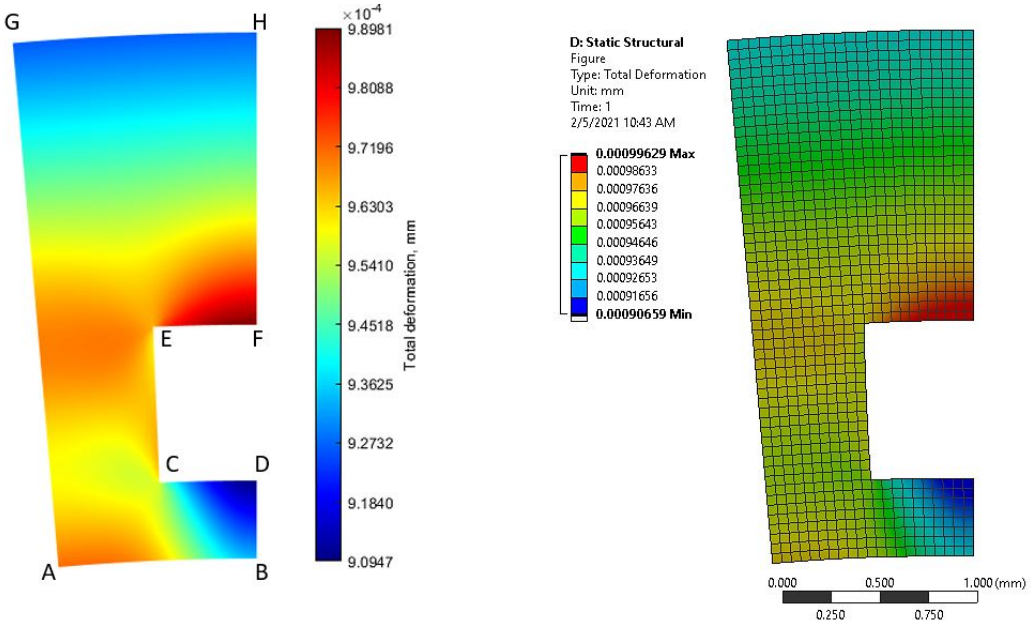

Figure 3.10: Comparison of nodal displacement at the nozzle throat, predicted using TDCAS (left) and Ansys 2020 R2 (right).

A quantitative comparison at the eight labeled nodes is presented in Table 3.2 for the nodal deformation in both the x-direction and y-direction. This table reveals a good agreement between the two numerical solvers, though some moderate deviations (absolute difference >0.75%) exist at nodes C and E. In the mesh, these nodes correspond to the two 90° corners of the cooling channels. At the nodes C and E in the mesh, the surface traction boundaries of edges E-F and C-E as well as C-D and C-E overlap. It is believed that this could be a cause for the larger difference. Nevertheless, at the nodes A and B, where stresses are generally highest [39], the comparative analysis shows a good agreement, with an absolute difference of less than 0.5%.

It is important to mention that differences between TDCAS and Ansys do not necessarily imply that one solver is right and the other is wrong. One has to recall that both programs resolve the same partial differential equation, but may use a completely different algorithm to do so. Without experimental measurements, it is hard to address which of the two solvers provides the most accurate representation of reality. Nevertheless, the predicted nodal displacements are in reasonable to good agreement between the two solvers, which provides confidence in the correct implementation of the numerical mechanical solver.

Table 3.2: Comparison of nodal displacements (in nm) in the x- and y-direction predicted by TDCAS and Ansys.

Node	TDCAS X	Ansys X	Difference	TDCAS Y	Ansys Y	Difference
A	-84.67	-85.01	0.40%	967.74	971.65	0.40%
B	0.00	0.00	0.00%	934.14	931.15	0.32%
C	-53.37	-53.84	0.88%	954.96	958.06	0.32%
D	0.00	0.00	0.00%	909.47	906.59	0.32%
E	-57.08	-58.29	2.08%	964.15	968.82	0.48%
F	0.00	0.00	0.00%	989.81	996.29	0.65%
G	-80.74	-81.20	0.57%	922.82	928.07	0.57%
H	0.00	0.00	0.00%	926.89	932.69	0.62%

Comparison based on Ansys mesh with 1034 elements.ts.

During a final software verification test, the temperature-induced loads were added to the pressure-induced loads studied in Figure 3.10. When simulating the engine, it was observed that the equivalent stress in the wall exceeded 2500 MPa, as depicted in Figure 3.11. This value is far above the yield stress of Inconel 718. For reference, the commercial vendor EOS [102] reports a vertical offset yield strength of 1145 MPa and horizontal offset yield strength of 1240 MPa for AM Inconel 718, when heat treated per AMS 2774. Recall from the introduction of this report that AM parts typically have anisotropic material properties in the direction normal to the build plate (vertical) and tangential to the build plate (horizontal). EOS also reports an ultimate tensile strength of 1375 MPa in the vertical direction and 1505 MPa in the horizontal direction for AM Inconel 718. From these values, one can clearly observe that the stress predicted under the linear elasticity assumption exceeds the yield criterion of AM Inconel 718.

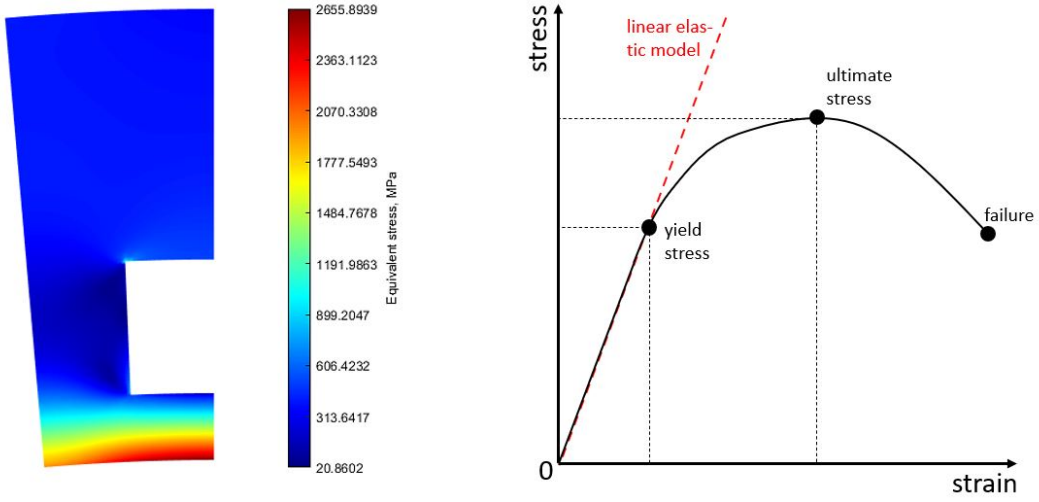

Figure 3.11: Invalid equivalent stress at the throat plane (left) and arbitrary stress-strain diagram of a ductile metal (right).

Similar observations of stress exceeding the yield criterion were made when the same setup was simulated in Ansys 2020 R2 with the linear elasticity assumption. Interestingly, the high stresses only occur in the wall separating the cooling channel from the combustion gas, whereas the rib and closeout show stresses that do not exceed the yield criterion. Physically, these high stresses in the chamber wall imply

that the material is either facing plastic deformation or failure. Both these phenomena are not taken into account in the thermo-elastic simulation that is used in TDCAS. The reason for this significant overprediction of the stress is explained in Figure 3.11 on the right, which shows an arbitrary engineering stress-strain diagram of a ductile metal, together with the linear elasticity assumption that is used in TDCAS. For any given value of strain, the linear elasticity assumption relates the stress to the strain conform Hooke's law, which is indicated with the dashed line. In practice, this law is only valid when the equivalent stress lies *inside* the yield surface. This surface is typically bounded by the (offset) yield stress. Beyond the yield stress, the slope of the stress-strain curve flattens, until the ultimate stress is reached. In this plastic deformation regime, the equivalent stress lies *on* the yield surface. When the chamber wall is deforming plastically, strain hardening of the material may occur, which alters the yield surface [97]. As a result, the stress, strain, and deformation of the wall become dependent on the loading and unloading history. The nonlinear relation between stress and strain, as well as potential strain hardening effects, are not taken into account when using a linear elastic model. Therefore, stresses are greatly overpredicted.

The engine studied in this verification simulation operates at a chamber pressure of 4 MPa. As a final attempt, several simulations were carried out where the chamber pressure was reduced to 1 MPa. Since the convective heating from the hot gas reduces with pressure (Equation 2.28), a great reduction in wall temperature, and consequently thermal strain, can be expected. Nevertheless, even at this reduced pressure, the predicted equivalent stress (1293 MPa) still exceeded the yield criterion. Operation at even lower chamber pressures will likely result in reasonable results when using the linear elasticity assumption since the offset yield stress of AM Inconel 718 is in the range 1145-1240 MPa. Nevertheless, operating the Mk-II thruster at such low pressures greatly impacts the overall competitiveness of the chamber, from a technical performance point of view (recall from section 2.2 that low chamber pressures reduce the thrust coefficient and increase the required chamber volume). Therefore, it can be concluded that even in a small engine like the Mk-II, the use of a linear elastic assumption to predict mechanical loading of the wall is invalid, when using AM Inconel 718 as material.

To resolve the structural domain numerically, an elastoplastic numerical solver would be required. Yet, these types of solvers are considerably more complex to program and require detailed knowledge about the plastic behavior of the material, which is not available in the current phase of this study. Besides, modeling the plastic domain was not considered within the scope of this study. Hence, it was decided to constrain the maximum thermal loading of the wall by a limit wall temperature, rather than a limit value for the equivalent stress (similar to the approach suggested in refs. [36, 86]).

3.5. Chapter Summary

In this section, several verification techniques were discussed and applied to TDCAS, to gain confidence in the correct implementation of the code. A grid convergence study demonstrated that the numerically obtained results are independent of the mesh spacing (section 3.1). The wall temperatures and hot gas heat transfer obtained from TDCAS were compared to 1-D results predicted by RPA, a validated software package that can predict heat transfer in rocket engines (section 3.2). The comparison demonstrated a good agreement between the two solvers. Uncoupled from the thermal domain, the linear elastic analysis performed in TDCAS showed good agreement with analytical models and other numerical software packages (sections 3.3 and 3.4). When coupled to the thermal domain, stress magnitudes that exceeded the yield criterion were observed, which invalidated the linear elasticity assumption. As a result, it was decided to continue the design with a maximum service temperature of the wall, rather than constraining the design based on mechanical stress.

4

Experimental Validation

In chapter 3, the (intermediate) results of TDCAS were verified. However, these activities only learn something about the correctness of implementation and not necessarily about the correctness of the model based on real-world measurements. In this chapter, experimental data is used to validate the simulations performed in TDCAS. First, in section 4.1, the rough channel convection correlations are compared to measurements in AM cooling channels. Second, in section 4.2, the hydrogen peroxide film cooling models are calibrated and validated against experiments in research thrusters. Third, in section 4.3, the regenerative cooling model is compared against measurements with the current iteration of the Mk-II engine developed by Dawn Aerospace. It is noted that this data set is unique, since it covers regenerative cooling with hydrogen peroxide, which is not often seen in the open literature. Fourth, immersion screening tests with AM Inconel 718, conducted as a part of the ESA FLPP project, are briefly discussed in section 4.4. These tests are used to validate the chemical compatibility of AM Inconel 718 with concentrated hydrogen peroxide.

Lastly, it is worth noting that the data sets that were available to the author could only provide partial validation of TDCAS. For example, the use of AM Inconel 718 in the context of the thrust chamber could not be fully validated yet. These hot-fire tests are planned for fall/winter 2021 as a part of the ESA FLPP project. A brief description for the FLPP tests that are required to fully validate TDCAS is provided in Appendix A.

4.1. Rough Channel Heat Transfer Experiments in the Literature

In subsection 2.4.1, three empirical Nusselt correlations were introduced to model the hydrogen peroxide convective heat transfer in rough conduits, based on the work of Nunner, Norris, and Dipprey-Sabersky. For all correlations, limited to no experience could be found in the literature regarding the applicability to AM cooling channels. In this section, the proposed convection models are compared to heat transfer experiments in AM channels described in the open literature.

4.1.1. Experimental Setup

The experimental data set considered in this thesis is based on the research of Stimpson et al. [25] and Wildgoose et al. [76]. Both research groups studied heat transfer in AM cooling channels manufactured from Inconel 718 (and cobalt-chrome). It is worth mentioning that several outcomes of these test campaigns were already introduced in subsection 2.4.1.

The experimental setup of both research groups is depicted in Figure 4.1 on the left. Air is discharged through an AM coupon, illustrated in Figure 4.1 on the right, which has small rectangular and circular cooling channels. Stimpson et al. only consider rectangular channels fabricated under an AM build angle of 45°. Wildgoose et al. on the other hand consider circular channels and experiments with build angles of 0°, 30°, 45°, 60°, and 90°. Only the latter three build angles are deemed relevant in the application of the thrust chamber, when adopting the definition of the build angle presented in Figure 2.12. All cooling channels of the AM test coupons have a hydraulic diameter in the range

of 0.4 mm to 1.3 mm. The experiments are carried out at Reynolds numbers up to 4×10^4. In the Mk-II thruster, the Reynolds number in the cooling passages typically does not exceed 1×10^5 at the throat, and 5×10^4 in the chamber, which is reasonably close to the data range of Stimpson et al. and Wildgoose et al. Besides, the maximum hydraulic diameter used in the Mk-II thruster cooling channels does not exceed 1.3 mm, which falls within the investigated experimental range.

During the flow tests, the pressure and temperature of the air upstream and downstream of the AM coupon are measured. This is achieved with pressure transducers and thermocouples. Moreover, the mass flow rate is measured with a laminar flow element. The air in the cooling channels is indirectly heated via copper blocks that surround the AM coupon. The purpose of these blocks is to ensure a uniform temperature distribution along the length of the channels. To minimize conduction losses, thermal paste is applied at the interfaces between the AM coupon and copper blocks. The temperature inside the copper blocks is also monitored using thermocouples. The full test section is isolated from the environment with rigid foam. For a more detailed explanation of the test setup and measurement equipment that is used, the reader is referred to the original pieces of literature [25, 76].

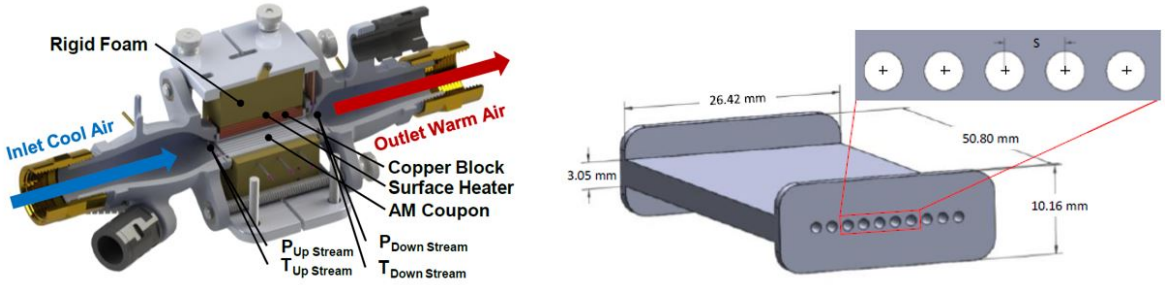

Figure 4.1: Schematic representation of test setup and typical additively manufactured test article used in the heat transfer studies of Stimpson et al. and Wildgoose et al. (reprinted from ref. [76]).

It must be mentioned that several differences exist between the air flow experiments in the literature and coolant flow in the AM Mk-II thruster. For instance, the maximum wall temperature and heat flux that are obtained in the Mk-II thruster are much higher. In addition, a fluid with different thermophysical properties is being used. Unfortunately, heat transfer experiments with hydrogen peroxide, or a more representative fluid like water, in AM channels could not be found in the open literature. As a result, the experiments of Stimpson et al. and Wildgoose et al. represent the best available dataset that could be acquired within the scope of this thesis. Despite the earlier mentioned difference between the Mk-II and air flow experiments, it is expected that the experimental work of Stimpson et al. and Wildgoose et al. can be used to learn more about the applicability of proposed heat transfer models to flow in small AM cooling channels.

4.1.2. Description of Experimental Data

Both research groups provide experimental data on the hydraulic diameter, equivalent sand grain roughness, friction factor, Reynolds number, and Nusselt number. One must be aware that only the hydraulic diameter is directly measured using CT scans. All other aforementioned parameters are *derived* from the measured mass flow rates, temperatures, and pressures. Raw data for mass flow rate, temperature, and pressure is not provided.

The first five columns of Table 4.1 provide an overview of the derived Reynolds number, Nusselt number, equivalent sand grain roughness (k_s/D_h), and friction factor augmentation (f/f_0). One may recall that the friction factor is a function of the Reynolds number and surface roughness, conform Equation 2.37. The table only lists experiments that have a bulk flow Reynolds number greater than 1×10^4. Experiments at lower Reynolds numbers are considered less relevant, considering the typical Reynolds numbers observed in the cooling channels of the Mk-II thruster.

Table 4.1: Comparison of experimental heat transfer studies in additively manufactured cooling channels with proposed Nusselt correlations (measurements from refs. [25, 76]).

measurements			Friction		Dittus-Boelter		Modified Nunner		Norris		Dipprey-Sabersky	
Test ID	Reynolds	Nusselt	k_s/D_h	f/f_0	Nusselt	Error	Nusselt	Error	Nusselt	Error	Nusselt	Error
M-2x-In	1.2E+04	63.1	0.20	3.40	35.8	-43.3%	61.4	-2.7%	77.5	+22.8%	71.6	+13.5%
	1.7E+04	79.4	0.20	3.76	48.9	-38.4%	89.1	+12.2%	112.9	+42.3%	97.2	+22.4%
L-1x-In	1.1E+04	52.5	0.18	3.09	33.2	-36.7%	55.0	+4.8%	67.7	+29.0%	65.2	+24.3%
	1.4E+04	61.8	0.18	3.30	40.6	-34.2%	70.0	+13.2%	86.4	+39.9%	79.5	+28.6%
L-2x-Co	1.4E+04	57.0	0.12	2.62	42.7	-25.2%	68.1	+19.5%	78.4	+37.4%	77.3	+35.6%
	2.4E+04	81.5	0.12	2.96	63.0	-22.8%	108.2	+32.7%	124.9	+53.3%	113.8	+39.6%
	4.0E+04	110.3	0.12	3.36	95.4	-13.6%	177.3	+60.6%	205.0	+85.8%	172.0	+55.9%
S-2x-Co	1.2E+04	75.2	0.18	3.18	36.1	-52.0%	60.8	-19.2%	75.0	-0.3%	70.8	-5.9%
	1.3E+04	91.1	0.18	3.27	39.2	-56.9%	67.1	-26.3%	82.9	-9.0%	76.8	-15.7%
	1.8E+04	120.4	0.18	3.58	51.9	-56.9%	93.7	-22.2%	116.1	-3.5%	101.1	-16.1%
M-2x-Co	1.2E+04	72.4	0.23	3.82	37.8	-47.7%	67.5	-6.7%	88.2	+21.8%	77.8	+7.5%
	1.8E+04	90.9	0.23	4.22	51.6	-43.2%	97.7	+7.5%	128.2	+41.1%	105.3	+15.9%
1.00C45	3.0E+04	127.6	0.13	3.28	75.8	-40.6%	137.1	+7.5%	160.5	+25.8%	138.6	+8.6%
	3.5E+04	145.5	0.13	3.41	85.8	-41.0%	158.9	+9.3%	186.1	+27.9%	156.8	+7.8%
1.00C60	3.0E+04	113.0	0.09	2.59	75.7	-33.0%	125.2	+10.8%	138.2	+22.3%	129.4	+14.5%
1.00C90	3.0E+04	103.0	0.07	2.38	75.7	-26.5%	120.8	+17.2%	130.9	+27.1%	126.0	+22.3%
1.25C0	3.0E+04	107.9	0.19	4.17	75.8	-29.7%	148.4	+37.6%	186.8	+73.2%	147.9	+37.1%
	3.9E+04	127.7	0.19	4.47	95.3	-25.4%	194.7	+52.5%	245.3	+92.1%	185.2	+45.1%
1.25C30	2.9E+04	117.4	0.17	3.87	75.2	-35.9%	143.8	+22.5%	176.7	+50.6%	144.0	+22.7%
1.25C45	3.0E+04	115.0	0.11	2.98	75.8	-34.1%	132.5	+15.2%	151.2	+31.4%	134.9	+17.3%
1.25C60	3.0E+04	104.1	0.07	2.31	75.6	-27.4%	119.1	+14.4%	128.3	+23.3%	124.7	+19.7%
	3.5E+04	115.0	0.07	2.40	85.8	-25.4%	138.4	+20.3%	149.2	+29.7%	141.7	+23.2%
	3.9E+04	135.9	0.07	2.48	95.0	-30.1%	156.3	+15.0%	168.4	+24.0%	157.2	+15.7%
1.25C90	3.0E+04	106.0	0.09	2.73	75.8	-28.5%	128.1	+20.9%	143.1	+35.0%	131.5	+24.1%
	3.9E+04	124.3	0.09	2.93	95.2	-23.4%	168.1	+35.2%	187.8	+51.0%	165.4	+33.1%

Upper part table (M-2x-In to M-2x-Co) corresponds to data Stimpson et al. Lower part table (1.00C45 to 1.25C90) corresponds to data Wildgoose et al.

4.1.3. Comparison Experiments to Model

The sixth to the thirteenth column of Table 4.1 show the Nusselt number that is predicted by TDCAS. These predictions are based on:

- The Dittus-Boelter equation for smooth channels (Equation 2.34) without roughness corrections.
- The Dittus-Boelter equation with modified Nunner surface roughness correction (Equation 2.35).
- The Dittus-Boelter equation with Norris surface roughness correction (Equation 2.36).
- The Dipprey-Sabersky correlation for flow in rough channels (Equation 2.38).

All simulations are executed based on the measured Reynolds number and a (constant) Prandtl number equal to 0.71. Errors with a "-" sign correspond to an underprediction of the Nusselt number in TDCAS. On the other hand, a "+" sign indicates an overprediction of the Nusselt number.

From the comparison with experimental data in Table 4.1, one can observe that the uncorrected Dittus-Boelter yields are considerable underprediction of the heat transfer and is hence considered unsuitable for the simulation of heat transfer in AM cooling channels. The modified Nunner correlation provides a reasonable first-order estimation, but differences up to 61% exist. The average error for this equation is 14.1%. The Nusselt number correction factor of Norris tends to overpredict the heat transfer in almost all experiments. Interestingly, an excellent agreement is observed in test S-2x-Co. The exact reason for this could not be settled on, given the data available in the literature. The correction factor of Norris has an average error of 35% with the test data. The equation of Dipprey and Sabersky shows a trend similar to that of Nunner, yet has a slightly larger average deviation from the test data (19.9% respectively).

To observe potential trends in the data, the errors listed in Table 4.1 are plotted against the bulk flow Reynolds number and friction factor augmentation, as illustrated in Figure 4.2. From this plot, one can observe that the error in the prediction of the Nusselt number tends to grow with increasing Reynolds number. This is consistent for all three modeling approaches (modified Nunner, Norris, and Dipprey-Sabersky). Furthermore, there seems no clear relation between the friction factor augmentation and the error in Nusselt number prediction.

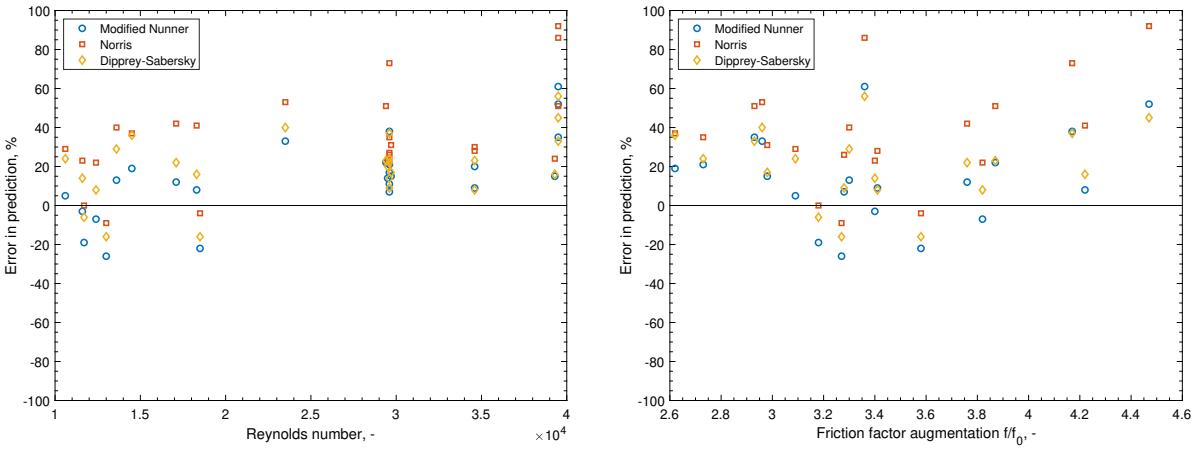

Figure 4.2: Error in prediction of AM channel Nusselt number for different roughness models as a function of the Reynolds number and friction factor augmentation.

It is important to mention that the data of Stimpson et al. and Wildgoose et al. do not conclude on the applicability of the considered Nusselt correlations in AM thrust chambers cooled with hydrogen peroxide. However, it does provide relevant information on the applicability in AM cooling channels, with a size comparable to those in the Mk-II thruster. In light of the observations, the modified Nunner correlation seems most promising to predict the heat transfer in rough AM channels, followed by the Dipprey-Saberrsky correlation. Yet, more experiments are required - ideally with hydrogen peroxide - to fully understand the impact of high surface roughness on heat transfer. The impact of the uncertainty in prediction will be evaluated in sensitivity studies later in this report.

4.2. Film Cooling Experiments in the Literature

To calibrate and validate the film cooling model, experimental data available in the open literature is used. Two relevant pieces of research were found in the work Heo et al. [55] and Kwak [62]. Both utilize hydrogen peroxide film cooling in the application of a small bipropellant thrust propelled by 90% hydrogen peroxide and kerosene. In subsection 4.2.1, the experimental setup that is used in both publications is briefly discussed. Hereafter, in subsection 4.2.2, typical test results of both pieces of literature are discussed. These results are compared to the proposed film cooling model in subsection 4.2.3.

4.2.1. Experimental Setup

Both data sets are based on research at the Korean Advanced Institute of Science and Technology. As a result, the experiments have many similarities in terms of the measurement setup that is used. Both thrust chambers (Heo and Kwak) feature a thick-walled geometry without internal cooling channels. Therefore, cooling of the chamber is only achieved by the hydrogen peroxide film and by radiation from the chamber wall to the environment. The tests are performed in a laboratory environment at ambient conditions, in which the thruster is fired in a horizontal position (see also Figure 4.3).

The kerosene core flow and hydrogen peroxide film flow are injected in the liquid phase, whereas the hydrogen peroxide core flow is injected in the decomposed state (oxygen and steam, 1019 K). The hydrogen peroxide is decomposed in a catalytic reactor that is placed upstream of the injector. This design concept is identical to the Mk-II engine. For injection of the core flow, both research thrusters use a showerhead type injector, which is different from the injector configuration that is used in the Mk-II engine. To transfer the propellants from the storage tank to the thrust chamber, both research thrusters use a pressure-fed setup with high purity nitrogen gas as a pressurant.

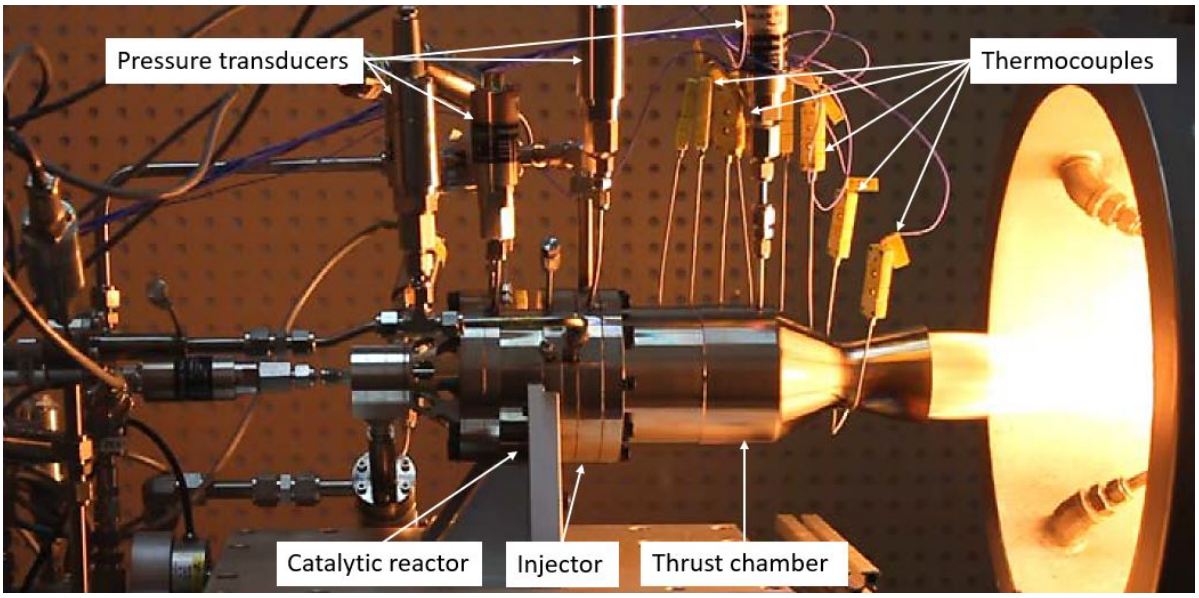

Figure 4.3: Hot-fire test of hydrogen peroxide film-cooled research thruster of Heo et al. (adapted from ref. [55]).

A brief overview of the most important engine design characteristics, as well as the typical operating regime, is listed in Table 4.2. From this table, one can conclude that the research thruster of Heo is most comparable to the Mk-II in terms of size and thrust output. Primary differences between the Mk-II engine and the thruster of Heo are a much higher chamber pressure and much shorter characteristic length in the Mk-II. As a result, the Mk-II thrust chamber has a much smaller size.

In both thrusters, the mass flow rates are obtained from differential pressure measurements over a venturi tube (core flow) or orifice plate (film flow). The relation between differential pressure and mass flow rate follows directly from Bernoulli's principle and the geometry of the venturi tube or orifice plate. Other sensors used in the test setup include pressure transducers to measure fluid pressures and K-type thermocouples to measure the temperature of the thrust chamber wall. All thermocouples are

mounted at the upper side of the thrust chamber, concerning the horizontal test configuration depicted in Figure 4.3. At the nozzle throat, both experiments featured an additional thermocouple at the lower side of the thrust chamber. The exact placement of the thermocouples, with respect to the injector plane and inner chamber perimeter, is mentioned in the original pieces of literature and not repeated here.

Table 4.2: Engine design parameters of hydrogen peroxide film-cooled thrusters (data from refs. [55, 62]).

Parameter	Heo	Kwak
Mixture ratio	7.11-9.51	7.01-.7.35
Vacuum thrust	∼2500 N	∼800 N
Chamber pressure	1.80-2.11 MPa	1.59-1.84 MPa
Characteristic length	1.34 m	0.95 m
Chamber diameter	80 mm	60 mm
Throat diameter	29.25 mm	16.83 mm
Nozzle exit diameter	47.3 mm	37.44 mm

A detailed overview of all hot-fire tests relevant to this study is presented in Table 4.3. This table summarizes the measured film fraction (ω), total mixture ratio (MR), chamber pressure (p_o), oxidizer flow rate ($\dot{m}_{ox}$), fuel flow rate ($\dot{m}_{fu}$), and film flow rate ($\dot{m}_{cf}$). Both researchers perform long-duration tests (> 10 seconds) in a film-cooled configuration and short-duration reference tests without the presence of the film coolant. In these tests, the chamber is essentially operated as a heat sink that is radiating heat to the environment. These reference tests (labeled R1-R3 in Table 4.3) are used in combination with the film-cooled tests (labeled F1-F8 in Table 4.3) for estimating losses in characteristic velocity when film cooling is applied.

The research of Kwak also describes tests with two different film coolant injectors. The difference between these two injector designs is merely the number of orifices uses (36 versus 32), whereas the orifice diameter (0.3 mm) is kept constant. As a result, the film flow rate is slightly higher in experiments KWAK-F4 to KWAK-F6. The test campaign described by Heo does not include thrust measurements. Kwak only reports the thrust force for tests KWAK-R1, KWAK-F2, and KWAK-F3.

Table 4.3: Overview of test conditions of 90% hydrogen peroxide film-cooled thrusters of Kwak [62] and Heo [52, 55].

Test ID	ω	MR	p_o, MPa	$\dot{m}_{ox}$, g/s	$\dot{m}_{fu}$, g/s	$\dot{m}_{cf}$, g/s	Test conditions
KWAK-R1	0.00	7.15	1.82	247.5	34.6	0.0	1 sec burn, no film coolant
KWAK-R2	0.00	7.12	1.83	246.4	34.6	0.0	2 sec burn, no film coolant
KWAK-R3	0.00	7.11	1.80	246.1	34.6	0.0	2 sec burn, no film coolant
KWAK-F1	0.20	9.52	2.11	246.0	33.0	68.2	3 sec burn
KWAK-F2	0.18	9.17	2.06	243.6	33.4	62.7	3 sec burn
KWAK-F3	0.16	8.83	2.04	241.4	33.3	52.8	3 sec burn
KWAK-F4	0.18	9.23	2.10	245.6	33.3	61.9	3 sec burn, diff. injector
KWAK-F5	0.20	9.51	2.08	245.0	33.2	70.6	3 sec burn, diff. injector
KWAK-F6	0.21	9.49	2.06	243.3	33.3	72.6	3 sec burn, diff. injector
KWAK-F7	0.17	9.15	2.02	241.6	32.6	56.7	30 sec burn
KWAK-F8	0.21	9.50	2.09	243.4	33.3	73.0	30 sec burn
HEO-R1	0.00	7.27	1.84	749.2	103.1	0.0	5 sec burn, no film coolant
HEO-F1	0.12	7.24	1.70	624.1	99.5	96.2	10 sec burn
HEO-F2	0.15	7.01	1.65	587.4	101.8	126.0	9 sec burn
HEO-F3	0.20	7.26	1.61	564.8	100.0	161.6	11 sec burn
HEO-F4	0.23	7.35	1.59(1)	553.4	101.2	190.4	15 sec burn

(1) Chamber pressure estimated based on mass flow rate, characteristic velocity, and throat diameter.

4.2.2. Description of Experimental Data

Typical test results that are obtained during the film-cooled hot-fire test of the thrusters are reprinted in Figure 4.4. These plots show the measured wall temperatures as a function of time, for the tests HEO-F1 and HEO-F3. In Figure 4.4 on the left, a clear steady-state condition with wall temperatures <200 °C can be observed at thermocouple locations T1-T4. Temperature readouts in the convergent section of the nozzle (T5 and T6) and at the nozzle throat (T7 and T8) reveal that no steady-state is reached. Since the throat temperatures approach the melting temperature of the thrust chamber wall, the test is terminated ten seconds into the burn. This corresponds to a time of 15.6 seconds in Figure 4.4).

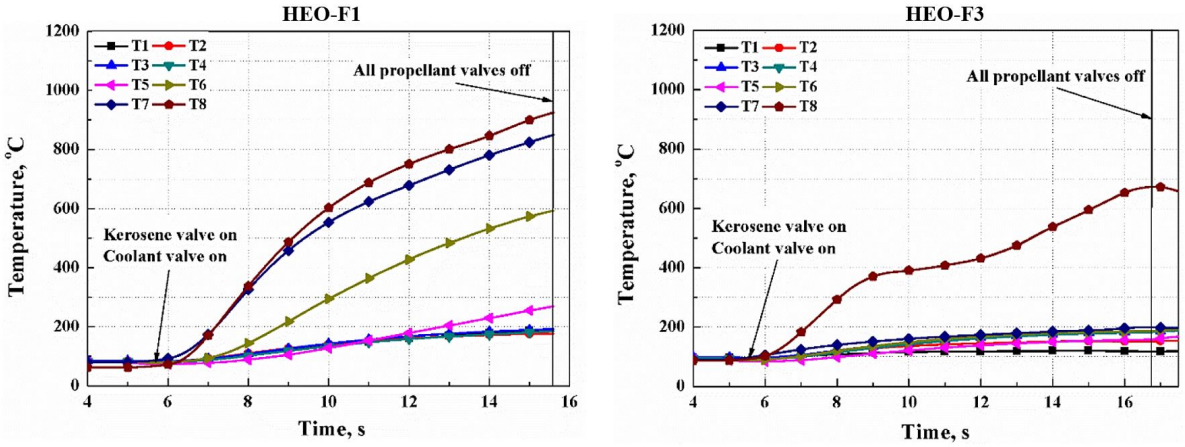

Figure 4.4: Wall temperature measurements in the film-cooled thruster of Heo (reprinted from ref. [52]).

When the film flow rate is increased from 96.2 g/s to 161.6 g/s, the liquid dry-out point moves downstream, towards the throat. This is visible in Figure 4.4 on the right, where almost all thermocouple readouts record temperatures below 200 °C. Surprisingly, the throat temperature readout at the lower side of the chamber (T8) is still in transient, whereas the throat readout at the upper side of the chamber (T7) has reached a steady-state. Small differences (∼100 °C) at the nozzle throat are also clearly visible in Figure 4.4 on the left.

Since the liquid film essentially acts as a heat sink between the hot gas and the wall, it is reasonable to assume that the wall temperature at locations where the liquid film exists is close to identical to the temperature of the liquid film [85]. For reference, the saturation temperature of 90% hydrogen peroxide at the chamber pressure observed in HEO-F1 is 210 °C (see also Figure 2.4), which is very close to the observed wall temperature at T1-T4. Based on this assumption, one can expect the liquid dry-out zone to be located between T4 and T5 in Figure 4.4 on the left and between T6 and T7/T8 in Figure 4.4 on the right.

The trends observed for the other experiments of Heo and Kwak compare well to those shown in Figure 4.4: all data sets show a clear transition point in the wall temperature measurements. This point is related to the transition of liquid film cooling to gaseous film cooling and was also clearly visible in Figure 2.18. In all measurements of Heo and Kwak, this transition point is typically located in the convergent section of the nozzle or the vicinity of the nozzle throat. These data sets are not reprinted in this work, but are available in the original pieces of literature [52, 62].

4.2.3. Comparison Experiments to Model

In section 2.5, an analytical 1-D film cooling model was introduced, based on the work of Stechman et al. and NASA SP-8124. To validate the applicability of this model to a small bipropellant thruster film-cooled with 90% hydrogen peroxide, the simulated wall temperatures are compared to the experimental data introduced in the previous subsection. In this investigation, only the results of Heo are used for validation of the wall temperatures, since this thruster is most comparable to the Mk-II engine. The combined data set with measurements of Heo and Kwak is used for validation of the film cooling performance model that was introduced in subsection 2.2.4.

Calibration of the Liquid Film Effectiveness and Validation of the Wall Temperatures

The first test considered for validation of the inner wall temperatures is HEO-F1, with operating conditions as specified in Table 4.3. In TDCAS, the problem is solved without cooling channels, but with a radiative coupling from the outside chamber wall to the environment. This radiative coupling follows from Equation 2.67, with an ambient temperature of 294 K, emissivity of 0.8 or 0.6, and a unity view factor. Furthermore, for the wall thermal conductivity, the properties of steel are assumed. In addition, a reference entrainment factor of 0.425 is used in the gaseous film cooling model, together with a unity local entrainment factor and decomposition rate constant of 3000 s^{-1}.

One of the most important scaling parameters in the liquid film cooling model is the film effectiveness. In Figure 2.19, this empirical parameter was plotted as a function of the film coolant Reynolds number, based on the work of Stechman et al. For test HEO-F1, where the film flow is characterized by a Reynolds number of 996, this approach provides a liquid film effectiveness of 0.79. In other words, the real cooling potential represents only 79% of the theoretical potential. Simulations in TDCAS of tests HEO-F1, HEO-F2, and HEO-F3 reveal that this particular effectiveness results in the absence of a dry-out point, or a dry-out point located far downstream of the nozzle throat. When considering test data presented in Figures 4.5, 4.6, and 4.8, these simulations are clearly not realistic. In all these illustrations, the dry-out point is located in the convergent section of the nozzle, or near the nozzle throat. It is suspected that the liquid vaporization rate is strongly augmented by the decomposition of the hydrogen peroxide film, an argument which was already brought up in subsection 2.5.1. Consequently, a lower liquid film effectiveness is expected. For the considered hot-fire tests, a liquid film effectiveness of 0.46 seems more realistic. All simulation data plotted in Figures 4.5, 4.6, and 4.8 is based on the film effectiveness of 0.46. This particular value is also in better agreement with simulations of Heo[1], shown in Figure 4.5 on the right.

At all times, the reader must bear in mind that the liquid film effectiveness is an empirical constant that is based on both simulation and measurement data. As a result, the exact magnitude of this parameter depends on the simulation setup. For all simulations with TDCAS performed in this work, an effectiveness of 0.46 is used, which is in better agreement with test data than the empirical parameter reported by Stechman et al. Different results may be obtained when using an alternate simulation framework. More hot-fire tests, ideally at a chamber pressure closer to that of the Mk-II thruster, are required to better understand the impact of the chamber operating conditions on the liquid film effectiveness. In the absence of this data, the effectiveness is treated as a constant in this work. The impact of this assumption is studied in a sensitivity analysis presented in subsection 5.3.3.

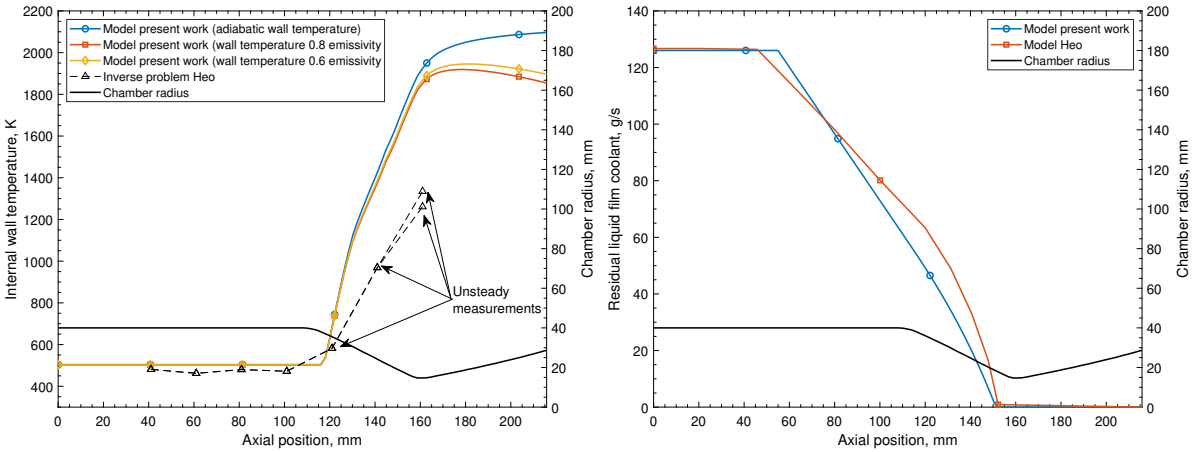

Figure 4.5: Comparison of film cooling measurements with simulation Heo and TDCAS for test HEO-F1 (data from ref. [52]).

[1]This simulation is based on the droplet evaporation research of Allison [88] and film cooling model of Grisson [103] and resolves the conservation of mass, energy, and species in the vaporization, monopropellant, and bipropellant flame layer. Hydrogen peroxide decomposition is modeled using the Arrhenius equation, where the pre-exponential constant is treated as an empirical constant to obtain an agreeable result with experiments. The Arrhenius equation, noted as $k = A\exp(-E_a/RT)$, where k is the reaction rate constant, A the pre-exponential factor, E_a the activation energy, R the gas constant, and T the temperature is frequently used in (chemical) reaction mechanics to model the reaction and evolution of species.

The simulated temperatures, illustrated in Figure 4.5 on the left, are compared to the inner wall temperature at the end of the burn. Since the thermocouple is placed *inside* the wall of the thrust chamber and not exactly *at* the inner wall, an inverse heat transfer problem is solved to estimate the temperature at the inner wall. The solution of this inverse problem, as proposed by Heo, is indicated in Figure 4.5 with the dashed line. The triangle markers indicate the thermocouple locations (T1-T8 in Figure 4.4). It is important to note that this inverse problem does not provide the steady-state wall temperature, but rather the transient temperature evaluated at the inner wall location.

A first glance at Figure 4.5 reveals a trend in the wall temperature that is very similar to experiments and simulations in MMH film-cooled thrusters, which were introduced in Figure 2.18 earlier in this report. A clear transition between the liquid and gaseous film cooling regime is observed, with a dry-out point located at an axial position of 100-120 mm. The measured wall temperature upstream of the dry-out point behaves almost constant, which is also observed in the simulations in TDCAS. Simulations in TDCAS are also compared to an analytical simulation of Heo, which is depicted in Figure 4.5 on the right. The first part of this curve, 0-58 mm, corresponds to the heating of the liquid from the injection temperature to the saturation temperature. The second part, 58-150 mm, corresponds to the vaporization of the film layer. The slope of the residual liquid film coolant differs slightly between the model of Heo and TDCAS. Nevertheless, the estimated liquid dry-out zone shows an excellent agreement between the two analytical models.

Unfortunately, only limited conclusions can be drawn concerning the validity of the simulations downstream of the dry-out zone. The steady-state temperatures that are predicted using the NASA SP-8124 model are much higher than the transient temperature measurements of Heo. Data in Figure 4.4 indicates that the throat temperature is still increasing with approximately 46 K/s whereas the temperature just upstream of the throat (T6) is increasing at a rate of 40 K/s. Therefore, it is reasonable to expect the steady-state temperature at these axial locations to be much higher than transient values reported in Figure 4.5. This trend is also observed in the simulation data of TDCAS.

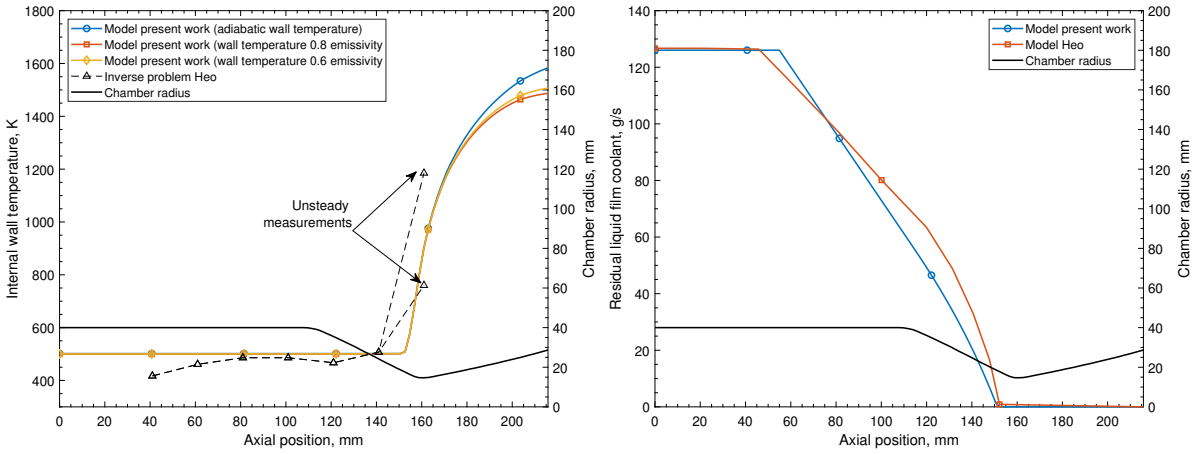

Figure 4.6: Comparison of film cooling measurements with simulation Heo and TDCAS for test HEO-F2 (data from ref. [52]).

In test HEO-F2, transient measurements were only recorded at the nozzle throat, as depicted in Figure 4.6 on the left. All other measurement locations reveal a steady-state temperature. At the end of the burn, the temperature at the upper side of the nozzle (T7) is increasing by 50 K/s, whereas the temperature at the lower side of the nozzle (T8) increases by approximately 29 K/s. The predicted steady-state wall temperature at the upper side of the nozzle throat is roughly 200 K higher than the transient measurements. On the contrary, the wall temperature at the lower side of the throat exceeds the predicted steady-state temperature. It is expected that this is caused by peripheral variations in the liquid film dry-out point. The film cooling theory used in TDCAS is based on the fundamental assumption that there exists a fixed dry-out point located at a certain distance downstream of the injector. The test data reveals that the transition from liquid to gaseous film cooling is better treated as a dry-out zone, as illustrated in Figure 4.7. Axial variation in the liquid dry-out point are also visible in film cooling simulations in ref. [104]. It is unclear if such variations in the liquid film dry-out zone are also observed in the MMH film-cooled thrusters of Preclik et al. [44], which were introduced in section 2.5.

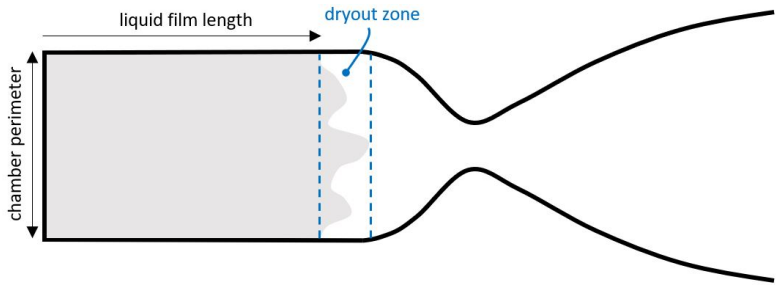

Figure 4.7: Schematic representation of liquid film distribution over perimeter of wall.

Several parameters could impact the large peripheral changes in liquid dry-out location, such as:

- **Tolerances in the film cooling injector**. Simulations in TDCAS are based on the assumption that the discharge behavior of each film cooling injector orifice is constant. In reality, due to manufacturing tolerances, small variations may exist. This can locally increase or decrease the film flow rate, thereby resulting in an uneven distribution of the film layer over the wall of the thrust chamber.
- **2-D heat transfer effects**. Simulations in TDCAS are based on the fact that each kerosene or hydrogen peroxide injector orifice/element has identical discharge characteristics and that the gas composition only varies in the axial direction. In reality, radial and peripheral changes in the hot gas composition and temperature may be present. These could be introduced by the injection pattern, as shown in ref. [105], and result in an uneven film heating.
- **Imperfections in the thrust chamber**. Local imperfections in the interior surface of the thrust chamber could potentially cause the liquid film to break up faster. These imperfections can be interpreted as physical damages (scratches), but also peripheral variations in the surface roughness.
- **Gravity**. The experiments of both Heo and Kwak are conducted with a horizontally placed thrust chamber. Therefore, gravity could potentially impact the distribution film layer.

The first two hypotheses are expected to be the most probable causes for the uneven film distribution. The impact of these peripheral variations in liquid dry-out points seems to become more relevant when the dry-out point approaches the nozzle throat, as depicted in Figure 4.8. This plot shows the data of test HEO-F3 compared to the modeling approach of Heo and TDCAS. Interestingly, both simulations predict that the liquid film extends beyond the throat, which can be concluded from the nonzero residual liquid film coolant at the throat. This is in line with temperature readouts at the upper side of the nozzle throat (T7). Nevertheless, a considerably higher temperature is measured at the lower side of the nozzle throat (T8), which has not reached a steady-state at the end of the burn. Since this temperature is far above the saturation temperature of hydrogen peroxide, it is reasonable to assume that the film at the lower side of the nozzle throat is in the gaseous phase.

It is important to note that the hot-fire tests of Heo only represent a small dataset in which the different film cooling operating points are only investigated once. Hence, it is hard to assess if the test results are repeatable. The predicted wall temperature with the liquid film cooling model provides an overall good agreement with observations during hot-fire tests. Even though the predicted steady-state temperatures in the gaseous film cooling regime cannot be validated with the (transient) experimental data set, the trends observed tend to agree well. Not only with the hydrogen peroxide film cooling experiments of Heo, but also with the MMH film cooling experiments of Preclik et al., introduced in section 2.5. Based on the simulation set-up in TDCAS, a liquid film effectiveness of 0.46 provides a fair agreement with measurements of Heo at the upper side of the chamber. At the lower side of the chamber, the dry-out point tends to be located slightly more upstream. This location can, however, not be estimated, since only one temperature readout is available at the lower side of the chamber (at the throat). In this investigation, the constant of 0.46 is used throughout the remainder of this report. The uncertainty of this parameter on the design of the Mk-II thruster is evaluated in a sensitivity analysis, discussed in subsection 5.3.3.

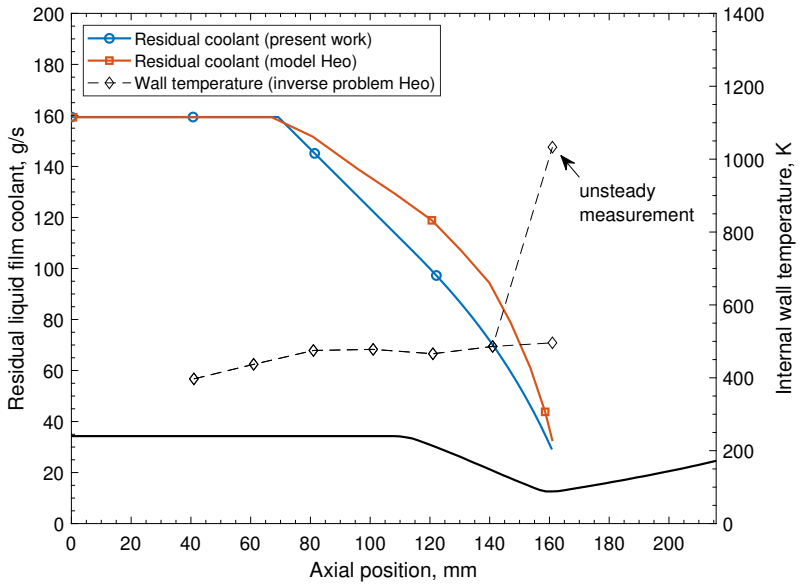

Figure 4.8: Comparison of film cooling measurements with simulation Heo and TDCAS for test HEO-F3 (data from ref. [52]).

Several uncertainties are still present, such as the impact of the chamber pressure on the liquid film effectiveness. This is especially relevant since the Mk-II thruster operates at much higher pressures than the research thruster of Heo. At these higher pressures, the hydrogen peroxide saturation temperature is also higher, whereas the enthalpy change of vaporization is lower. Moreover, the hot gas heat transfer coefficient is higher, whereas the chamber surface area that has to be covered with the film coolant is smaller[2]. In addition, the rate at which the hydrogen peroxide film coolant decomposes may also be impacted by the pressure. To quantitatively assess the impact of chamber pressure, more hot-fire tests are required. These tests will be performed as a part of the FLPP project, around the fall/winter of 2021.

Validation of the Film Cooling Performance Model

In section 2.5, it was mentioned that the characteristic velocity efficiency typically reduces under the presence of a film coolant. Besides, it was assumed that the impact of the film coolant on the thrust coefficient is very small. Kwak performed three tests in which the thrust is recorded:

- **KWAK-R1**, with no film cooling, where a thrust force of 522.1 N is recorded. This corresponds to a thrust coefficient of 1.29 and an efficiency (η_F) of 0.934, based on ideal sea level values at the operating pressure and mixture ratio.
- **KWAK-F2**, with 18% film cooling, where a thrust force of 595.2 N is recorded. This corresponds to a thrust coefficient of 1.30 and an efficiency (η_F) of 0.920, based on ideal sea level values at the operating pressure and mixture ratio.
- **KWAK-F3**, with 16% film cooling, where a thrust force of 591.6 N is recorded. This corresponds to a thrust coefficient of 1.31 and an efficiency (η_F) of 0.926, based on ideal sea level values at the operating pressure and mixture ratio.

From these measurements, one can observe that the impact of the film cooling on the thrust coefficient is indeed small. It is, however, recommended to conduct more tests over a wider range of film cooling flow rates, to get a better insight into the potential reduction of the thrust coefficient as a consequence of film cooling. In retrospect, a large data set is available from measurements of Heo and Kwak regarding the characteristic velocity losses. This data set is listed in Table 4.4 and compared to the film cooling performance model that was introduced in subsection 2.2.4.

[2]Recall that, at a constant characteristic length, a higher chamber pressure results in a smaller chamber volume required.

Table 4.4: Comparison of predicted characteristic velocity to measurements in hydrogen peroxide film-cooled thrusters (measurements from refs. [55, 62]).

measurements					**model equations 2.20-2.21**				
Test ID	ω	MR	c^*, m/s	η_c	MR_g	c^*_{cf}, m/s	c^*_g, m/s	c^*, m/s	deviation
KWAK-R1	0.00	7.15	1437.6	0.900	7.15	935.2	1597.3	1439.1	+0.10%
KWAK-R2	0.00	7.12	1450.4	0.908	7.12	935.2	1597.1	1438.9	-0.79%
KWAK-R3	0.00	7.11	1428.9	0.895	7.11	935.2	1597.1	1438.9	+0.70%
KWAK-F1	0.20	9.52	1350.7	0.872	7.45	935.2	1598.2	1340.7	-0.74%
KWAK-F2	0.18	9.17	1349.1	0.864	7.29	935.2	1598.0	1346.6	-0.18%
KWAK-F3	0.16	8.83	1382.3	0.879	7.25	935.2	1597.8	1358.2	-1.74%
KWAK-F4	0.18	9.23	1367.5	0.877	7.38	935.2	1598.2	1348.2	-1.42%
KWAK-F5	0.20	9.51	1325.3	0.855	7.38	935.2	1598.2	1337.7	+0.93%
KWAK-F6	0.21	9.49	1310.4	0.845	7.31	935.2	1598.0	1334.8	+1.86%
KWAK-F7	0.17	9.15	1359.4	0.870	7.41	935.2	1598.2	1353.4	-0.44%
KWAK-F8	0.21	9.50	1330.2	0.858	7.31	935.2	1598.0	1334.4	+0.32%
HEO-R1	0.00	7.27	1450.7	0.908	7.27	935.2	1597.9	1450.7	+0.00%
HEO-F1	0.12	7.24	1389.3	0.870	6.27	935.2	1584.1	1379.1	-0.74%
HEO-F2	0.15	7.01	1358.4	0.851	5.77	935.2	1570.9	1350.3	-0.60%
HEO-F3	0.20	7.26	1309.9	0.820	5.65	935.2	1567.2	1327.4	+1.34%
HEO-F4	0.23	7.35	1267.3	0.793	5.47	935.2	1561.4	1308.8	+3.27%

In the model, a value for η_c of 0.901 taken for data of Kwak (average of KWAK-R1, KWAK-R2, and KWAK-R3). For the data of Heo et al., a value of 0.908 is used for η_c (corresponding to HEO-R1). All values of η_c are based on predictions in NASA CEA assuming shifting equilibrium flow conditions.

In Table 4.4, ω indicates the film fraction, MR the *total* mixture ratio, MR_g the *core* mixture ratio, c^* the total characteristic velocity, c^*_g the core characteristic velocity, and c_{fg} the film coolant characteristic velocity. The results of this validation activity demonstrate a generally good agreement between the proposed film cooling efficiency model and experimental data. At film fractions (ω) less than 0.20, the model tends to underpredict the delivered performance. This could be caused by the mixing of the oxygen-rich gaseous film layer with the core flow.

For film flow rates greater than or equal to 0.20, the model tends to overpredict the delivered performance. In practice, these film flow fractions correspond to hot-fire tests with a film dry-out in the vicinity of the nozzle throat. This suggests that higher losses in characteristic velocity can be expected when the liquid dry-out zone is located at, or downstream of, the throat. A potential cause for this is provided by Preclik et al. [44], who mention that a dry-out point downstream of the throat could result in non-vaporized film coolant droplets in the divergent section of the nozzle. The non-vaporized droplets have a much lower temperature and therefore provide a lower contribution to the characteristic velocity than droplets that are fully vaporized.

4.3. Regenerative Cooling Experiments of the Mk-II Thruster

The second validation activity considered consists of a comparison of simulation results in TDCAS with hot-fire tests of the current configuration of the Mk-II engine. This comparison is used to get an insight into the accuracy of prediction for the regenerative cooling analysis in TDCAS. The outline of this section is similar to that of the previous section and consists of an explanation of the test setup (subsection 4.3.1), an explanation of typical test results (subsection 4.3.2), and a discussion of the results with comparison to the proposed model (subsection 4.3.3).

The design and test results of the Mk-II engine are the intellectual property of Dawn Aerospace. As a result, the exact geometry and design specifications of the thruster cannot be shared. Therefore, all test results that are included in this section are normalized. This way, the reader is still able to detect important trends without disclosing the actual engine design and test data.

4.3.1. Experimental Setup

All hot-fire tests of the Mk-II bipropellant engine are conducted at the test facility of Dawn Aerospace in Christchurch, New Zealand. The full test setup, consisting of the propellant tanks, feed system, and thrust frame are mounted on a car trailer. The thrust chamber assembly, consisting of the catalytic reactor, injector, and thrust chamber, is attached to the thrust frame under an angle of 45°, as shown in Figure 4.9. This angle is selected so that the propellants would naturally drain out in case the hydrogen peroxide or kerosene are leaking into the chamber. For the FLPP hot-fire tests that will be conducted in fall/winter 2021, a horizontal mounting with integrated load cells is used. This way, the thrust force can be measured, something which is not done in the current test campaign of the Mk-II thruster. The catalytic reactor is placed upstream of the injector and has the purpose of decomposing the hydrogen peroxide in oxygen and steam. These hot decomposition products have a temperature of approximately 1019 K and are injected into the thrust chamber, where they react with the kerosene.

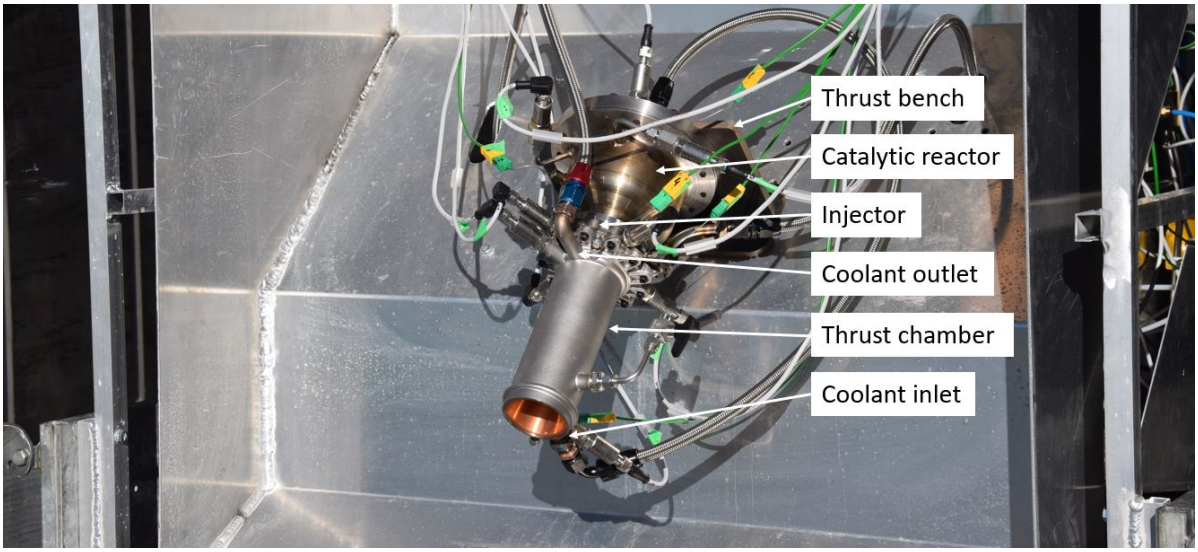

Figure 4.9: Static test bench of Dawn Aerospace with instrumented thrust chamber assembly.

In all hot-fire tests that are considered in this thesis, the Mk-II thruster is operated in a pressure-fed configuration, as depicted in Figure 4.10 on the left. Pressurization is achieved with industrial-grade nitrogen that is fed directly from the gas cylinders. The high pressure (>10 MPa) feed system for the kerosene and hydrogen peroxide is physically separated, to avoid a potential contact of the propellants upstream of the thrust chamber. A third nitrogen cylinder, operated at low pressure, is used to purge the feed system and thrust chamber post-fire. It is important to mention that Figure 4.10 only gives a high-level system architecture. Other fluidic components, such as check valves, burst disks, dump valves, and bleed valves are not included in the illustration but are present in the real Mk-II feed system. Besides, all pipe branches that can result in enclosed volumes, for instance between two pneumatic actuated valves, are equipped with manual fill/drain valves. This is an important safety feature, which is not indicated in the high-level architecture.

In the hot-fire tests of the Mk-II thruster, the pressures, temperatures, and mass flow rates are measured. This is done with pressure transducers, K-type thermocouples, and turbine flow meters. The pressure transducers and turbine flow meters are sampled at a frequency of 6.25 kHz using a National Instruments CompactRIO. All thermocouples are sampled at a frequency of 100 Hz. The thermocouples and pressure transducers are placed at the inlet and outlet manifold of the cooling jacket. Other locations where pressure is recorded include the propellant tanks, the catalytic reactor, the injector manifold, and the combustion chamber.

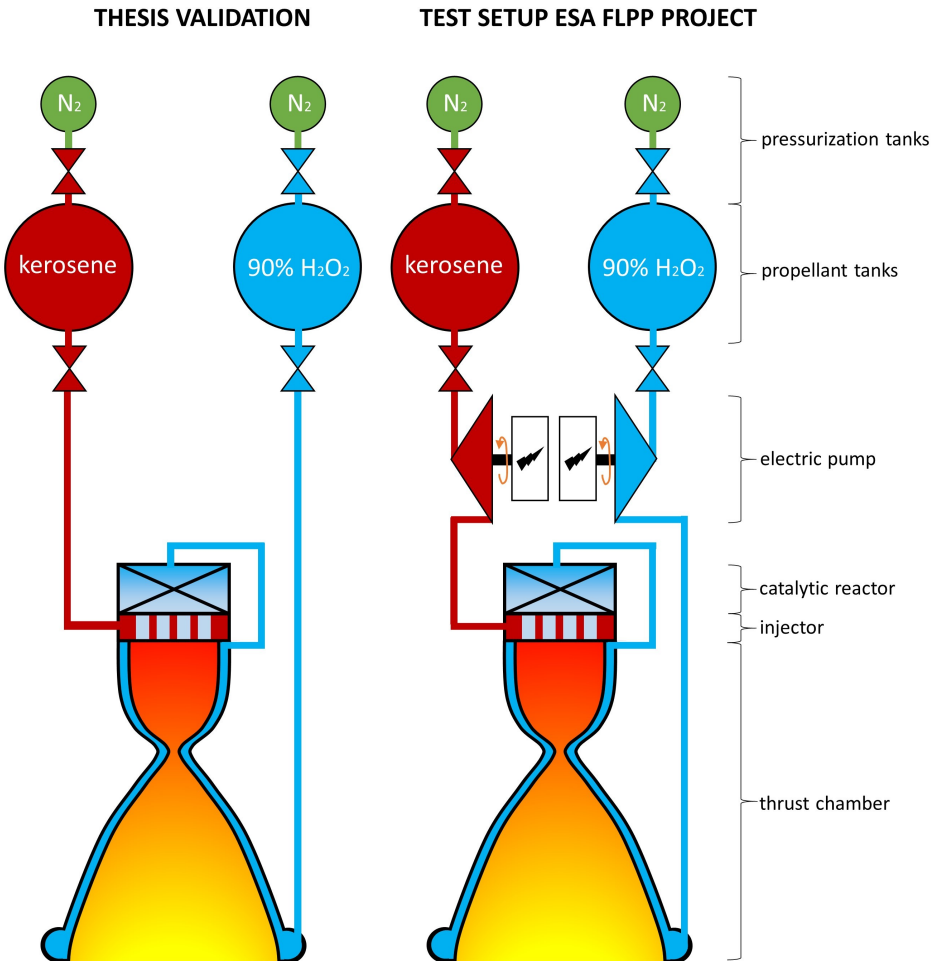

Figure 4.10: High-level pressure-fed and pump-fed feed system architecture of the Mk-II engine that are used in thesis validation experiments (left) in future ESA FLPP experiments (right).

A detailed overview of all recent bipropellant hot-fire tests of the Mk-II thruster is shown in Table 4.5. This table lists the test ID, the film flow fraction (ω), the target mixture ratio (MR), the normalized target chamber pressure (p_o), and the test conditions. In all experiments, except MKII-19, regenerative cooling is realized with 88% hydrogen peroxide. This concentration is assessed before the tests and based on a density-based approach. More information about this technique is provided in section 4.4. Tests MKII-20, MKII-21, MKII-24, MKII-26, MKII-27, MKII-29, and MKII-30 are not included in Table 4.5, because these experiments feature operation of the thruster in monopropellant mode. This implies that the kerosene is not injected into the thrust chamber, or failed to ignite. As a result, the temperature of the gas in the combustion chamber is much lower (~1019 K versus ~2700 K). Moreover, a failure occurred in the catalytic reactor during test MKII-33, resulting in the injection of pieces of the catalyst into the thrust chamber. Due to the anomalous trends in the recorded pressure and mass flow rate, this data is discarded for the validation of TDCAS. Test MKII-28 is also discarded, because of the poor quality of the recorded mass flow rate data. The reader must bear in mind that Table 4.3 indicates the *target* operating conditions. Actual measurements may deviate from the target values, as a consequence of the pressure-fed setup (where the mass flow rates and tank pressures are non-constant).

Table 4.5: Overview of recent Mk-II engine bipropellant tests conducted with 88% hydrogen peroxide and kerosene.

Test ID	ω	MR	p_o, Pa/Pa	Test conditions
MKII-19	0.00	7.90	0.93	2 sec burn, cooling with water
MKII-22	0.00	4.40	0.91	2 sec burn
MKII-23	0.00	4.40	0.91	2 sec burn
MKII-25	0.00	5.20	0.97	2 sec burn
MKII-28	0.00	5.20	0.97	2 sec burn, poor quality data
MKII-31	0.00	5.20	0.97	2 sec burn
MKII-32	0.00	5.20	0.97	4 sec burn
MKII-33	0.00	5.40	0.94	7 sec burn, failure in catalytic reactor
MKII-34	0.00	6.00	1.00	4 sec burn

All values in this table indicate the target operating conditions.

4.3.2. Description of Experimental Data

The experimental results that are obtained during a typical hot-fire test of the Mk-II thruster are depicted in Figure 4.11. The plot on the left-hand side shows both the (normalized) coolant temperature rise and mixture ratio as a function of time. The temperature rise is based on the difference between the fluid temperature logged in the coolant inlet manifold and outlet manifold. The mixture ratio is obtained from the fuel and oxidizer mass flow rate, which are recorded with the turbine flow meters. Since the mixture ratio is nonexistent in the monopropellant mode or during the shutdown, the data is trimmed for the bipropellant combustion mode. This trimming is based on the opening and closing sequence of the main kerosene valve, which marks the start and end of the bipropellant combustion mode.

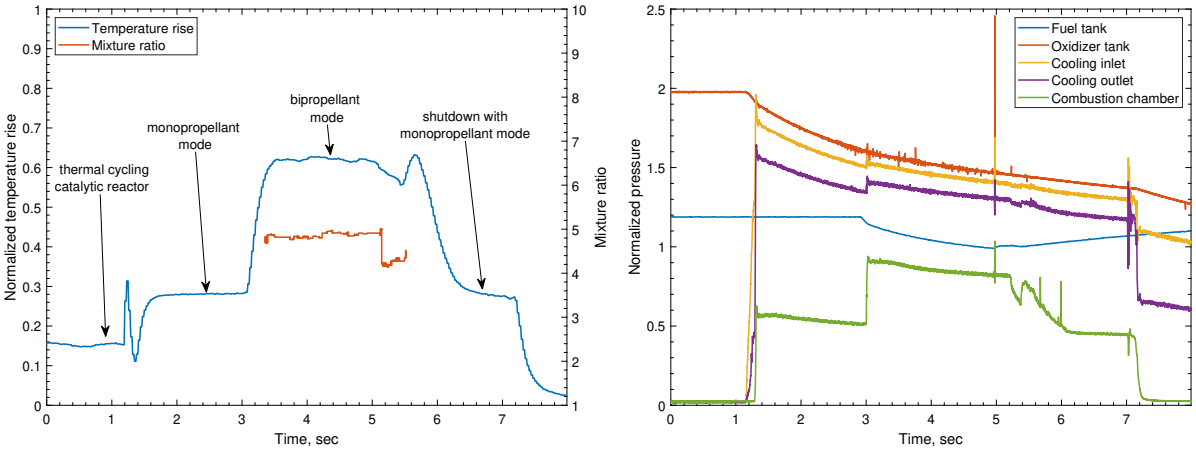

Figure 4.11: Normalized experimental data for Mk-II engine test 31.

In both plots that are shown in Figure 4.11, the reader can clearly distinguish the typical operating envelope of the Mk-II thruster. Before each test, the catalytic reactor is thermally cycled. During this cycling process, the reactor is repeatedly loaded with small amounts of hydrogen peroxide which, upon decomposition, increases the temperature of the catalyst[3]. This is done to get a clean and responsive startup of the engine. Hereafter, between one and three seconds, the engine is operated in monopropellant mode. During this phase, the main kerosene valve remains closed, which explains the constant fuel tank pressure in this phase. Once stable operation in the monopropellant mode is achieved, the kerosene fuel valve is opened. This initiates the bipropellant mode (upon ignition of the kerosene). The transition from monopropellant to bipropellant mode is characterized by a steep increase in the chamber pressure and coolant outlet temperature. In all tests considered in this thesis, the bipropellant mode lasts approximately two to seven seconds.

[3]Alternatively, one may use a heater. Heaters are often used in catalytic reactors when the catalyst has a poor performance, or when the hydrogen peroxide is very cold. In the Mk-II thruster, the hydrogen peroxide quality is sufficient to drive the reaction with the catalyst alone. Furthermore, the addition of a heater would increase the complexity and part-count of the assembly. Therefore, thermal cycling is used.

One may observe that the chamber pressure drops slightly during the burn. This is a direct consequence of the reduction in storage tank pressure. Since flow rates are a function of the storage tank pressure in a pressure-fed system, both the kerosene and hydrogen peroxide flow rates decrease during the burn. Therefore, the Mk-II thruster never runs in a “perfect” steady-state condition. Nevertheless, one can conclude from Figure 4.11 on the left that the impact of this phenomena on coolant temperature is small at short burn times. For the qualification of the current Mk-II configuration, long duration tests (in the order of minutes) are planned for the summer of 2021. In these tests, a propellant pump will be used, as depicted in Figure 4.10 on the right.

Test results for all other bipropellant tests of the Mk-II are depicted in Figure 4.13. The time axis used in these plots is set to zero at the start of the bipropellant mode and is therefore different from the (arbitrary) time axis that is used in Figure 4.11. Notice that this illustration is based on the integrated heat that is transferred to the coolant (Q), which follows from Equation 4.1.

$$Q = \dot{m} \int_{T_{in}}^{T_{out}} c_p \, dT \approx \dot{m} \bar{c}_p (T_{out} - T_{in}) \tag{4.1}$$

In this expression, $\dot{m}$ denotes the measured hydrogen peroxide mass flow rate, and $(T_{out} - T_{in})$ the measured hydrogen peroxide temperature increment over the cooling passages. For simplicity, the heat capacity ($\bar{c}_p$) is based on the average coolant temperature, between the inlet and outlet manifold. In Figure 4.13, the reader can observe a reasonably constant mixture ratio and decreasing chamber pressure for all conducted tests. Most heat load curves in Figure 4.13 on the top show a constant or decreasing trend. This follows directly from the decrease in chamber pressure (recall that the hot gas heat load is proportional to $p_o^{0.8}$, where p_o indicates the chamber pressure). For test MKII-34, a moderate increase in the heat load can be observed. It is expected that this is caused by the increase in mixture ratio, from 7 at the start of the burn to 7.6 at the end of the burn. This increase in mixture ratio is accompanied by an increase in gas temperature.

A picture of the exhaust plume during one of the hot-fire tests of the Mk-II is presented in Figure 4.12. Visual inspection reveals that the flame is more translucent and much less bright compared to the film-cooled thruster of Heo, shown in Figure 4.3. Moreover, one can also clearly see the presence of shock diamonds in the exhaust plume. The presence of these shock diamonds confirms that the flow, which is leaving the nozzle, is indeed supersonic.

Figure 4.12: Hot-fire test of the Mk-II thruster at the test facility in New Zealand.

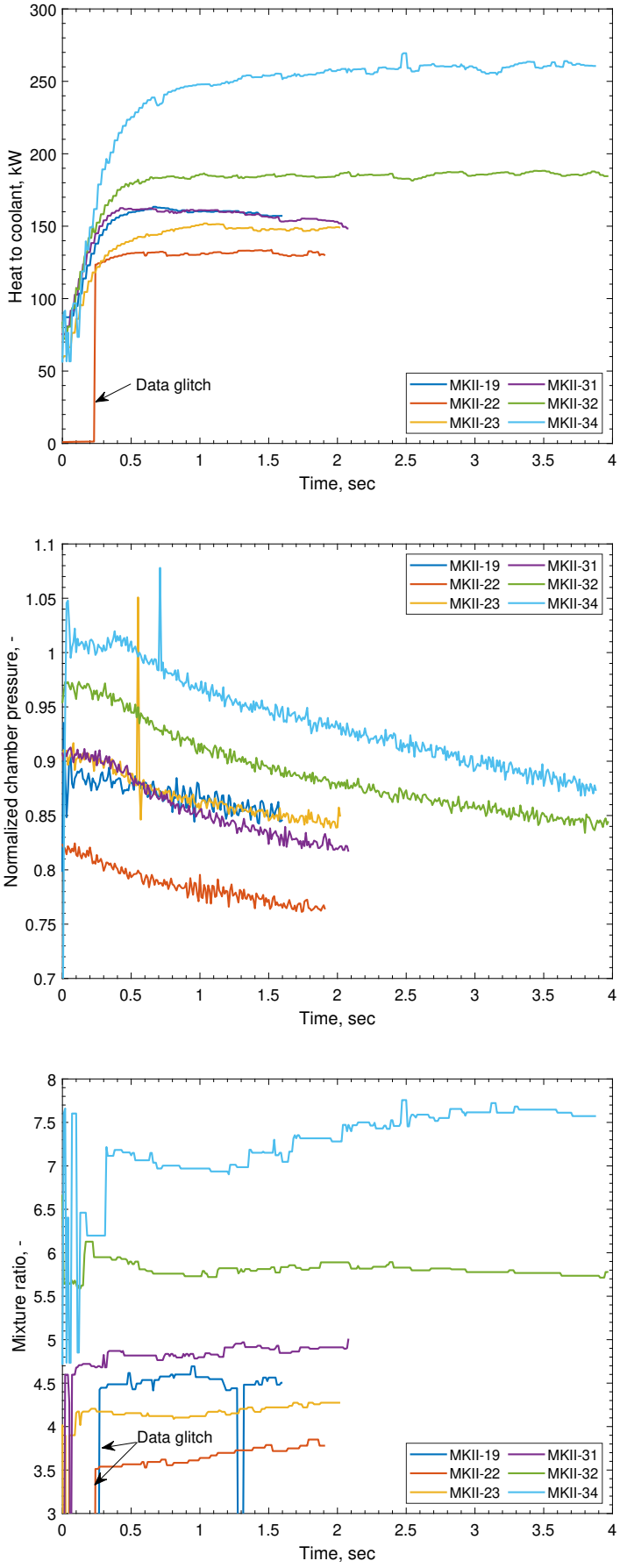

Figure 4.13: Integrated coolant heat load, chamber pressure, and mixture ratio for Mk-II bipropellant engine tests.

As a final step in the discussion of the test data, the characteristic velocity efficiency is determined. The experimental characteristic velocity is obtained using Equation 2.10, which was discussed earlier in this report. Chamber pressure and mass flow rate are measured, whereas the geometrical throat area is known from the design and assumed to be constant. Using this approach, the characteristic velocity at several time steps (0.5 seconds) of the conducted tests is depicted in Figure 4.14. Also indicated in this figure is the theoretical characteristic velocity, which is obtained from an analysis in CEA assuming shifting equilibrium flow. The results indicate that the measured characteristic velocity is slightly less than the ideal value. On average, a characteristic velocity efficiency of 99% is found to best fit the data.

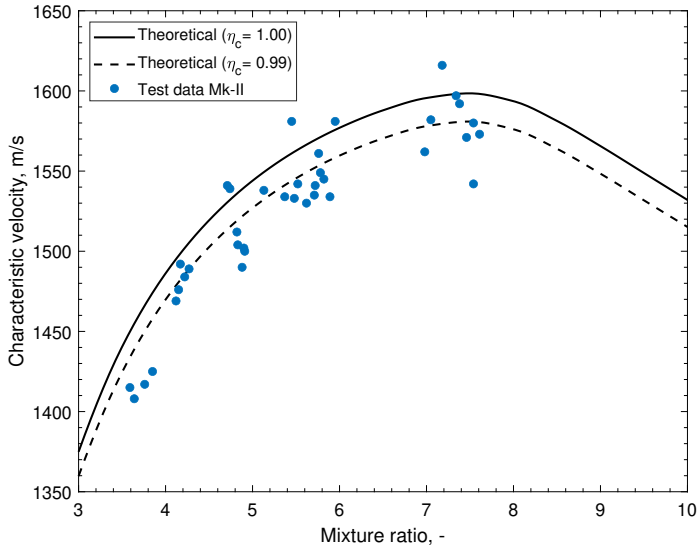

Figure 4.14: Theoretical and experimental characteristic velocity efficiency of the Mk-II thruster.

Since thrust is not measured in the current test configuration of the Mk-II, it is not possible to assess the quality factor for the thrust coefficient. If the thrust force was measured, the thrust coefficient could be obtained conform Equation 2.18. In the present work, a constant value of 96% is assumed, which is the average of typical values reported by Huzel and Huang [7] for liquid rocket engines. Consequently, the total specific impulse efficiency of the thruster, which is the product of the characteristic velocity and thrust coefficient quality factors, is taken as 99% $\times$ 96% = 95%. This value will be used throughout the remainder of this report.

4.3.3. Comparison Experiments to Model

Before analyzing the data for the Mk-II during hot-fire tests, measurements obtained during hydraulic characterization tests are considered. In these experiments, water is discharged through the regenerative cooling channels, whilst sampling the cooling jacket inlet pressure, outlet pressure, and mass flow rate. The hydraulic characterization tests can be used to estimate the equivalent sand grain roughness of the cooling passages, which is used to determine the frictional losses (Equation 2.37). Since there is no chemical reaction ongoing in the combustion chamber, it is reasonable to assume that the temperature rise of the water is negligible. Although friction losses in the cooling channel could also be estimated from hot-fire test data, this is much less straightforward since the coolant temperature, and therefore also transport properties, show a decent level of variation in these tests.

The experimental results of two hydraulic characterization tests in the Mk-II engine are presented in Figure 4.15. Also included in this illustration is the simulated pressure drop for different values for the equivalent sand grain roughness. These results are obtained from a batch analysis in TDCAS, where the coolant mass flow rate is incremented in steps of 0.1 kg/s and roughness in steps of 2 µm. One may observe that a good agreement exists for an equivalent sand grain roughness of 6 µm. It is interesting to note that this is in line with typical roughness values in machined cooling channels documented in ref. [36]. When comparing these new results with typical values in additively manufactured channels (Table 2.2), one can observe an almost 18 times lower surface roughness.

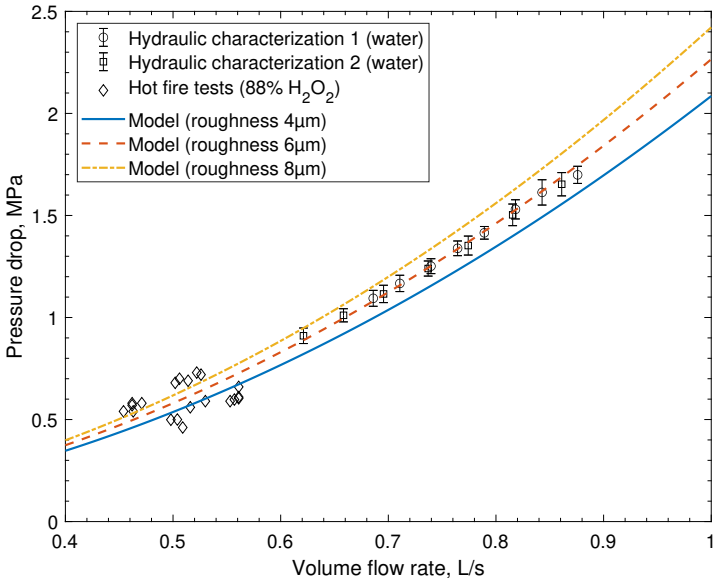

Figure 4.15: Measured pressure drop in coolant passages during water flow tests of the Mk-II, compared to simulations.

After *calibration* of the equivalent sand grain roughness based on hydraulic characterization tests with water, the pressure drop model can be *validated* against hot-fire tests of the Mk-II thruster. Data points taken from hot-fire tests are indicated in Figure 4.15 with the diamond markers. In these tests, the reference fluid is (heated) 88% hydrogen peroxide. The volumetric flow rate is obtained by dividing the measured mass flow rate by the density of 88% hydrogen peroxide at the average coolant temperature. Bear in mind that the density of hydrogen peroxide is roughly 1.4 times higher than that of water, which explains the lower volumetric flow rates. Overall, these measurements agree well with the data from the hydraulic characterization tests and only show minor deviations. There are several factors that could contribute to these deviations, such as:

- **Uncertainty in the fluid properties** of 88% hydrogen peroxide. Recall that the pressure drop is impacted by the density and viscosity of the fluid. Both these parameters are function of temperature *and* pressure. Provided the absence of this data in the open literature, only a temperature-dependency is considered for density and viscosity in this work. This may introduce errors, especially when the fluid is operated at high pressures (~8-10 MPa).
- **Thermal expansion of the liner** during the burn. During hot-fire tests, the copper alloy liner is operated far above room temperature. As a result, the liner expands. This could alter the cross-section area of the cooling channels. In TDCAS, variations in the cooling passage cross-section area during hot-fire tests are not taken into account.
- **Partial decomposition of the hydrogen peroxide** in the cooling channels. The gas that is evolved during this process may slightly increase the local coolant pressure. As a result, the overall pressure drop is less than the predictions of TDCAS. This may explain the data points below the 6 µm curve in Figure 4.15. A more elaborate discussion concerning partial decomposition in the cooling channels is provided later in this section.

In addition to the aforementioned parameters, uncertainties in the test measurements could also have contributed to the small deviations in Figure 4.15. Nonetheless, these are expected to be consistent for all data points, since the same measurement equipment is used.

Validation of the Coolant Heat Transfer

Based on the roughness of 6 µm, simulations of the Mk-II engine in TDCAS are carried out. In these simulations, the temperature-dependent thermal conductivity of the copper alloy liner is used. The reader may assume that the liner has thermal properties that are comparable to NARloy-Z, a copper

alloy that was used in the Space Shuttle Main Engine [34]. As mentioned in the introduction of this report, the cooling channels in the Mk-II thruster are plated with a proprietary metal alloy. This is done to avoid direct contact of the copper alloy with the hydrogen peroxide. Compared to the thickness of the thrust chamber wall (>1 mm), the thickness of the plating is very small (≪10 microns). Consequently, for ease of simulation, the impact of this plating is neglected in the simulations.

All simulations in TDCAS are set up with a mesh refinement depth of 1 and an axial spacing of 2 mm. The following empirical correlations for the hot gas and coolant boundary conditions are investigated:

- **B-MN:** Bartz correlation for hot gas convection (Equation 2.28) with modified Nunner correlation for coolant convection (Equation 2.35).
- **B-MN-R:** Bartz correlation for hot gas convection, with modified Nunner correlation for coolant convection and hot gas radiation model of Kirchberger (Equations 2.33 and 2.32).
- **B-DS-R:** Bartz correlation for hot gas convection, with Dipprey-Sabersky correlation for coolant convection (Equation 2.38) and hot gas radiation model of Kirchberger.
- **C-MN:** Cinjarew correlation for hot gas convection (Equation 2.30), with modified Nunner correlation for coolant convection.
- **C-MN-R:** Cinjarew correlation for hot gas convection, with modified Nunner correlation for coolant convection and hot gas radiation model of Kirchberger.
- **C-DS-R:** Cinjarew correlation for hot gas convection, with Dipprey-Sabersky correlation for coolant convection and hot gas radiation model of Kirchberger.

In all simulations, the measured chamber pressure, oxidizer mass flow rate, fuel mass flow rate, coolant inlet pressure, and coolant inlet temperature are inserted in TDCAS. These operating conditions are partially taken from the disclosed test data in Figure 4.13 in steps of 0.5 seconds, starting at a time of 1.0 second. This starting time is based on the observed transients in the integrated heat to the coolant at the start of the bipropellant mode. The simulation of the thruster at different time steps ensures that the decrease of coolant mass flow rate and the chamber pressure are captured in the validation. Alternatively, one could rely on a full transient heat transfer solver. This is, however, not (yet) possible with TDCAS.

Table 4.6: Comparison of the experimental coolant integrated heat load to predictions TDCAS.

Test ID	t, sec	p_o, -	MR, -	B-MN	B-MN-R	B-DS-R	C-MN	C-MN-R	C-MN-R
MKII-19	1.00	0.87	4.57	+1.0%	+4.4%	+6.3%	-23.0%	-19.6%	-18.0%
	1.50	0.85	4.56	+1.3%	+4.8%	+6.7%	-21.2%	-17.8%	-16.1%
MKII-22	1.00	0.80	3.64	-2.4%	-0.2%	+1.4%	-7.0%	-5.3%	-3.1%
	1.50	0.77	3.79	-3.4%	-0.9%	+0.6%	-13.3%	-11.2%	-9.3%
MKII-23	1.00	0.85	4.12	-2.7%	+0.1%	+1.8%	-18.1%	-15.5%	-13.8%
	1.50	0.85	4.22	+0.8%	+3.8%	+5.5%	-16.6%	-13.7%	-12.1%
MKII-31	1.00	0.85	4.80	+0.4%	+4.2%	+5.6%	-18.9%	-15.2%	-13.9%
	1.50	0.82	4.90	+1.8%	+5.8%	+7.3%	-16.8%	-12.9%	-11.5%
	2.00	0.82	4.91	+3.8%	+8.0%	+9.4%	-15.6%	-11.6%	-10.2%
MKII-32	1.00	0.91	5.73	-0.3%	+4.4%	+5.9%	-19.5%	-14.9%	-13.5%
	1.50	0.89	5.81	-0.7%	+4.1%	+5.5%	-19.6%	-14.9%	-13.5%
	2.00	0.88	5.89	-1.0%	+3.9%	+5.4%	-19.9%	-15.1%	-13.8%
	2.50	0.87	5.83	-0.9%	+3.9%	+5.3%	-20.6%	-15.9%	-14.6%
	3.00	0.86	5.78	-3.8%	+0.9%	+2.3%	-22.7%	-18.1%	-16.9%
	3.50	0.85	5.77	-6.1%	-1.5%	-0.2%	-24.6%	-20.1%	-18.9%
MKII-34	1.00	0.97	6.97	-16.3%	-11.6%	-10.4%	-33.0%	-28.4%	-27.2%
	1.50	0.95	7.15	-19.1%	-14.5%	-13.3%	-35.2%	-30.7%	-29.6%
	2.00	0.93	7.28	-21.0%	-16.4%	-15.3%	-37.2%	-32.7%	-31.6%
	2.50	0.92	7.76	-25.3%	-20.8%	-19.7%	-39.5%	-35.2%	-34.2%
	3.00	0.89	7.62	-24.0%	-19.4%	-18.4%	-39.5%	-35.0%	-34.0%
	3.50	0.88	7.65	-25.1%	-20.5%	-19.5%	-39.9%	-35.4%	-34.5%

One of the outputs of TDCAS, the integrated coolant heat load (Equation 4.1), is compared to measurements in Table 4.6. A "+" sign in this table represents an overprediction of the heat transfer, whereas a "-" sign corresponds to an underprediction of the heat transfer. In Table 4.6, t indicates the time stamp at which the measurement is taken (based on data in Figure 4.13), p_o the normalized chamber pressure, and MR the mixture ratio at this timestamp. The results that are listed in this table reveal an almost consistent underprediction of the heat load when using the correlation of Cinjarew. This underprediction originates from the lower heat transfer coefficient predicted using this empirical convection model, which was also observed in verification activities described in section 3.2. Based on the experimental data at hand, it can be concluded that the hot gas convection model of Cinjarew is unsuitable for this application. The hot gas convection correlation of Bartz is in much better agreement with experimental data. For both convection models, the addition of radiative heat transfer provides a small increase in the heat transfer, as expected.

Predictions of the temperature rise using the Dipprey-Sabersky correlation and modified Nunner correlations are close, with differences less than 2 percentage point. This is an interesting observation, since earlier verification activities revealed a higher discrepancy between the two models in AM channels. The fact that differences are much smaller in the Mk-II can be traced to the fact that the surface roughness is considerably lower than the experiments in AM channels. As a result, the impact of surface roughness on heat transfer is much smaller.

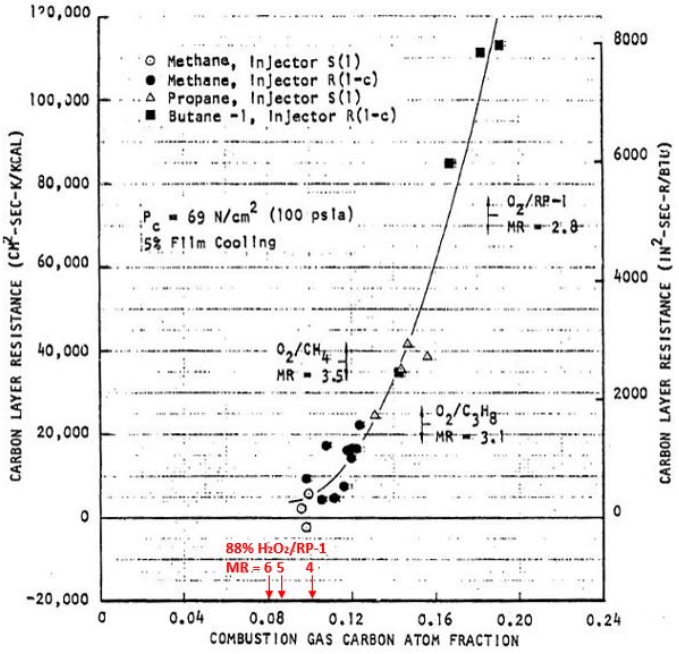

Figure 4.16: Carbon layer thermal resistance in hydrocarbon thrusters operated with film cooling, compared to the carbon atom fraction in the combustion gas of 88% hydrogen peroxide and kerosene at a mixture ratio of 4, 6 and 6 (adapted from ref. [6]).

.

It is worth noting that there are still several uncertainties in the simulation, which could explain the deviations of the model from measurements. The first potential uncertainty is the presence of carbon deposits on the chamber wall, which were observed in post-test inspections of the Mk-II thruster. The carbon layer isolates the hot gas from the wall and essentially acts as a natural thermal barrier coating. Modeling this phenomenon is complex due to its highly unsteady nature [65]. Research of Cook [6] has revealed that the thermal resistance of the carbon layer correlates well with the carbon atom fraction in the combustion gas, as well as the hot gas mass flux. Trends observed by Cook for common hydrocarbon propellant combinations are reprinted in Figure 4.16. This figure is extended with indicative values for the carbon fraction in the combustion products of 88% hydrogen peroxide and kerosene, based on an analysis in CEA. The three values for hydrogen peroxide and kerosene indicate an increasing trend in the carbon fraction with decreasing mixture ratio. Although the exact carbon layer resistance for the combustion of hydrogen peroxide with kerosene is unknown, one can observe a

lower carbon fraction compared to mixtures of oxygen and kerosene, oxygen and propane, or oxygen and methane. Based on this observation, it is reasonable to expect that this carbon layer has impacted the heat transfer in the thrust chamber at least to some extent. This could explain the overprediction of the Bartz equation with the Dipprey-Sabersky coolant model observed in tests MKII-19 and MKII-23 to MKII-32 in Table 4.6. Interestingly, test MKII-22 seems an outlier to this overpredictive trend. This test is characterized by the lowest mixture ratio (<4), thereby corresponding to very fuel-rich combustion. Although the exact reason for this discrepancy is not clear, it could be caused by errors in predictions of the hot gas properties in the CEA module which is integrated into TDCAS. An increasing deviation of CEA from experiments at low mixture ratios is also reported by Kirchberger [65] in the application of small hydrocarbon thrust chambers. According to Kirchberger, these deviations could be caused by the presence of soot, which is characterized by slow reaction kinetics. This deviation is irrelevant for the proposed AM thrust chamber, as this engine is designed to operate at much higher mixture ratios.

A second uncertainty in the simulation lies in the modeling of the heat transfer close to the propellant injector. The semi-empirical heat transfer correlations of Bartz and Cinjarew are derived for gas flow in the convergent-divergent nozzle and based on the assumption that the flow is fully developed and turbulent. In the cylindrical section of the thrust chamber, close to the injector, the hot gas flow is typically not fully developed [103]. Several studies [7, 65, 106] have indicated that heat transfer in this region is dominated by injector (spray) effects. During hot-fire tests of the Mk-II, the coolant temperature is only measured at the inlet and outlet of the cooling jacket. As a result, only the integrated heat load can be obtained, rather than the local heat load which is required to assess heat transfer close to the injector. Consequently, no quantitative conclusions can be drawn concerning the impact of the propellant injector on heat transfer in the combustion chamber.

A third uncertainty lies in the modeling of the coolant heat transfer in TDCAS. In the present work, the coolant flow is modeled based on the simplifying assumption that fluid properties only vary in the streamwise direction. This major simplification may not be able to capture thermal stratification in the channels, as well as turbulent mixing of the coolant [107], which could locally augment or alleviate the heat transfer.

The final uncertainty lies in the potential (partial) decomposition of the hydrogen peroxide in the cooling passages, which releases additional heat to the coolant flow. As a result, the measured outlet temperature is higher than the predicted results without considering decomposition. This could potentially explain the large deviation that is observed for test MKII-34 in Table 4.6. The hypothesis of hydrogen peroxide decomposition is shared by Kuntz et al. [26], who states that: “the use of 98% H_2O_2 as a regenerative coolant can be expected to result in its partial decomposition”. Although no claim is made about 90% hydrogen peroxide, similar results are expected.

The presence of partial coolant decomposition is also mentioned in the hydrogen peroxide heat transfer studies of Rousar & Van Huff [71] in electrically heated tubes. In at least thirteen samples, they observe an excess of sensible energy at the outlet of the tubes, ranging from 1.5% to 24%. Since heating of the coolant is carefully controlled and monitored, an additional heat source must be present in the system to explain this deviation. Under the assumption that the decomposition of hydrogen peroxide releases 97.9 kJ/mol, Rousar & Van Huff estimate that 0.1% to 0.6% of the hydrogen peroxide bulk flow must have decomposed to explain the excess of sensible energy. They also perform concentration measurements before and after the heating experiments, which reveal concentration reductions up to 0.89 percentage point (by weight).

Rousar & Van Huff present experimental data that relates the excess in sensible energy to the heat flux for short duration and extended duration experiments. These tests were also briefly mentioned in subsection 2.4.4 when the coolant operating limits were defined. In the present investigation, the reported energy balance is plotted against the heat-flux-to-velocity ratio, which was introduced in subsection 2.4.4. This plot, shown in Figure 4.17, reveals a decreasing trend in the energy balance with an increasing heat-flux-to-velocity ratio. In other words, the excess sensible energy at the channel outlet increases with increasing heat-flux-to-velocity ratio. Also included in this figure are the short duration ($1.29v$) and long duration ($0.86v$) heat transfer limits that were established in subsection 2.4.4. If one assumes that all excess energy is introduced by partial decomposition of the hydrogen peroxide, one may conclude that decomposition effects are primarily relevant when approaching the short duration heat transfer limit.

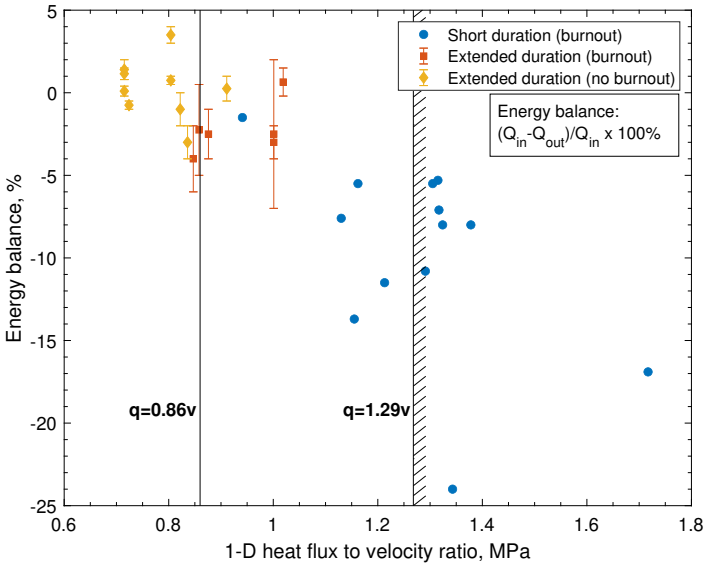

Figure 4.17: Correlation between energy balance and hot gas heat flux to coolant velocity ratio in heat transfer experiments with 98% hydrogen peroxide in Inconel 718 and AISI 347 tubes (measurements from ref. [71]).

To test the hypothesis of partial hydrogen peroxide decomposition in the cooling channels during test MKII-34, the average and peak heat-flux-to-velocity ratio are calculated, as shown in Table 4.7. The peak value is obtained at the nozzle throat, where the heat load is highest. In this table, one can observe that the calculated heat-flux-to-velocity ratio is highest in test MKII-34 and exceeds the recommended short duration limit. What is more, the maximum coolant temperature recorded during this test was much larger than the hydrogen peroxide service limit (408 K) that was established in subsection 2.4.4. In all other tests, the hydrogen peroxide bulk fluid temperature did not exceed the maximum service temperature. Despite the heat-flux-to-velocity ratio being highest in test MKII-34, differences with respect to other experiments with hydrogen peroxide as coolant are small.

Table 4.7: Calculated ratio of hot gas heat flux to coolant bulk velocity in Mk-II engine test cooled with 88% hydrogen peroxide.

Test ID	Mean q/v, MPa	Peak q/v, MPa	Peak coolant temperature
MKII-22	0.78	1.05	<408 K
MKII-23	0.81	1.08	<408 K
MKII-28	0.89	1.18	<408 K
MKII-31	0.91	1.21	<408 K
MKII-32	0.96	1.26	<408 K
MKII-34	1.02	1.32	>408 K

All simulations are based on the run case B-MN-R.

Since the hydrogen peroxide is directly injected into the catalytic reactor after leaving the cooling channels, no post-cooling concentration measurements could be taken. If these measurements were available, the potential decomposition of hydrogen peroxide in the cooling channels could be proven. An alternative method would be to conduct two hot-fire tests at an identical chamber pressure and mixture ratio. If these tests are conducted with both a stable (water) and a less stable (hydrogen peroxide) coolant, the potential impact of decomposition in the cooling passages can be estimated. These measurements were, however, not available to the author. Moreover, test MKII-34 represents only one experiment near the optimal mixture ratio. To confirm if the underpredictive trend is repeatable, more hot-fire tests are required at this mixture ratio. In Appendix A, a brief description is provided on how modeling uncertainties that were outlined in this section can be solved in future tests of the Mk-II engine as a part of the ESA FLPP project.

4.4. Inconel 718 Immersion Screening Test

An important trade criterion that was used in the literature study [4] for selecting Inconel 718 as thrust chamber material, was the expected chemical compatibility with hydrogen peroxide. In one-hour screening tests at 405 K, Kuntz et al. [26], measure a concentration change from 96.7% to 85% when Inconel 718 test articles are immersed in the hydrogen peroxide. Only signs of light bronzing were observed on the Inconel 718 test articles. It is important to note that this experiment is conducted with *mirror-polished* Inconel 718. Therefore, the surface roughness is considerably lower than AM Inconel 718.

It is generally accepted that the rate at which hydrogen peroxide decomposes is greatly impacted by the surface conditions [28]. As a result, AM Inconel 718 parts could augment the hydrogen peroxide decomposition rate. This could in term result in a reconsideration of Inconel 718 as chamber material for the AM Mk-II thruster. Since no data could be found in the open literature concerning the chemical compatibility of AM Inconel 718 (or any AM alloy in general) with hydrogen peroxide, immersion screening tests were conducted. In subsection 4.4.1, the sample preparation and test setup are briefly discussed. Hereafter, the test results are presented in subsection 4.4.2.

4.4.1. Sample Preparation and Test Description

For the immersion screening tests, as-built AM Inconel 718 test articles are used. This implies that no post-built surface finish improvements or heat treatments are applied. The test coupons are immersed in 40 mL of hydrogen peroxide with a concentration of approximately 90% by weight. The AM Inconel 718 test articles are rectangular and have a size of 20×10×3.4 mm. This volume and sample size corresponds to a surface-to-volume ratio of 0.15 cm^{-1} (0.38 in^{-1}). This particular value is chosen to have a surface-to-volume ratio similar to experiments of Kuntz [27] whilst keeping the size of the test articles and hydrogen peroxide volume small (for economic and safety reasons). Figure 4.18 shows a typical test piece that is used in the immersion screening tests. As expected, the sample is characterized by a surface of high roughness, which is a consequence of the AM production process.

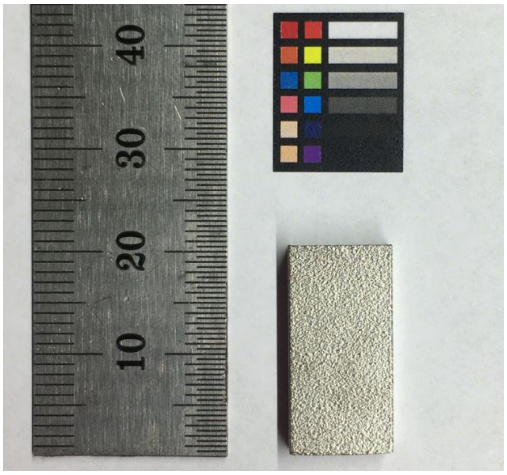

Figure 4.18: Typical AM Inconel 718 test article which is used in the immersion screening tests.

A technical grade hydrogen peroxide is obtained from a trusted industry partner at a concentration of 70% by weight. This solution already contains stabilizers that aid in improving the long-term storability. The 70% concentration is distilled in-house to approximately 90% by weight, which is used during the hot-fire tests of the Mk-II thruster and for the immersion screening tests. The exact concentration is measured before each screening test. For assay of the concentration, two techniques are used:

- **Density approach**. In this technique, exactly 100 mL of hydrogen peroxide is put in a *volumetric flask* and weighted down. The volumetric flask is calibrated for a volume of 100$\pm$0.1 mL at room temperature. One can determine this volume based on the meniscus of the fluid and a line that is placed on the neck of the flask. Based on the mass and volume of the fluid, the density can be calculated. The density is compared to values reported by Schumb et al. [54] for different concentrations and ambient temperatures. To reduce the experimental error, three independent measurements are taken.

- **Titration approach**. In this technique, a 1 mL hydrogen peroxide sample is taken from the solution. This sample is titrated with potassium permanganate ($KMnO_4$) until a pale pink color persists for fifteen seconds, as illustrated in Figure 4.19-C. The redox titration procedures are explained in detail in MIL-PRF-16005F [108] and not repeated here. To reduce the experimental error, the redox titration is repeated three times with three unique samples from the solution.

The primary advantage of the density-based approach is that it is fast in execution and requires minimal laboratory equipment. Nevertheless, large quantities of hydrogen peroxide are required. This makes the technique ideal for bulk concentration measurements. The titration approach is ideal when only small amounts of hydrogen peroxide are available, for instance, during the immersion screening tests.

Before each immersion screening test, the AM Inconel 718 articles are carefully cleaned and passivated. The procedure that is used for passivation is based on positive experience at Dawn Aerospace and recommendations of the hydrogen peroxide vendor. First, all test articles are cleaned in an ultrasonic cleaner at a temperature of 323 K. Hereafter, the test articles are rinsed with reagent water and immersed in a 30% nitric acid (HNO_3) solution. After two hours, the test articles are removed from this solution. After rinsing again with reagent water, the test articles are pat dried with a heat gun and stored in a vacuum-sealed plastic bag.

Figure 4.19: Laboratory setup used for immersion screening tests. A) Laboratory heater with boiling flask and thermometer. B) Boiling flasks with passivated and unpassivated test article immersed in hydrogen peroxide, as well as control group. C) Titration of a hydrogen peroxide sample with potassium permangenate.

In all experiments, Pyrex laboratory glassware is used, which includes a 100 ± 0.1 mL volumetric flask, a 100 ± 1 mL measuring cylinder, a 50 ± 0.1 mL burette, 250 mL Erlenmeyer flasks, 100 mL boiling flasks, and 100 mL beakers. To avoid potential contamination, all laboratory glassware is thoroughly rinsed with reagent water. Besides, all glassware in contact with hydrogen peroxide is passivated, based on the procedures described in MIL-PRF-16005F. Other relevant equipment that is used during the immersion screening tests includes two laboratory heaters (Figure 4.19-A), a 200 ± 0.01 gram pocket balance, and a thermometer. All experiments are conducted by experienced test personnel in the propellant processing facility of Dawn Aerospace in New Zealand. This facility is equipped with basic laboratory equipment, as well as a safety shower and eyewash station. For safe handling of the hydrogen peroxide, all test personnel is equipped with a face shield, apron, boots, and gloves.

During an immersion screening test, an Inconel 718 test article and 40 mL hydrogen peroxide solution are put in a 100 mL boiling flask, as depicted in Figure 4.19-B. The boiling flask is stored at a well-ventilated, dust-free place. In each immersion screening test, one control group is used. This control group comprises 40 mL hydrogen peroxide in a boiling flask, without immersion of an Inconel 718 test article. Within the scope of this thesis, the following experiments are conducted:

- **Ambient temperature, seven days**. During these tests, both passivated (IST-7 to IST-9 and unpassivated (IST-10 to IST-12) Inconel 718 test articles are immersed. Additionally, one control group is used (CON-4 to CON-6). This data corresponds to one test campaign with three experiments. All three experiments feature three titration measurements.
- **Temperature of 343 K, seven hours**. During these tests, passivated (IST-4, IST-5, IST-6) Inconel 718 test articles are submerged in the hydrogen peroxide solution. Additionally, one control group is used (CON-1, CON-2, CON-3). Both experiments are placed in a laboratory heater (Figure 4.19-A) which is set to 343 K.

After the specified immersion time, a visual inspection was performed using a microscope. Hereafter, the concentration was again assessed based on titration. One may observe that the 343 K immersion temperature is much lower than the maximum hydrogen peroxide service temperature of 408 K, established in subsection 2.4.4. The 343 K limit is internally decided based on safety concerns. Recall that all screening tests are conducted in a laboratory environment where the test operator works close to the heated hydrogen peroxide. This is vastly different from the hot-fire tests, which are conducted outside with all personnel at a much further distance.

4.4.2. Test Results and Discussion

Before starting the immersion screening tests, the concentration of the bulk hydrogen peroxide was determined. Four titration experiments were conducted following the procedures in MIL-PRF-16005F. The result shows a bulk concentration of 91.8$\pm$1.1%, 92.7$\pm$1.1%, 92.4$\pm$1.1%, and 92.4$\pm$1.1%. The titrations demonstrate good repeatability, with deviations that are within the measurement error. The average concentration of four measurements yields 92.3$\pm$1.1%. The titration results were validated against concentration measurements based on the density method. Using three independent measurements, a bulk concentration of 91.0$\pm$0.3% was obtained with the density approach. The two different concentration assessment techniques provide a seemingly close result, yet small differences exist. It is expected that the results from the density approach are most realistic. The primary argument for this is that a visual judgment of test personnel is required to determine the endpoint of the titration (pale pink color for fifteen seconds). This qualitative judgment could vary between different test personnel and can have a relevant impact on the assessed concentration. All titrations during the immersion screening tests are performed by the same test operator. Hence, it is assumed that this qualitative judgment is, at least, consistent. A better approach that eliminates this uncertainty would be to determine the endpoint quantitatively, for instance, with a potentiometer. This is a recommended upgrade for future experiments, but not considered in this work.

During the seven-day immersion screening tests, both passivated and unpassivated AM Inconel 718 were immersed in the hydrogen peroxide solution. Upon immersion of the unpassivated test pieces, small bubbles immediately appeared near the surface of the test article, as illustrated in Figure 4.20 on the right. This bubble formation did not occur at the start of the test with the passivated specimens, as shown in Figure 4.20. Nevertheless, after seven days, the bubbles were observed on the rough surface of both the passivated and unpassivated test articles. This indicates that there are probably some chemical reactions ongoing near the surface, albeit very small. No visual signs of excessive decomposition were observed during the screening tests.

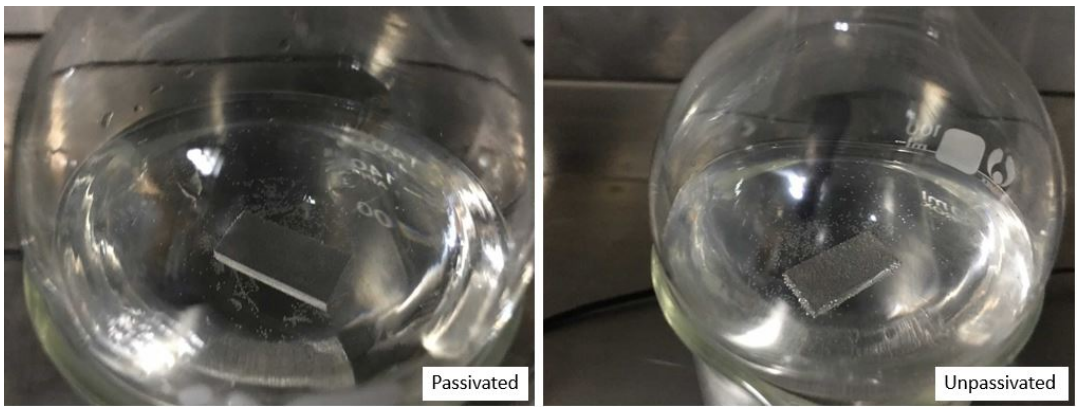

Figure 4.20: Immersion screening test of AM Inconel 718 in concentrated hydrogen peroxide at ambient temperature and pressure, showing significant bubble formation at the surface of the unpassivated specimen.

Quantitative results of the immersion screening tests at ambient temperature are listed in Table 4.8. For the passivated specimens, the average concentration post-immersion is found to be 90.6$\pm$1.1%, whereas the unpassivated specimens show an average concentration of 89.9$\pm$1.1%. The measured average concentration of the control group is slightly higher, namely 91.6$\pm$1.1%. In comparison, the average concentration pre-immersion was 92.3$\pm$1.1%. One can observe that slightly higher concentration losses occurred upon immersion of the passivated test article. This is an interesting observation

since the bubble formation on the surface occurred more rapidly with the unpassivated specimens. It must be mentioned that almost all concentration changes that are listed in Table 4.8 fall within the measurement error.

Table 4.8: Results of the immersion screening tests at ambient temperature for 7 days.

Test ID	Test article	Passivated	Final concentration	Delta concentration
IST-7	INC-6	Yes	92.1%	-0.2
IST-8	INC-6	Yes	90.0%	-2.3
IST-9	INC-6	Yes	90.9%	-1.4
IST-13	INC-11	No	91.8%	-0.5
IST-14	INC-11	No	91.7%	-0.6
IST-15	INC-11	No	92.3%	+0.0
CON-4	–	–	92.4%	+0.1
CON-5	–	–	92.7%	+0.4
CON-6	–	–	92.9%	+0.6

To investigate the impact of temperature on the rate of decomposition, seven-hour immersion screening tests at a temperature of 343 K were conducted with passivated Inconel 718 test articles. During the immersion screening tests, severe bubbling and boiling-like phenomena were observed, as depicted in Figure 4.21. This bubbling was also observed in the control group. Therefore, it is reasonable to expect that this is caused by the high temperature of the hydrogen peroxide solution. Nevertheless, no rapid (catalytic) decomposition of the hydrogen peroxide occurred. Similar to the ambient temperature tests, the bubbles formed close to the immersed test article. In the control group, the bubbles appeared evenly throughout the solution. Since the temperature is well below the boiling point of the hydrogen peroxide, it is expected that these bubbles are caused by the release of gaseous oxygen from the hydrogen peroxide.

Figure 4.21: Immersion screening test with AM Inconel 718 at 343 K, showing boiling-like phenomena.

Quantitative results of this test, listed in Table 4.9, are in line with the visual observations and highlight a significant reduction in the hydrogen peroxide concentration. On average, the concentration loss for the experiments with submerged Inconel 718 test article is 18.6$\pm$1.1 percentage point, whereas the control group shows a concentration loss of 16.6$\pm$1.1 percentage point. In both samples, some bubble formation was also observed on the surface of the immersed thermometer, which could also have contributed to the high concentration loss. The fact that both measurements are very close suggests that the majority of the decomposition is caused by the temperature, rather than the presence of the AM Inconel 718 test article. In the control group, a hydrogen peroxide mass loss of 6.63 g was observed after seven hours. On the other hand, in the sample with AM Inconel 718 immersed, a hydrogen peroxide mass loss of 7.07 g was observed after seven hours. The mass loss can be explained by gaseous oxygen which is released from the hydrogen peroxide when the fluid (partially) decomposes.

Table 4.9: Results of the immersion screening tests at 343 K for 7 hours.

Test ID	Test article	Passivated	Final concentration	Delta concentration
IST-4	INC-9	Yes	74.4%	-17.9
IST-5	INC-9	Yes	73.2%	-19.1
IST-6	INC-9	Yes	73.5%	-18.8
CON-1	—	—	76.2%	-16.2
CON-2	—	—	75.2%	-17.1
CON-3	—	—	75.8%	-16.5

After the concentration measurements, the impact of the hydrogen peroxide on the AM Inconel 718 was visually studied using a microscope with a magnification of roughly 100. After both test campaigns, no visible change had occurred to any of the passivated samples, as depicted in Figure 4.22. This observation is in line with the work of Constantine and Cain [28], who report no effect on the material after exposing non-AM Inconel X-718 to 90% hydrogen peroxide at 339 K for one day. Interestingly, Constantine and Cain observe severe bronzing on the non-AM test articles, after a seven-day exposure at the aforementioned temperature. Whether or not this is also the case for the AM test articles cannot be concluded from the test data at hand. It is, however, expected that the fluid temperature and exposure time have a relevant impact on the potential bronzing of the Inconel 718. More tests at higher temperatures are required to gain a better understanding of the potential bronzing of the test articles.

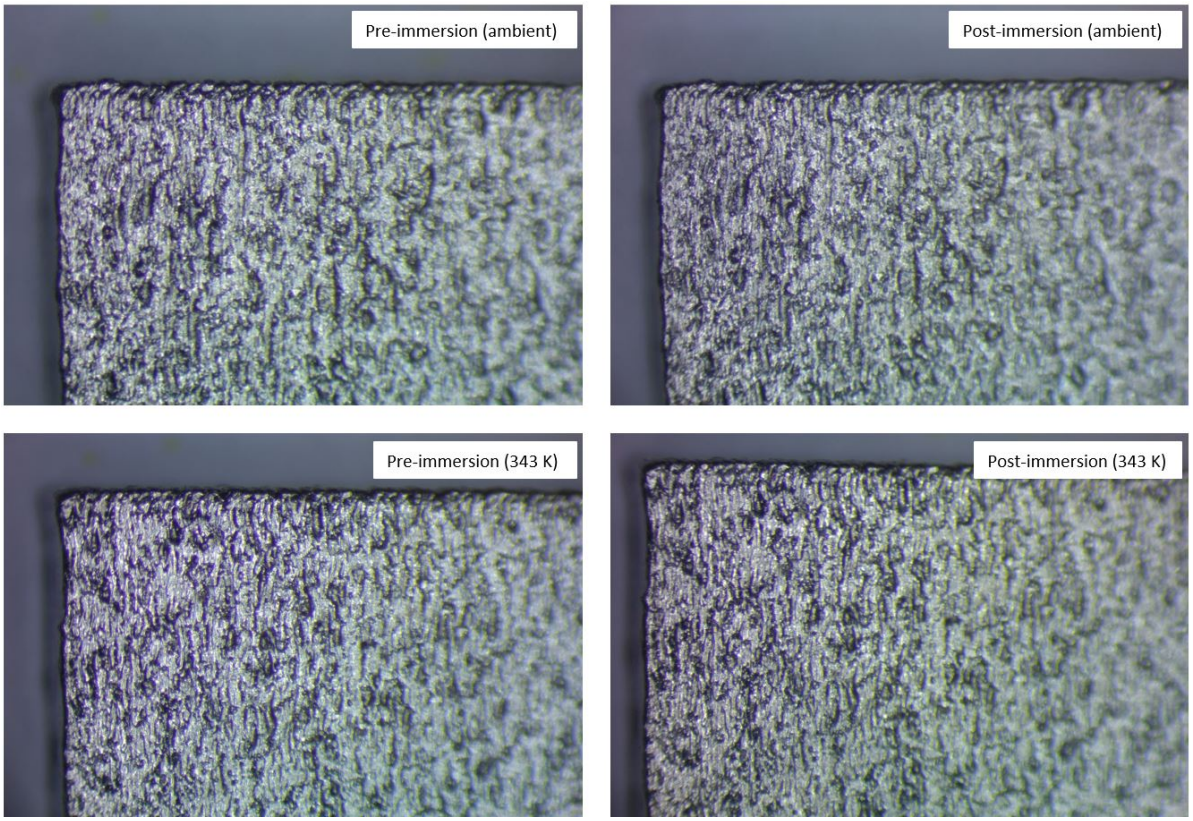

Figure 4.22: Microscope image of a passivated test article before and after immersion in hydrogen peroxide at ambient conditions and at 343 K.

To conclude, the immersion screening tests that are conducted in this study do not reveal any signs of major chemical incompatibility of AM Inconel 718 in hydrogen peroxide solutions with a concentration of ~90%. In a seven-day immersion at ambient temperature, no noticeable concentration occurred. In a seven-hour immersion at 343 K, a concentration loss of 18.6 ± 1.1 percentage point was observed for

the experiment with submerged Inconel 718 and a concentration loss of 16.6±1.1% in a control group. This suggests that the decomposition is primarily driven by the temperature, and not by the presence of the test article. The observations in this thesis with AM Inconel 718 are in line with the work of Schumb et al. [32], who state that “nickel and Inconel have very slight catalytic effect on hydrogen peroxide of all concentrations”. Nonetheless, this observation was, to the authors’ best knowledge, not yet made before in the literature for *additively manufactured* Inconel 718.

The results of the immersion screening test partially validate the selection of Inconel 718 as a material for AM thrust chamber for the ESA FLPP project. Full validation of the chemical compatibility is achieved through actual hot-fire tests, where the hydrogen peroxide is exposed to even higher temperatures and heat loads. These experiments are conducted as a part of the ESA FLPP project in fall/winter 2021.

4.5. Chapter Summary

This chapter describes all validation activities that are carried out throughout this thesis. In section 4.1, the empirical coolant heat transfer correlations were validated based on heat transfer experiments in small AM Inconel 718 channels. Of all proposed convection models, the modified Nunner and Dipprey-Sabersky correlation demonstrated the most promising correlation with test data, though large deviations are still present. More research, preferably with hydrogen peroxide, is required to fully characterize heat transfer in AM cooling passages with high surface roughness.

In section 4.2, the proposed film cooling model is compared to experimental results which are obtained in hydrogen peroxide film-cooled thrusters. The results reveal that the real liquid film cooling potential is much lower than the theoretical potential. The test results also indicate large peripheral variations in the dry-out point, which are expected to be caused by an uneven distribution of the film over the wall or circumferential variations in the core heat transfer. More research is required to quantitatively assess these effects. A comparison of the film cooling performance model demonstrates a good correlation between measured and predicted characteristic velocity.

The regenerative cooling simulations in TDCAS are validated against measurements in the bimetallic Mk-II thruster (section 4.3). The predicted pressure drop over the cooling passages is in good agreement with measurements during hydraulic characterization tests and hot-fire tests with hydrogen peroxide as coolant. Comparative heat transfer simulations show that the Bartz convection model is most suitable to predict the convective heating from the hot gas. For the coolant, both the modified Nunner correlation and Dipprey-Sabersky correlation yield similar results, with deviations less than 2 percentage point. To fully validate heat transfer effects in TDCAS, more experiments are required in which the local heat transfer effects are measured, for example near the injector.

The final validation activity involves immersion screening tests of AM Inconel 718 test articles, which are used to demonstrate the chemical compatibility (section 4.4). Results of a seven-hour test at 343 K and a seven-day test at ambient temperature show no signs of bronzing on the Inconel test articles. Besides, the impact of the Inconel 718 test articles on the hydrogen peroxide concentration appears small.

5

Model Results and Discussion

In this chapter, TDCAS is used to propose a preliminary design solution for the AM Inconel 718 thrust chamber. This preliminary design serves as the main input for the detailed design phase during the ESA FLPP project. First, the possible operating regime of the thruster is investigated in section 5.1, based on the customer requirements mentioned in the introduction of this report. Hereafter, in section 5.2, the design of a bimetallic thrust chamber, based on non-additive manufacturing techniques is discussed. This "reference" bimetallic design serves as a baseline for comparison to the proposed AM Inconel 718 solution. This is necessary for answering the primary research question: *"Is it advantageous to realize the thrust chamber of a small, hydrogen peroxide cooled, rocket engine as an integral additively manufactured structure, instead of a bimetallic structure created with traditional manufacturing methods?"*.

In its design, the reference bimetallic chamber is very similar to the real Mk-II thruster. Yet, several differences exist in the exact geometry of the chamber and operating conditions. This way, we can compare a Mk-II-like design to an AM chamber design, without disclosing the intellectual property of Dawn Aerospace. The selected bimetallic reference design is based on a NARloy-Z liner with Inconel 718 structural closeout. This material combination is selected for its excellent design heritage, for example in the Space Shuttle Main Engine [34]. Furthermore, NARloy-Z has thermal properties that are similar to the copper alloy that is used in the Mk-II thruster. The material properties that are used for NARloy-Z are taken from ref. [99].

The reference bimetallic design is followed by a description of the proposed AM Inconel 718 solution, in section 5.3. This section also includes a sensitivity study that investigates the impact of uncertainties on the design. The suggested AM chamber is compared to the reference bimetallic chamber in section 5.4. This comparison includes the impact on the pressure budget, dry mass, and estimated performance. Moreover, compliance with customer requirements is addressed in this section. Lastly, in section 5.5, the sub-questions that were posed in the introduction of this report are answered.

5.1. Design Study Guidelines

All designs that are considered in this thesis are based on a chamber diameter of 8 cm, a characteristic length of 0.6 m, a nozzle exit pressure of 65 kPa, and an 80% (Rao) bell nozzle. These particular values can be seen as constant input parameters and can loosely be traced[1] to the current Mk-II engine design. This way, the injector of the Mk-II engine can directly be integrated onto the proposed AM chamber, without introducing expensive redesigns. Furthermore, the propellant combination considered in this design study is 90% hydrogen peroxide with kerosene (RP-1). This follows directly from customer requirements REQ-005 and REQ-006. In all applications, hydrogen peroxide is used as a film and/or regenerative coolant. All simulations that are carried out in this section are based on the modified Nunner coolant convection model and Bartz correlation for the hot gas heat transfer.

[1] This implies that the values are not identical to the current Mk-II engine, but compare well. This is done to protect the intellectual property of Dawn Aerospace.

The following methodology is adopted for all chamber designs that are discussed in this chapter:

1. Select a nominal chamber pressure, mixture ratio, and coolant inlet temperature for the design.
2. Select the number of cooling channels, the wall thickness, the channel width, and the channel height at the nozzle throat. For this endeavor, a 2-D heat transfer analysis is conducted at the throat plane. The temperature results are compared to the maximum service temperature of the chamber wall, which is discussed in subsection 5.1.2.
3. Define the coolant geometry in the axial direction, by iterating against the hydrogen peroxide burnout heat flux and maximum service temperature of the wall. For simplicity, only the channel width is allowed to change in the axial direction, whereas channel height, wall thickness, and channel count are held constant.
4. Verify the acquired solution against the maximum pressure drop over the cooling channels (subsection 5.1.1), the maximum service temperature of the hydrogen peroxide (subsection 5.1.2), and the manufacturing constraints (subsection 5.1.3).

It is noted that the above-mentioned steps represent an iterative loop. If no adequate design is obtained in steps 2-4, the chamber pressure is adjusted. Altering the chamber pressure has a direct impact on both the hot gas heat transfer and the dimensions of the thrust chamber (since the characteristic length is held constant). If the obtained steady-state solution at the *nominal* design point complies with all hydraulic, thermal, and manufacturing constraints, the solution at the *off-design* point is verified. The off-design point, explained in subsection 5.1.4, represents the worst-case operating point of the chamber. When the solution complies with all customer requirements and design constraints, at both the nominal and off-design load point, the iteration is terminated.

The fact that a manual design routine is used implies that the obtained solution does not necessarily represent an *optimal* solution. Nonetheless, optimization of the thrust chamber or coolant geometry is not strictly required by the customer[2]. An optimization activity that could be considered in the future, is minimizing the pressure drop over the cooling passages. When the pressure drop over the cooling jacket is lowered, the pressure increase provided by the upstream hydrogen peroxide pump may also be reduced. The pressure increase delivered by the pump is proportional to the power needed by the electrical motor which drives the pump. Since this motor is powered by batteries, a reduction in pressure drop may result in fewer batteries required on-board the spaceplane, which reduces the vehicle dry mass. Such optimization could be implemented in TDCAS, but could also be considered as a separate study in commercial computational fluid dynamics software packages, like Ansys.

5.1.1. Hydraulic Constraints

Based on the customer requirements, listed in Table 1.3, the reader may observe that a wide range of chamber pressures is allowed. Likewise, the requirements only specify a minimum thrust level at sea level or in a vacuum. The maximum thrust, and thus mass flow rate, is not constrained in the set customer requirements. As a result, the feasible design space is very large. Based on the set customer requirements, one could propose an engine design that is considerably larger than the current Mk-II engine, provided that the dry mass does not exceed 12 kg (REQ-008). Internal discussions with the customer have revealed that the main goal of the ESA FLPP project is to demonstrate AM with an engine *similar* to the Mk-II thruster, rather than developing a propulsion system that is vastly different in size but would still meet the imposed requirements. Therefore, an upper limit on either thrust or mass flow rate should have been set in customer requirements, to avoid the presence of this unnecessarily large design space. At all times, the reader must be aware that the requirements in Table 1.3 were *given* to the author, and not *set* by the author. Modification of some of the requirements, which is currently already proposed to the customer, is only possible after confirmation of the customer.

Besides diverging from the primary goal of the ESA FLPP project, upscaling the engine in terms of thrust output may also require a redesign of fluidic components upstream of the thrust chamber. Examples include the injector, catalyst, feed system, and pump. All these upstream components are designed

[2] To quote Akin's 13th law of spacecraft design mentioned in ref. [109]: "Design is based on requirements. There's no justification for designing something on bit 'better' than the requirements dictate."

for an oxidizer flow rate of 1 kg/s and fuel flow rate of 0.125 kg/s, which follows loosely[3] from the current design of the Mk-II thruster. The upper limit on the chamber pressure follows from the maximum pressure difference that the propellant pump can deliver. Dawn Aerospace has readily developed a state-of-the-art hydrogen peroxide pump, which is designed to discharge the oxidizer at 1 kg/s with a pump outlet pressure of 9.3 MPa. A higher pump outlet pressure is not possible, since this would exceed the maximum allowable operating pressure of the assembly. To this extent, it can be concluded that the upper pressure limit of 12 MPa, defined in customer requirement REQ-007, cannot be reached without introducing an expensive redesign of the hydrogen peroxide pump. For all calculations in this thesis, the oxidizer flow rate (1 kg/s) and outlet pressure of the pump (9.3 MPa) are assumed to be constant over time.

Based on the available pressure of 9.3 MPa (p_{pump}), a pressure budget can be constructed, which is used to investigate the maximum possible chamber pressure. Based on the high-level pump-fed feed system architecture, illustrated in Figure 4.10 on the right, the pressure balance shown in Equation 5.1 can be derived.

$$p_o = p_{pump} - \Delta p_{reg} - \Delta p_{cat} - \Delta p_{inj} - \Delta p_{min} \tag{5.1}$$

In this balance, p_o denotes the chamber pressure, Δp_{reg} the pressure drop over the cooling passages, Δp_{cat} the pressure drop over the catalytic reactor, Δp_{inj} the pressure drop over the injector, and Δp_{min} the (minor) pressure losses over valves and tubing in the feed system. It is worth mentioning that the feed system pressure losses are proportional to the flow velocity squared. The designer can easily control the flow velocity by increasing or decreasing the size of the tubing and valves. For the preliminary design, Δp_{min} is assumed to be no more than 0.3 MPa. This value is found to be reasonable, based on experience in the pressure-fed Mk-II thruster that was used in the validation activities.

For the catalytic reactor, a pressure drop of 1 MPa is assumed. Hot-fire tests of the Mk-II thruster have demonstrated that this value is conservative yet realistic. It should be mentioned that the loss of 1 MPa comprises pressure losses over the injector inside the catalytic reactor, as well as pressure losses over the catalyst. For the main propellant injector, a pressure drop equal to 15% of the chamber pressure is taken. Based on pump outlet pressure of 9.3 MPa and the losses in the feed system, catalytic reactor, and propellant injector, Equation 5.1 can be rewritten to the form shown in Equation 5.2. In this expression, both the chamber pressure (p_o) and pressure drop over the cooling passages (Δp_{reg}) are in Pascal.

$$p_o = \frac{8 \cdot 10^6 - \Delta p_{reg}}{1.15} \tag{5.2}$$

Based on the customer requirements and chamber pressure scaling law defined in Equation 5.2, the feasible design space can be plotted, as depicted in Figure 5.1. In the illustration, the theoretical sea level and vacuum specific impulse are shown as a function of the mixture ratio and chamber pressure. The values are based on an analysis in CEA and assume a 99% characteristic velocity efficiency and 96% thrust coefficient efficiency. The former quality factor follows directly from hot-fire tests of the Mk-II thruster. Since the nozzle exit pressure is kept constant, each design curve corresponds to a different nozzle pressure ratio, and thus also a different expansion ratio. In both plots, the expansion ratio is indicated with “AR”. The hatched line labeled “minimum by requirement” represents the lower limit of the feasible design space, which can be traced to customer requirements REQ-003 and REQ-004. The dashed lines indicate the upper limit of the feasible design space and follow directly from Equation 5.2, at a cooling jacket pressure drop of 1 MPa and 2 MPa. A pressure loss of this magnitude is deemed realistic in light of the results obtained during the hydraulic characterization tests of the current iteration of the Mk-II thruster (see also Figure 4.15). Furthermore, one can observe that the maximum theoretical specific impulse is obtained at a mixture ratio of 8. Based on the driving specific impulse requirements, this mixture ratio is used throughout the remainder of the design.

[3] Again, this implies that the values are not identical to the current design, but compare well. This is done to protect the intellectual property of Dawn Aerospace.

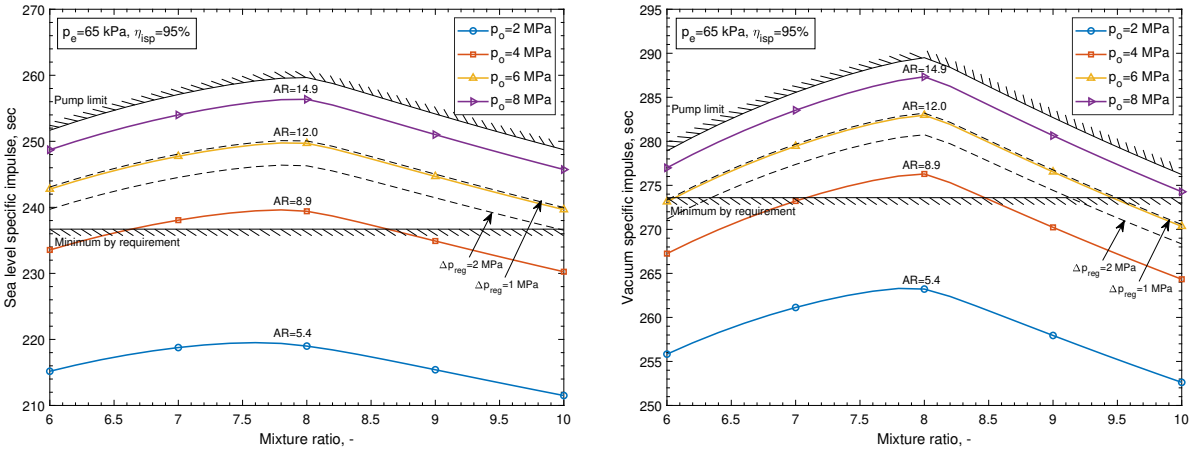

Figure 5.1: Predicted sea level and vacuum specific impulse at different chamber pressures (p_o) with operating boundaries at a fixed nozzle exit pressure (p_e) and specific impulse quality factor ($\eta_{c_{I_{sp}}}$). Nozzle expansion ratios are noted with "AR".

Besides specific impulse, the minimum thrust is also constrained by the customer, conform requirements REQ-001 and REQ-002. The feasible design space based on the theoretical thrust obtained at sea level and in a vacuum is presented in Figure 5.2. The design window is based on a total mass flow rate of 1.125 kg/s, nozzle exit pressure of 65 kPa, and thrust coefficient efficiency of 96%. The total mass flow rate originates from the 1 kg/s hydrogen peroxide mass flow rate and 0.125 kg/s kerosene mass flow rate. In the illustrations, one can also observe that the design space is large, compared to narrow design windows that follow from the specific impulse requirements. As a result, it can be concluded that the thrust force is not a driving requirement for the design of the AM Mk-II thruster.

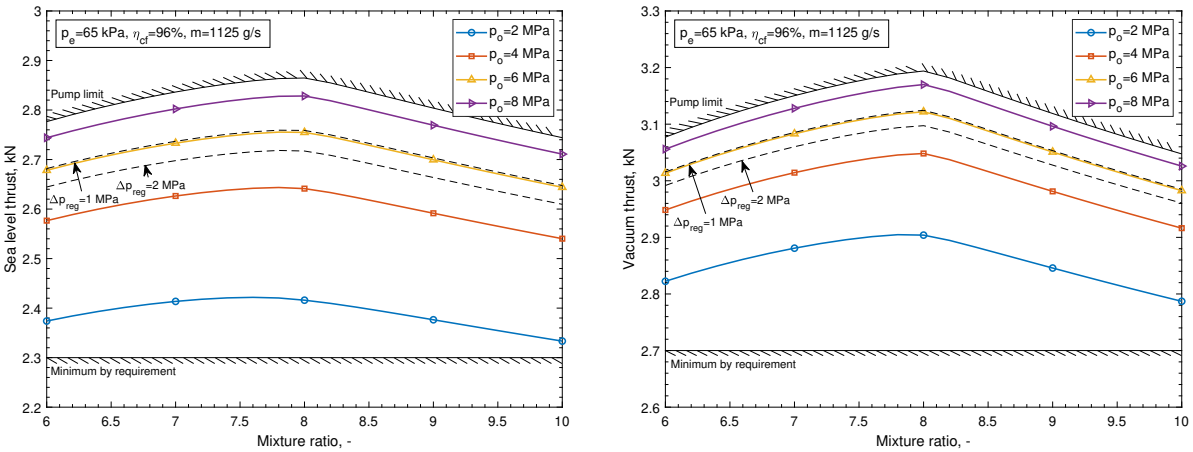

Figure 5.2: Predicted sea level and vacuum thrust at different chamber pressures (p_o) with operating boundaries at a fixed nozzle exit pressure (p_e), thrust coefficient quality factor (η_{c_F}) and mass flow rate ($\dot{m}$).

5.1.2. Thermal Constraints

The preliminary design of the AM thrust chamber is based on a maximum service temperature of the structure, as stated in section 3.4. In the bimetallic reference design, the limit temperature for the NARloy-Z liner is set to 811 K. This value is based on the maximum inner wall temperature that is proclaimed for the steady-state operation of the Space Shuttle Main Engine [73]. At this particular temperature, over 500 thermal cycles of the engine are noted in ref. [34]. Both the pressure- and temperature-induced loads are much smaller in Mk-II engine, compared to the Space Shuttle Main Engine[4]. Hence, it is reasonable to assume that this temperature is also suitable for the preliminary design of the Mk-II thruster, which has a maximum service life of only 100 thermal cycles (REQ-011).

[4]For reference, the typical flame temperature in Mk-II is ~2700 K and ~3600 K in the Space Shuttle Main Engine.

The maximum service temperature of the AM Inconel 718 thrust chamber is set to 1005 K. This value originates from research of Gradl et al. [15], who experimented with AM Inconel 625 in the application of a thruster propelled by liquid oxygen and kerosene. The engine is operated at a maximum chamber pressure of 8.6 MPa and regeneratively cooled with both kerosene and water. The designers demonstrate a maximum Inconel 625 wall temperature of 1005 K, which follows from heat transfer simulations where a scaled version of the Bartz equation is used for the prediction of the hot gas convection. This scaling follows from measurements during hot-fire tests. The publication mentions 28 restarts in a kerosene-cooled configuration and 19 restarts in a water-cooled configuration, with a total accumulated burn time of 1815 seconds. No failure of the AM Inconel 625 is reported after this accumulated burn time. Based on several similarities between Inconel 718 and Inconel 625, it is assumed that a maximum temperature of 1005 K is reasonable for the preliminary design of the AM Inconel 718 thrust chamber.

Lastly, for the hydrogen peroxide regenerative coolant, a maximum service temperature of 408 K is taken, together with a maximum heat-flux-to-velocity ratio of 0.86 MPa. These values can be traced to subsection 2.4.4.

5.1.3. Manufacturing Constraints

The last set of constraints considered for the preliminary design are based on the manufacturability of the chamber. These include the minimum thickness of the thrust chamber wall, as well as the minimum size of the cooling passages. The theoretical minimum wall thickness of chambers that are produced using the laser powder bed fusion AM technique is related to the focus spot size of the laser. For most commercial machines, this value is typically in the order of 0.1-0.15 mm [11]. In personal communication with a leading industry partner in the field of laser powder bed fusion, it is described that wall thicknesses up to 0.2 mm and channel diameters up to 0.5 mm have been realized in AM Inconel 718 heat exchangers. An important point that was shared in this communication is that such small dimensions are still highly experimental. As a result, the fabrication success rate depends heavily on the geometry of the part, as well as on the process settings that are used in the powder bed fusion machine. A more conservative value is mentioned in the research of Thomas [110], who recommends a minimum wall thickness of 0.4 ± 0.02 mm. The 0.4 mm thickness limit is in line with findings of Marchan et al. [111], concerning AM Inconel 718 structures. On the other hand, Patel et al. [14] use a minimum wall thickness of 0.6 mm and minimum channel width of 0.63 mm in an AM Inconel 718 thrust chamber. These values are slightly more conservative than earlier mentioned numbers.

Based on the experience described in the literature, it is decided to limit the wall thickness to 0.5 mm for the first iteration of the AM thrust chamber. In a second iteration of the thruster, this value could potentially be reduced, based on lessons learned in the AM fabrication process. This minimum thickness is also selected for the ribs in-between the cooling channels. To facilitate ease of post-build powder removal, which is a frequently observed problem in regeneratively cooled AM thrust chambers, a minimum channel width/height of 0.8 mm is adopted. This value can be seen as conservative based on findings in the literature.

5.1.4. Off-Design Operating Point

Hands-on experience of the author with experimental rocket engines has shown that it is incredibly difficult to operate an engine *exactly* at one fixed operating point, in terms of chamber pressure, mixture ratio, and coolant inlet conditions. Instabilities in the combustion, manufacturing tolerances for the injector, and/or ambient temperature changes can easily result in small changes in the conditions of the hot combustion gas or coolant flow. Therefore, instead of defining a definite operating point, an operating envelope is selected for the preliminary design. This operating envelope is bounded by the nominal and off-design operating point, a concept that was also introduced in ref. [112]. In the present work, the following off-design limits are adopted, which are set based on internal agreement at Dawn Aerospace:

- A 5% increase in chamber pressure,
- A propellant mixture ratio of 7.6,
- A coolant inlet temperature of 303 K.

The mixture ratio of 7.6 corresponds to operating case where the theoretical (adiabatic) flame temperature for the combustion of 90% hydrogen peroxide and kerosene is highest, as shown in Figure 5.3. This plot is based on an analysis in CEA with shifting equilibrium flow conditions. The nominal mixture ratio is set to 8, which corresponds to the maximum theoretical specific impulse, as demonstrated in Figure 5.1. Lastly, the nominal coolant inlet temperature is set to 293 K.

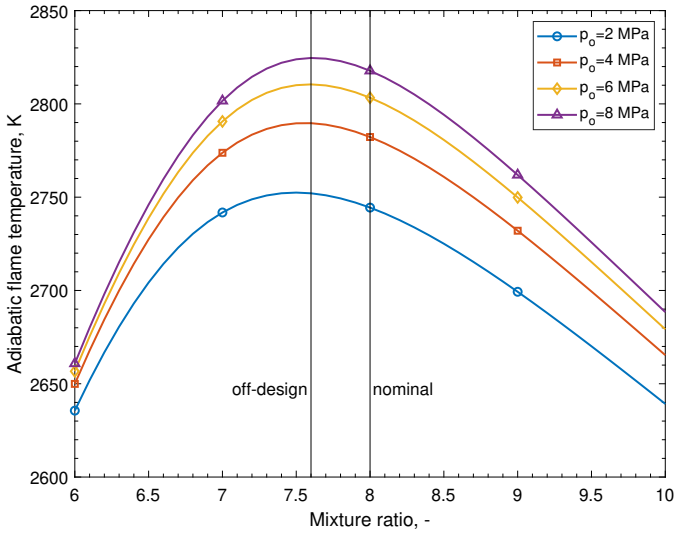

Figure 5.3: Predicted adiabatic flame temperature for the combustion of 90% hydrogen peroxide and kerosene, with nominal and off-design operating points.

5.2. Bimetallic Reference Thrust Chamber

In this section, the bimetallic thrust chamber design is proposed, which serves as a reference for the current design of the Mk-II. As explained in section 5.1, first the cooling channel geometry at the nozzle throat is defined. For this design step, a parameter study is conducted, where chamber pressure, wall thickness, and the number of cooling channels are varied. The channel height and width are kept constant and set to 0.8×0.8 mm, which follows from the manufacturing constraints. By selecting narrow channels at the throat, the number of cooling channels can be maximized, which has a positive impact on the wall temperature. For the bimetallic reference design, the chamber pressure is varied between 4 MPa and 6 MPa in steps of 1 MPa. The wall thickness is varied between 0.5 mm and 2.0 mm in steps of 0.5 mm, whereas the number of cooling passages is varied between 15 and 45. It is worth mentioning that the upper limit of 45 is still below the maximum channel count (N_{max}), which follows from Equation 5.3,

$$N_{max} = \frac{2\pi(r_t + t_w)}{(c_w)_{min} + (l_w)_{min}} = \frac{2\pi\left(\sqrt{\frac{c^* \dot{m}}{\pi p_o}} + t_w\right)}{(c_w)_{min} + (l_w)_{min}} \tag{5.3}$$

where c^* denotes the characteristic velocity, $\dot{m}$ the total mass flow rate, p_o the chamber pressure, t_w the wall thickness, c_w the minimum channel width (0.8 mm), and l_w the minimum rib width (0.5 mm).

The feasible design space that follows from the parameter study is depicted in Figure 5.4. One can observe that the maximum wall temperature decreases with increasing channel count, with improvements becoming small above 30 channels. Note that the maximum wall temperature is achieved below the rib, which translates to node A in Figure 3.1. As a result of 2-D conduction in the structure, the temperature directly below the cooling channel is lower. One may also note that the wall temperature increases with the thickness of the chamber wall, as expected.

The main design parameter that constrains the design space for the bimetallic reference engine is the heat transfer to the hydrogen peroxide coolant, as displayed in Figure 5.4 on the right. This plot shows

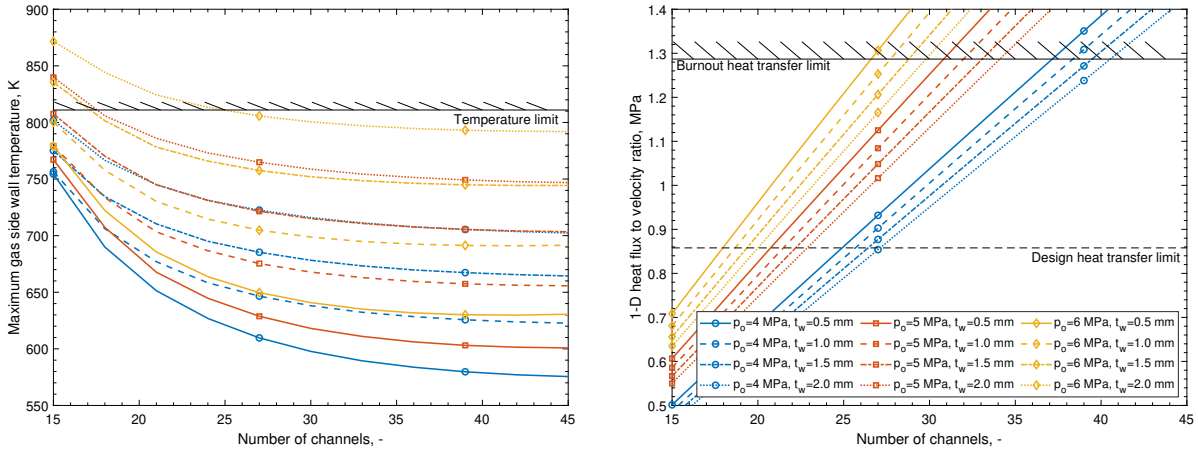

Figure 5.4: Parameter study showing the maximum gas side wall temperature (left) and heat transfer limits (right) for a bimetallic NARloy-Z/Inconel 718 thrust chamber as a function of chamber pressure (p_o), wall thickness (t_w), and channel count, at a constant cooling channel size of 0.8×0.8 mm.

the 1-D heat-flux-to-velocity ratio, a term which was readily introduced in subsection 2.4.4 in the context of the burnout heat transfer limits of the hydrogen peroxide[5]. Since the channel dimensions are kept constant in the parameter study, the effective flow area increases with channel count. As a result of the increasing flow area, the flow velocity decreases, which follows directly from the conservation of mass. Accordingly, a higher channel count results in a higher heat-flux-to-velocity ratio.

Based on the parameter study, an operating pressure of 5 MPa is selected, with a uniform wall thickness of 1.7 mm. This design point corresponds to 23 channels of size 0.8×0.8 mm at the nozzle throat plane. These values serve as the primary input for sizing of the cooling channels at axial stations upstream and downstream of the throat. For this endeavor, the iterative design approach that is described in section 5.1 is used, where the wall thickness, channel count, and channel height are kept constant. A suitable design solution that is obtained after several manual iterations at both the nominal and off-design operating point is presented in Figure 5.5.

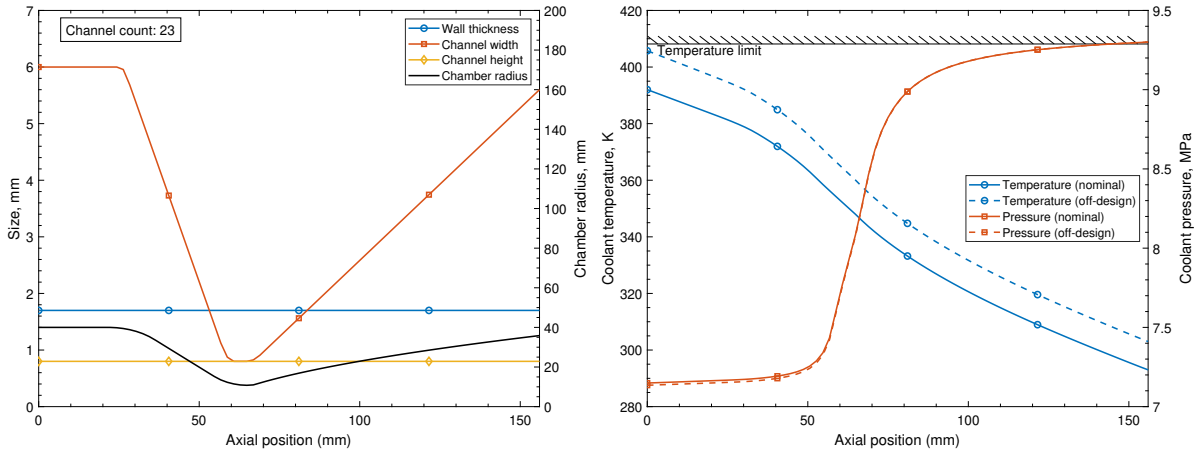

Figure 5.5: Cooling channel geometry (left) and coolant temperature and pressure (right) for the bimetallic NARloy-Z/Inconel 718 thrust chamber design, at a chamber pressure of 5 MPa and mixture ratio of 8.

The proposed bimetallic reference design has a maximum channel width of 6 mm at the injector plane and a rib width that varies between 2.6 mm and 5.5 mm. At the off-design point, the pressure drop over the cooling passages is 2.15 MPa, whereas the maximum temperature of the hydrogen peroxide temperature is 405 K. The inner wall temperature and hot gas heat flux for the proposed design are shown

[5]The term "1-D" originates from the fact that the heat flux is obtained from Equation 2.26 at the average gas-side wall temperature. Inside the structure, the heat flux is represented by a 2-D vector, which is numerically resolved using the finite element method.

in Figure 5.6. In the illustration on the left, one can observe that the temperature at the nozzle throat is well below the maximum service temperature of NARloy-Z. The thermal gradients in the circumferential direction are typically less than 40 K, which is very small. In the plot, this is visible in the difference between the “below rib” curve and “below channel” curve. This small circumferential thermal gradient is primarily caused by the high thermal conductivity of NARloy-Z (>300 W/(m K)). At the coolant side, the wall temperature does not exceed 540 K. This is well below the saturation temperature of 90% hydrogen peroxide, which is equal to 640 K at the coolant inlet pressure. In Figure 5.6 on the left, one can also see the impact of the coolant flow development on the predicted wall temperature (axial position >148 mm).

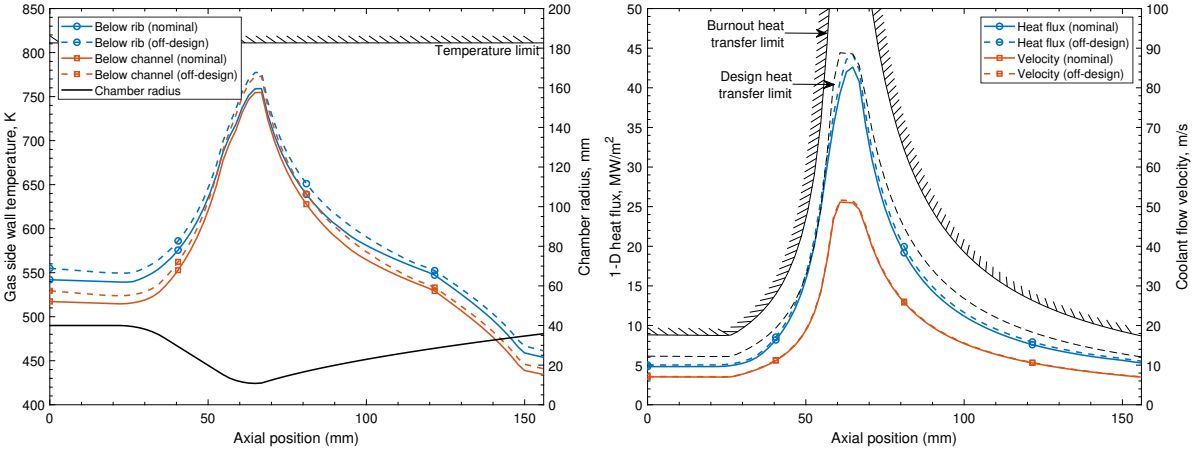

Figure 5.6: Gas side wall temperatures (left) and hot gas heat flux (right) for the bimetallic NARloy-Z/Inconel 718 thrust chamber design, at a chamber pressure of 5 MPa and mixture ratio of 8.

From Figure 5.6 on the right, one can conclude that the heat flux of the proposed design, at both the nominal and off-design operating points lies within the feasible design space, based on burnout heat transfer constraints. As a consequence of the high heat flux in the bimetallic reference design, high coolant velocities are required, up to 50 m/s. Despite the low surface roughness of the machined cooling channels (6 µm), this results in high pressure losses in the vicinity of the throat. If the chamber pressure is further increased, the hot gas convective heat load also further increases. This means that higher coolant velocities are required to satisfy the burnout heat transfer constraints. As a result, the pressure drop over the cooling passages is even higher. A higher pressure drop over the cooling channels is not possible with the current hydrogen peroxide pump design.

5.3. Integral Additive Manufactured Inconel 718 Thrust Chamber

In this section, the proposed AM thrust chamber for the ESA FLPP project is discussed, which comprises an integral Inconel 718 structure. For a proper comparison of the AM engine to the bimetallic reference engine, an identical chamber pressure (5 MPa) and mixture ratio (8) are used. This way, the differences between the two design solutions are merely the fabrication technique and selected material, whereas the thrust chamber geometry and operating conditions are identical. In the model, this translates to the use of a different temperature-dependent thermal conductivity (∼11 W/(m K) [40] versus ∼300 W/(m K) [99]), as well as a different equivalent sand grain roughness (121 µm versus 6 µm). During simulations in TDCAS, it was quickly discovered that it is not possible to operate the AM Inconel 718 design at a chamber pressure of 5 MPa when only relying on regenerative cooling. Such a design resulted in steady-state wall temperatures that exceeded the maximum service temperature of 1005 K. To operate the chamber at the target pressure of 5 MPa, a combination of regenerative and film cooling is needed. This design solution is detailed in subsection 5.3.2.

For completeness of the discussion, an AM Inconel 718 which relies solely on regenerative cooling is also introduced, in subsection 5.3.1. To satisfy the maximum wall temperature constraint, a lower chamber pressure is used in this design. This way, the impact of film cooling on the design of the thrust chamber can be evaluated. Lastly, the impact of design uncertainties is briefly evaluated in a sensitivity study, which can be found in subsection 5.3.3.

5.3.1. Results without Film Cooling

The design steps taken for the AM Inconel 718 chamber are similar to the bimetallic design described in the previous section. First, a parameter study is conducted at the nozzle throat plane, as shown in Figure 5.7. This is used to evaluate the maximum possible chamber pressure, in a configuration where no film coolant is utilized. The parameter study is based on a constant wall thickness of 0.5 mm and constant channel size of 0.8×0.8 mm. This wall thickness corresponds to the lowest possible value based on manufacturing constraints. The channel count is varied from 25 to N_{max} in steps of 3, whereas the chamber pressure is varied between 2 MPa and 4 MPa in steps of 0.25 MPa. At a chamber pressure of 4 MPa, the specific impulse requirements set by the customer can just be met, as illustrated in Figure 5.1. At lower chamber pressures, the specific impulse requirements REQ-003 and REQ-004 and pressure requirement REQ-007, cannot be met, based on the assumed overall engine efficiency of 95%.

The parameter study for the AM Inconel 718 chamber shows similar trends as the study that was conducted for the bimetallic reference chamber. Generally speaking, more cooling channels are required in this design to maintain the wall at an adequate temperature. This follows directly from the lower chamber pressure, which results in a larger nozzle throat area. Consequently, the surface area of the chamber which requires cooling is higher. A design point is selected at a chamber pressure of 2 MPa, which corresponds to 60 cooling passages at the throat plane. This design point provides a decent margin to the maximum service temperature of the wall. Several manual iterations are again performed at both the nominal and off-design operating point, to derive the cooling channel geometry which is depicted in Figure 5.8 on the left.

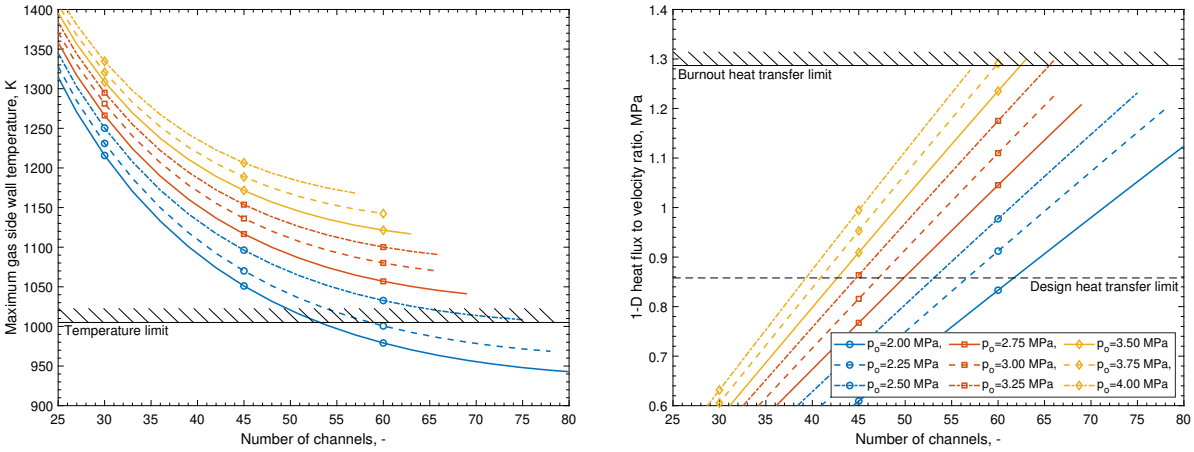

Figure 5.7: Parameter study showing the maximum wall temperature (left) and heat transfer limits (right) for a regeneratively cooled AM Inconel 718 chamber, at constant cooling channel size of 0.8×0.8 mm and wall thickness of 0.5 mm.

The first observation that can be made from Figure 5.8 on the left, is that a much longer chamber barrel is required, compared to the bimetallic reference design. This follows directly from the definition of the characteristic length, which was introduced in subsection 2.2.2. At a lower chamber pressure, a larger chamber volume is needed to achieve the same characteristic length. Since the chamber diameter is held constant (8 cm), the barrel length increases. Moreover, at a constant nozzle exit pressure and larger throat area, the nozzle expansion ratio is decreased.

The second observation that can be made from Figure 5.8 on the right, is that the pressure drop over the cooling passages is 1.67 MPa, which is lower than that of the bimetallic reference engine. This is an interesting observation since the equivalent sand grain roughness in the AM thrust chamber is much higher (121 µm). For an identical flow velocity, say 5 m/s, the pressure drop in the AM chamber is 0.86 MPa/m, and in the bimetallic chamber 0.35 MPa/m. This confirms that pressure losses in the AM structure indeed scale more steeply. Nonetheless, the flow velocity near the throat in the bimetallic chamber (50 m/s) is more than twice as high as the flow velocity at the throat of the AM design (19 m/s). Since the pressure drop scales with the velocity squared, the higher flow velocity in the bimetallic chamber results in a pressure drop at the throat which is roughly seven times higher. Even though the surface roughness is almost twenty times higher in the AM design, the friction factor is not (see also

Equation 2.37). For instance, at a throat Reynolds number of 5×10^4 and hydraulic diameter of 0.8 mm, the friction factor of the AM channels yields 0.130, whereas the friction factor of the machined copper alloy cooling passages equals 0.036 (which is 3.6 times lower). Hence, the flow velocity becomes dominant over the surface roughness.

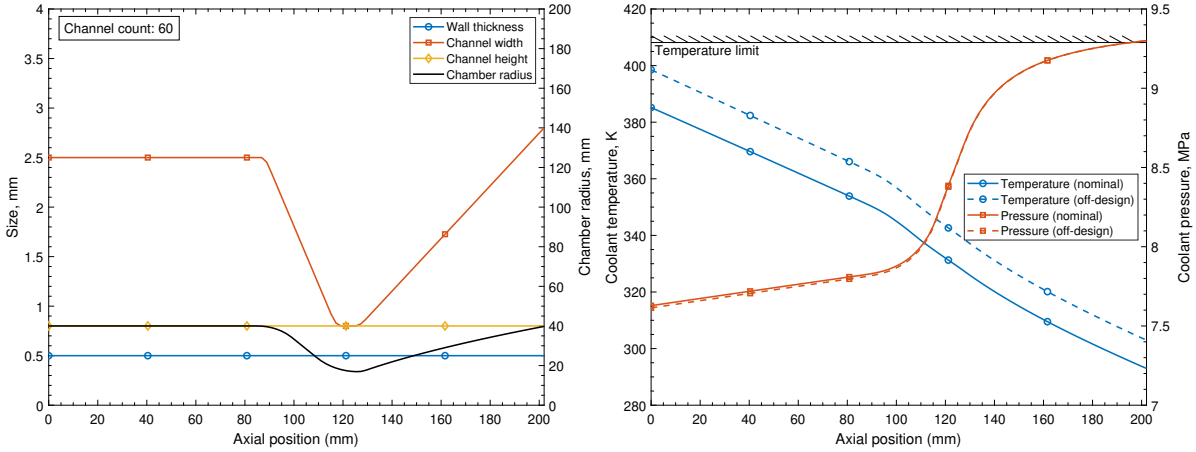

Figure 5.8: Cooling channel geometry (left) and coolant temperature and pressure (right) for an AM Inconel 718 thrust chamber, at a chamber pressure of 2 MPa and mixture ratio of 8.

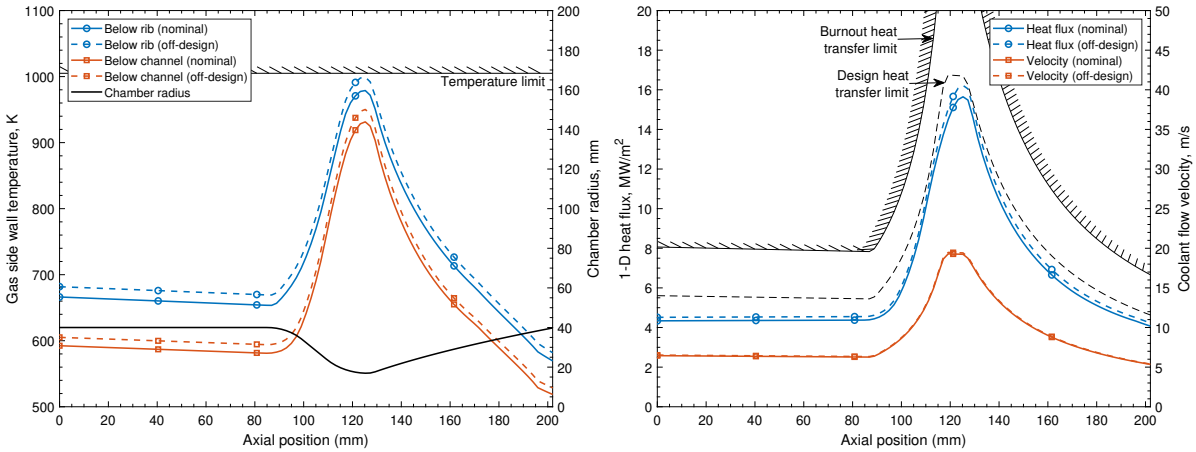

Figure 5.9: Gas side wall temperatures (left) and hot gas heat flux (right) for an AM Inconel 718 thrust chamber, at a chamber pressure of 2 MPa and mixture ratio of 8.

The maximum inner wall temperature and hot gas heat flux for the AM Inconel 718 design without film cooling are presented in Figure 5.9. From these plots, one can observe that the maximum wall temperature complies with the service temperature limit of 1005 K. At the coolant side, the wall reaches a temperature up to 488 K, which is well below the saturation temperature of hydrogen peroxide at the coolant inlet pressure. In comparison with the bimetallic reference design, one can observe much larger thermal gradients in the circumferential direction. This is a direct consequence of the low thermal conductivity of Inconel 718 ($\sim$11 W/(m K)). These thermal gradients are well-visible in Figure 5.10, which shows the predicted 2-D temperature field for different rib widths. In all illustrations, the channel width and height are kept constant at 0.8 mm. Local hot spots occur directly below the rib as a consequence of the long conduction path. When decreasing the rib width, a more “flat” temperature profile is obtained in the wall. A major challenge of decreasing the rib width - and thus increasing the channel count or channel width - is that the effective coolant flow area is increased. For a constant coolant mass flow rate, this results in a lower flow velocity, which challenges the burnout heat transfer constraints.

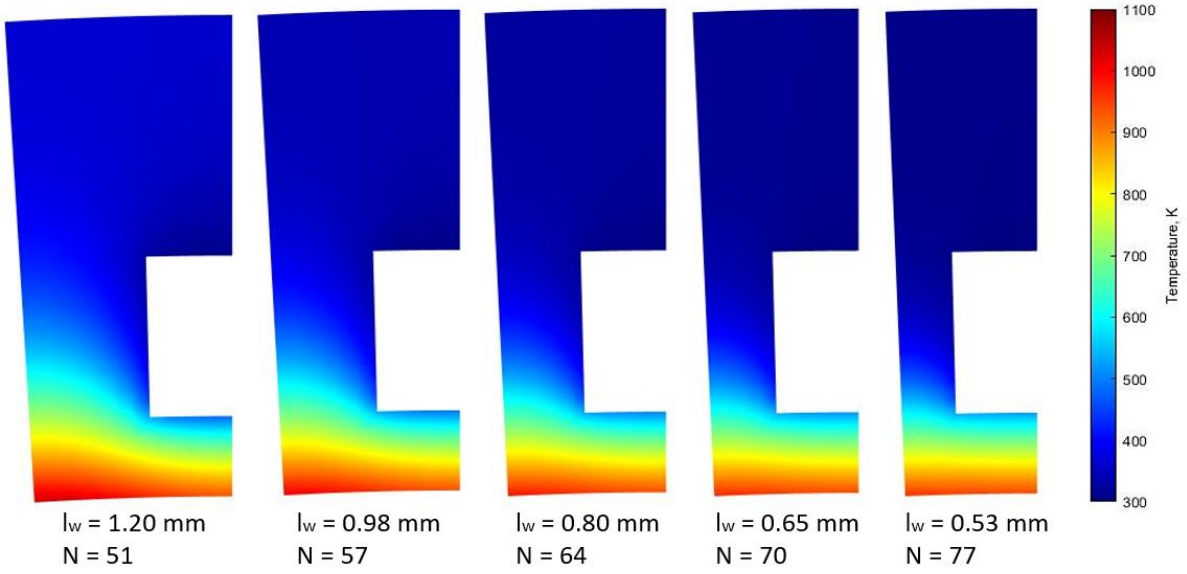

Figure 5.10: Impact of rib width (l_w) and channel count (N) on temperature distribution at the throat of the AM Inconel 718 thrust chamber with a chamber pressure of 2 MPa.

5.3.2. Results with Film Cooling

The second proposed AM design introduces a hydrogen peroxide film coolant in the combustion chamber. This way, the heat load to the wall can be further reduced, which is necessary to operate the chamber at the target chamber pressure of 5 MPa. First, a parameter study is again conducted at the nozzle throat plane. The purpose of this study is to evaluate the required amount of film cooling, which is assessed in terms of the film cooling fraction (ω). The fraction, which represents the ratio between the film flow rate and the total mass flow rate in the chamber, was introduced in subsection 2.2.4. In the parameter study, illustrated in Figure 5.11, the film flow fraction is varied between 0.5 and 1.3, in steps of 0.1. The wall thickness, channel geometry, and chamber pressure are kept constant, at 0.5 mm, 0.8×0.8 mm, and 5 MPa respectively.

Unless stated otherwise, all calculations in this section are based on a liquid film effectiveness ($\eta_{cf,l}$) of 0.46, a reference entrainment factor of 0.0425 (ψ_L), a unity local entrainment factor (ψ_M), and a decomposition rate constant (χ) of 3000 s^{-1}. For a more detailed explanation of these empirical constants, the reader is referred to subsections 2.5.2 and 4.2.3.

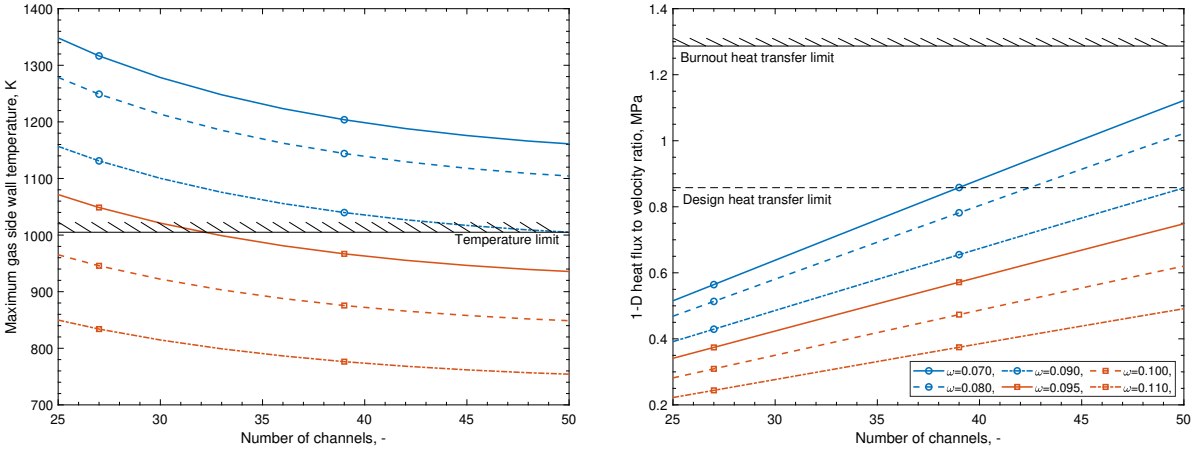

Figure 5.11: Parameter study showing the maximum wall temperature (left) and heat transfer limits (right) for a regeneratively and film-cooled AM Inconel 718 chamber, with a constant chamber pressure of 5 MPa, wall thickness of 0.5 mm, and a cooling channel size of 0.8×0.8 mm.

From the parameter study, one can observe a decrease in the throat wall temperature with increasing film flow fraction. Physically, this corresponds to the downstream movement of the liquid dry-out point. Moreover, one may observe that the burnout heat transfer margins are much higher under the presence of a film coolant. Based on Figure 5.11, a film fraction of 0.10 is selected, accompanied with 40 cooling channels. This design point provides a decent margin to the maximum service temperature of the wall, as well as the burnout heat flux.

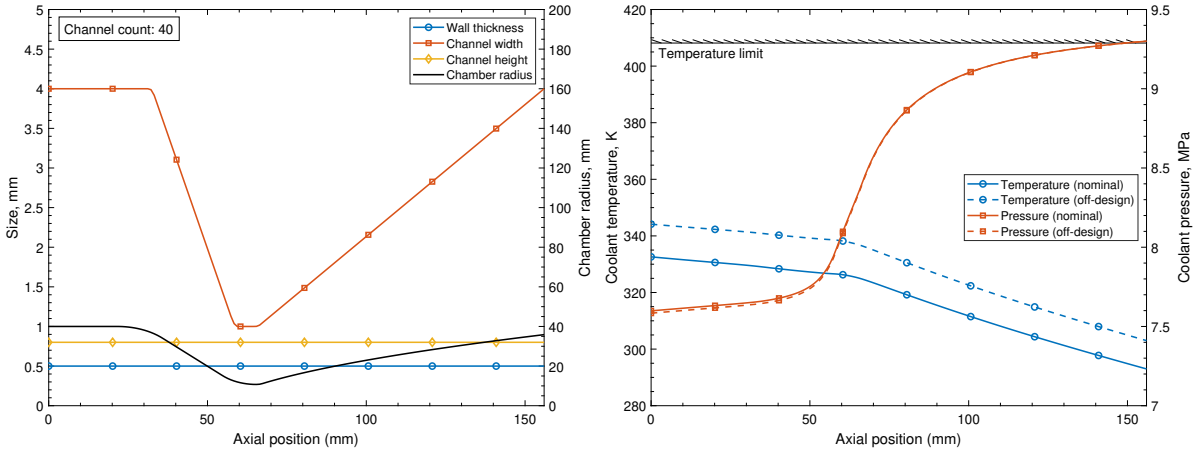

Figure 5.12: Cooling channel geometry (left) and coolant temperature and pressure (right) for an AM Inconel 718 thrust chamber at a chamber pressure of 5 MPa, mixture ratio of 8 and film cooling fraction of 0.10.

A promising design solution that is obtained after several manual iterations is depicted in Figure 5.12. Notice that the internal geometry of the chamber is identical to the geometry of the bimetallic thrust chamber. At a film flow fraction of 0.10 and chamber diameter of 8 cm, the peripheral film mass flow rate is 0.45 kg/(s m). This value compares well with the hydrogen peroxide film-cooled thruster of Heo et al. [52], who experimented with a peripheral flow rate of 0.38-0.76 kg/(s m), and is slightly higher than values used by Kwak [62], who experimented at a peripheral flow rate of 0.28-0.39 kg/(s m).

Under the presence of the hydrogen peroxide film coolant, the predicted regenerative coolant outlet temperature is significantly lower. Compared to the bimetallic design, which has an outlet temperature of 405 K, the AM solution with film cooling has a coolant outlet temperature of 344 K. Furthermore, one can observe that the heat transfer to the regenerative coolant is much smaller in the section where the liquid film exists, though not negligible. The predicted pressure drop over the cooling passages is 1.70 MPa, which compares well to the proposed AM design without film cooling.

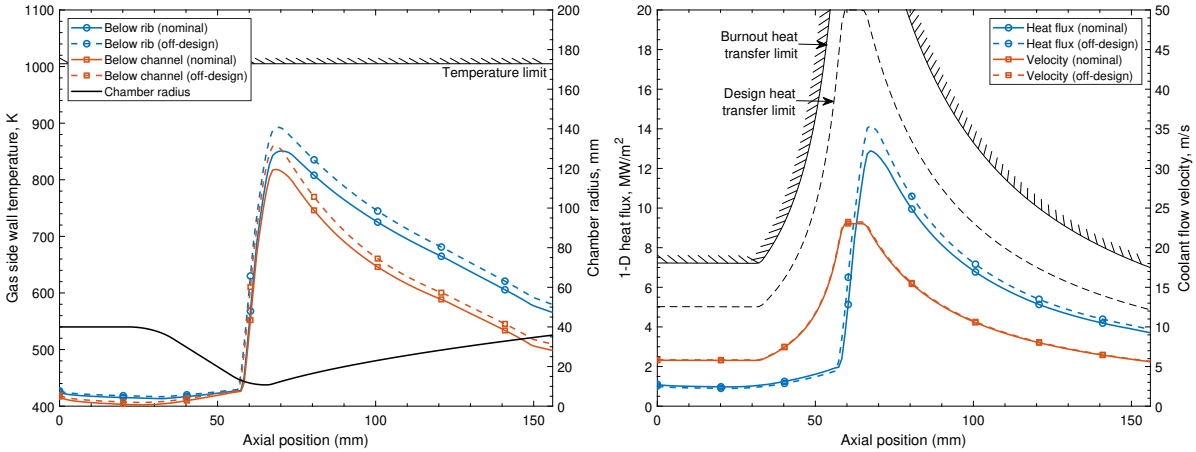

Figure 5.13: Gas-side wall temperature (left) and heat flux profile (right) for an AM Inconel 718 thrust chamber at a chamber pressure of 5 MPa, mixture ratio of 8 and film cooling fraction of 0.10.

The predicted axial temperature distribution and heat flux profile for the film-cooled design are shown in Figure 5.13. The illustration clearly shows the large impact of the liquid film on the predicted wall temperature. For the proposed design, the liquid dry-out point is located approximately 60 mm downstream of the injector. The sharp increase in wall temperature at the dry-out point agrees well with simulations and measurements in MMH film-cooled thrusters, which were presented in Figure 2.18. In practice, the temperature upstream of the dry-out point is expected to be slightly higher as a consequence of axial conduction in the chamber wall. This effect can, however, not be studied in TDCAS and would require further numerical research or testing.

A steep increase in heat flux can also be observed in the predicted heat flux profile, shown in Figure 5.13 on the right. The predicted heat flux for the nominal and off-design load points are well below the design heat transfer limit. In comparison, the bimetallic reference design and AM design without film cooling are operated very close to the design heat transfer limit at the off-design load point (see also Figures 5.6 and 5.9). Combined with the substantially lower wall temperature, it can be concluded that the film-cooled design can be operated with much larger margins from a thermal perspective.

5.3.3. Design Sensitivity Study

To verify the robustness of the proposed AM Inconel 718 design, a sensitivity analysis is conducted in the parameters that have the highest uncertainty. These parameters are:

- The convective heat transfer of the regenerative coolant in rough channels,
- The pressure drop in rough channels,
- The liquid film effectiveness,
- The gaseous film entrainment factor.

All AM chamber designs are based on a constant equivalent sand grain roughness. This value is taken as 121 µm, which is the average of typical values provided in Table 2.2. In the first sensitivity study, depicted in Figure 5.14, the maximum wall temperature and coolant pressure drop are examined, as a function of the surface roughness. The surface roughness is varied between 50% and 150% of 121 µm, in steps of 10 percentage point.

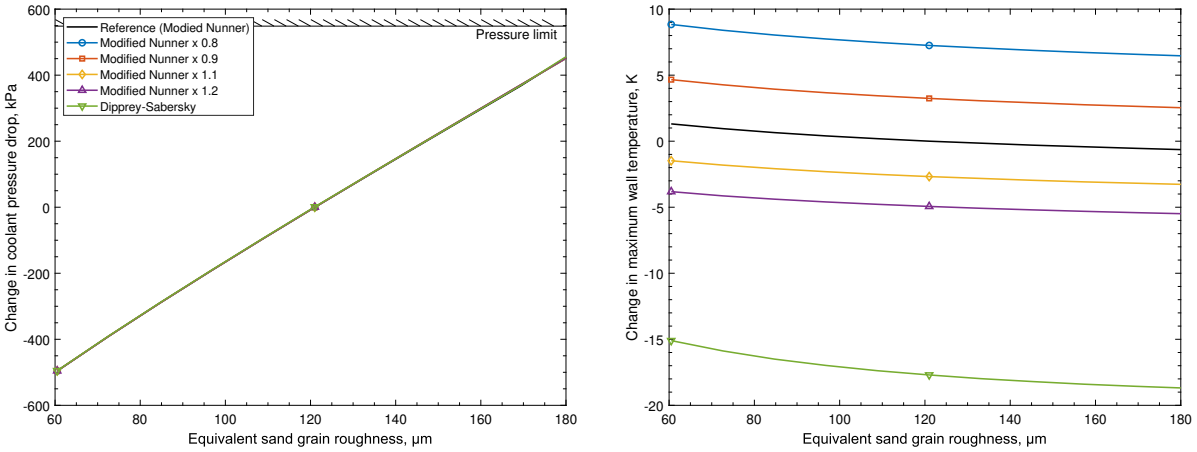

Figure 5.14: Impact of surface roughness and coolant convection model on the pressure drop and maximum wall temperature in the AM thrust chamber (with film-cooling).

Also included in Figure 5.14 is the potential impact of over- or underprediction of the modified Nunner heat transfer correlation. This effect is studied by multiplying the smooth channel Nusselt correlation that is used in the modified Nunner correlation (Equation 2.34) with a factor 0.8, 0.9, 1.1, and 1.2. For the same coolant Reynolds number and Prandtl number, a factor higher than one implies an increase in the overall Nusselt number, and consequently an increase in the heat transfer coefficient. For completeness, the results that are obtained from the Dipprey-Sabersky convection model are also included in the illustration.

Figure 5.14 reveals that the impact of different convection models, as well as the surface roughness, on the maximum wall temperature is small. Here, “small” implies that the maximum service temperature of the Inconel 718 wall or maximum available pressure provided by the pump are not exceeded at any of the design points studied. As expected, convection multipliers of 1.1 and 1.2, which increase the coolant heat transfer, provide a lower wall temperature. In general, the application of the Dipprey-Sabersky model results in lower wall temperatures. This is caused by the higher coolant Nusselt number that is obtained from this model, a trend which was also observed in section 4.1.

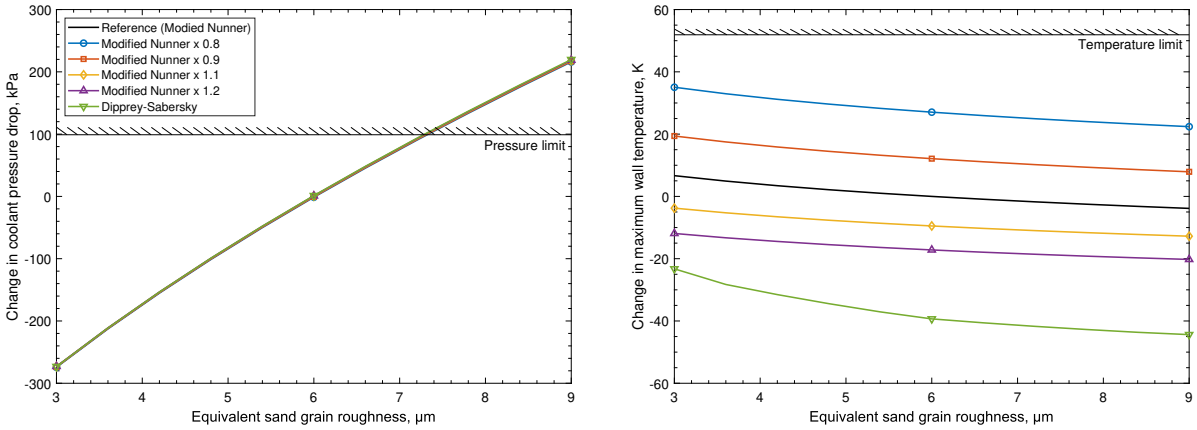

Figure 5.15: Impact of surface roughness and coolant convection model on the pressure drop and maximum wall temperature in the bimetallic reference thrust chamber.

For completeness of the discussion, a similar sensitivity study for the bimetallic reference chamber is depicted in Figure 5.15. As a result of the substantially higher thermal conductivity of the NARloy-Z liner, one can observe much larger fluctuations in the wall temperature as a function of the surface roughness. Nevertheless, temperature variations can still be considered small, since none of the studied cases exceeds the maximum service temperature of the NARloy-Z. On the contrary, pressure variations with surface roughness cannot be considered small. An increase in surface roughness greater than 20%, concerning the nominal roughness of 6 µm, results in an overall system pressure drop that exceeds the available pressure that is supplied by the pump. Therefore, one may conclude that the system is operated much closer to the design limits. The impact of the different convection models on the pressure drop is insignificant, which was also observed in Figure 5.14 on the left.

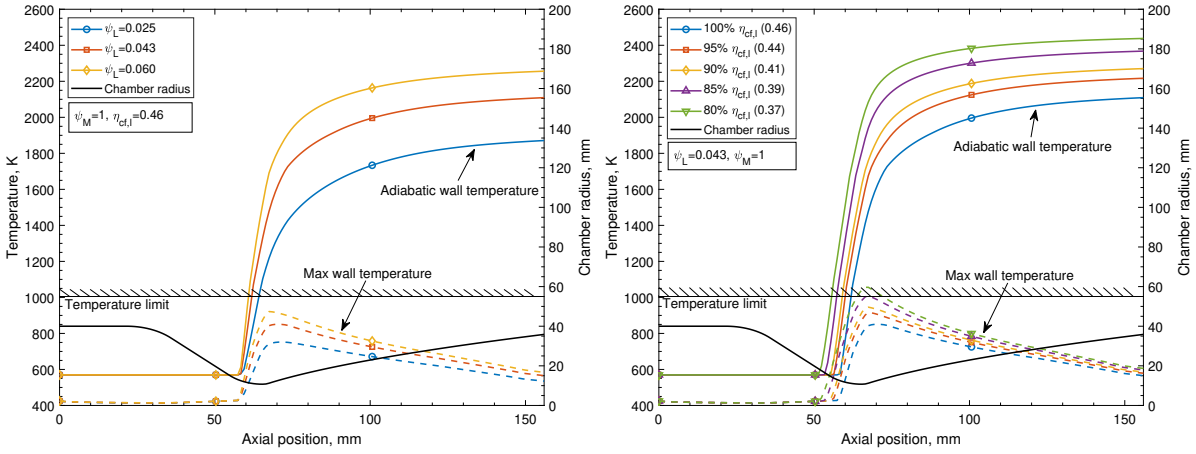

Figure 5.16: Reference (adiabatic) wall temperature and maximum gas-side wall temperature for different values of the liquid film effectiveness ($\eta_{cf,l}$) and reference entrainment factor (ψ_L).

The second sensitivity study conducted in this thesis captures the uncertainty in the film cooling model. Two parameters that have a relevant effect on the evolution of the liquid and gaseous film layer are the empirical liquid film effectiveness ($\eta_{cf,l}$) and gaseous film reference entrainment factor (ψ_L). Earlier

discussions in section 2.5 explained that the reference entrainment factor typically takes a value between 0.025 and 0.06 when the local entrainment factor (ψ_M) is unity. Furthermore, validation activities in section 4.2 showed a good correlation of TDCAS with experimental data if a liquid film effectiveness of 0.46 was used in the model. In Figure 5.16, both the reference entrainment factor (on the left) and liquid film effectiveness (on the right) are studied in detail. The maximum gas-side wall temperature is indicated with dashed lines, whereas the solid line represents the adiabatic wall temperature under the presence of the film coolant. The chamber design and operating conditions correspond to the AM Inconel 718 design, which is detailed in subsection 5.3.2.

In Figure 5.16 on the left, the liquid film effectiveness is held constant, whereas the reference entrainment factor is varied between 0.025 and 0.06. One can observe that a higher entrainment factor increases the wall temperature. Within the studied range, the maximum service temperature of the wall is not exceeded. In the plot on the right, the reference entrainment factor is kept constant and the liquid film effectiveness is varied. By lowering the liquid film effectiveness, the dry-out point moves upstream. From the illustration, one can conclude that a 15% reduction in liquid film effectiveness is possible before the maximum service temperature of the wall is exceeded.

Whether or not a maximum uncertainty of 15% in the liquid film effectiveness offers sufficient margin for the design of the AM Mk-II engine is not known at this phase of the design. However, if the reduction in the liquid film effectiveness turns out to be even higher than 15%, the film flow fraction could be increased to satisfy thermal constraints. If this fraction is increased, more of the hydrogen peroxide is used in the film layer and, consequently, less in the core stream. Therefore, a further drop in specific impulse can be expected, as shown in Figure 5.17. This sensitivity study shows the predicted sea level and vacuum specific impulse, as a function of the film cooling fraction. The plots are evaluated at a chamber pressure of 5 MPa based on shifting equilibrium flow conditions in CEA. Moreover, a thrust coefficient efficiency of 96% and core stream characteristic velocity efficiency of 99% are used.

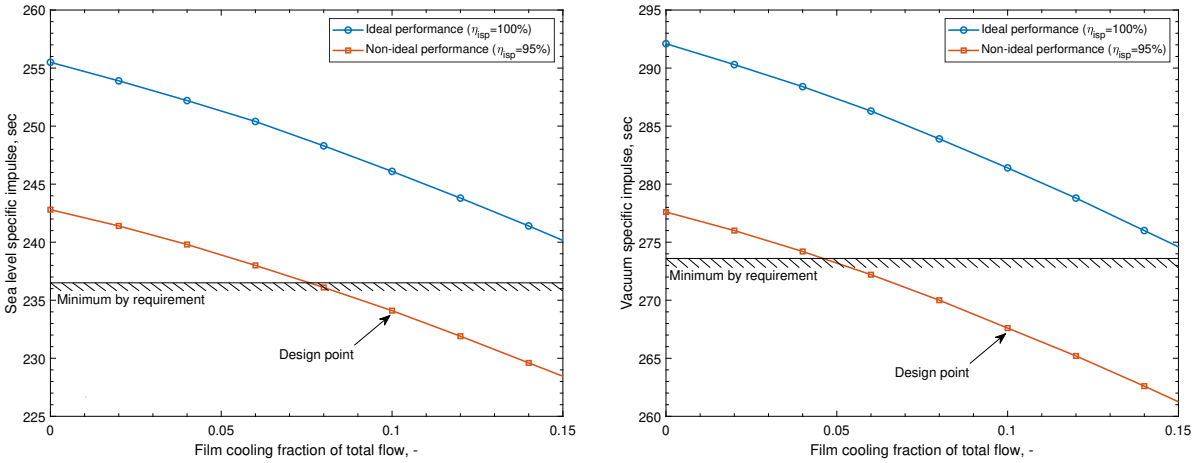

Figure 5.17: Parameter study showing the impact of film cooling on the specific impulse for the AM thrust chamber.

The results of the sensitivity study confirm the expected reduction in specific impulse at higher film flow rates. Besides, one may observe that the design point for the AM chamber based on non-ideal performance calculations does not comply with customer requirements REQ-003 and REQ-004. Simulations show that it is only possible to meet these requirements at a film fraction less than 0.06. At these film fractions, it is not possible to operate the chamber at an acceptable wall temperature. The ideal performance, on the other hand, does comply with customer requirements at the selected thruster operating point. This demonstrates that the proposed design *is* capable of meeting customer requirements if the specific impulse efficiency turns out to be higher than the assumed value of 95%. Whether or not this higher efficiency is achievable must be demonstrated in hot-fire tests.

5.4. Comparison of Design Options

In this section, the bimetallic reference design is compared to the proposed AM design solutions. First, in subsection 5.4.1, the impact on dry mass and interfaces are discussed. Second, in subsection 5.4.2, the pressure budget of the different design options are compared. This is followed by a comparison of the most important performance figures, in subsection 5.4.3. Lastly, compliance with customer requirements is discussed in subsection 5.4.5.

5.4.1. Impact on Dry Mass and Interfaces

In TDCAS, a simplified mass estimation is performed, which is based on the volume of the chamber liner and structural closeout. These volumes are directly obtained from surface areas of the planar mesh and axial spacing. It is worth noting that this mass estimation is optimistic and does not include mass components of the coolant manifolds and injector flange. For the AM Inconel 718 chamber without film cooling, the estimated dry mass is 856 grams. As a consequence of the higher chamber pressure (5 MPa versus 2 MPa), a shorter chamber barrel length can be used in the AM design with film cooling. The estimated mass for this design solution is 534 grams.

The mass estimation of the bimetallic reference design is slightly more sophisticated, owing to the different manufacturing and assembly techniques that are used in this assembly. As explained in the introduction to this report, the current Mk-II design is based on a removable copper alloy liner which is placed in a cylindrical structural closeout. The empty volume in the convergent and divergent section of the nozzle is occupied by a two-piece aluminum insert. Although the exact internal features of the Mk-II thruster cannot be disclosed, the reader can assume that these compare well with the design of Jones [113], which is depicted in Figure 5.18 on the left. The primary differences between the design of Jones and the Mk-II are the dimensions of the chamber and cooling channels, as well as the metal alloys that are used for the fabrication.

For the bimetallic reference engine, the mass estimation is based on a NARloy-Z liner, a two-piece aluminum nozzle insert, and a cylindrical Inconel 718 structural jacket. The structural jacket is not shown in Figure 5.18 on the left, but can clearly be distinguished in Figure 5.18 on the right. The estimated masses are 534 grams for the liner, 1044 grams for the nozzle insert, and 501 grams for the structural closeout. This adds up to a total dry mass of 2079 grams. It is worth mentioning that the calculation of the nozzle insert does not include the presence of (threaded) bolt holes or o-ring grooves. For reference, if the chamber was realized with the closeout directly deposited on the NARloy-Z liner (similar to the Vulcain engine, shown in Figure 1.2), the dry mass equals 904 gram. This is still higher than the proposed AM Inconel 718 design with film cooling.

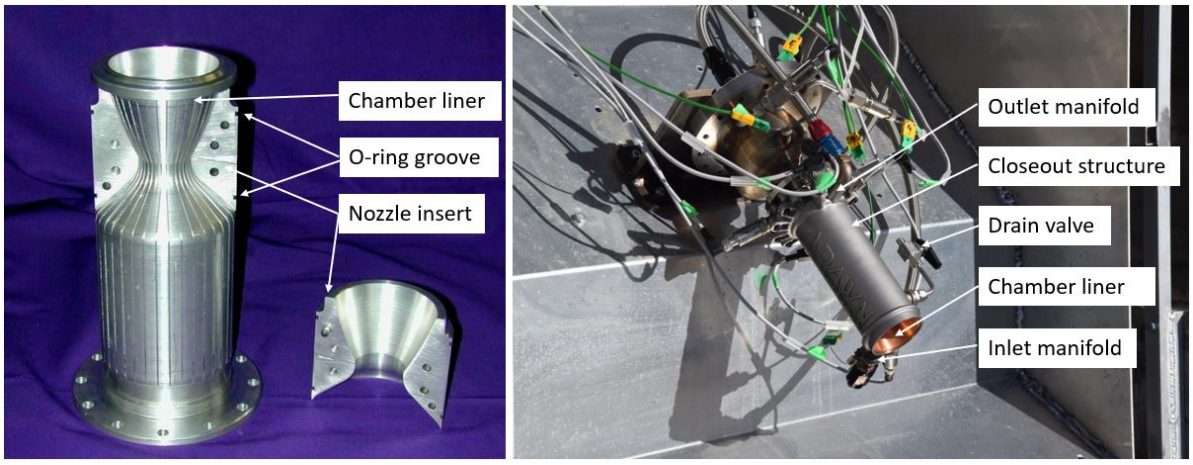

Figure 5.18: Left: thrust chamber design of Jones, with removable liner, nozzle insert and (not shown) cylindrical structural closeout (adapted from ref. [113]). Right: Mk-II thrust prior to hot-fire test.

The second part of this section covers the number of interfaces in the assembly. As the name suggests, the integral Inconel 718 thrust chamber consists of one single part with no internal sealing interfaces between the liner and closeout. Nevertheless, based on the high-level feed system diagram depicted in Figure 4.10, three sealing interfaces remain in the design, which are located at:

- The coolant inlet manifold, which connects the cooling jacket to the feed system between the chamber and the pump,
- The coolant outlet manifold, which connects the cooling jacket to the feed system between the chamber and the catalytic reactor,
- The injector flange, which connects the thrust chamber to the propellant injector.

It is worth mentioning that it *is* possible to integrate the propellant injector into the thrust chamber assembly during the AM fabrication process. This could remove the sealing interface between the injector and thrust chamber. Nevertheless, this introduces several major risks in the development. For instance, when the AM built fails, both the chamber and injector are discarded, which is much more expensive. Furthermore, when the injector is integrated into the thrust chamber assembly, quality inspection or post-machining of the inner chamber wall is only possible via the nozzle throat, which is not practical (considering that the throat diameter is less than 2 cm). Last but not least, when the injector is integrated into the thrust chamber assembly, the designer has much less freedom to implement changes during the hot-fire tests (for example, changing the propellant/film coolant injector)

In the bimetallic reference engine, the aforementioned three interfaces are also present, as depicted in Figure 5.18 on the right. Added to this are two o-rings for sealing between the nozzle insert and closeout and two o-rings for sealing between the removable chamber liner and closeout. As a result, the design counts seven sealing interfaces. Moreover, a drain valve is required between the two o-rings around the nozzle insert, to avoid the creation of an enclosed volume where hydrogen peroxide can accumulate. This drain valve is not required in the integral chamber design.

5.4.2. Impact on Pressure Budget

The pressure budget for the bimetallic reference engine and two AM designs is presented in Table 5.1. Pressure loss components for the injector, catalytic reactor, and upstream feed system are based on assumptions mentioned earlier in subsection 5.1.1. The established pressure budget is based on an equivalent sand grain roughness of 6 µm in the bimetallic chamber and 121 µm in the AM chamber. From the presented pressure budget, it can be concluded that the required pump pressure for all designs is below the available pump pressure of 9.3 MPa at a hydrogen peroxide mass flow rate of 1 kg/s. The reason for the higher pressure drop in the machined channels of the bimetallic design can be traced to the substantially higher coolant flow velocity, which was also discussed in section 5.3.

Table 5.1: Estimated pressure budget for the proposed engine designs. All pressures are in MPa.

Parameter	Reference bimetallic	AM integral no film	AM integral with film
Chamber pressure	5.00	2.00	5.00
Pressure drop injector	0.75	0.30	0.90
Pressure drop catalytic reactor	1.00	1.00	1.00
Pressure drop cooling passage	2.15	1.67	1.70
Pressure drop upstream feed system	0.03	0.03	0.03
Required pump pressure	8.93	5.00	8.63

5.4.3. Impact on Performance Figures

A comparison of all important operating and performance parameters of the bimetallic reference design and proposed AM designs are listed in Table 5.2. The estimated characteristic velocity, thrust coefficient, and specific impulse are based on an analysis in CEA, assuming shifting equilibrium flow conditions. All performance figures that are used in this table are based on non-ideal performance, with assumed quality factors noted in the table footnote.

Table 5.2: Comparison of the bimetallic reference design to the proposed additive manufactured integral designs.

Parameter	Reference bimetallic	AM integral no film	AM integral with film
Nominal chamber pressure, MPa	5.0	2.0	5.0
Mixture ratio	8.0	8.0	8.0
Contraction ratio	13.9	5.6	13.9
Expansion ratio	11.2	5.5	11.2
Characteristic velocity(1), m/s	1588	1580	1531
Thrust chamber dry mass, kg	2.08	0.86	0.53
Propellant flow rates			
a. Fuel (core), g/s	125	125	125
b. Oxidizer (core), g/s	1000	1000	888
c. Oxidizer (film), g/s	0	0	112
Sea level performance			
a. Thrust coefficient(2)	1.50	1.35	1.50
b. Thrust force, kN	2.70	2.46	2.70
c. Specific impulse, sec	242.2	217.1	233.5
Vacuum performance			
a. Thrust coefficient(2)	1.72	1.62	1.72
b. Thrust force, kN	3.11	2.92	3.11
c. Specific impulse, sec	278.5	261.4	268.5

(1) Based on an assumed value for the core flow characteristic velocity of 0.99.

(2) Based on an assumed value for the thrust coefficient efficiency of 0.96.

From Table 5.2, one can conclude that the specific impulse of the reference thruster bimetallic thruster is highest, at the target chamber pressure of 5 MPa. The application of a film coolant in the AM design greatly reduced the characteristic velocity, and consequently the specific impulse. The proposed design is, however, still more competitive than the AM solution without film cooling.

The combined impact of the thrust chamber dry mass and specific impulse on the overall design of the Mk-II vehicle can be assessed when considering the available delta-v (Δv). The available Δv embodies the maximum velocity change that can be obtained by the vehicle in a vacuum when expelling the propellants. The available Δv is calculated using the classical Tsiolkovsky equation, noted in Equation 5.4.

$$\Delta v = I_{sp} g_0 \ln\left(\frac{M_1}{M_0}\right) = I_{sp} g_0 \ln\left(\frac{M_{dry} + M_{prop} + M_{pay}}{M_{dry} + M_{pay}}\right) \tag{5.4}$$

In Equation 5.4, I_{sp} denotes the vacuum specific impulse, g_0 the gravitational acceleration at sea level, M_{dry} the dry mass of the vehicle, M_{prop} the propellant mass, and M_{pay} the payload mass. The Mk-II spaceplane has a maximum take-off weight (M_1) of 280 kg and a maximum payload mass of 4 kg. Equipped with the bimetallic thrust chamber, the vehicle has an operational empty weight of 75 kg. Thus:

- For the bimetallic reference design, the vehicle dry mass is 75 kg. At a specific impulse of 278.5 sec and maximum payload mass of 4 kg, this results in a total **available Δv of 3.46 km/s**.
- For the AM design without film cooling, the vehicle dry mass is 73.8 kg. At a specific impulse of 261.4 sec and maximum payload mass of 4 kg, this results in a total **available Δv of 3.28 km/s**.
- For the AM design with film cooling, the vehicle dry mass is 73.5 kg. At a specific impulse of 268.5 sec and maximum payload mass of 4 kg, this results in a total **available Δv of 3.38 km/s**.

Clearly, the available Δv for the spaceplane powered by the AM thrust chambers is inferior to the available Δv when using the bimetallic reference thruster. Since the AM chambers are much lighter, more propellants can be taken onboard. Under the assumption that the storage tank dry mass remains constant, this increase in propellant mass is depicted in Figure 5.19 on the right. This plot reveals that

the propellant mass which can be taken onboard is approximately 1.1-1.3 kg higher when powering the spaceplane with one of the AM chamber designs. Nonetheless, the larger propellant capacity of the AM designs still yields a Δv that is inferior to that of the bimetallic reference design, as illustrated in Figure 5.19 on the left. The is primarily caused by the higher specific impulse that is achieved with the bimetallic reference engine.

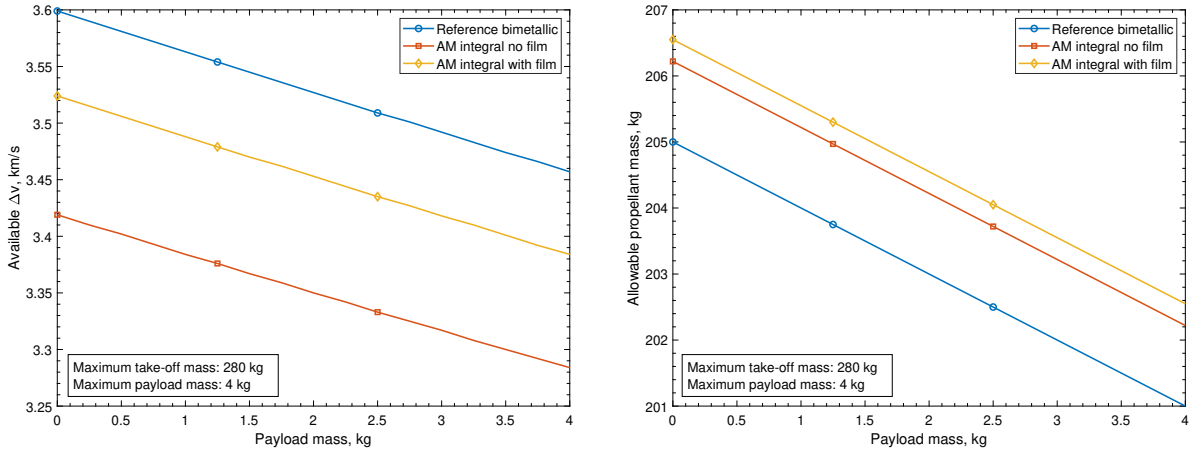

Figure 5.19: Available Δv and allowable propellant mass for the proposed engine designs.

Based on Figure 5.19 and the detailed comparison in Table 5.2, it is concluded that - from a vehicle performance perspective - it is not advantageous to change the copper-based bimetallic design to an integral Inconel 718 design. Bear in mind that this conclusion is based on the Mk-II spaceplane and may not be valid for vehicles that have a different mission profile.

5.4.4. Impact on Non-Technical Performance

The true strength of AM lies in the fact that the designer can rapidly turn a design concept into a functional prototype. On the contrary, “traditional” manufacturing techniques, such as machining, casting, and forming, often require a large initial investment to start up the production process. These production techniques often excel over AM at large production volumes but are less cost-effective for small production volumes [114]. A practical example of this is the copper alloy liner of the Mk-II thruster, which is realized with CNC machining techniques. Before manufacturing, a skilled operator programs the toolpath of the CNC machine, which is a time-consuming undertaking. Hereafter, the machine automatically follows the programmed path and removes the material from the copper alloy, until the chamber liner is realized. Provided that the liner design, wrought material, and machining tools remain unchanged, one can avoid expensive re-programming of the machine. The liner production process of the Mk-II clearly demonstrates a (relatively) high upfront investment, with decreasing costs for every consecutive part that is realized.

Whether or not the production of the AM thrust chamber with film cooling is more cost-effective than the current Mk-II thrust chamber design cannot be said in this phase of the design. Although the production costs for the current Mk-II thruster are well known, the production costs of the proposed AM design are not. The reader must be aware that the costs that are involved with the production of an AM thrust chamber stretch far beyond the costs of feedstock procurement and AM machine operation. These combined costs for several AM alloys were listed in Table 1.2. There are many other cost components associated with AM of thrust chambers, which must be considered in the estimations. Examples include buildshare[6], powder removal, hot isostatic pressing[7], heat treatments, CT scans, etc. Besides, functional (sealing) surfaces often still require post-built machining operations to improve the surface finish, which also increases the overall production costs.

[6]For parts that do not cover the full build plate of the AM machine, most commercial vendors offer the opportunity to share the build plate with parts of different customers. This usually results in lower production costs but provides less flexibility concerning the placement of the parts on the build plate.

[7]This is frequently used for densification of the part.

Several production steps, such as machining of the nozzle insert and electroplating of the copper alloy liner, can be avoided in the integral AM thrust chamber, as illustrated in Figure 5.20. At first hand, one could envision that the reduction in fabrication steps results in a reduction in production cost. However, one must take into consideration that AM removes some of the production steps, but also *introduces* new steps, such as powder inspection, powder removal, hot isostatic pressing, or CT scanning. These steps are not presented in Figure 5.20 but do contribute to the production time and cost. A detailed overview of the end-to-end production cycle and involved fabrication steps is presented in a recent publication of the author [11] and not repeated here.

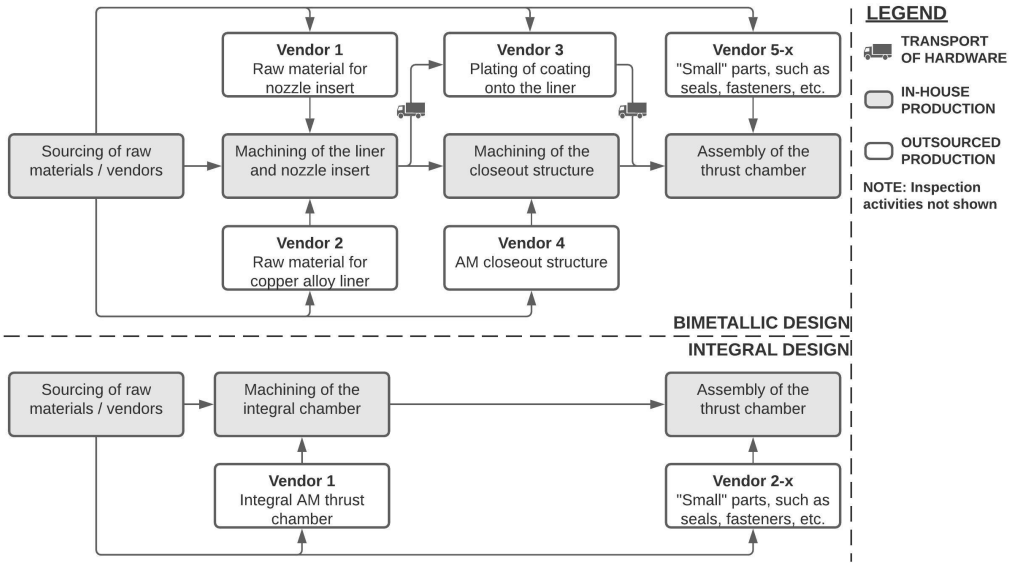

Figure 5.20: High-level production steps of the bimetallic and AM thrust chamber (inspections and sub-processes not shown).

One advantage that can be distinguished from Figure 5.20 is that the integral AM thrust chamber likely requires fewer parts to be sourced/procured, as a consequence of the lower part-count of the structure. Sourcing of materials and subcontractors is a time-consuming undertaking, which can have a large impact on the overall cost of the production process[8]. Outsourced AM parts are also noted to have shorter lead times compared to parts realized with traditional manufacturing processes [13]. This could also be seen as an additional non-technical performance advantage of AM parts, which ties in closely with rapidly turning a design concept into a functional prototype.

5.4.5. Compliance with Customer Requirements

As a final step of comparison, the compliance with customer requirements is evaluated for each design, as listed in Table 5.3. It is important to addresses that for all requirements, compliance is assessed *by design*, which is the best that can be done in this phase of the project. Experiments with the proposed thrust chamber are required to fully conclude on the compliance with customer requirements.

Based on the assumed specific impulse efficiency of 95%, the AM thrust chamber design with film cooling does not meet customer requirements REQ-003 and REQ-004. An increase in the sea level specific impulse of 3 seconds and a vacuum specific impulse of 5.1 seconds is required to satisfy the customer. This increase is reasonably small and assumed to be possible upon optimization of the injector and nozzle. Therefore, this requirement is labeled “correctable deficiencies”. For the AM design without film cooling, a sea-level specific impulse gap of 19.4 seconds and a vacuum specific impulse gap of 12.2 seconds must be bridged. The former increase is physically not possible without adjusting the chamber pressure (this would exceed the ideal specific impulse at sea level).

Lastly, since the linear elastic finite element analysis proved to be unsuitable for the Mk-II modeling application, the useful life of the thrust chamber could not be assessed. To numerically assess the useful chamber life, an elastoplastic (low cycle) fatigue analysis is required, which is not considered in this thesis. Therefore compliance with REQ-009 to REQ-011 remains undetermined.

[8] One often wants to source the most cost-effective parts, which typically requires consultation at multiple subcontractors.

Table 5.3: Requirement compliance matrix (by design) for the proposed Inconel 718 additively manufactured chamber design.

Identifier	Description	Reference bimetallic	AM integral no film	AM integral with film
REQ-001	The engine shall produce a thrust of at least 2300 N at sea level.	Met	Met	Met
REQ-002	The engine shall produce a thrust of at least 2700 N in vacuum.	Met	Met	Met
REQ-003	The engine shall have a specific impulse greater than 236.5 s at sea level.	Met	Not met	Correctable deficiencies
REQ-004	The engine shall have a specific impulse greater than 273.6 s in vacuum.	Met	Not met	Correctable deficiencies
REQ-005	The engine shall operate using stabilized 90% high test peroxide as oxidizer.	Met	Met	Met
REQ-006	The engine shall operate using kerosene as fuel.	Met	Met	Met
REQ-007	The engine shall operate at a chamber pressure between 40 and 120 bar.	Met	Not met	Met
REQ-008	The engine shall have a dry mass of no more than 12 kg.	Met	Met	Met
REQ-009	The engine shall survive a continuous operation of no more than 300 s.	Undetermined	Undetermined	Undetermined
REQ-010	The engine shall survive 10 restarts with an accumulated burn time of no more than 1500 s, without replacement of consumables.	Undetermined	Undetermined	Undetermined
REQ-011	The engine shall survive 100 restarts with an accumulated burn time of no more than 25000 s, without major overhaul.	Undetermined	Undetermined	Undetermined

5.5. Discussion

In this section, the sub-questions that are posed in the introduction of this report are answered. The answers to these individual questions are used to answer the primary research question, in chapter 6.

1. What is the short duration compatibility of the AM alloy with 90% hydrogen peroxide?
In this thesis, immersion screening tests are conducted with AM Inconel 718 test articles. The tests are executed at ambient conditions for seven days and at a temperature of 343 K for seven hours. Results show no major signs of decomposition at ambient conditions. On the other hand, tests at 343 K reveal a concentration loss of 18.6 percentage point for samples with immersed Inconel test articles and 16.6 percentage point for a control group with no immersed test article. This suggests that the concentration loss is primarily driven by the temperature, rather than the presence of the Inconel test article. Post-test inspections also revealed no signs of bronzing on the surface of the AM test articles.

2. Is it required to passivate the AM alloy before exposure to 90% hydrogen peroxide?
During the immersion screening tests, one experiment was prepared with unpassivated AM Inconel 718. Surprisingly, a smaller concentration loss was observed after seven days at ambient temperature. Nevertheless, differences with the passivated test article lie within the measurement error. More experiments are required to fully quantify the impact of surface passivation on chemical compatibility.

3. What is the (hydraulic) surface roughness of the AM alloy?
Based on an experimental data set of Stimpson et al. [25] and Wildgoose et al. [76], the estimated equivalent sand grain roughness in small AM Inconel 718 with a hydraulic diameter between 0.63 mm and 1.31 mm is 121 µm. This value represents the average of a data set of rectangular and circular build angles fabricated at an angle between 45° and 90°. A reduction in surface roughness is observed when the build angle approaches 90°. Yet, no clear correlation between surface roughness and build angle was observed in the data set at hand.

4. How can the steady-state thermal-mechanical loading of the thrust chamber wall be simulated?

1. **Which semi-empirical model is suitable to predict the gas-side heat transfer?**
   In this study, two frequently used semi-empirical heat transfer correlations are compared for the hot gas convective heat transfer: the method of Bartz and Cinjarew & Dobrovolsky. Results obtained from these two modeling approaches are compared to experimental data of the Mk-II thruster, a small bipropellant rocket engine propelled by 90% hydrogen peroxide and kerosene. The comparison of the two models revealed a consistent underprediction of the heat transfer when using the model of Cinjarew & Dobrovolsky. The results obtained from the Bartz equation showed a better correlation with the test data.

2. **Which semi-empirical model is suitable to predict the coolant side heat transfer?**
   In this study, the modified Nunner, Norris, and Dipprey-Sabersky correlations are compared for resolving the coolant heat transfer. All three expressions are based on fluid flow in channels with high surface roughness. The three models are compared to heat transfer experiments in small AM Inconel 718 channels. The Reynolds numbers and channel dimensions at which these tests are conducted compare fairly with the operating conditions of the Mk-II thruster. The modified Nunner and Dipprey-Sabersky equations show a comparable overpredicting trend of the Nusselt number, with an average deviation of 14.1% and 19.9% respectively. On average, the correlation of Norris provides a 35% deviation, which is much larger. In the context of the Mk-II thruster, which uses hydraulically smooth cooling channels with hydrogen peroxide as coolant fluid, the modified Nunner provides the most accurate prediction.

3. **Can a linear elastic structural model be used to predict the stress in the wall introduced by the combined thermal and hydraulic loads?**
   No, it is not possible to use a linear elastic structural model to resolve the stresses in the application of a Mk-II size thruster. When one only considers the strains introduced by the pressure loads, the obtained solution lies well within the yield surface. However, the coupling of the thermal domain introduces thermal strains in the structure that are several orders of magnitude larger than the pressure-induced strains. As a result, plastic deformation of the wall occurs, which is not captured in a linear elastic model. The plastic strains are only observed in the wall which separates the coolant from the hot gas. This corresponds to the location where the thermal gradient is highest. The linear elastic model could potentially be of use in structures that see much smaller thermal gradients in the wall, such as radiation-cooled thrust chambers or nozzle extensions.

For modeling the steady-state thermal loading in the chamber wall of a hydrogen peroxide-cooled thruster, the correlation of Bartz, combined with the modified Nunner model for coolant convection, seems most reasonable for a preliminary design. An important note that must be placed, is that all hot-fire results considered in this thesis are based on the *integrated* hydrogen peroxide heat load, in cooling channels with a low surface roughness (6 µm). This means that transfer to the coolant fluid is evaluated at the inlet near the nozzle exit plane and outlet at the injector plane. Therefore, *local* heat transfer trends, for example, close to the injector, cannot be validated.

For modeling the steady-state structural loading in the chamber wall, a linear elastic analysis is unsuitable. It is recommended to use an elastoplastic solver in future research for predicting the temperature- and pressure-induced stress in the chamber wall.

5. What is an adequate cooling configuration for an integral AM thrust chamber that meets customer requirements?

1. **Which parameters constrain the feasible operating space of the thruster?**
   This depends on the chamber material. For the bimetallic reference Mk-II design, which is based on a NARloy-Z liner, the maximum operating regime is primarily constrained by the heat transfer to the hydrogen peroxide coolant. This design requires high coolant velocities to satisfy the burnout heat transfer constraints. As a result, a high pressure drop is present in the cooling passages, which challenges the available pressure budget.

For the AM Inconel 718 design, the design space is primarily constrained by heat transfer in the chamber wall. Physically, this translates to limits imposed for the minimum wall thickness and maximum service temperature of the material. Based on the imposed constraints, operation of the thrust chamber at high pressures ($\gg$2 MPa) is not possible without the use of a film coolant that isolates the hot gas from the chamber wall.

2. **Can film cooling extend the operating regime of the proposed design?**
   Yes, simulations show that the AM Inconel 718 chamber can be operated at a pressure equal to that of the current bimetallic Mk-II engine. Based on the simulations with a hydrogen peroxide film-coolant, it is concluded that 10% of the total mass flow rate must be used for film cooling to operate the chamber at a pressure of 5 MPa. Hot-fire tests at this operating point are required to validate the proposed design solution.

The proposed Inconel 718 chamber operates at a pressure of 5 MPa and relies on both regenerative cooling and film cooling to keep the chamber wall at acceptable temperatures. Simulations show that a hydrogen peroxide film flow rate of 112 g/s is sufficient for the long-duration operation of the chamber. A secondary design, which relies only on regenerative cooling, is also proposed. Simulations show that this design can operate at a chamber pressure up to 2 MPa, which is substantially lower than the design with film cooling.

6. How does the proposed AM thrust chamber design compare to the current bimetallic thrust chamber used in the Mk-II spaceplane?
This sub question is answered based on the “reference Mk-II thruster”, discussed in in section 5.2, not the real Mk-II thruster.

1. **Which interfaces can be removed in the proposed AM design?**
   All, except the sealing interfaces at the injector, coolant inlet manifold, and coolant outlet manifold. The current bimetallic design counts seven sealing interfaces. Four of these interfaces can be removed in the AM design.
2. **How does the dry mass of the proposed AM design differ from the current design of the Mk-II?**
   The predicted dry mass of the bimetallic chamber is 2.08 kg. The AM Inconel 718 design with film cooling has an estimated dry mass of 0.53 kg. Both mass estimations do not consider the injector flange, coolant inlet manifold, and coolant outlet manifold.
3. **How does the coolant pressure drop of the proposed AM design differ from the current design of the Mk-II?**
   The pressure drop in the cooling passages of the reference design is 2.15 MPa, at a surface roughness of 6 µm. On the contrary, the pressure drop in the cooling channels of the film-cooled AM design is 1.70 MPa, at an assumed surface roughness of 121 µm. The higher pressure drop in the bimetallic design is a consequence of the much higher coolant flow velocity (almost twice as high).

To capture the impact of both the dry mass and specific impulse, the available Δv was calculated in the context of the Mk-II spaceplane. Compared to the current bimetallic chamber design, which has a total available Δv of 3.46 km/s at a payload mass of 4 kg, the proposed AM Inconel 718 design with film cooling has a total available Δv of 3.38 km/s, at the same payload mass. From a Δv perspective, the proposed AM design with film cooling is inferior to the bimetallic copper design.

The strength of the AM solution lies in the fact that only one single part is required for the thrust chamber, rather than an assembly with many sealing interfaces. This greatly simplifies the assembly steps and reduces the number of potential leak paths. Moreover, with AM, the designer can rapidly turn a design concept into a functional prototype. With traditional manufacturing techniques, high upfront investments are often required, which makes this process less suitable for rapid prototyping.

6

Conclusions and Recommendations

A startup new-space company, Dawn Aerospace, is developing a 2.5 kN class bipropellant thruster propelled by 90% hydrogen peroxide and kerosene, which is used in the application of a sub-orbital spaceplane, designated Mk-II. The thruster used in the Mk-II vehicle is regeneratively cooled with hydrogen peroxide and consists of a copper alloy liner with electroplated coating, that is placed inside a high-strength closeout structure. For the second iteration of this thruster, Dawn Aerospace wants to investigate the use of an integral additively manufactured (AM) design, rather than a bimetallic structure. Therefore, the following research question is addressed:

"Is it advantageous to realize the thrust chamber of a small, hydrogen peroxide cooled, rocket engine as an integral additively manufactured structure, instead of a bimetallic structure created with traditional manufacturing methods?"

The question is investigated in the context of a bimetallic structure, comprised of NARloy-Z and Inconel 718, and an integral structure, comprised of AM Inconel 718.

When purely looking at the expected performance of the thruster, in terms of specific impulse and vacuum Δv (delta-v), it is not advantageous to realize the chamber as an AM Inconel 718 structure. When operated at a chamber pressure of 5 MPa, a bimetallic thrust chamber with NARloy-Z liner can be operated in steady-state whilst relying solely on regenerative cooling with hydrogen peroxide. For the AM Inconel 718 chamber design, a combination of regenerative cooling and film cooling with hydrogen peroxide is required. In the context of the Mk-II spaceplane carrying a 4 kg payload, the total available Δv decreases from 3.46 km/s to 3.38 km/s when the bimetallic design is replaced with the AM design. To achieve the same Δv, the payload mass or vehicle dry mass must be reduced. The predicted dry mass of the AM thrust chamber is almost 75% lower. This decrease in dry mass is, however, not sufficient to achieve a comparable available Δv (a further reduction of the vehicle dry mass is necessary).

When ease of manufacturing and integration are also taken into account, the AM Inconel 718 chamber becomes a more competitive alternative to the bimetallic NARloy-Z/Inconel 718 chamber. The current bimetallic chamber design that is used by Dawn Aerospace is troubled by many sealing interfaces. The use of an integral AM design can reduce the total number of seals required by more than 50%. As a consequence of the poor chemical compatibility of hydrogen peroxide with copper-containing alloys, a proprietary coating is required on the cooling channels, which physically separates the copper alloy liner from the hydrogen peroxide in the bimetallic chamber. This coating requires rigorous inspection in-between hot-fire tests, which increases the turnaround time and costs. As a result of the (demonstrated) superior chemical compatibility of Inconel 718 with hydrogen peroxide, such a proprietary coating is not required in the AM design.

An important limiting factor to address in the research question is that the thrust chamber must be "hydrogen peroxide cooled". Due to the poor chemical compatibility of hydrogen peroxide with many highly conductive metal alloys, the AM design space is very narrow. As a result, the answer to the research question could be different when other propellants are considered for cooling.

Based on the outcome of this research, several recommendations are posed. First listed are recommendations for the future development of the AM Mk-II thruster:

- **Hot-fire test the proposed design solution.** This is required to fully validate the proposed design. The recommended steps for this hot-fire test campaign are briefly discussed in Appendix A.
- **Measure local heat transfer effects**. The current test setup of Dawn Aerospace only measures the coolant temperature and mass flow rate at the nozzle exit plane and injector plane. This setup allows designers to assess the integrated heat load, whereas local heat transfer in sections of the chamber remains unknown. To get a better insight into the heat transfer in the Mk-II thruster, it is recommended to develop a demonstrator engine with multiple cooling loops (calorimetric setup), or include thermocouples in the ribs of the thrust chamber liner (where possible). This way local heat transfer effects can be measured, which is valuable information for the validation of any thrust chamber thermal design software.
- **Conduct more hot-fire tests with water as coolant**. Almost all test data available for this thesis is based on hydrogen peroxide as a coolant. Upon validation, it was hypothesized that some of the hydrogen peroxide could have decomposed in the cooling channels. Nevertheless, the data at hand is not conclusive. If more tests are conducted with (stable) water as a coolant, this data could be compared to experiments with a hydrogen peroxide regenerative coolant. This way, potential decomposition effects can be quantified.
- **Measure the thrust force**. The current Mk-II test data only allows for a prediction of the experimental characteristic velocity. When the test setup is extended to include load cells for thrust force measurements, the thrust coefficient can also be determined. This way the proposed model can be adjusted to account for the real thrust coefficient efficiency, rather than typical values described in the literature.
- **Experiment with thermally stressed hydrogen peroxide in rough conduits**. These experiments can be used for further valuation of the hydrogen peroxide rough-channel Nusselt correlations. Besides, these experiments may further our understanding concerning the safe operating conditions of concentrated hydrogen peroxide in regenerative cooling applications. A good starting point for these experiments is the test apparatus developed by Rousar & Van Huff [71], in which the commercially smooth Inconel 718 could be replaced by AM Inconel 718 tubes.

Additionally, several recommendations are posed for future developments of the developed Two Dimensional Combustor Analysis Software (TDCAS):

- **Improve the structural analysis model**. This thesis has demonstrated that a linear elastic structural model cannot be used for predicting the stress, and consequently (low cycle) fatigue life, in the wall of the thrust chamber. For future research, it is recommended to extend the developed software to solve the displacement field in the wall based on elastoplasticity and (potentially) creep effects. These simulations could be used for numerical assessment of the chamber life, which is vital information for reusable propulsion systems.
- **Improve the hot gas heat transfer prediction**. The modeling approaches that are used in TDCAS are based on simple 1-D Nusselt correlations. A more accurate model would include the effects of the propellant injector and region upstream of the nozzle where the flow is not yet fully developed. This could, for example, be achieved by implementing a 2-D boundary layer code.
- **Include the upstream feed system and transients**. Dawn Aerospace has readily developed transient heat transfer codes for in-space micro-propulsion devices, as well as simulation tools for predicting the fluid flow in the feed system tubing and turbomachinery. It would be interesting to add all these codes to TDCAS. This way, the full burn of the thruster, including start-up and shut-down transients, can be resolved. This also requires the 2-D thermal solver in TDCAS to be extended to a 2-D transient thermal solver.

All in all, TDCAS provides a solid, object-oriented, baseline that can be used for many future thruster heat transfer simulations. The versatility of the developed code also allows the user to simulate different propellant combinations and thrust chamber materials. This makes the TDCAS interesting for rapid concept evaluation in the preliminary design phase of liquid rocket engines.

Bibliography

[1] Euroconsult. Prospects for the small satellite market, 4th edition, 2018.

[2] M. Tugnoli, M. Sarret, and M. Aliberti. *European access to space: business and policy perspectives on micro launchers*. Springer, Berlin, Germany, 2019.

[3] N. Nimmerfroh, D. Pauls, and S. McMahon. PROPULSE™ hydrogen peroxide: manufacture, quality, transportation & handling. In *36th AIAA/ASME/SAE/ASEE Joint Propulsion Conference and Exhibit*, 2000.

[4] F. Kerstens. Optimization of additive manufactured thrust chamber with reactive coolant for specific impulse and mass. Lit. study, Delft University of Technology, 2020.

[5] R. Quentmeyer, H. Kasper, and J. Kazaroff. Investigation of the effect of ceramic coatings on rocket thrust chamber life. In *14th Joint Propulsion Conference*, 1978.

[6] R. T. Cook. Advanced cooling techniques for high-pressure hydrocarbon-fueled engines. Tech. rep. NASA-CR-159790, Rockwell International Corp., 1979.

[7] D. K. Huzel and D. H. Huang. *Modern engineering for design of liquid-propellant rocket engines*. American Institute of Aeronautics and Astronautics, Washington, D.C, 1992.

[8] R. L. Ewen and H. M. Eversen. Liquid rocket engine self-cooled combustion chambers. Spec. pub. NASA-SP-8124, National Aeronautics and Space Administration, 1977.

[9] R. J. Quentmeyer. Rocket combustion chamber life-enhancing design concepts. In *26th AIAA/SAE/ASME/ASEE Joint Propulsion Conference*, 1990.

[10] P. R. Gradl and C. S. Protz. Technology advancements for channel wall nozzle manufacturing in liquid rocket engines. *Acta Astronautica*, 174, 2020.

[11] F. Kerstens, A. Cervone, and P. Gradl. End to end process evaluation for additively manufactured liquid rocket engine thrust chambers. *Acta Astronautica*, 182, 2021.

[12] A. A. Shapiro, Q. N. Borgonia, J. P. Chen, R. P. Dillon, B. McEnerney, R. Polit-Casillas, and L. Soloway. Additive manufacturing for aerospace flight applications. *Journal of Spacecraft and Rockets*, 53(5), 2016.

[13] P. Gradl et al. Additive manufacturing of liquid rocket engine combustion devices: a summary of process developments and hot-fire testing results. In *AIAA Propulsion and Energy Forum*, 2018.

[14] N. Patel, S. Standbridge, M. Van den Berghe, and V. Devalaraju. Design and additive manufacturing considerations for liquid rocket engine development. In *AIAA Propulsion and Energy 2019 Forum*, 2019.

[15] P. R. Gradl, C. S. Protz, and T. Wammen. Additive manufacturing and hot-fire testing of liquid rocket channel wall nozzles using blown powder directed energy deposition Inconel 625 and JBK-75 alloys. In *AIAA Propulsion and Energy 2019 Forum*, 2019.

[16] P. R. Gradl, C. Protz, K. Zagorski, V. Doshi, and H. McCallum. Additive manufacturing and hot-fire testing of bimetallic GRCop-84 and C-18150 channel-cooled combustion chambers using powder bed fusion and Inconel 625 hybrid directed energy deposition. In *AIAA Propulsion and Energy Forum*, 2019.

[17] S. Moriya et al. Feasibility study on additive manufacturing of liquid rocket combustion chamber. *Transactions of the Japan Society for Aeronautical and Space Sciences, Aerospace Technology Japan*, 16(3), 2018.

[18] Inovar Communications Ltd. Metal additive manufacturing and the new space race: the inside track with Launcher and AMCM. *Metal AM*, 6(4), 2020.

[19] J. Tulp and P. Beck. Rocket Lab: liberating the small satellite market. In *31st Annual AIAA/USU Conference on Small Satellites*, 2017.

[20] P. R. Gradl, S. E. Greene, C. S. Protz, D. Ellis, B. A. Lerch, and L. E. Locci. Development and hot-fire testing of additively manufactured copper combustion chambers for liquid rocket engine applications. In *53rd AIAA/SAE/ASEE Joint Propulsion Conference*, 2017.

[21] P.R. Gradl, C. Protz, K. Cooper, C. Garcia, D. Ellis, and L. Evans. GRCop-42 development and hot-fire testing using additive manufacturing powder bed fusion for channel-cooled combustion chambers. In *55th AIAA/SAE/ASEE Joint Propulsion Conference*, 2019.

[22] D. I. Suslov, J. Hardi, G. Kühlwein, and M. Oschwald. Hot fire testing of a subscale combustion chamber demonstrated made with selective laser melting. In *6th European Conference for Aeronautics and Space Sciences (EUCASS)*, 2015.

[23] F. P. Incropera, D. P. Dewitt, T. L. Bergman, and A. S. Lavine. *Fundamentals of heat and mass transfer*. Wiley, Hoboken, NJ, sixth edition, 2007.

[24] D. F. Dipprey and R. H. Sabersky. Heat and momentum transfer in smooth and rough tubes at various prandtl numbers. *International Journal of Heat and Mass Transfer*, 6(5), 1962.

[25] C. K. Stimpson, J. C. Snyder, K. A. Thole, and D. Mongillo. Scaling roughness effects on pressure loss and heat transfer of additively manufactured channels. *Journal of Turbomachinery*, 139(2), 2017.

[26] R. J. Kuntz, C. J. O'Brien, and N. E. Van Huff. Advanced propellant staged combustion feasibility program part 1. Tech. rep. AFRPL-TR-66-6, Aerojet Liquid Rocket Co., 1966.

[27] D. D. Davis, L. A. Dee, B. Greene, S. D. Hornung, M. B. McClure, and K. A. Rathgeber. Fire, explosion, compatibility and safety hazards of hydrogen peroxide. Tech. mem. NASA/TM-2004-213151, White Sands Test Facility, 2005.

[28] M. T. Constantine and E. F. C. Cain. Hydrogen peroxide handbook. Tech. rep. AFRPL-TR-67-144, Rocketdyne, 1967.

[29] M. C. Ventura. Long term storability of hydrogen peroxide. In *41st AIAA/ASME/SAE/ASEE Joint Propulsion Conference and Exhibit*, 2005.

[30] FMC Industrial Chemicals Group. Materials of construction for equipment in use with hydrogen peroxide. Bulletin No. 104, 1966.

[31] W. D. Callister Jr. and D. G. Rethwisch. *Materials science and engineering*. Wiley, 2014.

[32] W. C. Schumb, C. N. Satterfield, and R. L. Wentworth. Hydrogen peroxide - part one. Tech. rep., Massachusetts Institute of Technology, 1953.

[33] G. P. Sutton. *History of liquid propellant rocket engines*. American Institute of Aeronautics and Astronautics, Reston, VA, 2006.

[34] R. T. Cook and G. A. Coffey. Space shuttle orbiter engine main combustion chamber cooling and life. In *AIAA/SAE 9th Propulsion Conference*, 1973.

[35] A. Ponomarenko. RPA - Tool for rocket propulsion analysis. In *Space Propulsion Conference*, 2014.

[36] L. Denies. Regenerative cooling analysis of oxygen/methane rocket engines. Master's thesis, Delft University of Technology, 2015.

[37] W. H. Armstrong and E. W. Brogren. Three dimensional thrust chamber life prediction. Tech. rep. NASA-CR-134979, Boeing Aerospace Co., 1976.

[38] J. R. Riccius, E. B. Zametaev, O. J. Haidn, and G. de Boisvilliers. Comparison of 2D and 3D structural FE-analyses of LRE combustion chamber walls. In *42nd AIAA/ASME/SAE/ASEE Joint Propulsion Conference & Exhibit*, 2006.

[39] D. Kuhl, J. Riccius, and O. J. Haidn. Thermomechanical analysis and optimization of cryogenic liquid rocket engines. *Journal of Propulsion and Power*, 18(4), 2002.

[40] United States Department of Defense. Metallic materials and elements for aerospace vehicle structures, MIL-HDBK-5J, 2003.

[41] S. Gordon and B. J. McBride. Computer program for calculation of complex chemical equilibrium compositions and applications. Part 1: Analysis. Tech. rep. NASA-RP-1311, Lewis Research Center, 1994.

[42] J. D. Anderson. *Fundamentals of aerodynamics*. McGraw-Hill, Boston, fourth edition, 2007.

[43] D. R. Bartz. Turbulent boundary-layer heat transfer from rapidly accelerating flow of rocket combustion gases and of heated air. Tech. rep., Jet Propulsion Laboratory, 1963.

[44] D. Preclik, O. Knab, D. Estublier, and D. Wennerberg. Simulation and analysis of thrust chamber flowfields: storable propellant rockets. In *Liquid Rocket Thrust Chambers*, pages 493–525. American Institute of Aeronautics and Astronautics, 2004.

[45] R. C. Ahlert and C. A. Younts. Heat capacities of 90% hydrogen peroxide and commercial anhydrous hydrazine. *Journal of Chemical and Engineering Data*, 13(3), 1968.

[46] G. Scatchard, G. M. Kavanagh, and L. B. Ticknor. Vapor-liquid equilibrium VIII. Hydrogen peroxide-water mixtures. *Journal of the American Chemical Society*, 74(15), 1952.

[47] J. M. Monger, H. J. Baumgartner, G. C. Hood, and C. E. Sanborn. Explosive limits of hydrogen peroxide vapor. *Journal of Chemical & Engineering Data*, 9(1), 1964.

[48] C. N. Satterfield, G. M. Kavanagh, and H. Resnick. Explosive characteristics of hydrogen peroxide vapor. *Industrial & Engineering Chemistry*, 43(11), 1951.

[49] G. Cai, C. Li, and H. Tian. Numerical and experimental analysis of heat transfer in injector plate of hydrogen peroxide hybrid rocket motor. *Acta Astronautica*, 126, 2016.

[50] J. H. Corpening, S. D. Heister, W. E. Anderson, and B. J. Austin. Thermal decomposition of hydrogen peroxide, part 2: modeling studies. *Journal of Propulsion and Power*, 22(5), 2006.

[51] W. T. Foley and P. A. Giguère. Hydrogen peroxide and its analogues IV. Some thermal properties of hydrogen peroxide. *Canadian Journal of Chemistry*, 29(10), 1951.

[52] S. Heo. *Design and valiation of hydrogen peroxide/kerosene bipropellant thruster*. PhD thesis, Korea Advanced Institute of Science and Technology, 2018.

[53] H.-J. Kang. *Ignition and combustion characteristics of non-toxic hypergolic propulsion*. PhD thesis, Korea Advanced Institute of Science and Technology, 2017.

[54] W. C. Schumb, C. N. Satterfield, and R. L. Wentworth. Hydrogen peroxide - part two. Tech. rep., Massachusetts Institute of Technology, 1953.

[55] S. Heo, S. Kwon, and S. Jung. Development of hydrogen peroxide/kerosene 2500 N bipropellant thruster for long-term operation by film cooling. In *52nd AIAA/SAE/ASEE Joint Propulsion Conference*, 2016.

[56] D. E. Coats. Assessment of thrust chamber performance. In *Liquid Rocket Thrust Chambers*, pages 601–620. American Institute of Aeronautics and Astronautics, 2004.

[57] G. P. Sutton and O. Biblarz. *Rocket propulsion elements*. Wiley, New York, NJ, eighth edition, 2010.

[58] G. V. R. Rao. Approximation of optimum thrust nozzle contours. *ARS Journal*, 30, 1960.

[59] Y. Cong et al. Propulsive performance of a hypergolic H_2O_2/kerosene bipropellant. *Journal of Propulsion and Power*, 20(1), 2004.

[60] S. Jo, S. An, J. Kim, H. Yoon, and S. Kwon. Performance characteristics of hydrogen peroxide/kerosene staged-bipropellant engine with axial fuel injector. *Journal of Propulsion and Power*, 27(3), 2011.

[61] J. C. Hyde and G. S. Gill. Liquid rocket engine nozzles. Spec. pub. NASA-SP-8120, National Aeronautics and Space Administration, 1976.

[62] Y. Kwak. Film cooling characteristics of bipropellant rocket engine with storable propellant. Master's thesis, Korea Advanced Institute of Science and Technology, 2014. [in Korean].

[63] J.-G. Kim, K.-J. Lee, S. Seo, Y.-M. Han, H.-J. Kim, and H.-S. Choi. Film cooling effects on wall heat flux of a liquid propellant combustion chamber. In *42nd AIAA/ASME/SAE/ASEE Joint Propulsion Conference & Exhibit*, 2006.

[64] K. Berman and S. J. Andrysiak. Barrier film cooling study. *Journal of Spacecraft and Rockets*, 9(3), 1972.

[65] C. U. Kirchberger. *Investigation on heat transfer in small hydrocarbon rocket combustion chambers*. PhD thesis, Technical University of Munich, 2014.

[66] D. R. Bartz. A simple equation for rapid estimation of rocket nozzle convective heat transfer coefficients. *Journal of Jet Propulsion*, 27(1), 1957.

[67] G.B. Cinjarew and M.V. Dobrovolsky. *Zhidkostnye raketnye dvigateli: Teorija i Proektirovanie [Liquid rocket engines: Theory and Design]*. Gosudarstvennoe Izdatel'stvo Oboronnoj Promyshlennosti [State Publishing House of Defense Industry], Moscow, Russia, 1955. [in Russian].

[68] C. Kirchberger, R. Wagner, H.-P. Kau, S. Soller, P. Martin, M. Bouchez, and C. Bonzom. Prediction and analysis of heat transfer in small rocket chambers. In *46th AIAA Aerospace Sciences Meeting and Exhibit*, 2008.

[69] H. Chiu, K. Gross, and A. Krebsback. Radiation effect on rocket engine performance. In *28th Aerospace Sciences Meeting*, 1990.

[70] R. Siegel and J. Howel. *Thermal radiation heat transfer*. Hemisphere Publishing Corporation, Washington, D.C, third edition, 1992.

[71] D. C. Rousar and N. E. Van Huff. Heat transfer characteristics of 98% H_2O_2 at high pressure and high velocity. Tech. rep. AFRPL-TR-66-263, Aerojet Liquid Rocket Co., 1966.

[72] M. Niino, A. Kumakawa, N. Yatsuyanagi, and A. Suzuki. Heat transfer characteristics of liquid hydrogen as a coolant for the LO2/LH2 rocket thrust chamber with the channel wall construction. In *18th Joint Propulsion Conference*, 1982.

[73] T.-S. Wang and V. Luong. Hot-gas-side and coolant-side heat transfer in liquid rocket engine combustors. *Journal of Thermophysics and Heat transfer*, 8(3), 1994.

[74] W. Nunner. Heat transfer and pressure drop in rough tubes. *VDI-Forschungsheft 455, Series B*, 22, 1956.

[75] C. F. Colebrook and C. M. White. Experiments with fluid frictoin in roughned pipes. *Proceedings of the Royal Society of London. Series A - Mathematical and Physical Sciences*, 161(906), 1937.

[76] A. J. Wildgoose, K. A. Thole, P. Sanders, and L. Wang. Impact of additive manufacturing on internal cooling channels with varying diameter and build directions. In *Turbomachinery Technical Conference and Exposition*, 2020.

[77] M. H. Naraghi and M. Foulon. A simple approach for thermal analysis of regenerative cooling of rocket engines. In *ASME International Mechanical Engineering Congress and Exposition*, 2008.

[78] P. M. van den Berg, B. V. S. Jyoti, and R. J. G. Hermsen. Investigation of thermal behaviour of additively manufactured green bi-propellant thrusters in cubesat applications using transient thermal modelling. In *Space Propulsion Conference*, 2020.

[79] H. Ziebland and R.C. Parkinson. Heat transfer in rocket engines. Tech. Rep. AGARDograph 148, Advisory Group for Aerospace Research and Development, 1971.

[80] M. Bernier. An experimental investigation of heat transfer to hydrogen peroxide in microtubes. Master's thesis, Massachusetts Institute of Technology, 2004.

[81] T. J. Devine et al. Heat transfer characteristics of 98% hydrogen peroxide. Tech. rep., Pratt and Whitney Aircraft, 1961.

[82] R. C. Stechman, J. Oberstone, and J. C. Howell. Design criteria for film cooling for small liquid-propellant rocket engines. *Journal of Spacecraft and Rockets*, 6(2), 1969.

[83] S. J. Minton and T. Linton. Evaluation of the SSRCS engine with hydrazine as fuel, phase 1. Tech. rep. NASA-CR-157089, The Marquardt Company, 1978.

[84] D. Jang, Y. Kwak, and S. Kwon. Design and validation of a liquid film-cooled hydrogen peroxide/kerosene bipropellant thruster. *Journal of Propulsion and Power*, 31(2), 2015.

[85] H. Kang, H. Kim, S. Heo, S. Jung, and S. Kwon. Experimental analysis of hydrogen peroxide film-cooling method for nontoxic hypergolic thruster. *Aerospace Science and Technology*, 71, 2017.

[86] S. T. Koehler and B. T. C. Zandbergen. A comparison between film and transpiration cooling performance in a rocket combustion chamber. In *Space Propulsion Conference*, 2020.

[87] S. J. Minton and T. Linton. Evaluation of the SSRCS engine with hydrazine as fuel, phase 2. Tech. rep. NASA-CR-157956, The Marquardt Company, 1978.

[88] C. B. Allison and G. M. Faeth. Decomposition and hybrid combustion of hydrazine, MMH and UDMH as droplets in a combustion gas environment. *Combustion and Flame*, 19(2), 1972.

[89] J. Won, H. Kang, S. Baek, and S. Kwon. Experimental study on evaporation characteristics of a hydrogen peroxide droplet at elevated temperature. In *7th International Conference on Environment and Industrial Innovation*, 2017.

[90] M. Trotti. Modelling of liquid film cooling on a GOX/kerosene rocket combustion chamber. Master's thesis, Polytechnic University of Milan, 2012.

[91] D. C. Rousar and R. L. Ewen. Combustion effects on film cooling. Tech. rep. NASA-CR-135052, Aerojet Liquid Rocket Co., 1977.

[92] P. A. Giguère and I. D. Liu. Recommended values for the thermodynamic properties of hydrogen and deuterium peroxides. *Journal of the American Chemical Society*, 77(24), 1955.

[93] R. A. Gater and M. R. L'Ecuyer. A fundamental investigation of the phenomena that characterize liquid-film cooling. Tech. rep. NASA-CR-105904, Purdue University Jet Propulsion Center, 1969.

[94] A. Fröhlich, M. Popp, G. Schmidt, and D. Thelemann. Heat transfer characteristics of H2/O2-combustion chambers. In *29th Joint Propulsion Conference and Exhibit*, 1993.

[95] R. T. Cook, E. E. Fryk, and J. F. Newell. SSME main combustion chamber life prediction. Tech. rep. NAS3-23256, Lewis Research Center, 1983.

[96] C. M. Suryavanshi. Thermo-structural analysis of a rocket engine thrust chamber. Master's thesis, University of Pisa, 2018.

[97] K.-J. Bathe. *Finite element procedures*. Prentice Hall, Englewood Cliffs, N.J, 1996.

[98] O. C. Zienkiewicz, R. L. Taylor, and J. Z. Zhu. *The finite element method: its basis and fundamentals*. Elsevier, Oxford, 2005.

[99] J. J. Esposito and R. F. Zabora. Thrust chamber life prediction. Volume 1: mechanical and physical properties of high performance rocket nozzle materials. Tech. rep. NASA-CR-134806, Boeing Aerospace Co., 1975.

[100] L. Werling, T. Hörger, H. Ciezki, and S. Schlechtriem. Experimental and theoretical analysis of the combustion efficiency and the heat loads on a n_2o/c_2h_4 green propellant combustion chamber. In *8th European Conference for Aeronautics and Aerospace Sciences (EUCASS)*, 2019.

[101] I.-K. Sung and W. Anderson. A subscale-based rocket combustor life prediction methodology. In *41st AIAA/ASME/SAE/ASEE Joint Propulsion Conference & Exhibit*, 2005.

[102] EOS GmbH. EOS NickelAlloy IN718, material data sheet, 2020.

[103] W. M. Grisson. Liquid film cooling in rocket engines. Tech. rep. AEDC-TR-91-1, United States Air Force, 1991.

[104] S. Soller et al. Experimental and numerical investigation of liquid film cooling in small rocket engines. In *7th European Conference for Aeronautics and Aerospace Sciences (EUCASS)*, 2019.

[105] J. Görgen, T. Aichner, and M. Frey. Spray combustion and heat transfer modelling in LOX/H2, LOX/HC and MMH/NTO combustion chambers. In *3rd European Conference for Aerospace Sciences (EUCASS)*, 2009.

[106] O. Knab, M. Frey, J. Görgen, C. Maeding, K. Quering, and D. Wiedmann. Progress in combustion and heat transfer modelling in rocket thrust chamber applied engineering. In *45th AIAA/ASME/SAE/ASEE Joint Propulsion Conference & Exhibit*, 2009.

[107] M. Pizzarelli, F. Nasuti, and M. Onofri. A simplified model for the analysis of thermal stratification in cooling channels. In *2nd European Conference for Aerospace Sciences*, 2007.

[108] Military Specifications and Standards. Performance specification propellant, hydrogen peroxide, MIL-PRF-16005F, 2003.

[109] E. Gill. Identifying stakeholder needs. Lecture Slides Course AE4-S12, 2018.

[110] D. T. Thomas. *The development of design rules for selective laser melting*. PhD thesis, University of Wales Institute, 2009.

[111] R. Marchan, A. Oleshchenko, S. Vekilov, M. Arsenuk, and O. Bobrov. 3D printed acoustic igniter of oxygen-kerosene mixtures for aerospace applications. In *8th European Conference for Aeronautics and Space Sciences (EUCASS)*, 2019.

[112] R. P. Pauckert and R. D. Tobin. Space shuttle orbit maneuvering engine reusable thrust chamber program. Tech. rep. NASA-CR-140321, Rockwell International Corp., 1975.

[113] D. Jones. Reusable rocket propulsion for space tourism vehicles. In *40th AIAA/ASME/SAE/ASEE Joint Propulsion Conference and Exhibit*, 2004.

[114] J. O. Milewski. *Additive manufacturing of metals*. Springer, Berlin, Germany, 2017.

[115] C. Kirchberger, G. Schlieben, R. Wagner, H.-P. Kau, C. Mäding, S. Soller, and P. Martin. Design and commissioning of a combustion chamber for cooling and material investigations. In *44th AIAA/ASME/SAE/ASEE Joint Propulsion Conference & Exhibion*, 2008.

[116] R. Arnold, A. Götz, P. Philipp, C. Mäding, G. Obermaier, and J.-N. Caruana. Technology development program for a new storable propellant low-thrust engine demonstrator. In *4th European Conference for Aerospace Sciences (EUCASS)*, 2011.

A

Preliminary Test Plan ESA FLPP Project

As explained in chapter 4, the test data at hand provides limited validation of the developed model. To assess the impact of additive manufacturing on heat transfer and coolant channel flow, more tests are required in a relevant (additively manufactured) configuration. This section briefly describes an experimental approach that may be used for the development of the Mk-II engine as a part of the ESA FLPP project. The development tests proposed in this work are grouped in four different test phases, as illustrated in Figure A.1. In each subsequent phase, the engine is operated closer to the final design point and the risks involved increase. After phase D, the engine development program may be concluded with flight qualification (not included in the figure).

It is important to note that Figure A.1 only outlines test phases that involve the actual AM thrust chamber. Before phase A (non-)destructive tests with witness coupons created during the AM process shall be conducted. The purpose of these tests is to get a better insight into the thermo-mechanical properties of the selected material, as well as chemical compatibility. Examples of this are the immersion screening tests at ambient and moderate temperatures, which are already conducted (section 4.4). Other tests that could be considered before phase A include tensile tests, cycle life tests, and thermal conductivity measurements. These tests are not yet conducted.

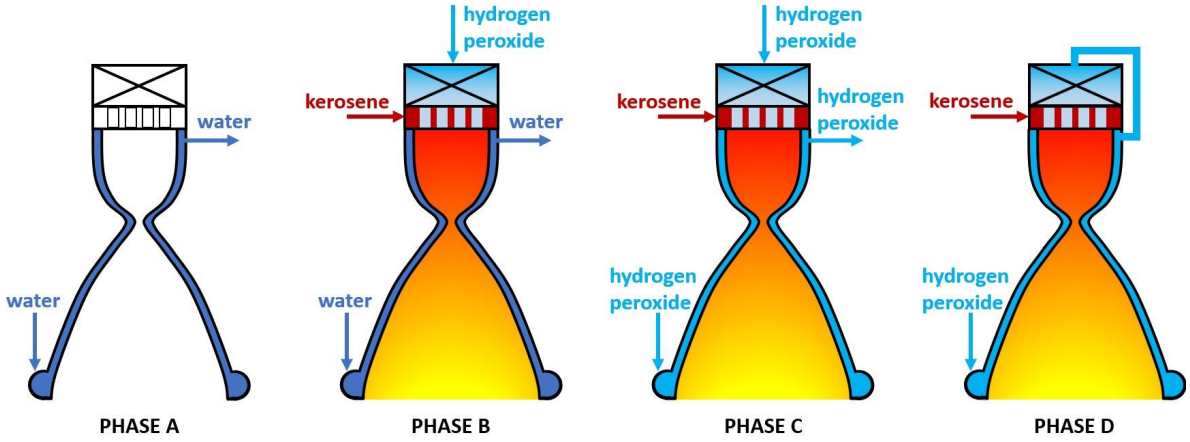

Figure A.1: Schematic overview of different phases of the Mk-II FLPP development program.

Phase A testing of the thrust chamber involves non-destructive tests with the thrust chamber, without an ongoing combustion reaction. Water is used as a simulant fluid for hydrogen peroxide. Examples of experiments that should be conducted in this phase are leak tests and hydraulic characterization tests. The results of phase A tests can be used to:

- Extend the validation of the pressure drop model introduced in section 2.4 to AM channels. This can be done by measuring mass flow rate and pressure at the cooling jacket inlet and outlet,

similar to the approach taken in Figure 4.15.

- Validate the discharge characteristics of the propellant injector and film coolant injector.
- Demonstrate leak-tightness of the cooling jacket.
- Demonstrate structural integrity of the thrust chamber, without the presence of a thermal load.

Phase B testing of the thrust chamber involves the hot-fire test of the chamber in both monopropellant and bipropellant mode. In these experiments, water is used as a coolant fluid. The advantage of this approach is that the fluid properties of water are well-described in literature and that potential decomposition effects in the cooling channels can be neglected. It is recommended to start hot-fire tests at a mixture ratio or chamber pressure below the nominal design point. These operating conditions can be increased after each test. This way, the thermal loading of the wall can be carefully controlled. For this design, it is strongly recommended to use an instrumented chamber setup, similar to refs. [115, 116]. The results of phase B tests can be used to:

- Extend the validation of the hot gas heat transfer models used introduced in subsection 2.5.2 in both the nozzle and cylindrical section of the chamber (close to the injector). This can be done using thermocouple readouts or measurements of the coolant temperature rise in different cooling loops along the chamber length.
- Extend the validation of the analytical film cooling model introduced in section 2.5 to higher operating pressures and the injector/chamber configuration of the Mk-II. This can be done by means of thermocouples placed in the ribs of the wall, similar to the approach taken by Heo [52].
- Validate the local wall temperatures predicted by TDCAS, by means of thermocouple readouts.
- Demonstrate structural integrity of the thrust chamber, under the presence of a thermal load.

Tests executed in phase C are similar to those in phase B. The primary difference is that hydrogen peroxide is used as a coolant, in an open configuration (similar to dump cooling). These experiments can be used to identify potential decomposition effects in the cooling channels. This can be achieved by collecting the hydrogen peroxide at the outlet of the cooling jacket. Concentration measurements before heating (inlet) and after heating (outlet) may be used to further our understanding of potential decomposition effects in the cooling channels. This measurement approach is similar to that taken by Rousar & Van Huff who experimented with 98% hydrogen peroxide in Inconel 718 tubes. Moreover, the open-loop architecture allows the designer to control the coolant mass flow rate independently of the core mass flow rate. This way, experiments with different coolant mass flow rates, and thus coolant flow velocities, can be conducted. Results of phase C may also be used to validate the rough channel convection models introduced in section 2.4.

In phase D tests, the outlet of the cooling jacket is attached to the catalytic reactor, thereby closing the engine cycle. With the feed system attached to the combustion chamber, the complete Mk-II engine (pumps, thrust chamber, injector, reactor) can be qualified to ECSS-E-ST-35C. The results that are obtained during these tests summarize tasks 8A, 8B, and 9 of the ESA FLPP project, which were presented in Figure 1.5, and can be used to experimentally validate compliance with the customer requirements.

B

Specifications of the Verification Engine

This appendix contains a comprehensive overview of the design parameters of the verification engine. This engine design is used extensively throughout this work for verification of TDCAS. The verification engine is a **hypothetical engine design** which is created in the Rocket Propulsion Analysis software to meet similar requirements as the Mk-II thruster. A complete set of thrust chamber design specifications is provided in Table B.1. Additionally, the chamber contour and cooling channel parameters are presented in Figure B.1. This data allows other researchers to recreate this engine an reproduce results that are discussed in this work.

Table B.1: Design parameters of the thrust chamber which is used for verification of TDCAS.

Oxidizer	90% H_2O_2	Coolant	90% H_2O_2
Fuel	RP-1	Coolant flow direction	Opposite to gas
Mixture ratio	8	Coolant inlet temperature	20 °C
Chamber pressure	4 MPa	Coolant inlet pressure	12 MPa
Total mass flow rate	1.1 kg/s	Coolant mass flow rate	0.98 kg/s
Contraction ratio	10	Number of channels	30
Expansion ratio	10	Channel bifurcations	none

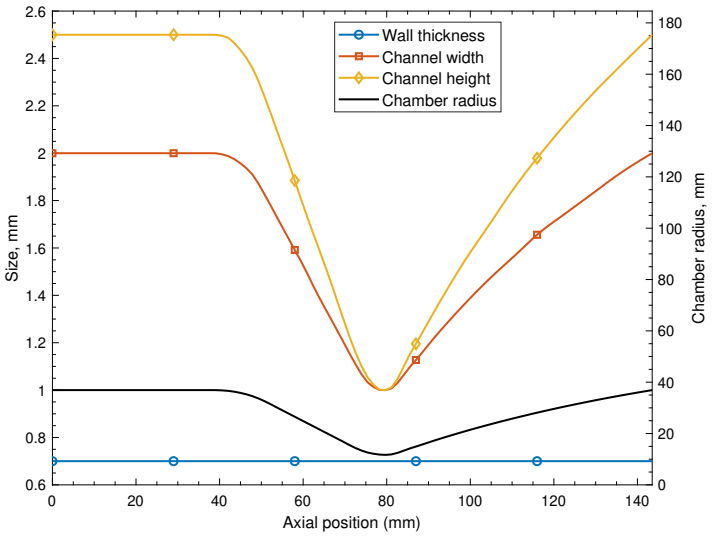

Figure B.1: Cooling channel and wall geometry of the verification engine described in Table B.1.

C

Additional User Information for TDCAS

User Inputs

This section briefly describes the required user inputs in TDCAS, based on the proposed AM chamber design with film cooling (see also subsection 5.3.2). The first input block includes the basic design parameters of the thruster, in terms of chamber pressure, mixture ratio, and propellant flow rates.

```
engine.design.chamber_pressure = 1.0*50e5;                    % Pa
engine.design.mixture_ratio = 8;                              % –
engine.design.total_flow_rate = 1.125;                        % kg/s
engine.design.oxidizer = 'H2O2_90';                           % –
engine.design.fuel = 'RP1';                                   % –
```

Second, the user must define the geometry parameters of the thrust chamber. This can be done with a source file that is imported into TDCAS. The source file is a .csv file that includes the coordinates of the thrust chamber, the wall thickness, the number of cooling channels, the cooling channel width, the cooling channel height, and the radius of curvature. All channel and contour dimensions are defined in millimeters.

```
% 1) Source file for chamber/channel definition.
engine.design.source = readmatrix('inconel_design_film.csv');          % .csv
```

The purpose of the source file is to avoid TDCAS from re-calculating the thrust chamber geometry when a design is fixed (e.g. for the chambers that are considered for the validation of the code). Alternatively, TDCAS can calculate the geometry of the thrust chamber and cooling passages, which is based on the following user inputs:

```
% 2A) Automatic sizing of the chamber/channels
engine.design.lstar = 0.6;                                    % m
engine.geometry.radius_chamber = 0.04;                        % m
engine.geometry.convergent_angle = 45;                        % deg
engine.design.chamber_curvature = 0.5;                        % r/r_chamber
engine.design.upstream_nozzle_curvature = 1.4;                % r/r_throat
engine.design.downstream_nozzle_curvature = 0.382;            % r/r_throat
engine.design.nozzle_length_fraction = 0.8;                   % –
engine.design.exit_pressure = 65000;                          % Pa

engine.design.channel_count_throat = 40;                      % –
engine.design.minimum_wall_thickness = 0.5;                   % mm
engine.design.channel_input = 'cw';                           % 'cw'/'lw'
```

```
% 2B) Channel definition | pos, - | tw, mm | cr, mm | cw/lw, mm |
engine.design.channel = [...
    0.00, 0.5, 0.8, 4.0;
    0.50, 0.5, 0.8, 4.0;
    0.90, 0.5, 0.8, 1.0;
    1.00, 0.5, 0.8, 1.0;
    1.01, 0.5, 0.8, 1.0;
    2.00, 0.5, 0.8, 4];
```

The chamber curvature, upstream nozzle curvature, and downstream nozzle curvature represent the radius of curvature of the chamber, divided by the chamber radius or nozzle throat radius. The entrance and exit angles of this parabolic curve are automatically calculated as a function of the expansion ratio and nozzle length fraction, based on typical values provided by Rao [58]. For sizing of the cooling channel geometry, the user has the option to define either the channel width “cw” or land/rib width ”lw”. Sizing is based on a channel definition matrix that includes the non-dimensional position, the wall thickness (in mm), the channel height (in mm), and the channel width or land width (in mm). A non-dimensional position of 0 corresponds to the injector plane, 1 to the nozzle throat plane, and 2 to the nozzle exit plane. Stations in-between these three locations can be defined for local optimization of the cooling channel geometry. Based on the input matrix, the channel geometry at all computational stations is determined utilizing linear interpolation.

Third, the user inputs the materials of the liner and closeout, the outer wall emissivity, and the burst safety factor. The wall and liner files are inserted via Matlab functions that relate material properties to temperature. If the wall emissivity is set to 0, radiation of the chamber wall to the environment is neglected.

```
engine.wall.liner_file = @Inconel_718;                % @filename
engine.wall.closeout_file = @Inconel_718;             % @filename
engine.wall.emissivity = 0;                                % -
engine.wall.burst_safety_factor = 2;                       % -
```

The fourth set of inputs include the estimated characteristic velocity efficiency, thrust coefficient efficiency, hot gas convection file, and hot gas radiation model. For the hot gas convection file, the user has the option to select the correlation of Bartz or Cinjarew & Dobrovolsky. For the hot gas radiation, the method of Kirchberger et al. is used. For more information on these methods, the reader is referred to section 2.3.

```
engine.performance.combustion_efficiency = .99;            % -
engine.performance.nozzle_efficiency = .96;                % -
engine.hotgas.file = @bartz;                          % @filename
engine.hotgas.include_radiation = true;               % true/false
```

Fifth, the film coolant modeling inputs are defined. If the film cooling fraction is set to 0, the presence of the film coolant is neglected in the simulations. It is worth noting the current release of TDCAS does not allow the user to easily change the simulation inputs for the NASA SP-8124 model (film entrainment factors, decomposition rate constants, heat capacities, decomposition temperature, etc.). These are all included in the model file and are manually varied during the sensitivity study of this thesis. As a result, it is more difficult to change these values, which is an important improvement for a future release of the code. The definition of the film coolant file is similar to the definition of the liner and closeout files and based on integrated Matlab functions that provide the coolant properties as a function of temperature.

```
engine.film.type = 'oxidizer';                    %'oxidizer'/'fuel'
engine.film.coolant_file = @H2O2_90;                  % @filename
engine.film.fraction = 0.1;                                % -
engine.film.orifice_diameter = 0.3/1000;                   % m
engine.film.orifice_count = 40;                            % -
engine.film.injection_temperature = 298;                   % K
engine.film.characteristic_velocity = 935.2;             % m/s
engine.film.liquid_effectiveness = 0.46;
```

Sixth, the regenerative coolant is defined. For convective heat transfer, the user can select the modified Nunner correlation and Dipprey-Sabersky correlation, as explained in subsection 2.4.1. Furthermore, the user can select the coolant flow direction to be parallel to the direction of the hot gas flow, or in the direction opposite to the gas flow.

```
engine.coolant.file = @H2O2_90;                          % @filename
engine.coolant.model = 'modified-nunner';                % 'model'
engine.coolant.direction = 'counter';                    % 'counter'/'parallel'
engine.coolant.mass_flow_rate = 1.0;                     % kg/s
engine.coolant.wall_roughness = 121e-6;                  % m
engine.coolant.inlet_temperature = 273+20;               % K
engine.coolant.inlet_pressure = 93e5;                    % Pa
```

Last, the simulation settings are defined for the setup of the 2-D finite element algorithm. The user can select a 2-D temperature solution of the wall (response2D='all') or a 1-D temperature solution of the wall (responseD='none').

```
engine.solver.response_2D = 'all';                       % 'all'/'none'
engine.solver.axial_spacing = 1/1000;                    % m
engine.solver.mesh_refinement = 1.0;                     % -
engine.solver.maxiter = 200;                             % -
engine.solver.tol_convergence = 1e-6;                    % -
engine.solver.solve_mechanical = false;                  % true/false
engine.solver.ambient_temperature = 294;                 % K
engine.solver.ambient_pressure = 101325;                 % Pa
```

To initiate TDCAS, the user selects the "run job" command, as shown below. This automatically starts the chamber sizing routine and 2-D analysis of the chamber wall, following the routines depicted in Figure 2.1.

```
engine = run_job(engine);
```

Mesh Structuring

As mentioned in subsection 2.2.3, TDCAS automatically generates a structured mesh, based on a user-defined mesh refinement depth. The mesh consists of a matrix that stores the nodal coordinates and a matrix that stores the nodal connectivity. An example of the nodal coordinate matrix (for the first five nodes) is shown below,

```
% engine.mesh.nodes (94050x4 double)
1        -0.00281430143053995    0.0357590901657499    0.156000000000000
2        -0.00267393204991734    0.0357698603494143    0.156000000000000
3        -0.00253352147948871    0.0357800795267023    0.156000000000000
4        -0.00239307188216773    0.0357897475401958    0.156000000000000
5        -0.00225258542146922    0.0357988642409666    0.156000000000000
```

where the first column indicates the node number, the second column the x-coordinate of the node, the third column the y-coordinate of the node, and the fourth column the z-coordinate of the node. All these coordinates are based on the reference frames established in Figure 2.6. For the element connectivity matrix, the following format is used,

```
% engine.mesh.elems (83700x6 double)
1        1        1        2        23       22
2        1        2        3        24       23
3        1        3        4        25       24
4        1        4        5        26       25
5        1        5        6        27       26
```

where the first column indicates the element number, the second column the material identifier, and the last four columns the nodal connectivity of the element. For instance, the first quadrilateral element

(southwest corner in Figure C.1) comprises the nodes with numbers 1, 2, 13, and 12. The element numbering is initiated in the southwest corner of the mesh (below the rib).

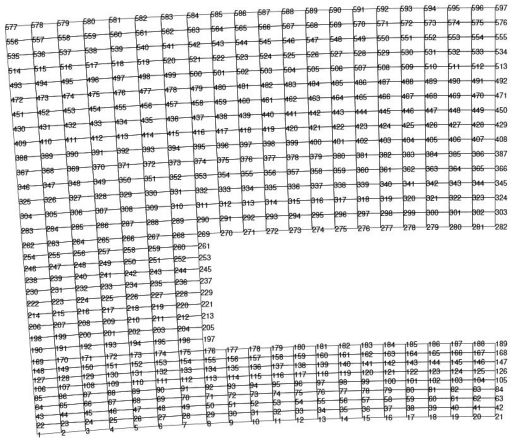

Figure C.1: Structured mesh with nodal numbering.

A second part of the mesh definition are the boundary conditions, which are automatically evaluated based on user inputs. The format used for storing boundary conditions is shown below, for the first five elements on the gas-side boundary.

```
% mesh.edges.gas_side
1   1   2   0.0763826971675482   −0.997078574423004   12
2   2   3   0.0722289151410433   −0.997388080847946   12
3   3   4   0.0680738799645324   −0.997680282889551   12
4   4   5   0.0639176637266909   −0.997955175478198   12
5   5   6   0.0597603385365592   −0.998212753844588   12
```

The first column in the edge matrix contains the element number and the second and third column the boundary node numbers. For instance, in the first element, only nodes 1 and 2 are located on the gas-side boundary, which also becomes clear upon inspection of Figure C.1. The fourth and fifth columns indicate the outward unit normal vector, and the sixth column the edge location in the isoparametric reference frame (which is used in the finite element method). Here, “12” implies that the boundary lies on the edge between (-1,-1) and (+1,-1) in the isoparametric reference frame. For more details on the physical meaning of isoparametric coordinates, the reader is referred to the literature [97, 98].

Program Outputs

Once the code is finished, all results are stored in “engine” object handles. This way, individual outputs of the code are easily accessible for further investigation. The following object handles are used in TDCAS:

```
engine
├── design
├── performance
├── geometry
├── wall
├── hotgas
├── film
├── coolant
├── solver
└── mesh
```

It is worth mentioning that the outputs “geometry” and “wall” have several points of overlap. The output set “geometry” contains the geometrical parameters of the thrust chamber, such as the chamber geometry and cooling channel definition. These outputs can be used in the follow-up detailed design in computer aided design software. The output set “wall”, on the other hand, contains solutions of the 2-D finite element analysis.

D

Publication Acta Astronautica

In the literature study that was conducted prior to this thesis, a detailed summary was provided regarding the current state-of-the-art and capabilities of AM applied to the construction of liquid rocket engine thrust chambers. The results of the literature study are summarized and published in a journal article in Acta Astronautica, which is co-authored by TU Delft supervisor Dr. Angelo Cervone and Paul Gradl, a leading industry expert in the field of AM who is working for NASA Marshall Space Flight Center. The article can be found under the following citation:

F. Kerstens, A. Cervone, and P. Gradl. End to end process evaluation for additively manufactured liquid rocket engine thrust chambers. Acta Astronautica, 182, 2021. doi: 10.1016/j.actaastro.2021.02.034.

For a more detailed explanation of the different AM production techniques applied to liquid rocket engines, the reader is encouraged to study this paper. The abstract of the accepted article is presented below:

Abstract
High performance liquid rocket engines require cooling to maintain structural integrity of the combustion chamber which is exposed to high thermal and environmental loads. For many systems, this is achieved by means of regenerative cooling, where a cold coolant flows through passages around the chamber wall whilst extracting heat from the wall. A novel production technique that is often considered for this is metal additive manufacturing (AM). The use of additive manufacturing opens up new opportunities for engine design, which can result in more competitive designs, from both a technical and economical perspective.

This paper provides a detailed literature review on the current state-of-the-art, challenges, and opportunities for designing additively manufactured liquid rocket engines by means of the laser powder bed fusion and powder or wire-based directed energy deposition (DED) techniques. A detailed, systematic explanation is provided on the steps involving the creation of additively manufactured thrusters including the process considerations, AM techniques and post-processing operations.